ACS SYMPOSIUM SERIES 978

Polymer Durability and Radiation Effects

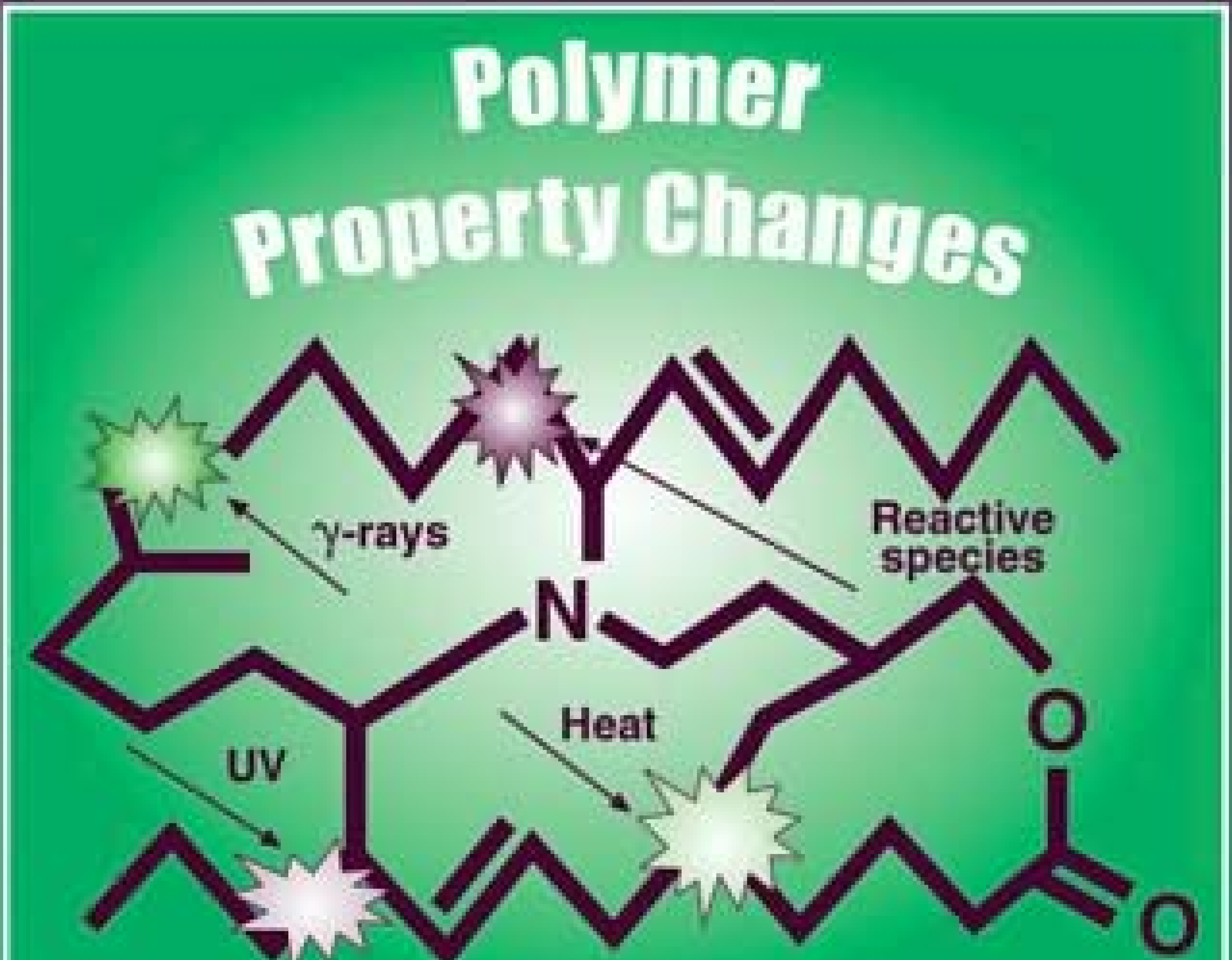

EDITED BY
Mathew C. Celina and Roger A. Assink

Polymer Durability and Radiation Effects

ACS SYMPOSIUM SERIES **978**

Polymer Durability and Radiation Effects

Mathew C. Celina, Editor
Sandia National Laboratories

Roger A. Assink, Editor
Sandia National Laboratories

Sponsored by the
Division of Polymer Chemistry, Inc.

American Chemical Society, Washington, DC

Library of Congress Cataloging-in-Publication Data

Polymer durability and radiation effects / Mathew C. Celina, editor, Roger A. Assink, editor ; sponsored by the Division of Polymer Education, Inc.

p. cm.—(ACS symposium series ; 978)

Includes bibliographical references and index.

ISBN 978-0-8412-6952-1 (alk. paper)

1. Polymers—Effect of radiation on—Congresses. 2. Polymers—Deterioration—Congresses.

I. Celina, Mathew C. II. Assink, Roger A. III. American Chemical Society. Division of Polymer Chemistry.

QD381.9.R3P65 2007
620.1'9204228—dc22

2007060793

The paper used in this publication meets the minimum requirements of American National Standard for Information Sciences—Permanence of Paper for Printed Library Materials, ANSI Z39.48-1984.

Copyright © 2008 American Chemical Society

Distributed by Oxford University Press

All Rights Reserved. Reprographic copying beyond that permitted by Sections 107 or 108 of the U.S. Copyright Act is allowed for internal use only, provided that a per-chapter fee of $36.50 plus $0.75 per page is paid to the Copyright Clearance Center, Inc., 222 Rosewood Drive, Danvers, MA 01923, USA. Republication or reproduction for sale of pages in this book is permitted only under license from ACS. Direct these and other permission requests to ACS Copyright Office, Publications Division, 1155 16th Street, N.W., Washington, DC 20036.

The citation of trade names and/or names of manufacturers in this publication is not to be construed as an endorsement or as approval by ACS of the commercial products or services referenced herein; nor should the mere reference herein to any drawing, specification, chemical process, or other data be regarded as a license or as a conveyance of any right or permission to the holder, reader, or any other person or corporation, to manufacture, reproduce, use, or sell any patented invention or copyrighted work that may in any way be related thereto. Registered names, trademarks, etc., used in this publication, even without specific indication thereof, are not to be considered unprotected by law.

PRINTED IN THE UNITED STATES OF AMERICA

Foreword

The ACS Symposium Series was first published in 1974 to provide a mechanism for publishing symposia quickly in book form. The purpose of the series is to publish timely, comprehensive books developed from ACS sponsored symposia based on current scientific research. Occasionally, books are developed from symposia sponsored by other organizations when the topic is of keen interest to the chemistry audience.

Before agreeing to publish a book, the proposed table of contents is reviewed for appropriate and comprehensive coverage and for interest to the audience. Some papers may be excluded to better focus the book; others may be added to provide comprehensiveness. When appropriate, overview or introductory chapters are added. Drafts of chapters are peer-reviewed prior to final acceptance or rejection, and manuscripts are prepared in camera-ready format.

As a rule, only original research papers and original review papers are included in the volumes. Verbatim reproductions of previously published papers are not accepted.

ACS Books Department

Preface

The performance of polymeric materials and the science of polymer degradation and material reliability are of ever increasing importance for sustainable global economic development. Many of the challenges we face require better performing, less costly and more specialized polymers ranging from composites and thermo-sets to thermoplastics and elastomers. Whether they find their way into consumer products, energy applications, microelectronics, defense areas, or space exploration, the one commonality is a requirement for improved reliability and the ability to predict their behavior in a variety of environmental conditions. - Polymer performance is governed by the polymer's ability to resist chemical and physical degradation processes under thermal, photo, radiation, hydrolytic, and biological conditions.

The 27 chapters in this symposium series book provide an overview of the current research and development trends related to the performance, degradation, and reliability of polymers. This book is an extract of the 46 excellent papers presented at the symposium *Polymer Performance and Degradation* at the Pacifichem conference held in December 2005 in Honolulu, Hawaii. This symposium expands upon previous special symposia on radiation effects in polymers that were organized as part of the Pacifichem conferences held every five years. Despite the unavoidable progression of established researchers like Clough, George, Gillen, Hill, Seguchi, and many others into their retirement, there is a sustained research interest, and it is with great satisfaction that we continue to witness contributions from new talents entering this field. In fact, as this book demonstrates, the complexity of this field is broader than ever before. Once again, it has been a great opportunity for the Pacific Rim researchers to interact and discuss the latest trends in the durability, radiation effects, and improved performance of polymers. Due to the success of the symposium, many presenters inquired about the possibility of contributing a chapter to a conference proceedings

book. We hope that we were able to present here a selection and overview of the many research activities that were being addressed. Many of the contributing authors are recognized as experts in their respective fields and have contributed innovative concepts.

The authors and the editors sincerely hope that this overview will improve the understanding of the degradative behavior of polymers and will assist our fellow research and development scientists in their pursuit of improved materials.

Mathew C. Celina
R&D, Organic Materials Department
Sandia National Laboratories
P.O. Box 5800, MS 1411
Albuquerque, NM 87185

Roger A. Assink
R&D, Organic Materials Department
Sandia National Laboratories
P.O. Box 5800, MS 1411
Albuquerque, NM 87185

In Polymer Durability and Radiation Effects; Celina, M., et al.;
ACS Symposium Series; American Chemical Society: Washington, DC, 2007.

Polymer Durability and Radiation Effects

In Polymer Durability and Radiation Effects; Celina, M., et al.;
ACS Symposium Series; American Chemical Society: Washington, DC, 2007.

Chapter 1

Reassessing Polymer Lifetime Prediction Methods with Improved Characterization and Diagnostics

Robert Maxwell[1], Sarah Chinn[1], Rid Gee[1], Bryan Balazs[1], Naida Lacevic[1], Julie Herberg[1], Erica Gjersing[1], Mogon Patel[2], Hilary Wheeler[3], and Mark Wilson[3]

[1]Lawrence Livermore National Laboratory, 7000 East Avenue, L–235, Livermore, CA 94551
[2]Atomic Weapons Establishment, Aldermaston, Reading RG7 4PR, United Kingdom
[3]Honeywell FM&T, Kansas City Plant, 2000 East 95th Street, Kansas City, MO 64141–6159

A combination of Magnetic Resonance Imaging (MRI), Multiple Quantum Nuclear Magnetic Resonance (MQ-NMR), Molecular Dynamics modeling, and traditional mechanical testing approaches have been used to provide a more scientific prediction of the aging behaviors of two silica-filled siloxane polymers. These materials are especially prone to part-to-part and service condition variablilities, and thus a combination of non-destructive magnetic resonance techniques and atomistic modeling has been used to determine physical and chemical inhomogeneities which are, respectively, already present in the material and potentially occurring as a result of cavitation upon applied stress. To elucidate the overall degradation behavior of the polymers studied and thus add scientific evidence to their lifetime predictions several different damage mechanisms (thermal, radiation, and mechanical) have been studied individually and in combination to elucidate the overall aging behavior for a variety of service conditions. Running concurrent to these experimental and modeling efforts, an analysis has been done to more precisely define the operational capabilities of the polymers relative to their requirements, leading to an even more accurate lifetime prediction capability due to the ability to define performance margins with their associated uncertainties.

 © 2008 American Chemical Society

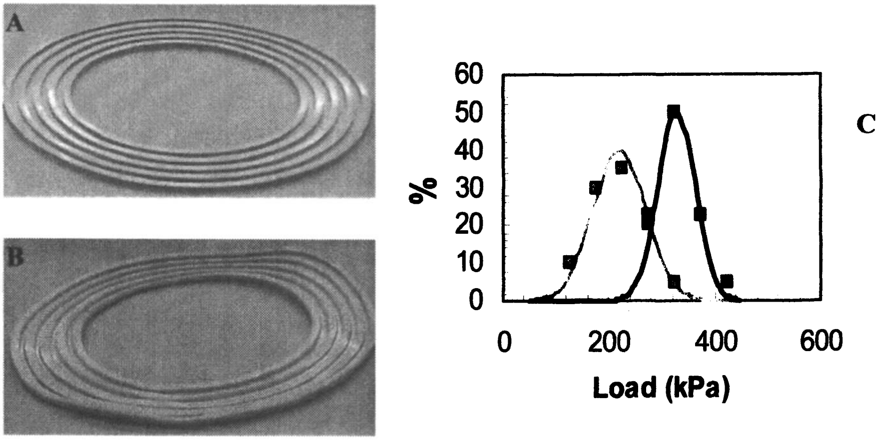

Figure 1. Photographs of (A) undamaged and (B) damaged DC745U ribbed pads; (C) histogram of percent load retention at a given compressive gap for open celled foam of M97 components at production (black) and disassembly 2-20 years after service (gray). (See page 1 of color inserts.)

Introduction

Accurate predictions of the effective lifetimes of polymeric components and composites are made more difficult by several factors inherent in the chemistry and aging behavior of these materials. First, compounding and processing of the materials often leads to inhomegeneities in the structure, resulting in dissimilar behavior between components or between different locations within an individual component., as shown in the photos of the pristine and a typical service return component shown in Figure 1A and 1B. Furthermore, testing of typical samples at both production and upon disassembly is often characterized by broad distributions in the mechanical performance, as shown in Figure 1C. These distributions can be due to part-to-part variations or from differences in service conditions, thus complicating the determination of accurate lifetimes.

Second, extrapolations of short-term test data suffer from a variety of deficiencies: acceleration of an inappropriate aging mechanism relative to real service conditions, wide error bars in the test data leading to ever-increasing uncertainty in extrapolated lifetimes, and, often, the inability to unobtrusively measure the real aging properties of interest in an *in situ* test. Third, such materials often exhibit non-linear aging behavior, where the variation of an aging parameter outside of a particular bound leads to rapid degradation of the component, i.e., a "cliff". Finally, in many cases the exact failure criteria may not even be firmly established, e.g., it may be readily ascertained when an adhesive bond fails, but the point at which a cushioning component is deemed to failed its functional requirements is often not well defined.

To address each of these factors above, we have applied specific techniques to two silica-filled silicone polymers with the aim of reducing the uncertainty associated with life-performance predictions of these particular polymers. To characterize inhomogeneities within components or between components, we use non-destructive MRI techniques to assess variations in polymer dynamic motion behavior. To provide realistic extrapolations of accelerated-aged samples, we couple laboratory testing of individual acceleration inputs to multi-damage-mode tests, accented by atomistic and molecular modeling simulations which allow access to temporal and spatial damage conditions not realistically obtained by laboratory testing. Wear-out approaches are used to locate regimes of rapid degradation of the materials, and these tests are validated by the laboratory tests above. Finally, we engage in a close examination of what specific engineering performance criteria a particular component has, and how aging trends affect actual component performance relative to these criteria. Described here is an outline for polymer assessments and lifetime predictions--one based on an understanding of the production variations, on the engineering and chemistry requirements for the component, on testing and modeling of several aging mechanisms, and on the validation of laboratory and modeling data with that collected during in-service assessments.

Experimental

Experiments were performed on DC745U and M97 silica-filled silicone polymers as described elsewhere [1-5]. The gum stocks for all formulations were co-block polymers of dimethylsiloxane, diphenylsiloxane, methylphenylsiloxane, and/or methylvinyl siloxane. The gum stock was reinforced with high surface area silica filler and crosslinked with peroxide curing agents. These materials were tested in both new as well as "service return" conditions.

Static, uniaxial NMR relaxometry experiments were performed using spin-echo decay curves obtained via a Carr-Purcell-Meiboom-Gill [6] pulse sequence on an NMR Mobile Universal Surface Explorer (MOUSE) from Bruker Optics operating at 16 MHz [5,7]. Decay curves were processed with the Contin application from Bruker Optics, which uses an inverse Laplace transform to yield the distribution of T_2 relaxation times. All MRI experiments were performed on a Bruker Avance 400 MHz spectrometer equipped with a high-resolution Micro5 microimaging system with either a 25 mm coil or a 5 mm coil depending on the size of the sample. A (Hanh-echo) T_2 weighted Single Point Imaging (SPI) pulse sequence was used as described in ref. 4. Multiple Quantum (MQ) NMR was also applied to these materials as described elsewhere and insight was obtained on the network structure from the distributions of the residual dipolar couplings extracted from the MQ growth curves using a fast Thikonov regularization (FTIKREG), algorithm [1,5].

In Polymer Durability and Radiation Effects; Celina, M., et al.;
ACS Symposium Series; American Chemical Society: Washington, DC, 2007.

For our Molecular Dynamics studies, we used a united-atom model representation of PDMS that treats each carbon and its bonded hydrogen atoms as a single united particle. An extensive study of the structural and dynamical properties of this PDMS united-atom model used in this paper is described by Frischknecht *et al* [8,9]. Our simulations consisted of 40 120-mer PDMS polymer chains (19,200 total 'atoms'), where each PDMS monomer contains a single Si, and O atom and 2 CH_3 united-atoms, simulated using 3D cubic periodic boundary conditions. The simulations were generated using constant particle number, pressure, and temperature (*NPT*) dynamics at a pressure of 0 Pa using the standard Nose-Hoover method for constant *NPT* dynamics [10]. The velocity Verlet time integration method was used with a time step of 1 *fs*. The bulk PDMS ensemble was then initially simulated at 550 K, where the periodic box was allowed to relax under *NPT* conditions. The volume equilibration process was carried out for a minimum duration of 5 *ns*. Following this step, the system was cooled in *NPT* runs in increments of 50 K and equilibrated for 5 *ns* at eacho of the incremental temperatures down to 300 K. After the initial equilibration process, simulations were performed at 300 K in $N\sigma T$ MD runs under constant stress, σ, applied uniaxially along the y-axis of the periodic simulation cell (initial dimensions of 8.5 × 8.5 × 8.5 nm). In all extension simulations the applied tensions ranged from 40-80 MPa. The normal stress on the other faces of the simulation box is set to zero. The coupling constants for the barostat and thermostat are 1000 fs and 100 fs respectively, and were kept constant for all extension simulations. All computations were carried out with a modified version of LAMMPS [11].

Results and Discussion

Field returned Samples:

The results of 2-D T_2 weighted MRI experiments on two used ribbed DC745U pads, one with visually evident areas of permanent deformation and one without (see Figure 1A and 1B) are shown in Figure 2. The contrast parameter in this figure is the T_2 relaxation time, which has been shown to be a sensitive measure of the polymer segmental dynamics and thus the network structure [12]. The undamaged pad section (on the left of Figure 2) is characterized by a fairly uniform T_2 throughout the material part with the exception of the lower signal intensity at the surface, while the damaged pad (on the right of Figure 2) was characterized by areas of brighter signal due to increased T_2 relaxation time, or higher mobility of the polymer network. It is important to note that brighter signals are present in patches in the interior of the polymer pads, which may be due to the combined effects of cross-link density and compression set. The MRI data strongly suggests that the deformation is due to aging of an originally heterogeneous network structure.

The MRI results shown above were confirmed with non-imaging unilateral relaxometry via the NMR MOUSE. The NMR MOUSE employs CPMG [6] spin-echo based relaxometry methods, which have been shown to have empirical correlations to differences in crosslink density [4]. The results of these studies are shown in the histograms shown in Figure 3. Here, we clearly observed an altered value of the crosslink density indirectly through a change in the measured relaxation time. Experiments have been performed on approximately 40 damaged pads and in all cases clear statistical differences (T_2 (damaged) – T_2

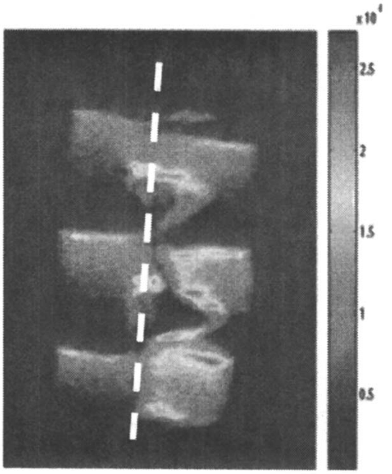

Figure 2. T_2 weighted MRI image back-to-back ribbed DC745U pads (undamaged on left, damaged on right). Intensity scale on right from low (blue) to high (red) T_2. (Reproduced with permission from reference 4. Copyright 2006 Elsevier.) (See page 1 of color inserts.)

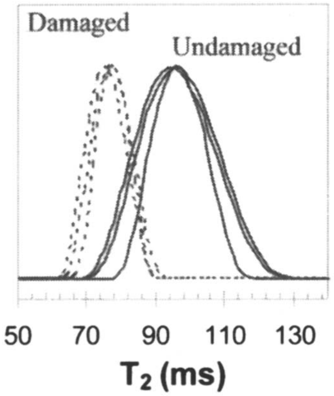

Figure 3. Results of uniaxial relaxometry using the NMR MOUSE of the damaged and undamaged DC745 parts shown in Figures 1 and 2. Multiple lines are replicate runs on different damaged or undamaged spots on the same pad. (Reproduced with permission from reference 4. Copyright 2006 Elsevier.)

(undamaged)) > 7 σ_{T2}) between damaged areas and undamaged areas were observed. In these studies, damaged pads were observed to have a lower T_2 than the undamaged pads – a trend reverse of what is seen in high field Hanh-echo based experiments, like the MRI results shown above. The origin of this reversal is still under investigation and could be due to susceptibility gradients from the pad shape or internal gradients and chain diffusion. Such reversals have been observed in other studies [29-31].

Two possible origins of the damage have been investigated: localized high levels of load at the point of deformation and chemical heterogeneity at

production that leads to heterogeneous aging during service. Attempts to reproduce the deformation in pads with over testing with significantly higher loads than seen in service have, to date, been unable to reproduce the deformation. In order to provide credence to our hypothesis that the deformation observed was due to structural heterogeneities present in the pad at production, several new pads were analyzed with the NMR MOUSE.

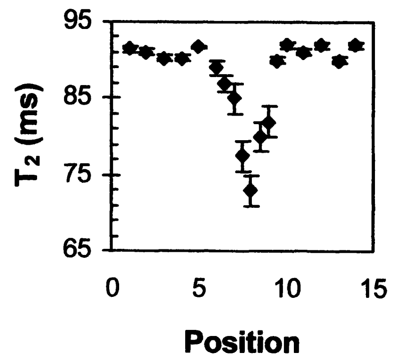

Figure 4. Results of unilaterial relaxometry via the NMR MOUSE on a pristine DC745 ribbed pad scanned along the circumference of one rib. Areas of low T_2 map out areas of abnormal crosslink density that presumably lead to increased compression set upon service aging.

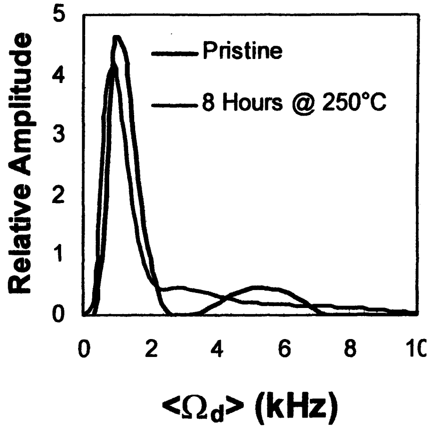

Figure 5. Distributions of residual dipolar couplings obtained from a Thikonov regularization of the MQ-NMR growth curve for thermally aged silicone foam. The residual dipolar coupling has been shown to be an indirect measure of crosslink density and represents essentially a histogram of the crosslink density in the polymer network. Aged samples have been shown to undergo chain scissioning reactions.(See page 2 of color inserts.)

Figure 4 shows the results of scanning over a region of a new pad, clearly identifying an area of low T_2 relaxation time, potentially correlating to an area of future susceptibility to damage. Accelerated aging of one such new pad was observed to lead to deformation.

Accelerated Aging Tests:

Accelerated aging by both single mechanisms or multiple mechanisms is typically used to gain insight into the consequences of aging. We have

previously reported the results of our studies on the effects of radiation and desiccation on the properties of these materials by NMR, DMA, and solvent swelling techniques [1-5, 13-18]. These studies have indicated that desiccation leads to significant reductions in the segmental dynamics of the polymeric material, presumably due to modification at the filler-polymer interface [15]. Exposure to ionizing radiation (alpha and gamma) resulted in crosslinking of the polymer network and dose and atmosphere-dependent changes in the filler-polymer interactions [1-3]. Thermal degradation of the polymer leads to complex changes in the network structure as determined by the distribution of residual dipolar couplings obtained by multiple quantum NMR methods [1, 5, 19, 20]. Figure 5 shows the results of MQ-NMR analysis of the residual dipolar couplings for thermally aged samples. The residual dipolar coupling has been shown to be an indirect measure of crosslink density, and the plot shown in Figure 5 represents essentially a histogram of the crosslink density in the polymer network. As can be seen in the figure, the polymer network is characterized by two broad distributions at high residual dipolar coupling and low residual dipolar coupling. These two populatons have been assigned to areas of low and high crosslink density. The data show that upon thermal exposure, the average residual dipolar coupling in both populations– and thus the crosslink density – decreased. Thus, the degradation of these materials in high temperature environments is likely to be due to chain scissioning reactions.

We have also studied the combined effects of mechanical strain and either radiation exposure or thermal degradation. When exposed to gamma radiation while under tensile strain, DC745 and M97 materials have been shown to take a permanent tensile set, as shown in Figure 6A [5]. ^{1}H relaxation and multiple quantum NMR studies have shown that the tensile strain creates strain dependent order that is locked in upon exposure to radiation. Dewetting at the polymer-filler interface and evidence supporting the formation of microvoids were also observed [5]. Elastomeric foams of M97 are subject to increased compressive set when exposed to gamma radiation while under compression which has been shown to affect the load at a given gap, as shown in Figure 6B. The tendency of these materials to take a compression set under exposure to radiation has also been studied by X-ray based tomography [23].

Thermal degradation in the presence of compression has been studied by variable temperature compression set experiments, as described in Patel, et al 2002 [21] – and shown in Figure 7. The time dependence of the compression set at multiple temperatures is shown in Figure 7A, indicating a thermally activated process. Time-Temperature-Superposition treatment of the data has provided a master curve to predict compression set at room temperature and is shown in Figure 7B and has measured an activation energy for network relaxation of 78 kJ/mol – consistent with thermally activated degradation of the network chains rather than physical relaxation processes which would be expected to have an activation energy near 25 kJ/mol [21].

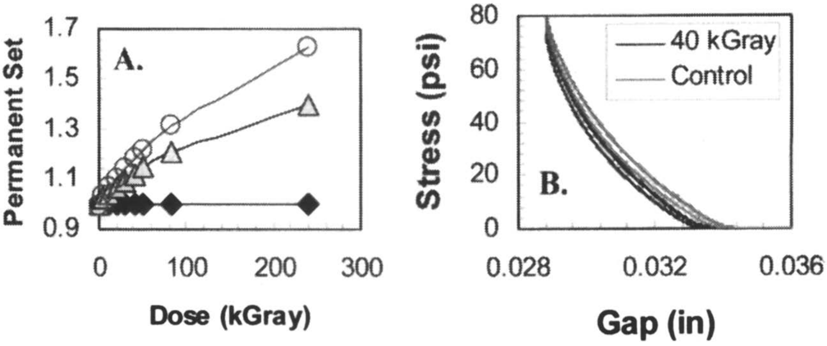

Figure 6. (A) Permanent tensile set in M97 solid elastomers exposed to gamma radiation while under no elongation (solid diamonds), 150% of unperturbed length (triangles), and 200% of unperturbed length (circles). (B) Stress as a function of compressed gap for M97 foam aged under compressed to 25% (deposited gamma radiation dose of 0 and 40 kGray). Note the delayed onset to stress at low compression due to permanent compression set. (See page 2 of color inserts.)

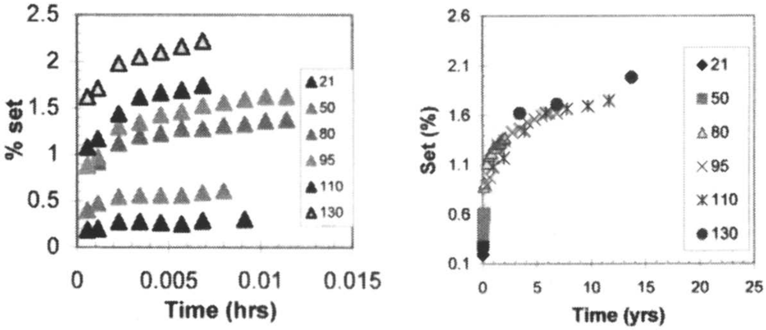

Figure 7. Results of time and temperature dependent studies of compression set in open-celled, porous M97 silicone foams. (A) % compression set as a function of time for the temperatures (°C) listed; (B) Master curve at 21 °C derived from a time-temperature-superposition analysis of the data in (A). The activation energy derived from this analysis was 78 kJ/mol. (See page 3 of color inserts.)

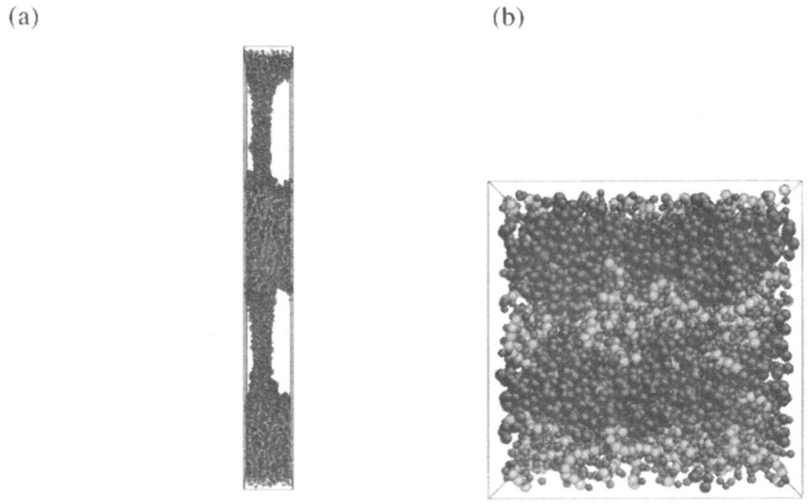

Figure 8. (a) Snapshot of the PMDS melt at σ = 60 MPa and t = 1.5 ns. Particles that are on the surface of the cavity are colored green. (b) Initial configuration of the PDMS melt and cavity particles are traced back to the initial configuration and colored green. (Reproduced with permission from reference 26. Copyright 2006 Elsevier.) (See page 3 of color inserts.)

Accelerated aging studies must be used with care, as has been pointed out by Clough, et al [23]. If available, accelerated aging studies should be validated by comparison to field return samples. This however, limits the predictive ability to time frames where field returns actually exist. In cases where validating with service returns is impractical due to time or cost issues, novel approaches employing aging of old samples can be employed. These have been described in detail by Gillen, et al (2001) [24]. Such methods provide increased ability to gauge aging of polymeric materials beyond current service aged sample inventory.

MD Studies of Aging Mechanisms:

The above experimental studies illustrate a range of mechanisms that contribute to the aging of filled silicone elastomers over decades. The experimental data also highlights a significant difficulty in studying complex, multimode aging of components. The presence and effects of some aging mechanisms can only be inferred from bulk behavior and thus are hard to predict with high confidence. Changes at the filler-polymer interface, changes in polymer chain order in the bulk due to strain and/or aging, and the formation of nano-scale voids, are three such mechanisms where bulk NMR data has

suggested involvement in aging mechanisms [25-26]. We have employed molecular dynamics (MD) methods to understand these mechanisms and their potential effect on the chemical and physical properties of filled silicone materials [25-26].

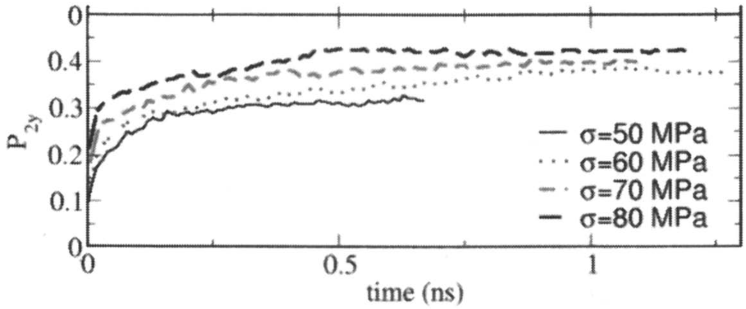

Figure 9. Time dependence of the orientational parameter P_{2y} at various stresses. Stress values increase from the bottom up. (See page 4 of color inserts.)

Previously, we have shown that dehydration of the silica filler leads to increased interaction of the interfacial polymer chains with the inorganic surface by the removal of the coulombic screening affect of the interfacial water [25], thus affecting the polymers' segmental dynamics. Recently, we have also studied bulk PDMS melts upon uniaxial extension via MD simulations. Visual inspection of the PDMS melt configurations after the application of tensile stress indicates that voids/cavities form at sufficiently high stresses, as shown in Figure 8. The appearance of cavities is known to lead to mechanical failure in elastomeric systems. The particles that form the cavity surface (green "atoms" in Figure 8) are initially in a "lamella" like structures before uniaxial extension, where the lamellae are perpendicular to the axes of extension at the initial time. This demonstrates that cavitation is a highly localized process because the lamellae remain preserved until cavity formation. Further, particles forming the cavity surface move very little during the void formation.

These studies have also shown that the PDMS chains become elongated and ordered as a function of applied tension [26]. Since monomer alignment on the surface of the cavity may have significant effect on the PDMS/filler system upon extension, we investigate the evolution of the global orientational order parameter, P_{2y}, for the melt and particles that belong to the cavity:

$$P_{2y} = \left\langle \frac{3\cos^2\theta_y - 1}{2} \right\rangle, \qquad (1)$$

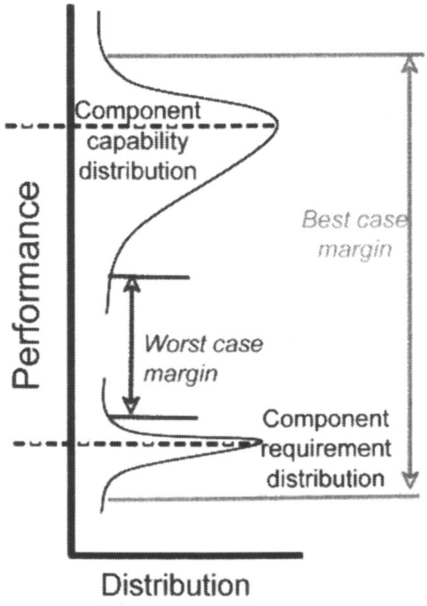

Figure 10. Comparison of hypothetical set of distibutions for a component's capability versus its requirement, with potential variations in performance margins illustrated. (See page 4 of color inserts.)

where θ is the angle between two "chord" vectors and $\langle ... \rangle$ denotes the average over all chord pairs, and where θ_y is the angle between the chord vector and the direction in which the stress is applied. A "chord" is defined as a line segment connecting two second nearest neighbors on the same chain. The angle, θ, is the dot product between every other chord vector defined in this way.

Figure 9 shows the time dependence of P_{2y} for the monomers which will form the surface of the cavity at late times. At the initial time, the monomers are randomly oriented with respect to the direction of extension, reflected in the near zero values of P_{2y}. At later times, P_{2y} increass, which is a manifestation of the onset of fibril formation about the cavity. This may have a significant effect on the filled PDMS system because the chains may also align on the surfaces of the filler particles.

The Role of Detailed Understanding of Failure Criteria:

As discussed in the Introduction, accurate predictions of polymer component lifetimes must consider not only the aging behavior of the material

but also an assessment of what constitutes component failure and how much variability is associated with these criteria. This is shown graphically in Figure 10. Of course, there may be several failure criteria representing multiple chemical, engineering, or other performance requirements. Furthermore, different component applications can have very different distributions of performance and requirements than the one example shown in Figure 10. For example, medical implants and deep space probes are examples where a wide separation in the two distribution bands representing capability and requirement, as well as narrow widths of the bands, are highly desired. On the other hand, cheap, easily replaceable consumer products (e.g., rubber bands) are not driven by such rigorous requirements. For all of our DC745U and M97 polymer components, we have assessed all functional requirements including: chemical stability, strength, compression set, load bearing behavior, outgassing characteristics, and radiation resistance. In each of these areas, we independently assess each of the component behaviors as a function of age, with the effective minimum lifetime being defined as the shortest lifetime from the set of all of the behaviors.

Conclusions

We have combined MRI, NMR, and MD simulations to obtain increased insight into component structural and chemical homogeneities, property distributions, between capabilities and requirements, and the aging mechanisms that contribute to life limiting degradation in two families of silica-filled silicone elastomers. MRI results characterized chemical heterogeneities internal to the component and also confirm that the damaged DC745U pads can be non-destructively assessed during or after service lifetimes in terms of their spatial inhomogeneities in the mobility of the polymer network. Unilateral NMR relaxometry has been used to characterize chemical heterogeneities in the original pristine material that lead to the damage observed visually and by MRI. Accelerated aging studies using strain, desiccation, and radiation and elevated temperature exposure have been performed and MQ-NMR experiments have allowed us to characterize the changes in distributions of crosslink density, filler-polymer interaction, void formation, and chain ordering in these materials as a function of accelerated age. Molecular Dynamics simulations have been used to investigate subtle aging mechanisms and effect that are difficult to characterize experimentally, such as localized chain ordering and the initial stages of void formation while experiencing high degrees of strain. This data is being input into models that account for complex service requirements to develop high-fidelity lifetime estimates.

Acknowledgements

The authors would like to thank Steve DeTeresa for his help performing and interpreting much of the mechanical property assessments and for designing multimechanism aging experiments. This work was performed under the auspices of the U. S. Department of Energy by University of California Lawrence Livermore National Laboratory under contract No. W-7405-Eng-48.

References

1. Maxwell, R. S.; Chinn, S. C.; Solyom, D.; Cohenour, R. *Macromolecules*, **2005**, *38*, 7026.
2. Chien, A.; Maxwell, R. S.; Chambers, D.; Balazs, B; LeMay, J. *Rad. Phys. Chem.* **2000**, *59*, 493.
3. Maxwell, R. S.; Balazs, B. *J. Chem. Phys.*, **2002**, *116*, 10492.
4. Herberg, J. L.; Chinn, S. C.; Sawvel, A. M.; Gjersing, E.; Maxwell, R. S. *Poly. Deg. Stab.*, **2006**, *91*, 1701.
5. Chinn, S. C.; DeTeresa, S.; Sawvel, A.; Shields, A.; Balazs, B.; Maxwell, R. S. *Poly. Deg. Stab.*, **2006**, *91*, 555.
6. Meiboom, S.; Gill, D. *Rev. Sci. Instr.* **1958**, *29*, 688.
7. Eidmann, G.; Savelsberg, R.; Blumer, P.; Blumich, B. *J. Mag. Res. A* **1996**, *122,* 104.
8. Frischknecht, A. L.; Curro, J. G. *Macromolecules* **2003**, *36*, 2122.
9. Sun, H.; Rigby, D. *Spectrochimica Acta A Molec. Biomol. Spect.* **1997**, *53*, 1301.
10. Nose, S. *Molecular Physics* **1984**, *52*, 255.
11. Plimpton, S. J. *J. Comp. Phys.* **1995**, *117*, 1.
12. Cohen-Addad, J. P. *Prog. NMR Spect.* **1993**, *25*, 1.
13. Patel, M.; Morrell, P. R.; Murphy, J. J.; Skinner, A.; Maxwell, R. S. *Poly. Deg. Stab.* **2006**, *91*, 406.
14. Balazs, B.; DeTeresa, S.; Maxwell, R.; Kokko, E.; Smith, T. *Poly. Deg. Stab.* **2003**, *82*, 187.
15. Maxwell, R. S.; Balazs, B.; Cohenour, R.; Prevedel, E. *Macromol. Symp.* **2003**, *202*, 291.
16. Maxwell, R. S.; Balazs, B. *Nucl. Inst. Meth. B* **2003**, *208*, 199.
17. Maxwell, R. S.; Cohenour, R.; Sung, W.; Solyom, D.; Patel, M. *Poly. Deg. Stab.* **2003**, *80*, 443.
18. Chien A. T.; Felter T.; LeMay J. D.; Balooch, M. *J. Mat. Res.* **2000,** *15*, 838.
19. Saalwachter, K.; Ziegler, P.; Spyckerelle, O.; Haidar, B.; Vidal, A.; Sommer, J.-U. *J. Chem. Phys.* **2003**, *119*, 3468.

20. Gjersing, E.; Chinn, S. C.; Maxwell, R. S.; Eastwood, E.; Bowen, D.; Stephens, T. *Macromolecules*, **2006**, submitted.
21. Patel, M.; Skinner, A. R. *Poly. Deg. Stab.* **2001**, *73,* 399.
22. Kinney, J. H.; Marshall, G. W.; Haupt, D. L. *J. App. Poly. Sci.* **2001**, *80*, 1746.
23. Clough, R. L.; Billingham, N. C.; Gillen, K. T. (eds), *Polymer Durability, Degradation, Stabilization, and Lifetime Prediction, Advances in Chemistry Series #249*; ACS: Washington, D.C. 1996.
24. Gillen, K. T.; Celina, M. *Poly. Deg. Stab.* **2001**, *71*, 15.
25. Gee, R. H.; Maxwell, R. S.; Balazs, B. *Polymer* **2004**, *45*, 3885.
26. Lacevic, N. M.; Maxwell R. S.; Saab A.;Gee R. H. *J. Phys. Chem. B* **2006**, *110*, 3588.
27. Dompas, D.; Groeninckx, G. *Polymer* **1994**, *35*, 4743.
28. Castellano, M.; Conzatti, L.; Costa, G.; Falqui, L.; Turturro, A.; Valenti, B.; Negroni, F. *Polymer* **2005**, *46*, 695.
29. Luo, H..; Kluppel, M.; Schneider, H. *Macromolecules* **2004**, *37*, 8000.
30. Saalwachter, K. *Macromolecules* **2005**, *38*, 1508.
31. Kenny, J.C.; McBrierty, V.J.; Rigbi, Z; Douglass, D.C. *Macromolecules* **1991**, *24*, 436.

Chapter 2

Aging Complexities Induced by the Organotin Catalyst in Foamed Polysiloxane Elastomers

Mogon Patel, Steve Black, and Julian Murphy

Atomic Weapons Establishment, Aldermaston, Reading RG7 4PR, United Kingdom

An organotin ingredient, Tin 2-ethylhexanoate, is used as a catalyst in the synthesis of foamed polysiloxane elastomers. We report on the nature of residual catalyst species and the influence on polymer thermal and nuclear relaxation properties. Our results show that the catalyst plays an active part in the chemistry and is chemically modified as a result. Mössbauer spectroscopy shows that the tin (IV) phase predominates in the as-synthesised material, representing some 67% of the total tin signal, with the remainder being unreacted tin (II) species. Thermal ageing causes changes in the dispersion of the tin species, including oxidation of the tin(II) phase and the in-situ production of stannic oxide. Furthermore, increases in total tin catalyst content appear to induce chain confinement effects, restricting segmental chain dynamics and hindering polymer crystallisation phenomena. It is likely that the soluble tin (II) compounds are catalytically active in polymer hydrolysis and network rearrangement processes, therefore, careful control of the amounts of catalyst used, as well as dispersion, are important for material reliability.

 © 2008 American Chemical Society

Introduction

An important route to the production of foamed polysiloxane rubbers relies on the use of a low molecular weight silicone gum and on a series of tin catalysed cure and gas formation reactions. Normally, a dihydroxy terminated poly dimethylsiloxane containing a small amount of silica filler, together with a polyfunctional crosslinking agent (e.g. tetrapropylsilicate), is used as the starting material.

Tin (II) and Tin (IV) catalysts are frequently used to catalyse the condensation chemistry of dihydroxy terminated polydimethylsiloxane with alkoxysilanes. For polyfunctional crosslinking agents, this will result in gelation[1]. Also initiated by the tin catalyst, is the reaction of terminal or side-chain silane hydrogen with hydroxyl groups on the polysiloxane chains, generating hydrogen gas as the blowing agent in these systems [2].

Van Der Weij [3] has shown that the true catalyst is an organotin hydroxide which is a hydrolysis product of the tin carboxylate ligands. The formation of the reactive tin hydroxide is dependent on finite levels of water within the gum and carboxylic acid is produced as a byproduct during the hydrolysis reaction. The acid can have a significant impact on the thermal degradation properties of the polymer. In the presence of residual tin catalyst, it is likely to accelerate protonation of the siloxane bond and reduce the energy barrier for hydrolysis of the polymer [4]. Stein et al [5] has shown that the tin catalyst, together with water, induces siloxane bond rearrangement (cleavage and recombination of siloxane linkages) effects that can accelerate chemical stress relaxation effects. Furthermore, our previous studies have shown that the tin species in the rubber have a significant influence on the important load bearing characteristics of the material as well the low temperature thermal properties [6].

Since it is very likely that tin compounds are catalytically active in hydrolysis and network rearrangement processes, an understanding of the nature of the tin species in silicone elastomers is required. Of particular interest is the change in the nature of these species with age and the influence on polymer mechanical properties. We have utilised recoilless nuclear resonant fluorescence (better known as Mössbauer spectroscopy) to assess the tin compounds in the rubber. ^{119}Sn is Mössbauer active, undergoing a resonant absorption on irradiation with gamma rays. The difference in the position of resonance of a sample relative to the source is referred to as the isomer shift (IS). This parameter is particularly sensitive to the electron density in the 5s-valence orbital in tin. In addition, the interaction of the nuclear quadrupole with the electric field gradient produces a phenomenon called quadrupole splitting (QS). This parameter is sensitive to any imbalance in the p and d orbital electron distribution and is, in general, more diagnostic (providing chemically useful information) than the isomer shift [2].

In Polymer Durability and Radiation Effects; Celina, M., et al.;
ACS Symposium Series; American Chemical Society: Washington, DC, 2007.

We have also used Nuclear Magnetic Resonance (NMR) based spin-spin relaxation measurements to look at ageing effects as minor changes in the polymer structure, under long term or accelerated ageing conditions, can be monitored using this technique [7].

Materials

The elastomers investigated were prepared by curing a silicone resin (supplied by Rhodia Silicones) containing a blend of ingredients: polysiloxane-diols, small amounts of hydrogen-methyl polysiloxane, tetraalkoxy silane and fumed silica filler. An organotin ingredient, stannous 2-ethylhexanoate, supplied as a 77% w/w solution in 2-ethyl hexanoic acid, was used as a cure initiator. Typically, 5 wt. of initiator is mixed into the polysiloxane resin. After the initial cure, the material is post-cured at 70°C for 16 h in an air oven.

Results and Discussion

Mössbauer experiments were performed in transmission mode using a calcium stannate source. Spectra were deconvoluted using standard methods to separate contributions from Tin (II) and Tin (IV) peaks. The Mössbauer spectrum of the cured rubber (see ***Figure 1***) shows the Tin (II) and Tin (IV) oxidation states, with the Tin (IV) species representing approximately 67% of the total tin signal. Overall, the IS/QS values suggest that the Tin (IV) species formed in the rubber is most probably Tin (IV) oxide, SnO_2. The presence of some residual unreacted Tin (II) catalyst within the cured rubber is clearly evident.

In an earlier publication [8], our Mössbauer work on the pure organotin catalyst showed that the Tin (II) phase (with an IS of 3.2 and a QS of 1.98, *Figure 1*) represents some 79% of the total tin resonance. These results demonstrate that the organotin catalyst is not behaving as a true catalyst as it is chemically modified (oxidised) as a result of the synthesis process.

The oxidation of the Tin (II) phase coincides with the conversion of 2-ethylhexanoate ligands to carboxylic acid and the accumulation of acidic species within the polymer matrix [9]. The presence of acid, combined with the unreacted or residual Tin (II) compounds in the rubber, is of significant concern, as these species can be catalytically active in polymer hydrolysis and network rearrangement processes.

Thermal Ageing Effects

The area under any peak in the Mossbauer spectrum is the resonance area and is generally related to the number of resonant nuclei per unit area of cross

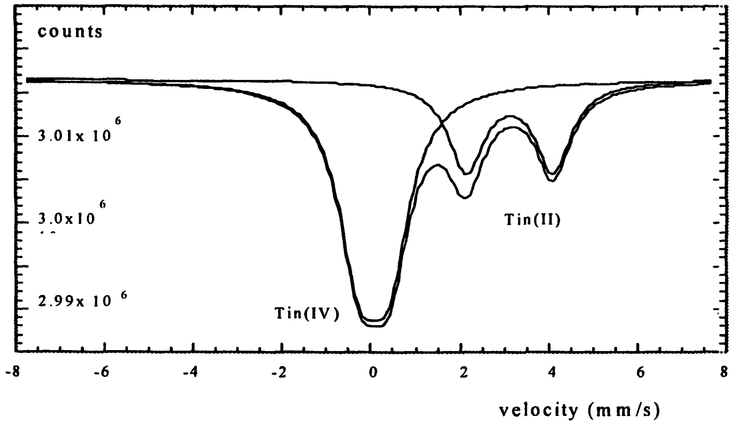

Figure 1. Mössbauer spectrum from the cured rubber showing the predominant Tin (IV) oxidation state

section in the material. The Mossbauer tin intensities as a function of age are shown in *Figure 2*. Clearly, artificial ageing, for short periods at high temperatures in air or in sealed (inert atmosphere) conditions, leads to almost complete conversion of the Tin (II) to Tin (IV). In comparison, samples aged for long periods (5 years) at room temperature (real-time aged), show no detectable Tin (II), implying total conversion to the higher oxidation state. Although the Tin (II) peak is not eliminated by the toluene extraction, it is very much reduced in relative area, suggesting that a fraction of the original residual catalyst has been extracted by the toluene. Furthermore, there appears to be no reduction in the intensity of the tin (IV) peak suggesting that these tin fragments are strongly resistant to extraction. This may be because this phase is strongly bound to the polymer chains or insolubility of the residue in toluene. Overall, these results suggest that cured samples contain both a mobile tin phase (which is essentially toluene extractable) and relatively strongly bound tin species (most probably the SnO_2).

Further supporting evidence for the extent of incorporation of the tin species within the polymer network comes from Neutron Activation Analysis (NAA) studies. NAA studies have shown a reduction in the total tin content in toluene extracted rubbers suggesting that some of the tin species is at least partially extractable [6].

Overall, our results suggest that solvent extraction has little impact on the Tin (IV) species, implying a phase that has strong interactions with the polymer network. In contrast, the Tin (II) species appears to be partially extractable, suggesting a more mobile component. To further assess the mobility and to map the tin distribution, we have used X-ray fluorescence studies. *Figure 3* shows the

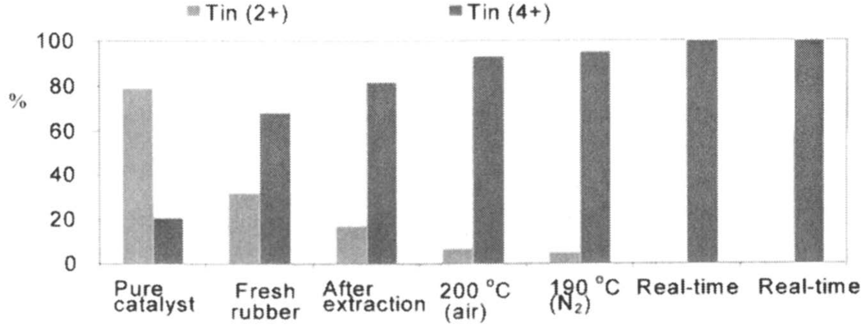

Figure 2. Mossbauer tin intensities (from integrated peak area measurements) as a function of age. Also shown is the effect of solvent extraction. Real-time aged samples were obtained from field trials.

tin distribution by X-ray fluorescence in fresh and thermally aged samples, shown in cross section. The yellow coloured areas are representative of the tin species present within the blue coloured polysiloxane foamed structure. The dark areas are the pores. The tin has an uneven distribution with regions of relatively high concentration (hot spots) and areas showing very little tin. Furthermore, thermal ageing causes a change in the tin dispersion, with a layering effect that appears to be concentrated under the skin of the elastomer. At this stage, it is unclear whether the mobility of the tin is influenced by gravity or by polymer density effects. These results, together with those in *Figure 2*, suggest that the mobile tin phase in the X-ray florescence images is most likely to be Tin (II) species, as this phase is toluene extractable and therefore less tightly bound to the polymer.

In summary, there is a gradual oxidation of the Tin (II) to Tin (IV), the release of hydrolysis inducing carboxylic acid and migration of tin phases. Taken together, these results suggest that the material is continuously changing with time, and it is also becoming more inhomogenous. This is very undesirable as life limiting stress relaxation processes can vary in different parts of the same sample. Ways to minimise these effects are to reduce the tin catalyst concentration used in synthesis and/or to apply effective post cure treatments.

Chain Confinement Effects

We have used thermal analysis to study the impact of the tin species on polymer transitional behaviour. Differential Scanning Calorimetry studies shows that the polymer has a glass transition temperature (T_g) at $-120^{o}C$ and a

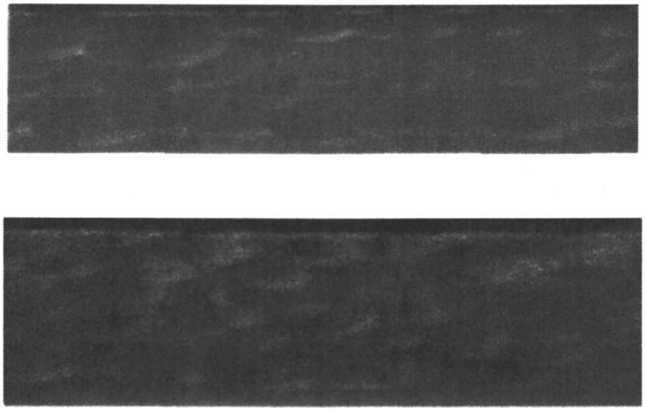

Figure 3. Cross section of Tin distribution by X-ray fluorescence (top, unaged material; bottom, thermally aged at 50 °C for 3 months)

crystallisation melting transition (T_m) centred at –45°C, see *Figure 4*. In addition, *Figure 5* shows that increasing the catalyst concentration has a significant influence on the rate of crystallisation. Higher catalyst levels lead to a significantly reduced melting (T_m) transition.

Studies reported by Maxwell et al [7] show that this behaviour is analogous to the effects of gamma radiation, with high gamma doses causing chain crosslinking effects that reduce crystallization rates. In addition, our studies using model siloxanes of different crosslink density provide additional supporting evidence that increased chain binding interactions influence chain mobility and crystallisation phenomena [6]. Crystallisation is a phenomenon strongly dependent on the ability of polymer chains to align or move into required positions and it is presumably more difficult for a polymer with a high crosslink to carryout this process. This effect could be considered similar to the impact of bulky side groups (e.g. phenyl rings) which will also reduce the ability of a polymer to crystallise.

Taken together, its therefore likely that the results presented in *Figure 5* may be indicative of chain confinement effects induced by the presence of the tin species. Its possible that the tin species can physically interact with adjacent polymer chains, reducing the ability of the polymer chains to align sufficiently for crystallisation. The most likely source for the increased interaction is the tin (IV) oxide (SnO_2) phase within the rubber. This could have active surface groups (e.g. OH), that might increase the effective crosslink density of the polymer by forming hydrogen bonding type interactions [2].

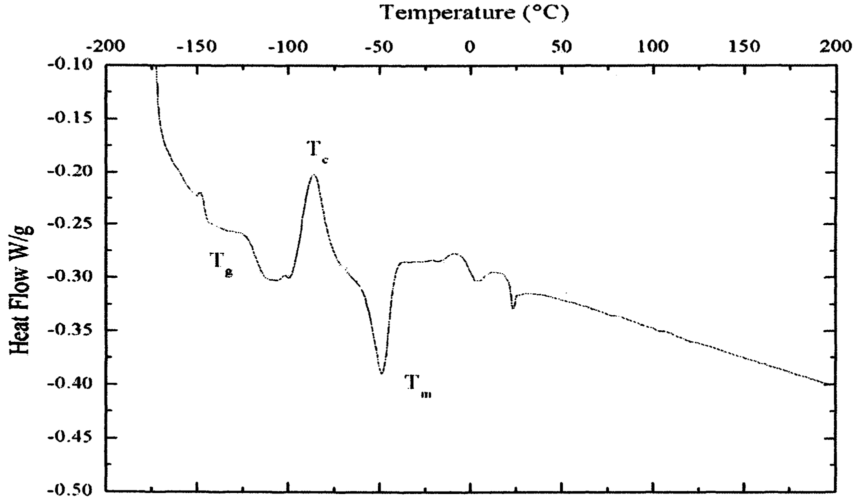

Figure 4. Typical DSC Trace of foamed elastomer.

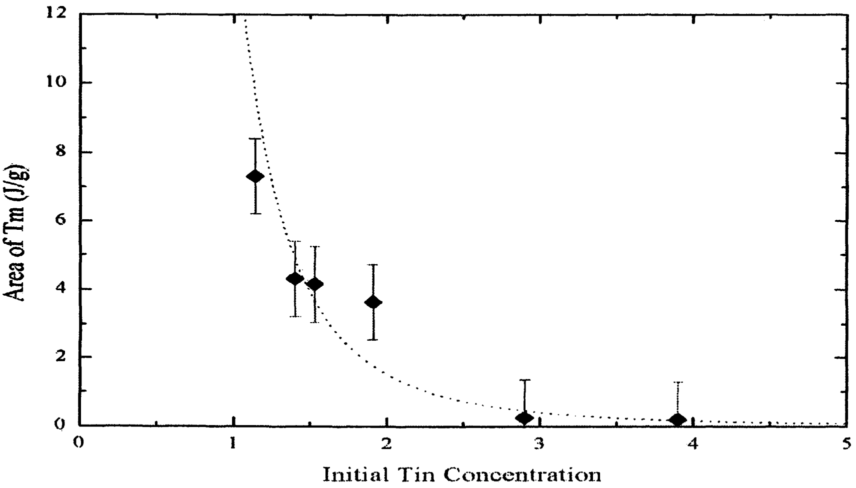

Figure 5. Crystalline melting peak area as a function of tin concentration (% tin by NAA).

Segmental Chain Dynamics

To shed further light on the potential chain confinement effects of the tin phase, we have carried out spin-spin or transverse relaxation (T_2) measurements. NMR relaxation data of stereochemically different nuclei will give useful information on the local environments of these nuclei. The more resticted the environment around a given group type, the more rapidly it will relax.

A NMR Mouse (Mobile Unit for Surface Exploration) and a CPMG spin echo sequence were used to assess T_2 as a function of tin content. *Figure 6* and *Figure 7* show that as the catalyst levels in the reaction mixture are increased, the level of chain restiction is increased and the T_2 is lowered. These results suggest that the tin affects the mobility of the more rigid environments (short T_2, such as crosslinks) as well as the mobility of chain ends and mid chain components (long T_2).

These results, together with the thermal analysis studies, illustrate the chain confinement and reductions in chain mobility induced by the tin phase. The concerns are that these species can therefore potentially influence the important stress relaxation or compression set properties of the elastomer, thus influencing material reliability.

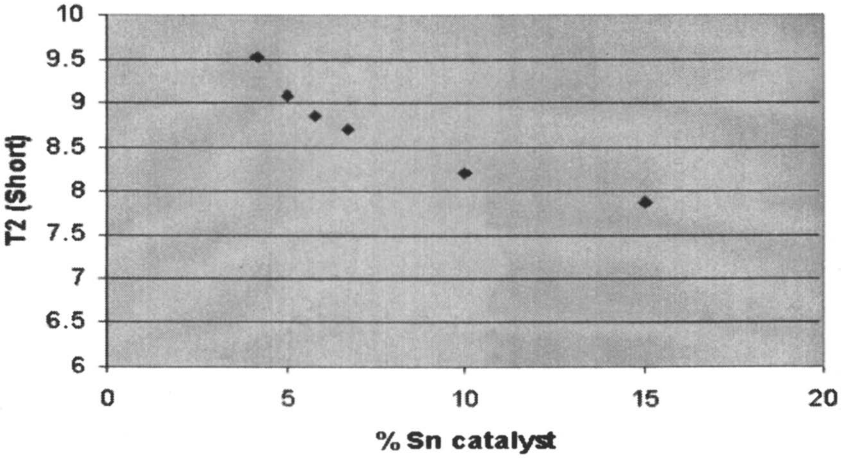

Figure 6. Short T_2 as a function of tin catalyst concentration.

Conclusions

In summary, our studies on tin cured polysiloxanes have shown that careful control of the amounts of catalyst used, as well as dispersion, are important for

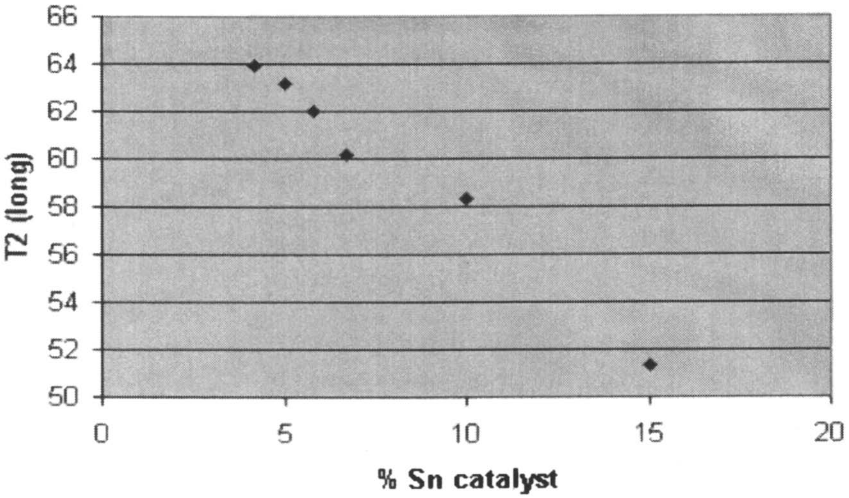

Figure 7. Long T_2 as a function of tin catalyst concentration.

material reliability. The soluble Tin (II) compounds are likely to be catalytically active in the hydrolysis and network rearrangement reactions that lead to chemical stress relaxation of the rubber network. An additional complexity arises from chain confinement effects induced by the Tin (IV) phase.

These effects have the potential to influence the important time dependent stress relaxation characteristics of foamed components, possibly accelerating compression set. Clearly evident from this work is the need to minimise residual catalyst and cure associated acid levels within the rubber so as to maximise material reliability over extended timescales.

Acknowledgments

The authors would like to express their thanks to the following people that have contributed to the work: Professor Norman Billingham (University of Sussex, UK), Bernard Mahieu (Universite de Louvain, Belgium) for the Mossbauer spectra, George Havrilla (Los Alamos National Laboratories, USA) for the XRF measurements and Jenny Cunningham (AWE, UK) for the NMR results.

References

1. Wen, J.; Mark J.E.; Fitzgerald J.J. *Macromolecular reports*, **1994**, *A31*, 429.
2. Harrison, P.G."Chemistry of Tin", Chapman and Hall, 1989
3. Van Der Weij, F.W. *Makromol. Chem.* **1980**, *12*, 2541.
4. Cypryk M.; Apeloig Y. *Organometallics* **2002,** *21*, 2165.
5. Stein J.; Prutzman L.C. *J. Applied Polym. Sci.* **1988**, *36*, 511.
6. Patel, M.; Morrell, P.R.; Skinner, A.R. *Macromol. Symp.* **2002**, *180*, 109.
7. Maxwell, R.S., Cohenour, R.; Sung, W.; Solyom, D.; Patel, M. *Polym. Deg. Stab.* **2003**, *80*, 443.
8. Patel, M.; Skinner, A.R.; Chaudhry, A.; Billingham N.C.; Mahieu B. *Polym. Deg. Stab.* **2004**, *83*, 157.
9. Patel, M.; Skinner, A.R. ACS Symposium Series 838, **2003**, 138.

Chapter 3

Acceleration Factors for the Oxidative Aging of Polymeric Materials

Roger A. Assink, Mathew C. Celina, and Julie M. Elliott

Department of Organic Materials, Sandia National Laboratories, Albuquerque, NM 87185–1411

Three methods that were used to measure the chemical changes associated with oxidative degradation of polymeric materials are presented. The first method is based on the nuclear activation of ^{18}O in an elastomer that was thermally aged in an $^{18}O_2$ atmosphere. Second, the alcohol groups in a thermally aged elastomer were derivatized with trifluoroacetic anhydride and their concentration measured via ^{19}F NMR spectroscopy. Finally, a respirometer was used to directly measure the oxidative rates of a polyurethane foam as a function of aging temperature. The measurement of the oxidation rates enabled acceleration factors for oxidative degradation of these materials to be calculated.

 © 2008 American Chemical Society

Predicting a polymer's useful life is difficult because its mechanical properties can be a nonlinear function of aging time. Thus extrapolation of short-term behavior may not be an accurate predictor of long-term behavior. Many lifetime prediction methods revolve around the concept of "accelerated aging" in which high-temperature short-term aging is extrapolated to low temperature long-term aging. Uncertainty arises, however, when the rates need to be extrapolated over an extended temperature range [1].

We are investigating the chemical changes occurring during the oxidative aging of polymers. In addition to providing insight into the aging mechanism, it is often possible to measure chemical changes associated with aging more accurately than mechanical changes associated with aging. This increased sensitivity can be used to measure the very low rate of degradation at ambient conditions, so that extrapolation from high temperature behavior to low temperature behavior can be made in a scientific manner.

Three methods that are capable of measuring the chemical changes associated with low levels of oxidative degradation are presented. The first method relies on nuclear activation resulting in the $^{18}O(\gamma,p)^{17}N$ reaction. This method was used to measure the concentration of oxidative products in a hydroxy-terminated polybutadiene (HTPB) elastomer that had been thermally aged in an atmosphere of $^{18}O_2$. The second method relies on a previous study that has shown that the primary oxidative degradation products of an HTPB elastomer are alcohols. The alcohol groups were functionalized with trifluoroacetic anhydride (TFAA) and the concentration of the resulting trifluorinated esters measured by ^{19}F NMR spectroscopy. Finally, a commercial differential fuel cell respirometer is used to measure oxidation rates of a polyurethane foam as a function of temperature. This instrument has been successfully employed for measuring the respiratory cycles of small animals and insects in real time [2,3]. We modified the operation of the instrument in order to measure the extremely low oxidation rates of the foam at ambient temperatures in a relatively short period of time. The acceleration factors for the oxidation rate are compared to those for the foam's compressive strength and used to predict the service life for the compressive strength of the foam aged under ambient condtions.

Nuclear Activation of ^{18}O

Samples consisting of two grams of HTPB elastomer were placed in vials containing approximately 125 torr of $^{18}O_2$ gas and aged at 95°C for times ranging from 6 to 956 hrs. The samples were removed and the amount of oxygen consumed by the polymer determined by the ultrasensitive oxygen consumption method (UOC) [4,5,6]. The net amount of ^{18}O in each sample was calculated by adding the amount of consumed ^{18}O to the 51 ppm background ^{18}O due to the

0.204% natural abundance of ^{18}O. The samples were analyzed on a 20 MeV electron LINAC owed and operated by the Idaho Accelerator Center at Idaho State University. The LINAC operates at a peak energy between 19 and 22 MeV with a beam current of approximately 80 mA. The electrons are allowed to pass through a thin tungsten sheet that converts the electron energy to photon energy through bremsstrahlung production. The neutron detector was composed of four proportional counters consisting of BF_3 gas-filled tubes at a pressure of 70 cm Hg. Futher details of the instrumental procedure have been published [7].

Water enriched with $^{18}O_2$ was first analyzed in order to verify ^{17}N detectability. The output was clearly exponentially with a half-life of 0.419 +/- 0.33 s compared to a published value of 4.17 s. Figure 1 shows a comparison of the neutron counts from the HTPB samples with their expected $^{18}O_2$ concentrations. The linearity is excellent and demonstrates sensivity to ^{18}O at concentrations below 100 ppm. The nuclear activation method measures relative concentrations, so the analysis of samples containing unknown amounts of ^{18}O would need to employ well characterized standards such as the HTPB samples prepared for this study.

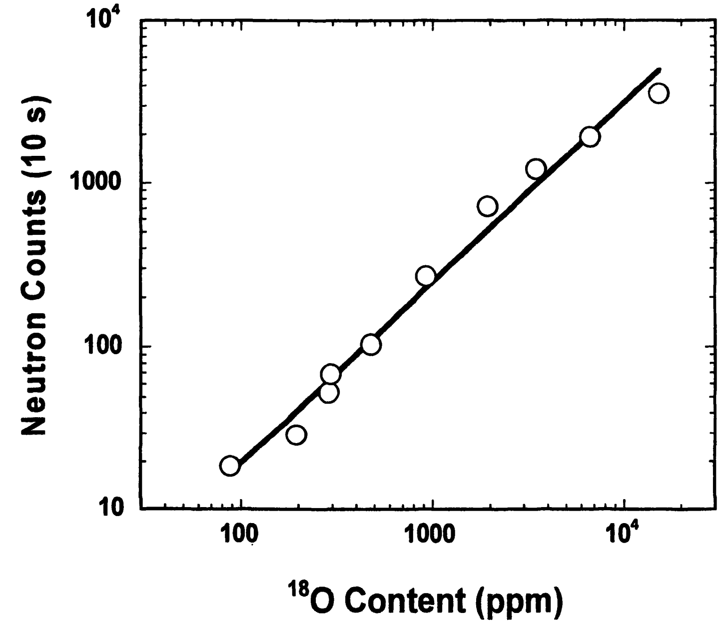

Figure 1. Neutron counts vs. ^{18}O content of HTPB samples that were thermally aged at 95°C in an $^{18}O_2$ atmosphere.

Chemical Derivatization of Alcohol Groups

In a previous study, ^{13}C and ^{1}H NMR were utilized to identify and quantify the oxidative degradation products of an HTPB elastomer [8]. A reliable relationship between extent of oxidation and the nature of the oxidation products was established, with the finding that alcohols comprise approximately 60% of the functional groups produced. In this study, we utilize the anhydride-alcohol esterification reaction shown in Scheme I to convert all of the alcohol groups in HTPB to trifluorinated esters. We have shown that this conversion is relatively straightforward and quantitative. The intensity of the ^{19}F NMR signal from the trifluorinated esters is then used to determine the concentration of alcohol groups that were present in the polymer. The resultant ^{19}F NMR signal of the $-CF_3$ group is over 14,000 times as intense as the ^{13}C NMR signal of the alcohol so detection of extremely low concentrations is possible.

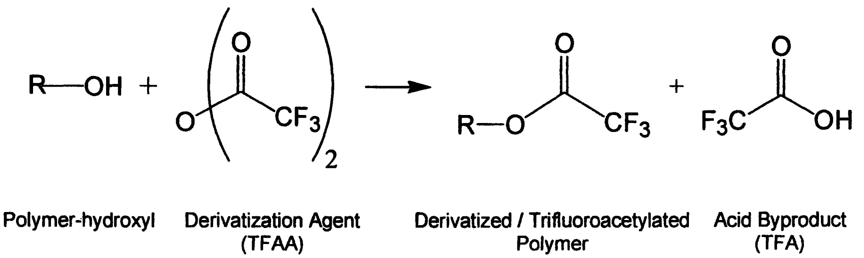

Scheme I. The ^{19}F derivatization reaction for an alcohol group.

Figure 2. shows the ^{19}F NMR spectra obtained in approximately 1 minute of 10 mg of HTPB elastomer that had been aged at 80°C and then derivatized with TFFA. The details of the derivatization process and the NMR sample tube configuration required in order to obtain a high resolution ^{19}F NMR spectrum have been described in the literature [9].

Samples of HTPB elastomer that had been aged at 80°C for times ranging from 14 to 221 days were derivatized and their ^{19}F NMR spectra recorded. The signal intensities of the derivatization products were converted to absolute alcohol concentrations by comparision to the signal from a solution with a known amount of TFAA. Figure 3 shows the alcohol concentration vs. aging time determined by ^{19}F labeling and by the UOC method combined with knowledge of the relative distribution of oxidative products obtained by ^{13}C NMR spectroscopy. The slopes of the two methods are comparable, confirming that each measures the same amount of alcohol production as a function of aging

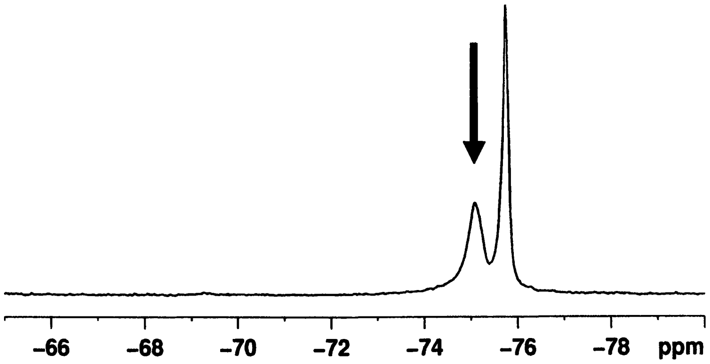

Figure 2. The ^{19}F NMR spectrum of the derivatization product of HTPB elastomer aged at 80°C. The arrow denotes the trifluoroester. The upfield resonance originates from the trifluoroacetic acid byproduct.

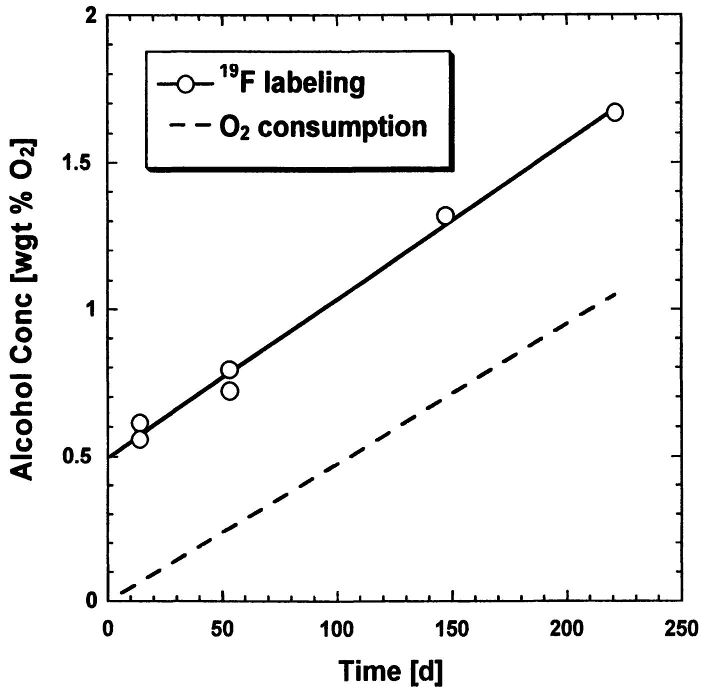

Figure 3. The alcohol concentration in HTPB as a function of aging time at 80°C. The slopes of the ^{19}F derivatization and UOC methods are comparable.

In Polymer Durability and Radiation Effects; Celina, M., et al.;
ACS Symposium Series; American Chemical Society: Washington, DC, 2007.

time. The nonzero intercept of the ^{19}F derivation method is attributed to hydroxy group present in the cured but unaged elastomer.

Differential Respirometer

The respirometer, an Oxzilla II Dual Absolute and Differential Oxygen Analyzer from Sable Systems International (Las Vegas, NV), is based on sensitive fuel cell detectors. The output of each fuel cell detector depends on the concentration of oxygen in the air stream directed to that fuel cell. The output of the fuel cell connected to the sample chamber is subtracted from the output of the fuel cell connected to the reference flow and the difference is used to calculate the amount of oxygen that was consumed by the polymer sample during aging. A simplified outline of the arrangement is shown in Scheme II. The respirometer and a gas multiplexer (also purchased from Sable Systems International) are controlled by a laboratory PC, which was also used to record the data. Ultrapure air was supplied by Matheson Inc.

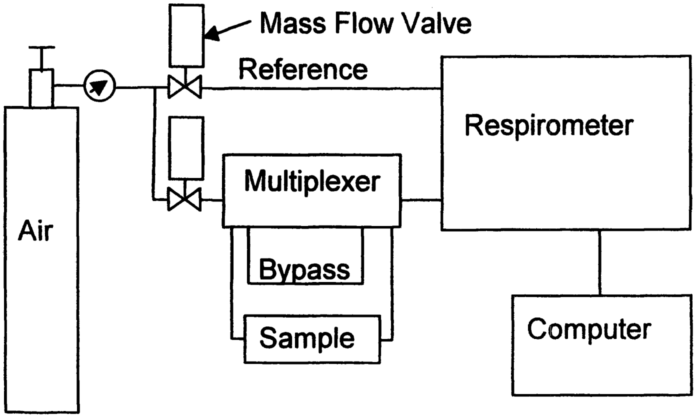

Scheme II. Outline of the respirometer, associated plumbing and data interface.

A known amount of polymer was placed in a sample chamber. The vessel was evacuated; cylinder air at 40 cm^3/min was passed over the sample for several minutes and the chamber sealed. After an interval of at least one hour, air was again passed over the sample in order to completely eliminate any contribution originating from ambient air dissolved in the sample. The chamber was removed from the manifold and placed in an air-circulating oven. After aging, the sample chamber was reconnected to the manifold and the short sections of the

connecting gas pathways that had been exposed to atmosphere were evacuated and refilled with cylinder air. At time = 0, the multiplexer was instructed to switch the air flow from the bypass loop to the sample chamber. The difference between the oxygen concentration of its air flow and the reference air flow was recorded as a function of time. The difference reached a maximum after 60 seconds, and recovered after approximately 3 minutes. The total amount of oxygen depletion was calculated from the integral of the difference in oxygen concentration. Details of the procedure and calculations have been published [10].

Figure 4 shows the oxygen deficit trace from a sample chamber containing 0.207g of a carbon filled natural rubber that had been aged for 16 hrs at 80°C. The dual detectors were first balanced with identical air streams flowing through both channels. The hatched area represents the total oxygen deficit which was calculated to be 0.0819 cm^3 O_2 at STP or 117 μg O_2. This amount of oxygen corresponds to an oxidation rate of 3.06×10^{-10} mol O_2 STP/g sample/s. This oxidation rate compared favourably to that measured by the conventional UOC method.

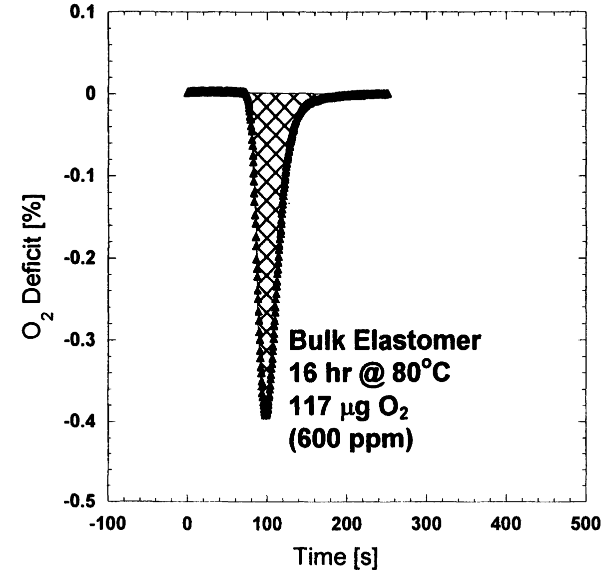

Figure 4. The O_2 deficit trace of a filled natural rubber that had been aged for 16 hr at 80°C.

The oxygen deficit trace of a 0.1 g/cm^3 polyurethane foam sample aged at 23°C for 555 hours is shown in Figure 5. The low density of the foam limited

the amount of sample that could be easily placed into the chamber to 1.07 g. Additional material would have lead to compression of the foam and obstruction of the free flow of air through the chamber. Aging at room temperature represents the lowest oxidation rate that needs to be measured for normal aging conditions. The oxygen deficit range of the respirometer was set to maximum sensitivity. Although the trace exhibits considerable fluctuation (the response was not time-filtered), the integral represented by the crosshatched area could be measured reliably. The total deficit equals 0.00149 cm^3 O_2 STP or 2.1 μg for the 1.07 g sample and predicts an oxidation rate of 3.12×10^{-14} mol O_2 STP/g sample/s.

Figure 6 shows a comparision of the oxidation rates measured by the respirometer and the UOC method for a range of temperatures. Temperatures for the UOC were limited to 37°C and above, because a year of aging was required for sufficient response at that temperature. The respirometer extended oxidation rates measurements to 23°C and even at that temperature, only 23 days of aging were required. In addition to being able to use shorter aging times, the respirometer data exhibited significantly less scatter than the UOC data. Note that some of the respirometer data overlay each other; there are a total of 6, 4, 3 and 6 measurements at 110, 80, 50 and 23°C, respectively.

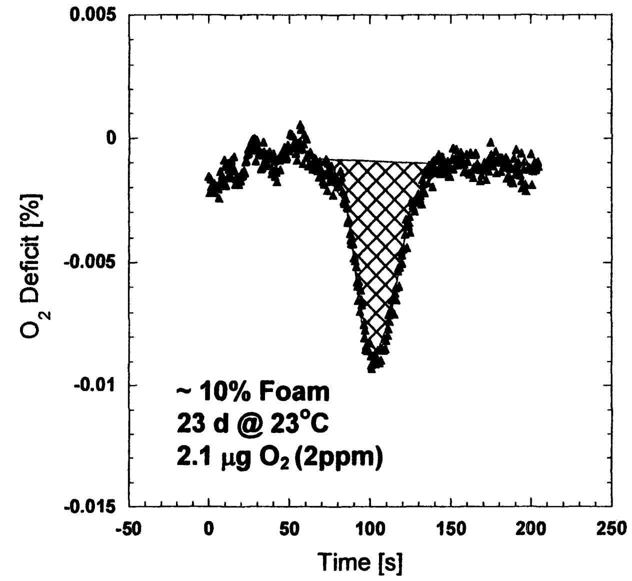

Figure 5. The O_2 deficit trace of a polyurethane foam that has been aged for 23 days at 23°C.

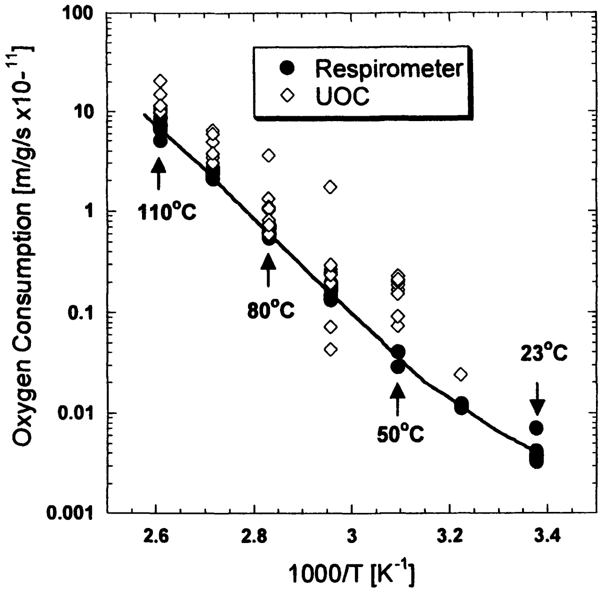

Figure 6. A comparison of the oxidation rates measured by the respirometer and UOC methods.

The oxidation rates measured by the respirometer were used to calculate acceleration factors for the oxidative aging of the polyurethane foam. The oxidation rates at each temperature were averaged and used to calculate acceleration factors that were normalized to 1.0 at 95°C. The results versus inverse temperature are shown in Figure 7. The acceleration factor plot exhibits some curvature in the lower temperature region of the curve. The activation energy of the relatively linear region between 50 and 110°C is 92 kJ/mol.

The purpose of measuring acceleration factors for oxidation is to apply these same acceleration factors in the low temperature region to a mechanical property of interest. The foam is used as a packaging material to protect items from shock and vibration. An important property for the performance of this task is the compressive strength of the foam. The force of foam samples at 50% compression were measured as a function of aging time and temperature. Aging the samples for 14 months caused significant changes in the compressive strength of the foam only at temperatures of 95°C and above. The shape of the compressive strength curves for samples aged from 95 to 140°C are reasonably similar and suggest that a time-temperature superposition is possible. The acceleration factors derived from the time-temperature superpostion are also plotted vs. inverse temperature in Figure 7. The acceleration factors for the

compressive strength of the foam correlate reasonably well with the acceleration factors for the rate of oxidation of the foam. If one assumes that the compressive strength is closely coupled to the rate of oxidation over the entire temperature range, then the low temperation acceleration factors for oxidation can be used to predict the behavior of the compressive strength when the foam is aged at low temperatures. Similar assumptions coupling oxidation rates to mechanical properties of polymers have proven quite useful for a variety of polymers.

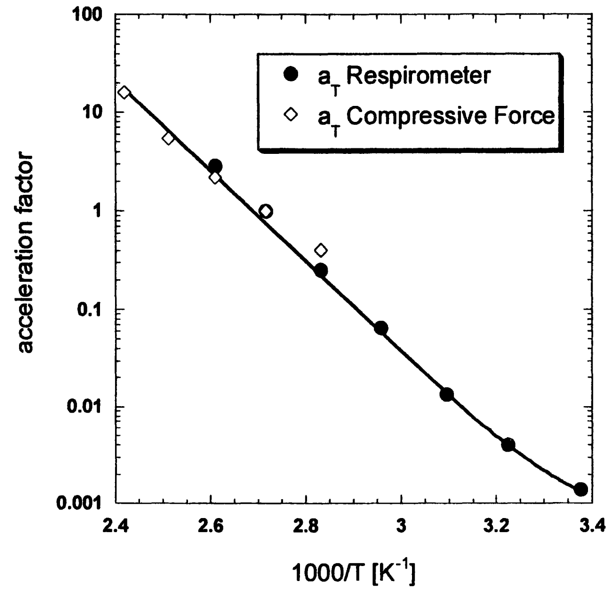

Figure 7. The accelerator factors for the oxidation rate and compressive force of a polyurethane foam.

Conclusions

We have demonstrated three techniques that measure the chemical changes associated with the oxidative degradation of polymers. Each of these techniques has the potential to measure very low concentrations of chemical change. The ability to measure slow oxidation rates enable the degradation process to be monitored at the low temperatures more closely related to the material's service conditions. Thus, more accurate service life predictions can be made without relying on extrapolation of high temperature behavior to low temperatures.

Acknowledgements

Sandia is a multiprogram laboratory operated by Sandia Corporation, a Lockheed Martin Company, for the United States Department of Energy's National Nuclear Security Administration under Contract DE-AC04-94AL85000. The technical assistance of Sean T. Winters and Ana B. Trujillo is gratefully acknowledged.

References

1. Celina, M.; Gillen, K. T.; Assink, R. A. *Polym. Degrad. Stab.* **2005**, *90*, 395-404.
2. Greenlee, K. J.; Harrison, J. F. *J. Exp. Biol.* **2004**, *207*, 497-508.
3. Josephson, R. K.; Malamud, J. G.; Stokes, D. R. *J. Exp. Biol.* **2001**, *204*, 4125-4139.
4. Gillen, K. T.; Clough, R. L. In: *Radiation Effects on Polymers;* Clough, R. L.; Shalaby, S. W., Eds.; ACS Series #475, Washington D.C. 1991. pp 457-472.
5. Wise, J.; Gillen, K. T.; Clough, R. L. *Polym. Degrad. Stab.* **1995**, *49*, 403-418.
6. Wise, J.; Gillen, K. T.; Clough, R. L. *Polymer* **1997**, *38*, 1929-1944.
7. Webb, T; Beezhold, W; DeVeaux, L; Harmon, F; Petrisko, J; Spaulding, R; Assink, R; "Photonuclear and Radiation Effects Testing with a Refurbished 20 MEV Medical Electron LINAC", Particle Accelerator Conference, Knoxville, TN 5/16-20/2005.
8. Harris, D. J.; Assink, R. A.; Celina, M. *Macromolecules* **2001**, *34*, 6695-6700.
9. Skutnik, J. M.; Assink, R. A.; Celina, M. Polymer **2004**, *45*, 7463-7469.
10. Assink, R. A.; Celina, M.; Skutnik, J. M.; Harris, D. J. *Polymer* **2005**, *46*, 11648-11654.

Chapter 4

Interactive Behavior in Polymer Degradation

Mathew C. Celina, Roger L. Clough, and Gary D. Jones

Department of Organic Materials, Sandia National Laboratories, Albuquerque, NM 87185–1411

A novel dual stage chemiluminescence detection system has been applied to study remote interaction effects occurring during polymer degradation. There has long been speculation that infectious agents and reactions transferring initiators or antioxidants are important aspects in polymer aging. Evidence is presented that in an oxidizing environment a degrading polymer (i.e. PP) is capable of infecting a different polymer (i.e. polybutadiene) over a relatively large distance. Similarly, traces of thermally sensitive peroxides in the vicinity of PP are found to induce degradation remotely. These observations document cross-infectious phenomena. Likewise, inhibitive volatiles from stabilized elastomers were shown to retard a degradation process remotely. Such interactive phenomena are important to better understand polymer interactions, fundamental degradation processes and long-term aging effects of multiple materials in a single environment.

© 2008 American Chemical Society

Background and Experimental Approach

There is some evidence that the aging of polymers may involve heterogeneous processes and that degradation can be initiated via impurities, catalysts or other chemical reagents (1-4). It has also long been recognized that the thermal degradation of polymers under oxidative conditions as described by the complex auto-oxidation scheme first established in the 1940-50's (5-7) involves the participation of peroxides and other oxidized species resulting from oxidation. Importantly, for the degradation of polypropylene (PP) samples composed of individual reactor particles, the induction time and thus degradation timing of the weakest particles was found to control the lifetime of the collective sample of this material (2). Such observations resulted in the suggestion of a heterogeneous model (1,2) allowing for localized reactions, active intermediates and propagation of degradation reactions throughout the material (3,4,8) with the notion that infectious volatile could carry the degradation from particle to particle via the gas phase (2). Similar infectious phenomena for materials in 'nature' have been described for the 'cross-talk' ripening of fruit via ethylene transfer (9-11), or the tin disease (tin pest) (12).

A suitable experimental method to study such degradation phenomena in polymers is the sensitive technique of chemiluminescence (CL) (1,13), with the broad application of CL as applied to polyolefin degradation having recently been reviewed (14). All thermal oxidation reactions of hydrocarbon based polymers are accompanied by the emission of visible photons, with the intensity being an indicator of the activity of the degradation process (1,2,14). CL is an ideal tool to analyze in-situ polymer degradation reactions (1,2) as it provides information on the degradation process as a function of time and temperature. For this study a novel highly sensitive dual-stage CL instrument was developed and utilized to study the synergistic interaction of two different polymeric materials in a thermo-oxidative environment, as well as transfer processes of volatile initiators (peroxides) or inhibitors (antioxidants).

As shown in the schematic setup in Figure 1, the CL instrument was designed to incorporate two individually temperature-controlled hot stages and a highly sensitive single photon counting photomultiplier tube (PMT) (15). A large diameter PMT is capable of collecting the simultaneous CL signal from both stages. The left and right hot stage are separated by approximately 25 mm. The initiating polymer, as well as peroxides or antioxidants, were placed on the left stage with a carrier gas (oxygen flow ranging from 25 to 250 cc/min) directing any gaseous volatiles, infectious or inhibitive agents towards the right sample stage.

To allow for infectious phenomena between two different polymers to be studied, the experiments required a fast and actively degrading polymer, and a receiving one with a slower response. Polypropylene (PP) was chosen as the particularly reactive polymer and was used as an unstabilized reactor powder

material with typical samples of 10 mg. For the polymer interaction experiments unstabilized HTPB (cured hydroxyl-terminated polybutadiene) (16) was selected and used as thin films of approximately 5 mg cut from a 2 x 6 mm strip sample. Due to the fact that the CL emission from PP at 150°C is considerably higher and would swamp any signal originating from HTPB at lower temperatures, the PP sample holder was covered with Al-foil. This allowed only approximately 1% of the total signal to reach the PMT, which was still sufficiently intense to clearly identify the PP degradation peak and its relative timing features. For the benzoyl peroxide (BPO) or azoisobutyronitrile (AIBN) experiments, commercial materials (Aldrich 99%) were dissolved and diluted in toluene, with small quantities deposited on the PP or in samples pans using a standard micro liter syringe and subsequent solvent evaporation.

affects

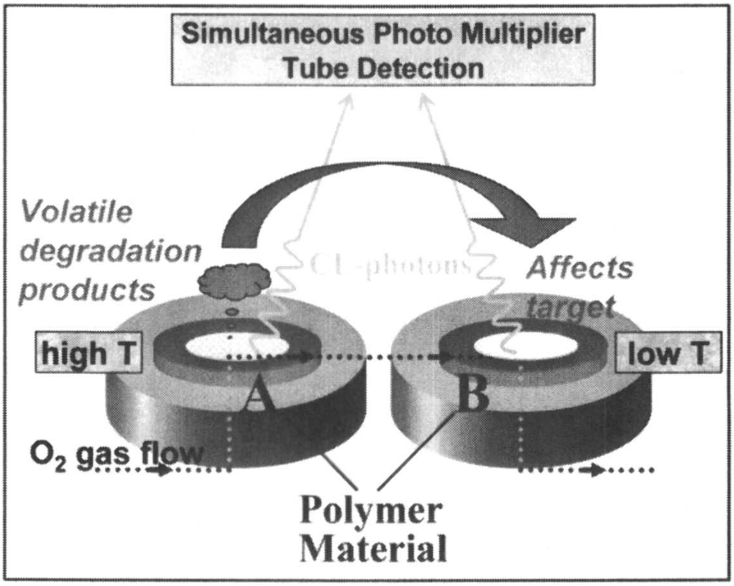

Figure 1. Schematic of instrumental setup with photon emission and detection from two hot stages allowing infectious and inhibitous phenomena to be explored.

Infectious Cross-talk between Polymers

A range of experiments were conducted to explore if a degrading polymer (i.e. PP) is capable of initiating thermal degradation in a different polymer (HTPB). As an example of PP infecting HTPB, Figure 2 shows the signal of

two individual samples, the PP at 150°C displaying the individual peak degradation intensity at ~1h and the HTPB at 50°C showing a main peak at ~120 hours. Included in Figure 2 is the predicted combined CL signal obtained by simply adding the PP and HTPB signals, which should be observed in an experiment of two individual samples if no interaction processes were present. Included in Figure 2 is also the actual CL trace resulting from an experiment where both samples are simultaneously placed on their respective hot stage. It is clear that the normally slower HTPB sample has degraded considerably faster in the presence of the initiating PP on the left sample stage, as the HTPB peak was observed after only ~33 hours, or ~28 % of its normal peak position. Additional experiments were conducted at different temperatures with similar results. It is also noteworthy to mention that in a similar experiment conducted with the PP degrading at the lower temperature of 130°C, the HTPB also showed a shorter degradation peak, demonstrating that infectious volatiles also originated from the lower temperature PP. The shift in the HTPB's responses are best presented in an Arrhenius diagram (Figure 3) of the HTPB t_{max} data versus inverse temperature. The longer aging times correspond to the individual material's behavior, whereas the shorter times relate to the peak position time in the presence of the initiating PP (at 150°C) in combined experiments. The shift towards shorter degradation times is significant and apparent for all temperatures investigated. Even for an HTPB exposed at 40°C a peak time of ~300 hours would be predicted based on linear Arrhenius extrapolation, however, in the presence of the initiating PP a significantly shortened peak is observed after only 100 hours.

Remote Action of Peroxides

The above experiments clearly show that some organic volatiles must have infectious properties and act as pro-degradants that are carried across from the faster degrading polymer. A likely candidate for such infectious agents are peroxides or fragments thereof that are key intermediates in thermal polymer degradation. To test the hypothesis that even traces of peroxides would be sufficiently reactive and could act as remote initiators, a few simple overview experiments were conducted.

Benzoyl peroxide (BPO) is an organic peroxide that degrades rapidly at temperatures above 100°C (i.e. 1 hour half life time at 92°C). Figure 4 shows the degradation of a PP sample at 100°C with a small amount of this peroxide directly deposited on the PP. Even traces are capable of accelerating the degradation. The effect could still be detected for 0.01µg BPO on a 10 mg sample (equals 1ppm) (17). Larger amounts of 100ppm and above accelerate the degradation significantly. Similar results were also observed for the thermal degradation of PP at 110°C and 120°C. As expected the peroxide will decompose quickly producing free radicals and initiating oxidation of the PP.

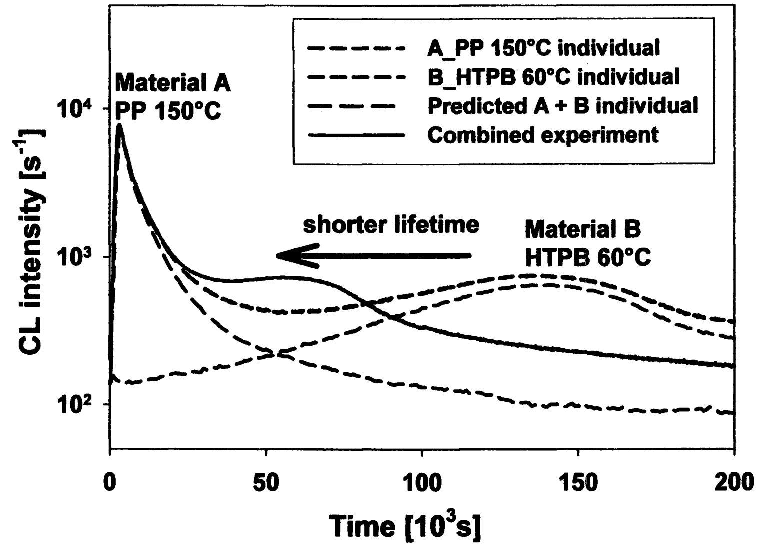

Figure 2. Individual and combined degradation of PP (150°C) and HTPB (50°C) samples monitored by chemiluminescence.

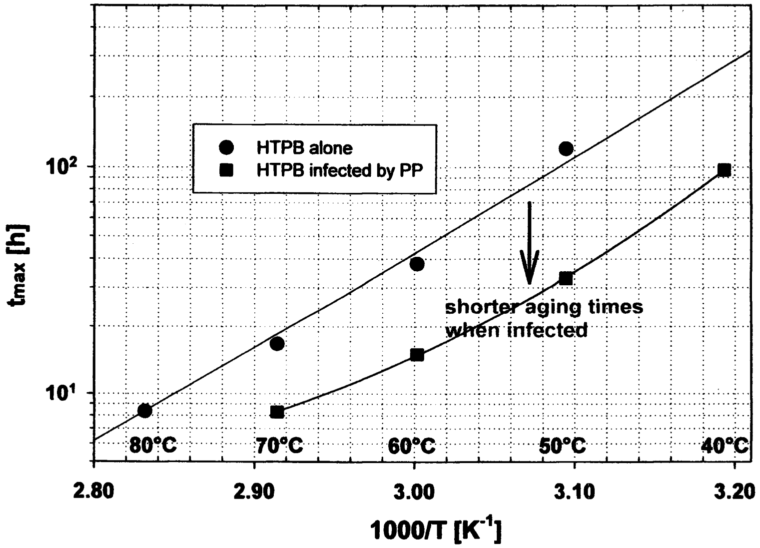

Figure 3. Arrhenius plot of the t_{max} times for HTPB at different temperatures showing the faster degradation when infected by the degrading PP at 150°C.

As a follow-up experiment, small amounts of the peroxide were placed on the left sample stage and any remote influence on the PP sample located on the right stage (i.e. 10 µg) was evaluated. An example is included in Figure 4 for the degradation of a PP sample at 100°C. It is clear that the PP sample was affected by the presence of the decomposing BPO via volatile fragments, since the degradation is considerably faster than without the BPO. The small amount of peroxide can clearly infect the PP sample on the right stage located 25 mm away. Similar experiments were also conducted with AIBN, a non peroxide-based radical initiator with similar thermal decomposition features. AIBN was also found to be capable of leading to remote initiation of PP. These experiments clearly demonstrate that small amounts of initiators can act as infectious agents and can be carried successfully via the gas phase. Whether the infectious species in this case are un-decomposed initiator, its degradation products or a combination thereof is presently unclear. As discussed above, it is well known that PP degradation involves the evolution of gaseous species that can be infectious and similar evidence was demonstrated for an EPDM material (2,18). The potential for peroxidic species to be involved and the very small amounts that can lead to infectious behavior, even when physically separated from the sample, is demonstrated here.

Remote Action of Antioxidants

Of further interest was to identify if a common phenolic antioxidant would be volatile enough to affect the degradation of unstabilized PP in a similar remote fashion as observed for the remote activity of radical initiators. A small amount (50 µg) of Vanox MBPC (2,2′-methylene-bis 4-methyl-6-*t*-butylphenol), an antioxidant with a molecular weight of 340.5 g/mol and melting point of 125°C, was deposited via a suitable toluene solution onto a DSC sample pan. Figure 5 shows the CL monitored degradation of an individual PP sample at 110°C (10 mg) and the corresponding CL signal when the PP sample is placed on the right stage in the presence of 50 µg AO on the left stage (also at 110°C). The PP degradation process is clearly retarded by traces of the AO or possibly any of its thermal decomposition products that would have been transferred onto the PP sample. This is intriguing since the AO due to its high melting point and molecular weight would not be regarded as a particularly volatile substance. Furthermore, the PP consists of powder particles with large surface areas, which would make it difficult for traces of antioxidant to uniformly inhibit any degradation process. However, even traces (i.e. 1 µg) of AO deposited directly on the PP were found to result in a low-level stabilization effect (i.e. 0.01%). This would certainly support the observation of remote stabilization. Similar transfer of antioxidative species leads to successful inhibition of the PP sample also at higher temperature, as well as for BHT, a slightly more volatile antioxidant.

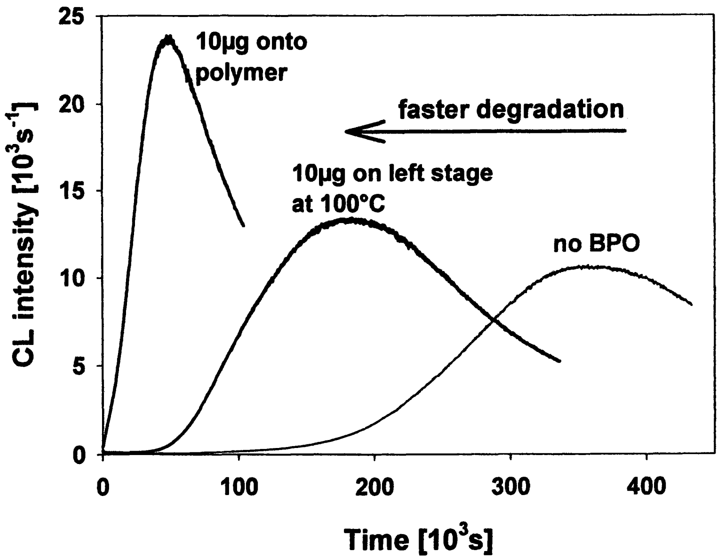

Figure 4. PP (10mg) degradation at 100°C and initiation by small amounts of benzoyl peroxide deposited either on the sample or independently on the left stage.

It was further explored if a stabilized elastomer sample with dissolved AO in the matrix could give off antioxidant in sufficient quantities to measurably inhibit the degradation of the PP. A 5 mg sample of stabilized HTPB with 1% Vanox MBPC was placed on the left stage and a 2.5 mg PP sample on the right stage. For such experiments no significant effect on the PP was observed, which suggests that insufficient quantities of the AO were transferred across or are too diluted by the time they reach the PP. For example, a 5mg sample of HTPB contains ~50 µg of antioxidant, but the available quantities for desorption (surface effects) and transfer will be considerably lower. The antioxidant will be mostly retained in the polymer matrix and its limited volatilization will lead to relatively low quantities in the gas phase, which might be very diluted at the right sample location in the current experimental setup. It will also be an issue of volatility versus affinity (adherence) to either the elastomer or the PP. To explore if cross-inhibitive effects could nevertheless occur between different polymers, the two polymer samples were positioned closer together but not touching, thereby increasing the local volatile concentrations by placing them in one sample pan (~7 mm diameter). Figure 6 shows the results for such a combined experiment of PP and HTPB at 140°C. It is obvious that the degradation of the PP material in this experiment is now considerably inhibited due to sufficient antioxidative species being transferred from the HTPB. The t_{max} of the PP is shifted from about 2.1 h to 7.9 h. No infectious effect of the PP

on the HTPB is apparent (identical peak position of the HTPB). A similar experiment was repeated using stabilized PBAN containing an amine antioxidant. The inhibition effect in the PP is similar as observed for the HTPB experiment demonstrating again that sufficient quantities of AO causing inhibition were transferred (19).

Such experiments demonstrate that antioxidants or their decomposition products with antioxidative properties can also be successfully transferred from a stabilized polymer and result in remote inhibitive effects in a neighboring polymer. The magnitude of this effect will depend on relative volatility, expected to be primarily controlled by its molecular weight, and concentration in the gas phase, as well as AO solubility and affinity to the polymer. It has long been speculated that such inhibitive remote interaction may be a potential problem in closed environments (closed aging ovens) where polymers age jointly. Larger amounts of stabilized polymers are expected to give off large enough quantities of antioxidants that could easily enhance the intrinsic stability of less stable polymers in their proximity.

Conclusions

A novel chemiluminescence technique has been introduced and applied to study potential interaction processes of polymer materials when they degrade. It was demonstrated that in an oxidizing environment a degrading polymer A (i.e. PP) is capable of infecting a different polymer B (i.e. polybutadiene, HTPB) over a relatively large distance. This suggests that materials degradation of completely different polymers can involve infectious processes, as discussed previously for the degradation of individual polymer samples. In the presence of the degrading material A, the thermal degradation of polymer B is observed over a significantly shorter time period.

Infectious intermediate volatiles from material A are able to initiate and shorten the degradation processes in material B. Considering that the initiating polymer is a sample of only 10mg, that the materials are separated by ~25 mm, and that a significant carrier gas flow is applied, all imply that an extremely reactive infectious volatile must be transmitted and that the receiving polymer must be susceptible to traces of such species. This observation is perhaps not unexpected, but has not been experimentally documented before. Understanding such infectious behavior is important for predicting polymer materials interactions, material degradation processes and long-term aging effects in combined material exposures. Long term efforts will require the identification of infectious agents. Perhaps even solid fragments (nanoparticles) of the degrading polymer carrying peroxides, a reactive macromolecular species, could act as an initiator. As expected, low quantities of a temperature sensitive peroxide in direct contact with PP were shown to be an extremely efficient initiator.

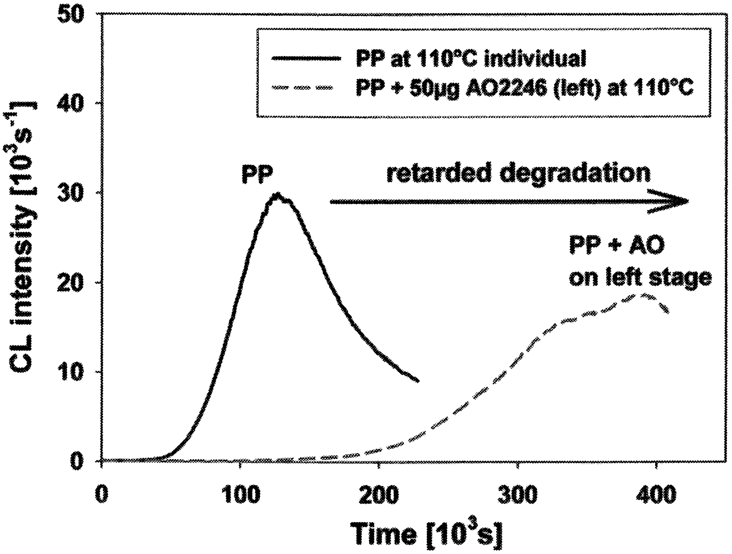

Figure 5. CL monitored degradation of PP (110°C) and inhibited by volatile antioxidant transferred from the left sample stage (50µg Vanox MBPC).

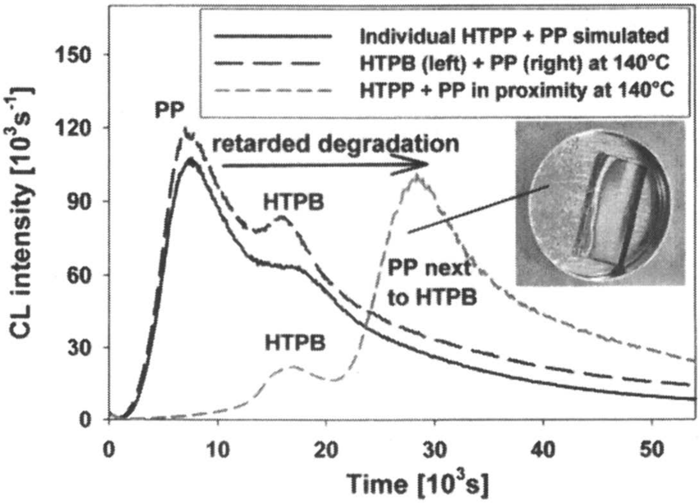

Figure 6. Simulated degradation of individual 4.6mg HTPB and 2.5mg PP samples, a combined experiment (left and right sample stage) and a single sample pan experiment showing the retarded peak of PP when in the vicinity of HTPB (all experiments conducted at 140°C).

In Polymer Durability and Radiation Effects; Celina, M., et al.;
ACS Symposium Series; American Chemical Society: Washington, DC, 2007.

Similarly, the activity of only trace amounts (micrograms) of peroxide in the vicinity of a receiving PP sample was sufficient to remotely initiate the degradation process.

For inhibitive interaction process, traces of common antioxidants or their decomposition products are sufficiently volatile to be carried between polymer samples and can lead to remote inhibition. There are some limits of this effect when the amounts of transferred AO from a stabilized elastomer are too low to result in significant retardation of the degradation in the receiving polymer. This is in contrast with the very low amounts of peroxidic species (micrograms) found capable of inducing remote initiation (17). However, when the separation is reduced between the polymers, remote inhibition indicative of cross-talk between the materials could be observed. This demonstrates that some antioxidants (or their degradation products) are sufficiently volatile to be transferred, but that critical concentrations are required to inhibit degradation in the receiving polymer.

In summary, these experiments have demonstrated that polymers can interact remotely, that small amounts of peroxides can lead to remote initiation, and also that remote inhibitive behavior via transfer of antioxidant between materials that age jointly is a distinct possibility. Variations in their individual stability due to such remote interactions may be observed in closed environments where polymers age jointly.

Acknowledgements

Sandia is a multiprogram laboratory operated by Sandia Corporation, a Lockheed Martin Company, for the United States Department of Energy's National Nuclear Security Administration under Contract DE-AC04-94AL85000. The technical assistance of Ana B. Trujillo is gratefully acknowledged.

References

1. Celina, M.; George, G. A. *Polym. Degrad. Stab.* **1993**, *40*, 323-335.
2. Celina, M.; George, G. A.; Billingham, N. C. *Polym. Degrad. Stab.* **1993**, *42*, 335-344.
3. Celina, M.; George, G. A. *Polym. Degrad. Stab.* **1995**, *50*, 89-99.
4. George, G.; Celina, M. in Hamid, S. H., ed. Handbook of polymer degradation. New York: Marcel Dekker, Inc., 2000. p 277-313.
5. Bolland, J. L.; Gee, G. *Trans Faraday Soc.* **1946**, *42*, 244-252.
6. Bateman, L. *Q. Rev. (London)* **1954**, *8*, 147-167.

7. Grassie, N.; Scott, G. Polymer Degradation and Stabilization. Cambridge: Cambridge University Press, 1985.
8. Goss, B. G. S.; Barry, M. D.; Birtwhistle, D.; George G. A. *Polym. Degrad. Stab.* **2001**, *74*, 271-282.
9. Clendennen, S. K.; Kipp, P. B.; May, G. D. *NATO ASI Series, Series 3: High Technology* **1997**, *34*, 141-148.
10. Pech, J. C.; Sharkawi, I.; Chaves, A.; Li, Z.; Lelievre, J. M.; Bouzayen, M.; Frasse, P.; Zegzouti, H.; Latche, A. *Acta Horticulturae* **2002**, *587*, 489-495.
11. Chen, P. M.; Varga, D. M. *Hort. Technol.* **1999**, *9*, 190-194.
12. Cohen, E. *Electrochem. Z.* **1911**, *17*, pp181.
13. Ashby, G. E. *J. Polym. Sci.* **1961**, *50*, 99-106.
14. Jacobson, K.; Eriksson, P.; Reitberger, T.; Stenberg, B. *Adv. Polym. Sci.* **2004**, *169*, 151-176.
15. Celina, M.; Clough, R.; Jones, G. *Polymer* **2005**, *46*, 5161-5164.
16. Celina, M.; Graham, A. C.; Gillen, K. T.; Assink, R. A.; Minier, L. M. *Rubber Chem. Technol.* **2000**, *73*, 678-693.
17. Celina, M.; Clough, R. L.; Jones, G. D. *Polym. Degrad. Stab.* **2006**, *91*, 1036-1044.
18. Ahlblad, G.; Reitberger, T.; Terselius, B.; Stenberg, B. *Polym. Degrad. Stab.* **1999**, *65*, 169-177.
19. Celina, M.; Clough, R. L. *Polymer* **2006**, *47*, 289-292.

Chapter 5

Mechanism of Action of Hindered Amines as Long-Term Heat Stabilizers

Pieter Gijsman[1,2] and Mikael Hamskog[2]

[1]DSM Research, P.O. Box 18, NL–6160 MD Geleen, The Netherlands
[2]University of Kristianstad, Kristianstad, Sweden

Although Hindered Amine Stabilizers (HAS) originally only were used as UV-Stabilizer, it is nowadays well known that they act as stabilizers against the thermo-oxidative degradation of polypropylene (PP) too. Their mechanism of action is different from the traditionally used phenolic antioxidants (PAO). A comparison was made between the effectivity of a PAO and a HAS as long-term heat stabilizer. It is found that both types of stabilizer interfere in different ways in the degradation of PP. These differences will be clarified using results on the degradation of unstabilized PP and model experiments with decalin, decalin / lauryladehyde mixtures and squalane. For oligomeric HAS types containing different aliphatic amines in their backbone, differences in activity were found. For these HAS types, it is shown that parts of the backbone can act as stabilizer too.

 © 2008 American Chemical Society

Introduction

Although Hindered Amine Stabilizers (HASs) originally only were used as UV-Stabilizer, it is nowadays well known that they act as stabilizers against the thermo-oxidative degradation of polypropylene (PP) too. However, their mechanism of action is different from the traditionally used phenolic antioxidants (PAOs). It was shown that polymers containing HASs and PAOs show a difference in decline of the mechanical properties during ageing. For PP containing phenolic antioxidants a sudden decline after a period of almost no changes is found, while PP containing HASs show a more or less linear decline in time [1,2,3].

A comparison between a HAS and a PAO as stabilizers against the oxidation of PP showed that they behave differently [4]. Based on experiment showing the ability of the HAS and the PAO to reduce the oxidation rate of decalin, squalane and decalin/lauryl aldehyde mixtures, it is shown that the HAS is mainly active in the presence of aldehydes. For unstabilized PP it is shown that aldehydes play an important role in its oxidation [5]. These results are used to propose an oxidation mechanism for PP and a mechanism underlying the action of HAS.

It was also shown that the effectiveness of HAS is not only related to their piperidinyl group. For oligomeric HAS types with deviations in chemical structure in the backbone, differences in activity were found. These differences were explained by studying the influence of parts of the backbone on the degradation mechanism [6].

Thermo-oxidation of Stabilized PP Films [4]

Stabilized PP films (thickness: 150μm) containing a high molecular weight HAS or a PAO (for chemical structure see Figure 1) were aged at 120°C in a Heraeus D-6450 Hanau oven. In all cases 0.1 wt.% Butylated Hydroxy Toluene was added to prevent degradation during processing. For more details about the polymer and the preparation of the films see ref. 4.

Changes in the visual appearance of films were recorded by scanning oven-aged films. The images were made on a black background. During degradation parts of the films became white (see Figures 2 and 3), these parts are brittle. The behavior of the samples depends on the type of stabilizer. In the phenolic-antioxidant-containing sample the degradation starts after 560 hours at the edges and propagates rapidly into the film (see Figure 2). After 682 hours more than 50% of the film is totally brittle.

The HAS-containing film behaves differently. Degradation starts more randomly and does not spread in the way observed in the PAO-containing

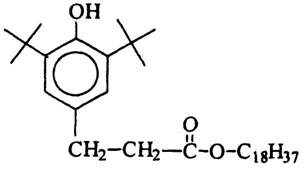

PAO-1(Irganox®1076)

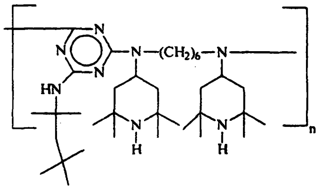

HAS-1 (Chimassorb®944)

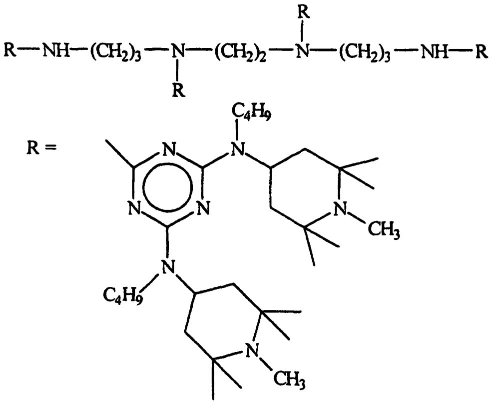

HAS-2 (Chimassorb®119)

Figure 1. Stabilizer chemical formulae and trade names.

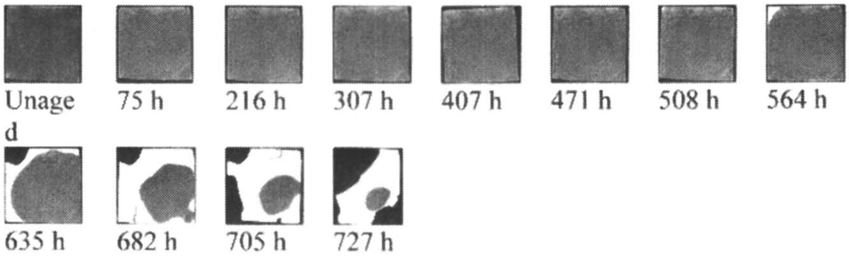

Figure 2. Images, scanned against a black background, of 150 μm thick PP films (4 x 4 cm2) containing 0.1% PAO-1 after oven ageing for different times at 120°C.

samples (see Figure 3). In the presence of HAS-1 parts of the film became white after only 300 hours, but the whitening spread very slowly. Even after 1100 hours the film was still not completely white. The nature of the whitening also differed: in PP stabilized with HAS-1 the white parts were less brittle than in PP stabilized with PAO-1.

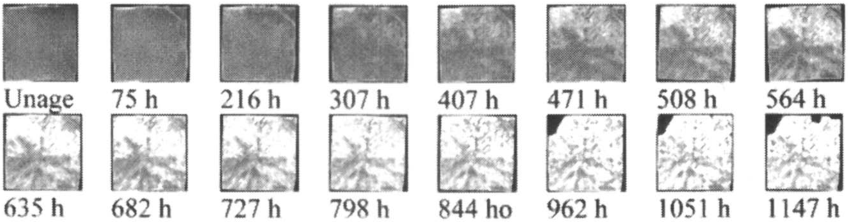

Figure 3. Images, scanned against a black background, of 150 μm thick PP films (4 x 4 cm2) containing 0.1% HAS-1 after oven ageing for different times at 120°C.

Imaging Luminescence (CL) of Preoxidized Stabilized PP

CL intensity-time curves were measured at 135°C for at the same temperature preaged PP samples. The plaques containing PAO-1 were preaged for 640 hours (for more details see ref. 7) and the compound containing HAS-1 for 2176 hours. For the PAO containing PP, chemiluminescence is only observed after an induction period. In Figure 4 the induction times for samples taken out along a horizontal line in relation to the distance from the left edge of the plaque is plotted. From this plot it is clear that in this case the degradation is very heterogeneous (for details see ref. 7).

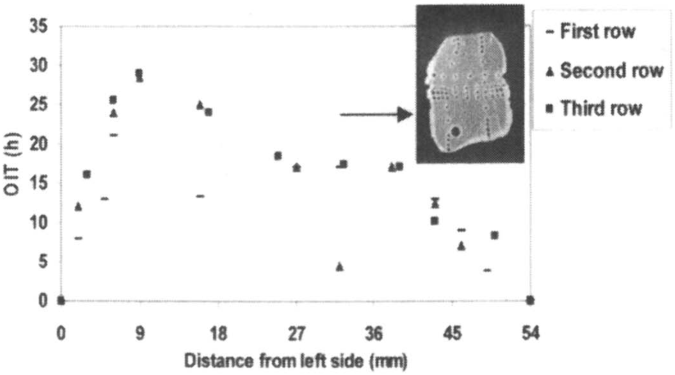

Figure 4. OIT values (measured at 135°C) from three experiments, each with 11 PP samples taken out along a horizontal line (see inserted picture). The PP samples were with PAO-1 stabilized and preaged for 640 h at 135°C.

The CL intensity-time curves for the HAS containing PP looks totally different. In this case a continuous low luminescence level is observed without an induction period, which is homogenous over the whole plaque (Figure 5).

Oxidation of Decalin, Squalane and a Mixture of Lauryl aldehyde and Decalin [4]

The influence of the stabilizers mentioned in Figure 1 was studied by oxidizing three different model compounds: decalin (a cyclic hydrocarbon which, like PP, contains secondary and tertiary carbons), squalane (a high molecular weight aliphatic hydrocarbon which also contains secondary and tertiary carbons), a mixture of 10% lauryl aldehyde in decalin, which could serve as a model for partly oxidized PP. All reactions were initiated with 1% of t-butylhydroperoxide and performed at 120°C (for details see ref. 4).

HAS-1 has almost no effect on the oxidation of decalin (Figure 6), there is no induction period, and only a small reduction of the oxidation rate was found. The effect of PAO-1 is much greater. In the presence of this stabilizer the oxidation of decalin shows an induction time (Figure 6). The oxidation rate after the induction period is comparable to that of the control, probably because the stabilizer is consumed during the induction period.

The addition of lauryl aldehyde (10%) to decalin has a tremendous effect on the oxidation rate as well as on the effectivity of the stabilizers. This mixture already starts to oxidize while it is being heated to its final oxidation temperature (120°C), which is the reason that the data are not shown in Figure 7. In this case the effectivity of PAO-1 and HAS-1 is comparable.

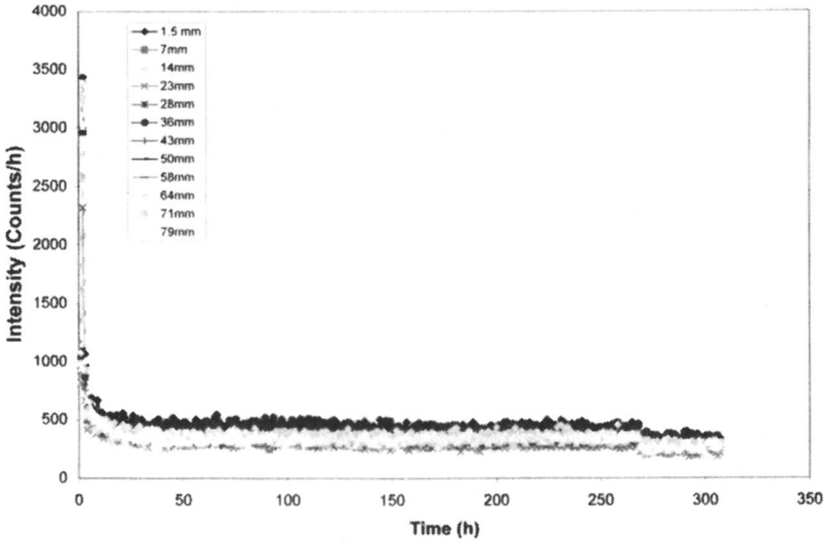

Figure 5. Luminescence intensity (at 135°C) for 11 PP samples containing HAS-1 taken out along a horizontal line (in insert distance from the left edge is shown). The PP was preaged for 2176 h at 135°C.

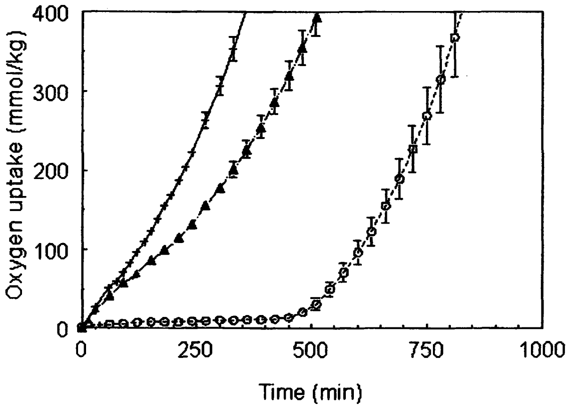

Figure 6. Influence of 0.1 wt.% stabilizer on the oxidation rate of decalin at 120°C.Control (+), HAS-1 (▲) and PAO-1 (o). Bars show the standard deviation.

The oxidation of squalane is slower than the oxidation of the mixture of decalin and lauryl aldehyde (compare Figures 7 and 8). Although squalane is a hydrocarbon similar to decalin, in squalane HAS are capable of reducing the oxidation rate effectively, while they were not effective against the oxidation of decalin. In squalane HAS-1 even outperformed PAO-1 (Figure 8).

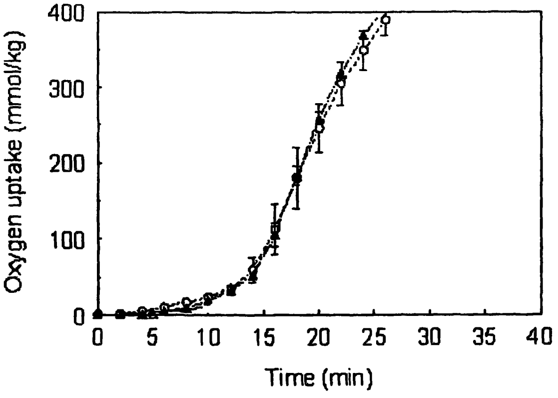

Figure 7. Influence of 0.1 wt.% stabilizer on the oxidation rate of a decalin/lauryl aldehyde mixture at 120°C. HAS-1 (▲) and PAO-1 (o). Bars show the standard deviation.

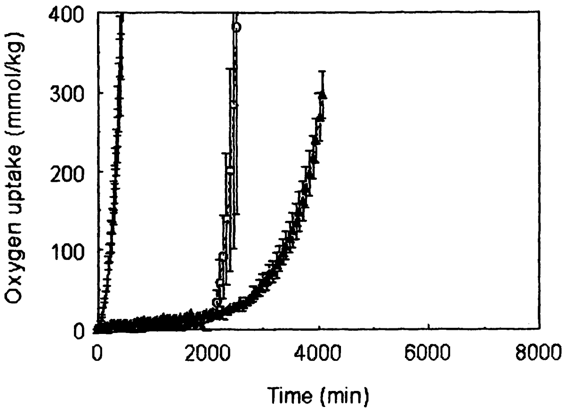

Figure 8. Influence of 0.1 wt.% stabilizer on the oxidation rate of squalane at 120°C. Control (+), HAS-1 (▲) and PAO-1 (o). Bars show the standard deviation.

It is clear that the efficiency of the different stabilizers highly depends on the model system. PAOs are effective in all systems, but HAS are not effective in decalin. The oxidation of decalin mainly takes place at the tertiary carbon, leading to cyclodecanone and cyclodecanol [8]. This oxidation does not lead to the formation of aldehydes and acids. When aldehydes are added to decalin HAS becomes effective, so HAS is effective against the oxidation of aldehydes. HAS is also effective against the oxidation of squalane, which, like decalin, is a hydrocarbon containing secondary and tertiary carbons. However, because of its

non-cyclic structure the oxidation of squalane can lead to aldehydes, thus HAS is effective when aldehydes are added or can be formed.

The above-mentioned results are all valid for model experiments in the liquid phase. The question still is: what is their relevance for the mechanism underlying the long-term heat-stabilizing action of HAS in PP? After all, the above-mentioned positive effects of HAS can only be of relevance when aldehydes play a major role in the oxidation mechanism of PP. In the following an attempt is made to show the important role played by aldehydes in the low temperature oxidation of unstabilized PP.

Oxidation of Unstabilized PP

The long-term thermal degradation of PP is due to an autoxidative process [9,10]. In this mechanism the decomposition reactions of the formed peroxides play an essential role. A possible way of studying this reaction is to determine the decrease in the concentration of peroxides of oxidized PP in an inert medium as a function of time (see Figure 9). It is shown that this decomposition takes place in two stages. Initially a fast decomposition was observed, which was followed by a slow decomposition. This type of decay could not be described by first or second order reaction. Assuming that the titrated concentration of peroxides consists of two fractions (both decomposing according to first order), the calculated data could be fitted with the experimental values (see Figure 9). The calculated k values are $4.2*10^{-6}$ per second for the fast decomposition reaction and $1.8*10^{-7}$ per second for the slow decomposition reaction. Besides the k values, the amounts of rapidly decomposing and slowly decomposing peroxides at the beginning of the decomposition were calculated using this model. As the peroxides are introduced into the polymer by first oxidizing the polymer, the concentrations of peroxides as a function of oxidation time can be calculated. From these calculations it can be concluded that at the beginning of the oxidation (induction period) mainly slowly decomposing peroxides are formed.

The influence of both peroxides on the oxidation rate was determined in an oxidation (O_2)-decomposition (N_2)-oxidation (O_2) experiment (Figure 10). During the oxidation the concentrations of both peroxides were built up, after several oxidation times the oxidized powder was placed in nitrogen and a decomposition experiment was started. In the last stage of this experiment, the influence of varying the ratio between the two types of peroxide on the oxidation rate was determined. Especially for the samples with the longest decomposition time a reduction in oxidation rate was found. Although these samples still contains (slow decomposing) peroxides an induction period is found (Figure 10).

In literature there is general agreement that peroxides in PP consist of a rapidly decomposing fraction and a slowly decomposing fraction, but there is no agreement on the origin of these fractions [11,12,13,14] According to

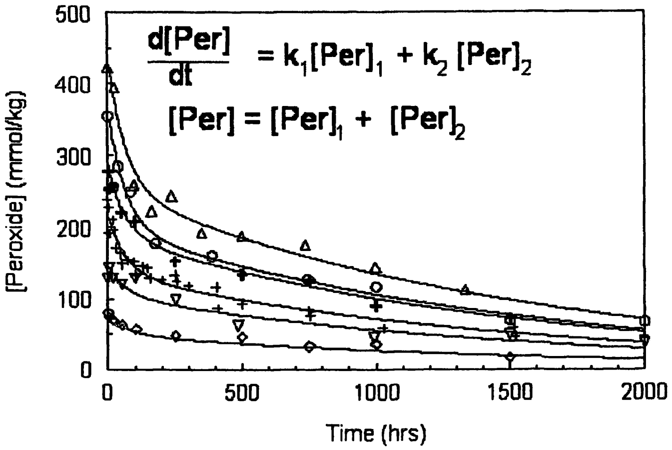

Figure 9. Peroxide concentrations as calculated according to the above-mentioned equations (lines) and determined by an iodometric method (points) during a peroxide decomposition experiment at 70°C with polypropylene pre-oxidized for several times at 70°C.

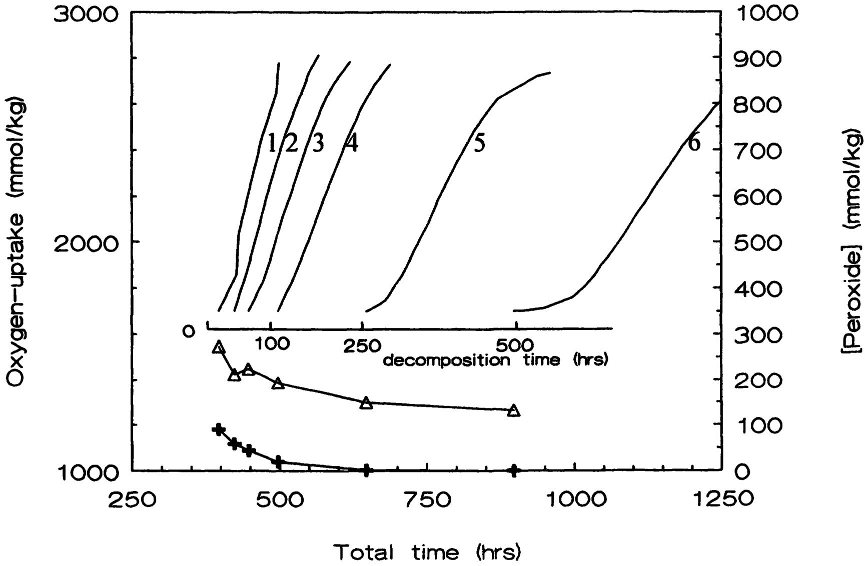

Figure 10. Oxygen uptake of PP at 70°C after 380 h of oxidation and 0 (1), 25,(2), 50 (3), 100 (4), 250 (5) and 500 (6) h decomposition in nitrogen. Also shown are the measured peroxide concentration(Δ) and the calculated concentration of rapidly decomposing peroxides (+) after the above mentioned decomposition times.

Zahradnikova et al. dimethyl sulphide (DMS) reacts much faster with peracids than with other types of peroxides [14]. Although there still is discussion about this method, from peroxide determination before and after treatment with DMS it was concluded that the fast decomposing peroxides are peracids [15], resulting from aldehydes which are formed via the decomposition of hydroperoxides .

Mechanism of Degradation of PP and Mechanism Underlying the Action of PAOs and HAS

It was shown that the radical formation rate of hydroperoxides (slowly decomposing peroxides) is too slow to explain the increase in oxidation rate (Figure 10). This increase in oxidation rate is ascribed to the decomposition of peracids that are formed as a result of the decomposition of hydroperoxides. This oxidation is so fast that it is hard to stop by antioxidants, so even in the presence of a PAO an oxidation can no longer be stopped once it has been initiated, leading to an infectious spreading of the degradation as shown in Figures 2 and 4. Model experiments with different hydrocarbons and aldehydes showed that HAS are not capable in reducing the oxidation of hydrocarbons, but they are capable in reducing the oxidation rate in the presence of aldehydes and prevent the formation of peracids. So in the presence of HAS the oxidation is not accelerated and the oxidation does not spread, although the primary oxidation is not stopped, which means that the polymer oxidizes from the beginning resulting in a homogeneous degradation and continuous low luminescence levels as shown in Figures 3 and 5.

Influence of Amines on the Oxidation of PP [6]

Oligomeric HAS types with a difference in the amines present in their backbone show a difference in activity. In the following it is shown that this can be due to a stabilizing effect of the backbone by showing the stabilizing effect of different amines.

The addition of an aliphatic amine did not have a major influence on the starting time of the degradation, but it had an influence on the spreading of the oxidation (Figure 11). As the spreading rate is determined by the oxidation of formed aldehydes, it is reasonable to assume that the aliphatic amines counteract the influence of these aldehydes. It is known that aliphatic amines can react with aldehydes to form more stable imines or enamines [16], which is a reasonable mechanism that explains the activity of aliphatic amines. Thus for oligomeric HAS with aliphatic amines in their backbone not only the piperidinyl groups is important, but also the chemical structure of the backbone.

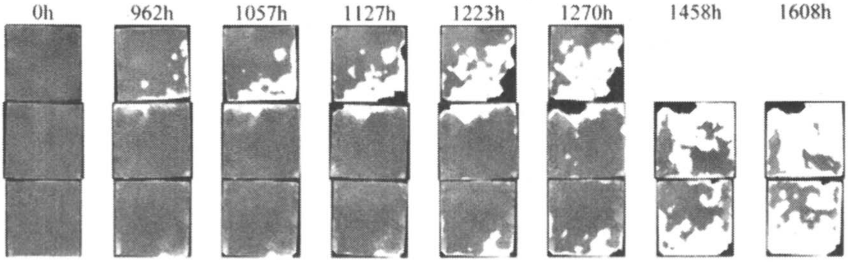

Figure 11. Scanned images of 150-μm PP films containing: 0.1 wt.% HAS-2 without additional additives (top), with 0.1% Distearylamine (middle) and with 0.1% of the stearic acid salt of N,N',N"-trimethylbis (hexamethylene)triamine (bottom) aged for different times at 120°C

Acknowledgements

Sabic-Europe b.v. is gratefully acknowledged for allowing us to publish the results presented in this paper.

References

1. Gugumus, F. *Polym. Degrad. Stab.* **1994**, *44*, 299-322.
2. Gensler R.; Plummer, C. J. G.; Kausch H. H.; Kramer, E.; Pauquet, J. R.; Zweifel, H. *Polym.Degrad. Stab.* **2000**, *67*, 195-208.
3. Gijsman, P. *Polym. Degrad. Stab.* **1994**, *43*, 171-176.
4. Gijsman, P.; Gitton, M. *Polym. Degrad. Stab.* **1999**, *66*, 365-371.
5. Gijsman P.; Hennekens J.; Vincent, J. *Polym. Degrad Stab.* **1993**, *42*, 95-105.
6. Gijsman, P.; Gitton, M. *Polym. Degrad. Stab.* **2003**, *81*, 483-489.
7. Hamskog, M.; Terselius, B.; Gijsman, P. *Polym. Degrad. Stab.* **2003**, *82*, 181-186.
8. Gijsman, P.; Internal DSM Report, 1985.
9. Gugumus F. in Plastic Additives Handbook, Eds. Gachter R., Muller H., Hanser Publishers, Munich, Vienna, New York, 1990, pp. 1-104.
10. Gugumus F. in Oxidation Inhibition In Organic Materials, Vol.I, eds. Pospisil J.; Klemchuk, P. P., CRC Press, Inc. Boca Raton, Florida, 1990, pp. 61-172.
11. Chien J. C. W.; Jabloner H. J. *J. Polym. Sci. Part: A-1* **1968**, *6*, 393-402.
12. Zolotova, N. V.; Denisov, E. T. *J. Polym. Sci. Part: A-1* **1971**, *9*, 3311-3320.
13. Shlyapnikov, Yu. A.; Bogaevskaya, T. A.; Kiryushkin, S. G.; Monakhova, T. V. *Eur. Pol. J.* **1979**, *15*, 737-742.
14. Zahradnikova, A.; Sedlar J.; Dastych, D. *Polym. Degrad. Stab.* **1991**, *32*, 155-176.
15. Gijsman, P.; Kroon, M.; van Oorschot, M. *Polym. Degrad. Stab.* **1996**, *51*, 3-13.
16. Morrison and Boyd, Organic Chemistry, 3rd edition, pp.858-859.

Chapter 6

Monitoring Free Radical Reactions in Degrading Polymers with a Profluorescent Nitroxide

Aaron Micallef, Steven Bottle, James Blinco, and Graeme George*

School of Physical and Chemical Sciences, Queensland University of Technology, Brisbane 4000, Australia

The relative concentration and distribution of alkyl radicals in degrading polypropylene has been determined by competitive scavenging of the radicals with a profluorescent nitroxide: 1,1,3,3-tetramethyldibenzo[e,g]isoindolin-2-yloxyl; TMDBIO. On scavenging the alkyl radicals to form the alkoxy amine, the fluorescence of the phenanthrene chromophore in TMDBIO (previously suppressed by the nitroxide) is now observed. The nitroxide also stabilizes the polymer as shown by an oxidation retardation period. By comparing the chemiluminescence from the hydroperoxide reactions of the same sample, the retarding effect of the nitroxide may be quantified in terms of the kinetic chain length (or spreading coefficient) of the oxidation as well as the radical scavenging efficiency from the fluorescence.

© 2008 American Chemical Society

The useful service lifetime of polyolefins on exposure to radiation and heat does not extend much beyond the induction period of the oxidation (*1*). This has been related to the cumulative and heterogeneous damage to the polymer such as chain scission and crosslinking that leads to localized changes in polarity, crystallinity and free volume that precede microcrack formation and consequent embrittlement. Because of the low overall extent of oxidation at failure, the study of the chemical changes preceding failure requires very sensitive methods for analysis of oxidation products, the free radical precursors, or other measures of damage that would allow the rate of the degradation reactions to be determined. In this chapter we will describe an approach that is based on a profluorescent nitroxide, 1,1,3,3-tetramethyldibenzo[e,g]isoindolin-2-yloxyl (TMDBIO) which is able to scavenge the primary free radicals, that are formed in the earliest stages of oxidation. This is illustrated for the scavenging of an alkyl radical R· such as the methyl radical, producing the adduct TMDBIOMe, which fluoresces with a spectrum identical to that of the chromophore, phenanthrene (*2*).

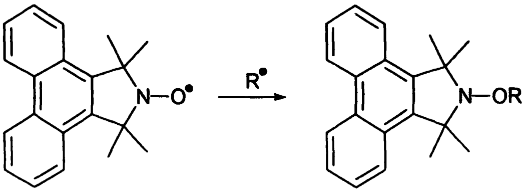

TMDBIO
profluorescent

R = CH_3; TMDBIOMe
FLUORESCENT

Free Radical Oxidation Reactions in Polyolefins

The generally-accepted sequence of reactions that are responsible for the chemical changes in a polyolefin on oxidation are shown in Figure 1. It is possible to associate an elementary rate equation with each reaction, although it is recognised that the true rates are difficult to measure both because of the physical state of the polymer, possible diffusion-controlled rate processes in the solid state and the many competing reactions. In a homogeneous rate model, this sequence of rate equations may be solved and a total reaction rate then fitted to the measured oxidation rate (*3*).

If a stabilizer is present then this reaction sequence is modified (Figure 2) by the competing reactions for the removal of polymer alkyl (**P·**) and alkyl peroxy (**POO·**) radicals. The nitroxide, **R_2NO•**, whether pre-formed, as in the case of TMDBIO above, or formed *in situ* through the oxidation of a hindered amine stabilizer, may scavenge only carbon centred radicals, **P·** . The hindered phenol antioxidant, **AH**, in contrast, will scavenge only oxygen centred radicals, and in

Initiation		
	Polymer	**→ P• + P• (eg γ-irradiation or POOH photolysis)**
Propagation		
	P• + O_2	**→ POO•**
	POO• + PH	**→ POOH + P•**
Chain Branching		
	POOH	**→ PO• + •OH**
	2POOH	**→ POO • + PO• + H_2O**
	PH + •OH	**→ P• + H_2O**
	PH + PO•	**→ P• + POH**
	PO•	**→ <u>various chain scission reactions</u> + P·**
Termination		
	POO• + POO•	**→ POOOOP → P=O + POH + O_2**
	POO• + P•	**→POOP**
	P• + P•	**→PP**

Figure 1. Sequence of free radical reactions that describes chemical changes to a polymer, PH, during oxidation. POOH represents the polymer hydroperoxide.

Propagation in <u>absence</u> of stabilizers:

P• + O_2	**→ POO•**	**Rate: k_2 [P•] [O_2]**
POO• + PH	**→ POOH + P•**	**Rate: k_p[POO•] [PH]**

Stabilizer reactions competing with these propagation reactions:

Nitroxide Retarder :

P• + R_2NO• → RNOP Rate: k_s[P·] [R_2NO·]

Hindered Phenol Inhibitor:

POO• + AH → POOH + A• Rate: k_{AH} [POO•][AH]

Figure 2. Elementary reactions and associated rates for the propagation reactions for the oxidation of a polymer PH without and with a nitroxide (R_2NO·) and a hindered phenol (AH) present.

particular the main propagating alkyl peroxy radical, **POO·**, and replace it with a stable radical **A•**. In Figure 2, the elementary reaction rates associated with the propagation and stabilizer reactions from Figure 1 are given.

In the sequence of reactions shown in Figure 1, the chain scission reactions of the alkoxy radical **PO•** are important in the formation of a crack and thus embrittlement. The reactions in the presence of the nitroxide and hindered phenol stabilizers are modified by competition with the stabilization reactions that lead to either an inert, non-radical alkoxy amine product (**R_2NOP**) or, for a hindered phenol, a stable radical (**A·**) that cannot initiate further oxidation.

It is recognised that the heterogeneous nature of the oxidation of a solid polymer makes it difficult to ascribe a physical meaning to a homogeneous analysis, but it is suggested that if a sufficiently small volume of the polymer is chosen, then the parameters may have a physical meaning. At the macroscopic scale a statistical approach is necessary in order to rationalize the heterogeneous aspects of the oxidative degradation *(1,4)*.

Chemiluminescence Analysis of Polymer Oxidation

The measurement of the weak visible light or chemiluminescence (CL) that accompanies the oxidation of polyolefins has been widely studied (*5*), particularly for polypropylene (*1,6*). While there are still uncertainties in the mechanism, there is general agreement that the CL – time curve is a sensitive measure of the process of hydroperoxide formation and decomposition in the polymer (*5*). Of some concern is whether the CL – time curve represents the kinetics of the propagation and branching reactions in Figure 1, or is instead the fraction of the total polymer through which the oxidation is spreading (*4,7*). In the former case the system is described by homogeneous kinetics (*1,3*) with the rate coefficients as shown in Figure 2 or in the latter case is described by a spreading parameter and the effect of temperature and added stabilizer on the CL – time profile is described with the mathematics of epidemiology (*4*).

Figure 3 shows the CL – time profile for samples of PP containing different concentrations of the profluorescent nitroxide TMDBIO. The CL curve for unstabilized PP shows that after a very short time, there is an exponential increase in CL corresponding to rapid oxidation and embrittlement of the polymer. The effect of the added nitroxide is not to decrease totally the CL from the PP, but rather to retard the emission so that there is a slower development of the CL emission intensity. There is thus an increase in the time taken to see the exponential increase in emission intensity, but the emission is not reduced to zero in this retardation period. In contrast, if a peroxy-radical scavenging, hindered phenol such as Irganox 1010 were to be added to the PP then the increase with time of the CL intensity would be totally suppressed and there would be an apparent induction period (*8*). This result may be interpreted within the framework of the free-radical reactions in Figures 1 and 2 above.

In Polymer Durability and Radiation Effects; Celina, M., et al.;
ACS Symposium Series; American Chemical Society: Washington, DC, 2007.

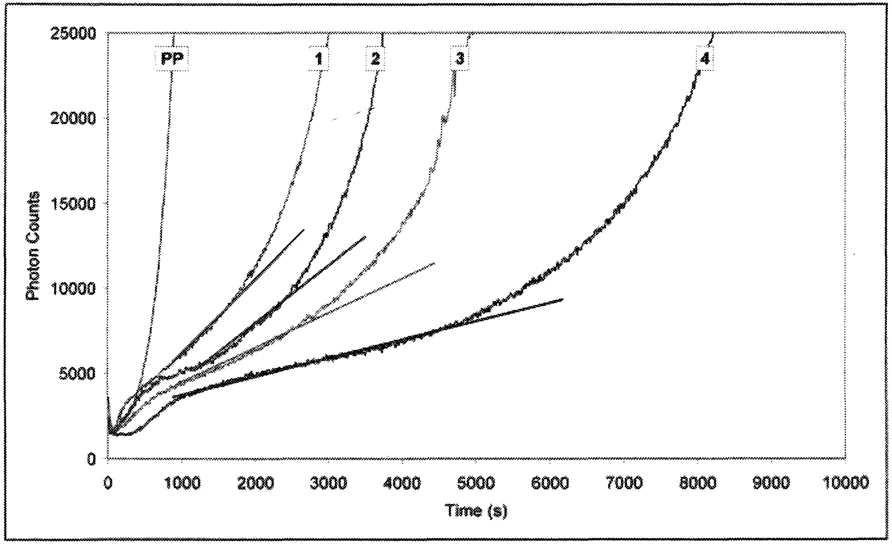

*Figure 3. The early stage of CL curves during the oxidation of PP at 150°C in oxygen with added TMDBIO at concentration of: **1**:0.01 wt%;**2**: 0.02wt%; **3**: 0.03wt% and **4**:0.05 wt%. The slopes in the retardation period are indicated.*

Kinetic Analysis of CL - Time Curves

When the nitroxide is present, the alkyl peroxy radicals **POO•** and the resultant hydroperoxide **POOH** are still formed, but the concentration is reduced due to the competition between oxygen and nitroxide for the alkyl radicals **P•**. The rates of these reactions are given in Figure 2 for homogeneous kinetics. The extent of this competitive reaction may be estimated by the decrease in the slope of the CL – time curves in the retardation period as shown in Figure 3 and also by the formation of the alkoxy amine $\mathbf{R_2NOP}$. The concentration of the alkoxy amine $\mathbf{R_2NOP}$ may be measured by fluorescence (see next section).

The change in slope in the retardation region of the CL curves (Figure 3) reflects the decrease in the rate of formation of **POOH** when the nitroxide is present. Considering initiation by n-th order decomposition of **POOH** with rate coefficient k_d and noting that the kinetic chain length, υ, is:

$\upsilon = R_{ox}/R_i = k_p[PO_2\cdot][PH]/\,k_d[POOH]^n$ then the change in CL with time is:

$$dI_{CL}/dt = \varphi(d[POOH]/dt) = n\varphi k_d[POOH]^n(\upsilon-1) \qquad (1)$$

where φ is the overall CL quantum efficiency. It is noted that while υ is derived for oxidation in homogeneous kinetics (Figure 2) it may also be regarded as related to the spreading factor in heterogeneous kinetics (*4*). The role of υ can be seen empirically in the nature of the CL – time profiles.

- When $\upsilon = 0$, the CL will decay with time with n-th order kinetics reflecting the decay of the particular fraction of the total hydroperoxide that results in CL. This decay of CL is seen when the polymer is heated in nitrogen (*9*).
- When $\upsilon = 1$, the CL will be steady ($dI_{CL}/dt = 0$) and this corresponds to inhibition of the oxidation since there is no increase in hydroperoxide ($d[POOH]/dt = 0$) and the oxidation cannot spread from the initiating sites.
- When $\upsilon > 1$, there is spreading of the oxidation with d[POOH]/dt being positive so the CL increases with time.

The effect of the retarding nitroxide is to lower the rate of spreading of oxidation but not to decrease it totally. This is consistent with the observation that hindered amine stabilizers function as retarders of thermo-oxidative degradation but do not totally inhibit it. Thus it is reported that there is a slow decrease in strength of polypropylene on thermal ageing with HAS rather than the virtually undetected change in strength of the polymer when hindered phenol antioxidant is present (*10*). The CL analysis thus provides a method for determining this competition.

As shown in Figure 4, the slope of the plot is a measure of the retarding effect of the nitroxide and reflects the competition between oxygen and

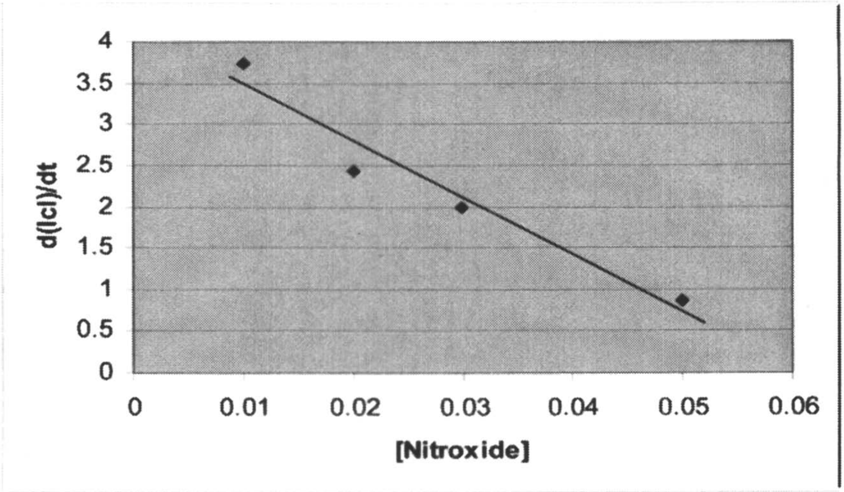

Figure 4. Plot of the slope of the retardation region of the CL curve from Figure 3 as a function of concentration of TMDBIO. The slope represents the effect of the nitroxide on the value of υ in equation (1).

TMDBIO for the alkyl radicals formed by initiator (hydroperoxide) thermolysis. The further quantitation of this reaction is difficult without assuming a kinetic model or obtaining further analytical information such as the actual concentration of nitroxide that has reacted during the retardation reaction. In the special case of the pro-fluorescent nitroxide, this can be achieved by fluorescence analysis of the formed alkoxyamine **R_2NOP**.

Fluorescence Analysis of Nitroxide Retardation of Oxidation

The pro-fluorescent nitroxide TMDBIO when it reacts with an alkyl radical generates a fluorescent alkoxy amine so the fluorescence then becomes an integral measure of the number of such reactions that have taken place (*2*). This is seen in Figure 5 below for a sample of PP before and after oxidation at 150°C.

It may be seen from the clear aromatic vibronic progression that the fluorescence spectrum is that of phenanthrene, the chromophore present in TMDBIO. This fluorescence, before trapping of the alkyl radicals, was suppressed by the spin-orbit coupling of the nitroxide group located on the iso-indoline framework as seen from its structure (Introduction). The dependence of the fluorescence on the nitroxide concentration may be seen in Figure 6.

The fluorescence intensity is a measure of alkoxyamine reaction product and it is seen that the emission intensity increases with time without any induction period. At the highest concentration, this is linear and a straight line has been

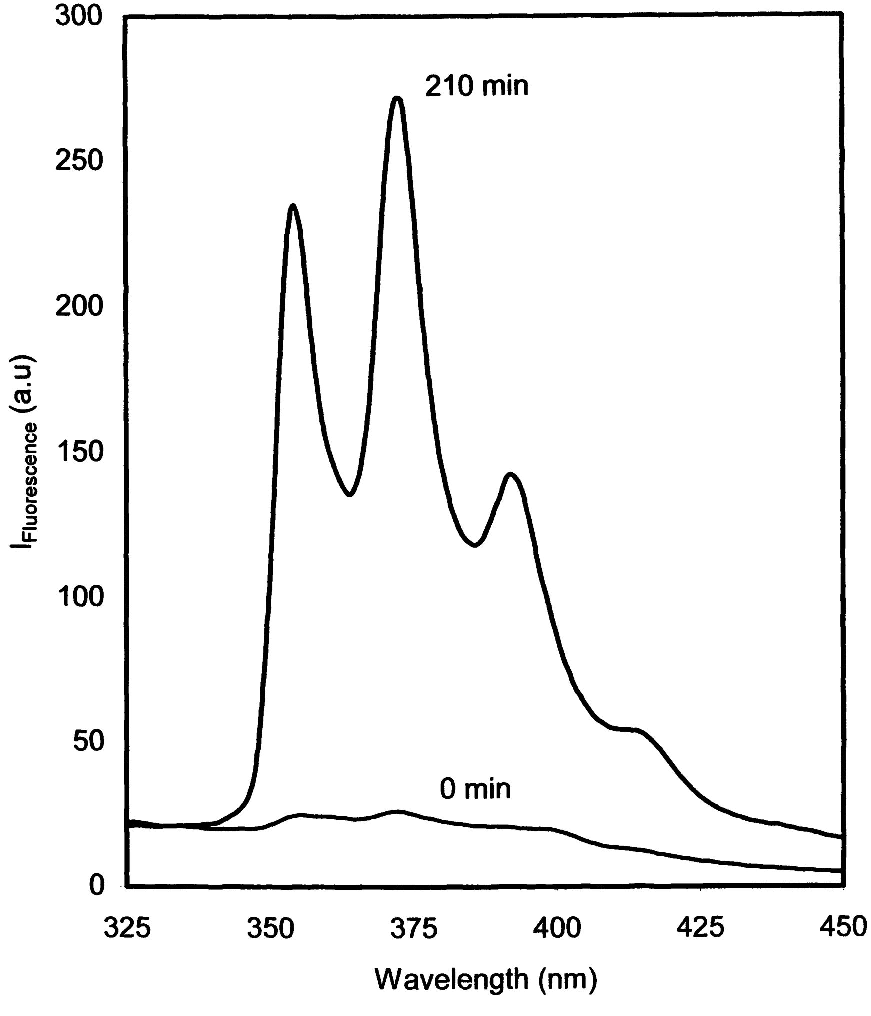

Figure 5. Increase in fluorescence at 23°C (294nm excitation) from PP +0.035wt % TMDBIO after 210 min 150°C in oxygen (2).

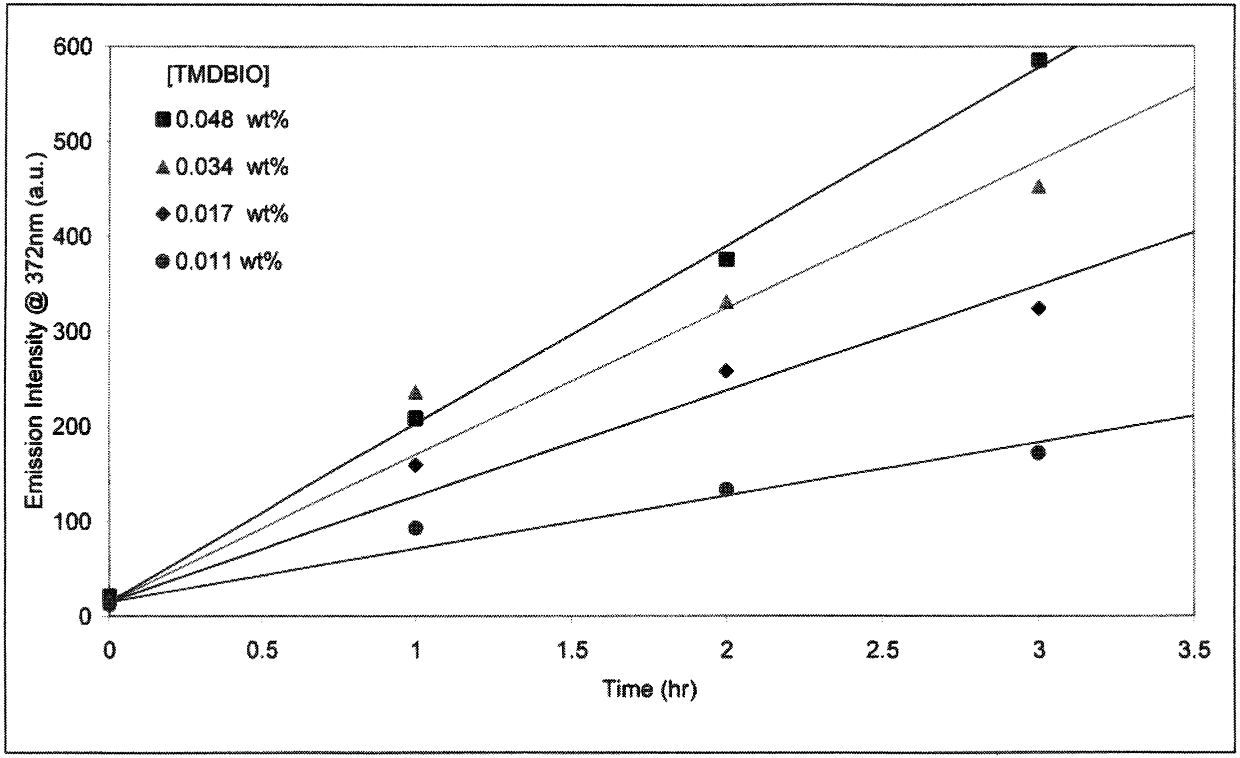

Figure 6. Growth in fluorescence with time of oxidation at 150°C for PP with different concentrations of TMDBIO.

fitted to each data set as shown in Figure 6. This is a much simpler relationship than the CL – time profiles shown in Figure 3 and may be analysed by consideration of the simple reaction kinetics in Figure 2.

Kinetic Analysis of Fluorescence Intensity – Time Curves

The scavenging of alkyl radicals **P·** by the nitroxide **R_2NO·** (TMDBIO) to give the product **R_2NOP** will result in the appearance of fluorescence with intensity $I_F = \varphi_F[R_2NOP]I_0$, where I_0 is the intensity of exciting light, and φ_F the fluorescence quantum yield of **R_2NOP**. Thus the change in fluorescence intensity with time (for the same I_0) when the bimolecular alkyl radical scavenging reaction of the nitroxide retarder in Figure 2 is considered, will be given by:

$$d\,I_F/dt = d[R_2NOP]/dt = \varphi_F\, k_S\, [P\cdot][TMDBIO] \qquad (2)$$

The slopes of the lines in Figure 6 are plotted as a function of [TMDBIO] in Figure 7 and the linear relation indicates that the simple bimolecular reaction of alkyl radicals described by equation (2) is appropriate.

The slope of this line is a measure of the alkyl radical scavenging efficiency, k_S, for a given temperature and is also an indication of the efficiency of the nitroxide radical in competing with oxygen for these radicals. There is clear

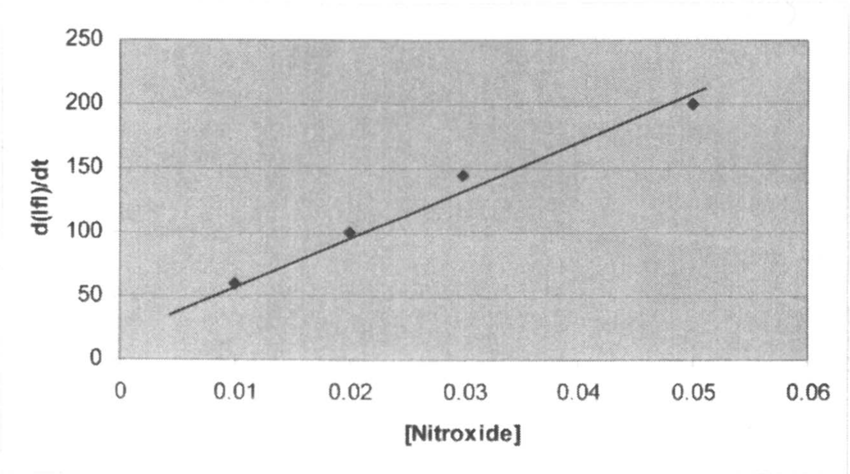

Figure 7. Plot of the increase in fluorescence intensity from TMDBIO doped PP with time of oxidation (Figure 6) as a function of [nitroxide] in wt%.

evidence that the alkyl radical population that is scavenged by the nitroxide is not from the primary initiation event since the intensity of fluorescence generated by the heating of the TMDBIO with PP in an inert atmosphere is much reduced from that when oxygen is present. The method is therefore able to trap a fraction of the radicals responsible for the spreading of the oxidation.

It is also found that the decay kinetics of CL differ from those for the growth of fluorescence under an inert atnmosphere, reflecting the complexity of the initiation process of hydroperoxide decomposition. One interpretation of this is that the CL arises from the fraction of the hydroperoxides that are able to spread the oxidation beyond the initial zone of initiation (*4*).

The use of a profluorescent nitroxide, in this case the phenanthrene analog TMDBIO, offers the prospect of not only quantifying the alkyl radical scavenging efficiency in the earliest stages of polyolefin oxidation (in the retardation period) as demonstrated here, but also integration over time of the total alkyl radical population formed on oxidation. Future prospects include imaging of the zones of degradation by fluorescence microscopy.

Acknowledgement

This work was produced (in part) with the support of the Australian Research Council under the ARC Centres of Excellence program.

References

1. George, G. A.; Celina, M. Homogeneous and heterogeneous oxidation of polypropylene. *Handbook of Polymer Degradation (2nd Edn)* S.Halim, Ed.; Marcel Dekker, New York, 2000; p. 277.
2. Micallef, A. S.; Blinco, J. P.; George, G. A.; Reid, D. A.; Rizzardo, E.; Thang, S. H.; Bottle, S. E. *Polym. Degrad. Stab.* **2005**, *89*, 427.
3. Verdu, J., Verdu, S. *Macromolecules* **1997**, *30*, 2262.
4. Goss, B. G. S.; Barry, M. D.; Birtwhistle, D.; George, G. A. *Polym. Degrad. Stab.* **2001**, *74*, 271.
5. Jacobson, K.; Eriksson, P.; Reitberger, T.; Stenberg, B. Chemiluminescence as a tool for polyolefin oxidation studies. *Advances in Polymer Science* **2004**, 169, (Long-Term Properties of Polyolefins), 151.
6. Goss, B. G. S.; Nakatani, H.; George, G. A.; Terano, M. *Polym. Degrad. Stab.* **2003**, *82*, 119.
7. Gijsman, P.; Hamskog, M. *Polym. Degrad. Stab.* **2006**, *91*, 423.
8. Matisova-Rychla, L.; Rychly, J. *J. Polym. Sci., Part A: Polym. Chem.* **2004**, *42*, 648.
9. Billingham, N. C.; Grigg, M. N. *Polym. Degrad. Stab.* **2004**, *83*, 441.
10. Zweifel, H. *Stabilization of Polymeric Materials.* First ed.; Springer-Verlag, Berlin, 1998.

Chapter 7

Lifetime Prediction of Elastomer for Radiation-Induced Degradation by Time Accelerated Method

Masayuki Ito

Advanced Research Institute for Science and Engineering, Waseda University, 3–4–1 Okubo, Shinjuku-ku, Tokyo 169–8555, Japan

The short time test was performed by the irradiation of Co-60γ ray up to 10 MGy at 70□ in air. Dose rate was 5.0 kGy /h. The samples used were ten kinds of EPDM that have different compounding formula. After irradiation, the mechanical properties were measured at room temperature. "Modulus-Ultimate elongation plotting" evaluated the ratio of scission and crosslinking occurred during irradiation. The ratio differed greatly on the compounding formula. "Tensile Energy (TE)" was proposed as a criterion for estimating the life time of elastomer. TE is the area of stress-strain curve which decreased with increasing dose. The dose at the life time where ultimate elongation decreased to 100% or TE decreased to 500 %·MPa was 4 MGy for the most radiation resistant EPDM in the experiment.

 © 2008 American Chemical Society

Introduction

Electric wires and cables used in nuclear power plant are exposed by low dose rate irradiation during the life time of the plant. In addition, loss of coolant accident (LOCA) that is a design basis accident brings about the degradation by heat and radiation on the electric wire and cables. The dose varies from plant to plant. IEEE std.323-1974 (*1*) estimated the dose 0.5 MGy for the period of the life time and 1.5 MGy for LOCA as one of the example. The standard estimated 40years and one year, for the lifetime of plant and duration of LOCA respectively.

The time accelerated aging method for electric wires and cables requires a high dose rate irradiation, but the exposure to polymer in air results only the oxidation of surface when the dose rate is higher. I previously reported the methodology study of time accelerated irradiation of elastomer (*2*). The study showed two appropriate methods, one was irradiation in pressurized oxygen at room temperature; the other was irradiation at 70°C in air. The article studied the effect of higher dose (up to 10 MGy) irradiation on ethylene-propylene-diene elastomer (EPDM) by using the time accelerated method. Irradiation at 70°C in air was chosen as the time accelerated irradiation condition because of the experimental convenience.

Experimental

Materials

EPDM is used for the insulating material of electric cable in nuclear power plant. As the properties of EPDM depend on their compounding formula, there are many receipts for improving heat resistant properties, durability against oil, resistance to ozone, and so on.

Table I-V shows the compounding receipt of the samples used in this study.In th etable phr means pers per hundred resin (rubber). The thickness of the samples was about 0.5 mm. EPDM-3, 4, 5, 6 and 7 are the series of the compounding formula of the curing by low sulfur. EPDM-2 contains the relatively higher sulfur with Hypalon (Chlorosulphonated polyethylene) that increases tensile strength of elastomer. EPDM-1, 8 and 10 were crosslinked by peroxide. Triallyl isocyanurate in EPDM-1 is a multi-functional compound that increases the concentration of network.

Table I. Compounding Formulation of EPDM-1

Ingredient	*phr*
Nordel 1070 (Du Pont)	70
EP11 (JSR)	30
Triallyl isocyanurate	2
Dicumyl peroxide	2.5
Zinc oxide	5
Ulltrafine magnesium silica	20
Hard clay	20
Carbon black (FEF)	20
Process oil	5
2-Mercaptobenzoimidazole	4
Polymer of 2,2,4-trimethyl-1,2 dihydroqinoline	1

phr : Parts per hundred resin

Table II. Compounding Formulation of EPDM-2

Ingredient	*phr*
Nordel 1070 (Du Pont)	100
Hypalon	5
Sulfer	1.5
Zinc oxide	10
Stearic acid	1
N-Cyclohexyl-2-benzothiazolyl-sulfide	1.5
Tetramethylthiuramdisulfide	0.5
Nickel dibutyldithiocarbamate	2
Hard clay	20
Ulltrafine magnesium silica	20
Carbon black (FEF)	20
Process oil	5

Table III. Compounding Formulations of EPDM-3, 4, 5, 6, 7, 9

EPDM *Ingredient*	*3* *phr*	*4* *phr*	*5* *phr*	*6* *phr*	*7* *phr*	*9* *phr*
Nordel 1070 (du pont)	100	100	100	100	100	100
Tetramethylthiuramamidisulfide	3	3	3	3	3	3
4,-4'-Dithiodimorpholine	2	2	2	2	2	2
Zinc dimethyldithiocarbamate	2	2	2	2	2	2
Zinc di-n-butyldithiocarbamate	2	2	2	2	2	2
Sulfer	0.5	0.5	0.5	0.5	0.5	0.5
Selenium		3			3	
Zinc oxide	5	5	5	5	5	5
Carbon black (FEF)	30	30	30	30	30	
Clay						30
Ulltrafine magnesium silica						70
Aromatic oil			15		15	15
Parafifinic oil	20	20		20		
Parafine			5			
Nickel dibutyldithiocarbamate	2	2	2			2
2-Mercaptobenzoimidazole				4	4	
Polymer of 2,2,4-trimethyl-1,2 dihydroqinoline				1	1	

Table IV. Compounding Receipt of EPDM-8

Ingredient	*phr*
Nordel 1070 (du pont)	100
Dicumyl peroxide	2.5
Zinc oxide	5
Lead peroxide	3
Carbon black (SRF)	4
Silane coated clay	110
Parafinic oil	15
Parafine	5
Vinyl-tris (beta-methoxyethixy) silane.	1
Polymer of 2,2,4-trimethyl-1,2 dihydroqinoline	1.5

Table V. Compounding Receipt of EPDM-10

Ingredient	*phr*
Esplen 301(Sumitomo Chemical)	100
Dicumyl peroxide	2.8
Zinc oxide	5
Sulfer	0.3
Stearic acid	1
Talc	100
Sonic 2000	20
p-Quinone dioxme	0.5
Polymer of 2,2,4-trimethyl-1,2 dihydroqinoline	0.5

Irradiation Conditions

The irradiation was performed by Co-60 γ ray at 70°C in an air oven. Dose rate was 5.0 kGy/h; the maximum dose was 10 MGy.

Tensile Testing

After irradiation, sample sheets were cut into a dumbbell shape (Japan Industrial K6301 Tensile testing standard, No.4) by using new type of cutter (Dumbbell co.). Tensile test were performed using Shimazu Model SC-500 Test Machine equipped with pneumatic grips. Samples were strained at ambient temperature at 500 mm/min using an initial jaw distance of 50 mm. No sample was cut near the grips in the tensile test, because the cutting procedure didn't give the defect on the cut surface. At each aging condition four samples were tested and averaged to obtain the results.

Result and Discussion

Ultimate Elongation

There were two types of the changes in ultimate elongation by irradiation. In the first type, ultimate elongation decreased almost straight with increasing dose during earlier period of irradiation as shown in Figure 1and 2 . The change was not the same by the samples after irradiation of 4MGy shown in Figure 1 and irradiation of 2MGy in Figure 2. In the second type, ultimate elongation

decreased rapidly by irradiation, but it remained the same value despite the increasing dose as shown in Figure 3. This type was not durable for irradiation. The latter section shows a detailed discussion of the reasons.

Tensile Strength

The relationship between tensile strength and dose depended largely on the compounding formula. Irradiation increased tensile strength of EPDM-4, 6 and 7 except the earlier stage as shown in Figure 4. Figure 5 shows one of the typical changes in tensile strength by irradiation. Tensile strength decreased significantly by relatively low dose irradiation, but the value started to increase from a certain dose.

EPDM-8, 9 and 10 were the other types that decreased the tensile strength with increasing dose as shown in Figure 6.

Tensile strength is an important mechanical property of elastomer. Five kinds of EPDM in the experiment kept the higher tensile strength at 10MGy than initial values showing the durability of the samples for irradiation.

On the view point of the life time prediction, tensile strength is not the appropriate factor, because there are three types of the relationship between the stress (dose) and the response (values of tensile strength) as shown in Figure 4, 5 and 6.

Relationship between Modulus and Ultimate Elongation

We studied the effect of quantitative addition of scission and crosslinking on the changes of the mechanical properties of elastomer and showed how the ratio of scission and crosslinking occurred during aging affects the mechanical properties (*4*). On the basis of the study, "Modulus-Ultimate elongation plotting" was proposed to calculate the changes of the ratio during the aging (*5*).

Figures 7, 8 and 9 show Modulus-Ultimate elongation plotting of ten kinds of EPDM. The simplest case is shown in Figure 7. Crosslinking was predominant in EPDM-2 throughout the period of irradiation. Figure 8 shows the plotting for EPDM-3 to 7. During the earlier stage of the aging, Modulus-Ultimate elongation plotting of the samples went down along Y axis showing the ratio of scission and crosslinking was the same. Crosslinking became to predominate from the certain period in all of five samples.

It is pointed out in the thermal degradation of polymer that as the radical concentration increases with passing the aging time, crosslinking reaction increases by the recombination of the radicals. A certain type of radiation induced degradation of elastomer may have the same tendency. Figure 9 shows the other types of modulus-ultimate elongation relationship. Irradiation raised

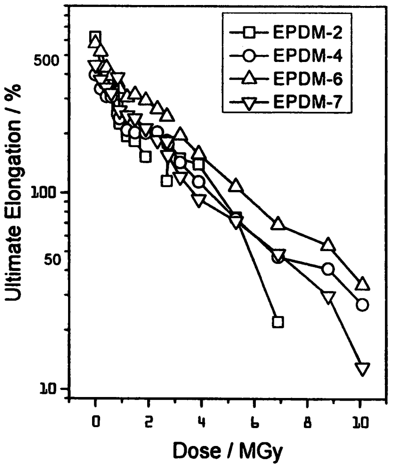

Figure 1. Decrease in ultimate elongation of EPDM-2,4,6,7.

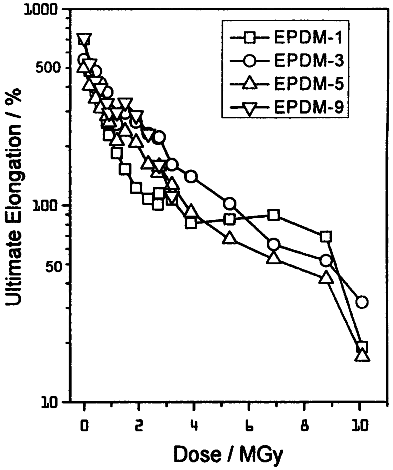

Figure 2. Decrease in ultimate elongation of EPDM-1,3,5,9.

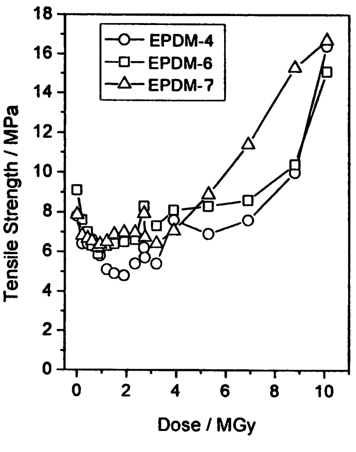

Figure 3. Decrease in ultimate elongation of EPDM-4,6,7.

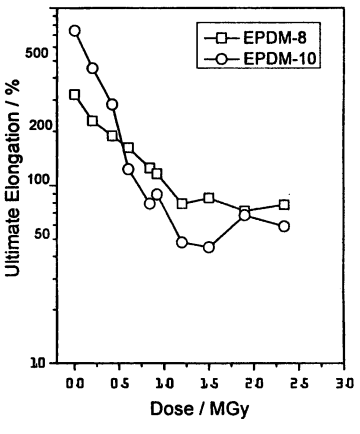

Figure 4. Changes of tensile strength of EPDM-8,10.

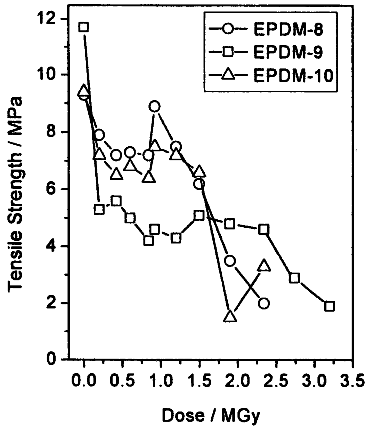

Figure 5. Changes of tensile strength of EPDM-8,9,10.

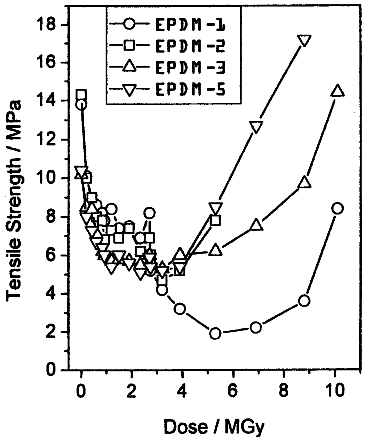

Figure 6. Changes of tensile strength of EPDM-1,2,3,5.

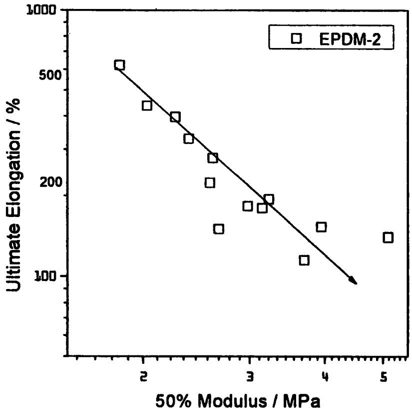

Figure 7. Modulus-Ultimate elongation correlation of EPDM-2.

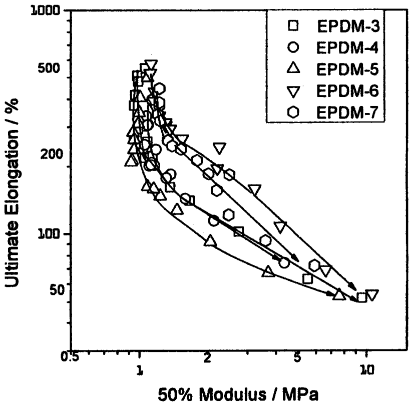

Figure 8. Modulus-Ultimate elongation correlation of EPDM-3 to 7.

almost the same amount of scission and crosslinking in the earlier aging stage of EPDM-1, but scission reaction predominated in the latter part of aging. EPDM-8, 9 and 10 had the similar form in Figure 9. Crosslinking predominated in the low dose region and scission predominated from the certain dose.

The scission lost the network concentration of elastomer and generated the low molecular chain. The large amount of scission breaks crosslinking structure of network chain in the elastomer and the sample become the mixture of non-crosslinked molecular chain and the small gel that was the part of crosslinking structure. EPDM-8 and 10 kept the values of ultimate elongation during the period from 1.0 to 2.5 MGy as shown in Figure 3, but the modulus decreased remarkably and the sample lost elasticity. In this case, the elongation in combination with modulus information may be useful for life time prediction.

Tensile Energy

Ultimate elongation of elastomer commonly decreases with increasing the period of aging time. Therefore, ultimate elongation is considered to be the factor that evaluate the life time of elastomer. Both scission and crosslinking of molecular chain resulted in decrease of ultimate elongation but the rate of decrease in ultimate elongation was slower in scission predominant condition than in crosslinking predominant condition (4).

Considering the evaluation of the life time of elastomer, Samay et al. pointed out that tensile strength has the same importance as ultimate elongation has. They proposed "Braking Energy (BE)" to estimate the life time of elastomer (*5*). Equation 1 defined BE.

$$\text{BE} = (\text{Ultimate elongation}) \times (\text{Tensile strength}) \quad (1)$$

As BE dose not contain modulus in the concept, the losing of elasticity of elastomer is not accounted. Hence, we proposed "Tensile Energy (TE)" as a factor to estimate the life time of elastomer (*6*). TE is the area under the stress-strain curve. Figure 10a and 10b suggest the difference between BE and TE. For both stress-strain curves, BE is 350 MPa·% where TE in Figure 10a is 125 MPa·% and TE in Figure 10b is 200MPa·%. The stress-strain curve of the elastomer shown in Figure 10b looks like it is tougher and more durable than that shown in Figure 10a. Therefore, TE is adequate to evaluate the degree of degradation of elastomer.

Figure 11, 12, and 13 show the changes of TE by irradiation. TE of all samples used in the experiment decreased with increasing dose. The result suggested that TE could be a factor for estimating the life time. There were three types of the relationship between TE and logarithm of dose. TE of EPDM-9 shown in Figure 11 accelerated the decay rate from about 3 MGy. On

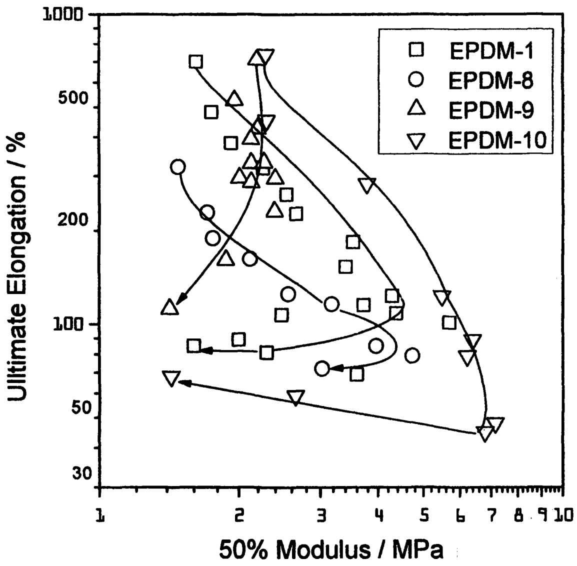

Figure 9. Modulus-Ultimate elongation correlation of EPDM-1,8,9,10.

the other hand, four samples shown in Figure 12 slowed down the rate of decrease in TE from a certain dose. In the third type, the relationship between TE and logarithm of dose was the linear as shown in Figure 13. Only the third case can define the rate of decrease of TE by irradiation from the slopes.

There are two considerable methods to estimate the life time by observed TE. The one takes the dose that the TE retained reaches a certain value. The other takes the dose that TE decrease a certain value. The former notices the change of the relative value in TE, the latter takes note of the value of TE decreased by irradiation.

The article takes the life time of elastomer when TE decrees to 500 MPa·% at which the elastomer is tough enough, considering the stress-strain curve in Figure 10b.

Figure 14 shows the map of the dose at which TE decreased to 500 MPa·% and the dose when ultimate elongation (Eb) decreased to 100% for all of the samples.

Conclusion

It was determined that the most radiation resistant sample in this study was EPDM-6, that kept 500 % MPa tensile energy at about 4 MGy and kept 100 %

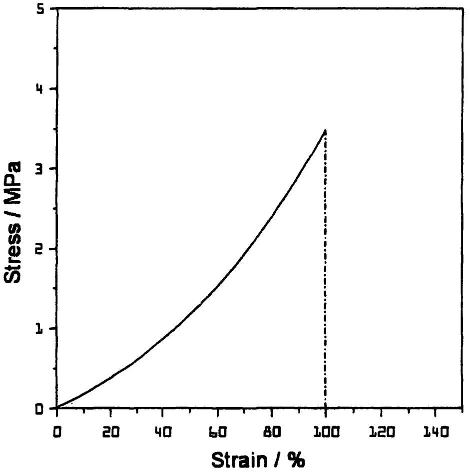

Figure 10a. Relationship between BE and TE, BE=350 MPa·% TE=125 MPa·%

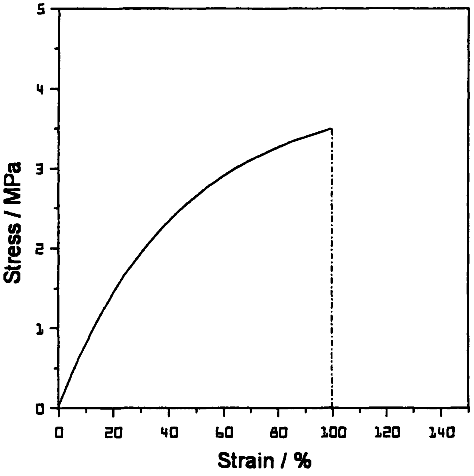

Figure 10b. Relationship between BE and TE, BE=350 MPa·% TE=200 MPa·%

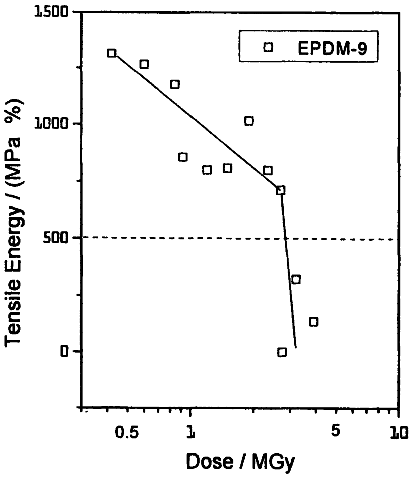

Figure 11. Decrease in TE of EPDM-9 by irradiation.

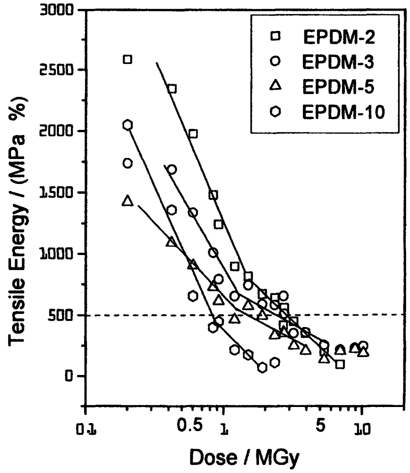

Figure 12. Decrease in TE of EPDM-2,3,5,10.

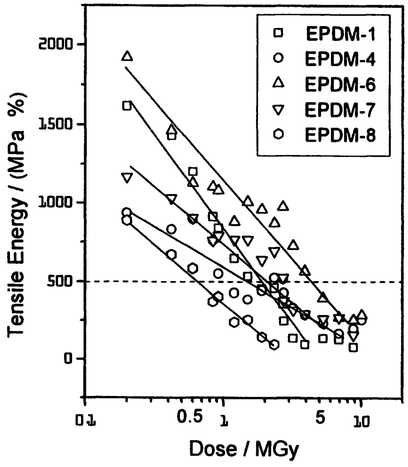

Figure 13. Decrease in TE of EPDM-1,4,7,8.

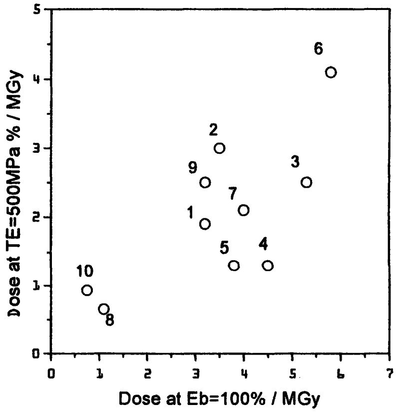

Figure 14. Map of life time based on TE and ultimate elongation.

ultimate elongation at about 6 MGy which is twice the dose of the highest reported value (*7*).

References

1. *IEEE Std.323-1974, IEEE standard for qualifying Class 1E equipment for nuclear power generating stations,* IEEE, **1974**.
2. Ito, M. *Nucl.Instr. and Meth. in Phys. Res.* **2005**, *B236*, 229.
3. Ito, M. *Nucl.Instr. and Meth. in Phys. Res.* **2005**, *B236*, 231.
4. Ito, M. *J. Soc. Rubber Ind. Japan* **1985**, *59,* 169.
5. Samay, G.; Palotas, L.; Seregely, Zs. 4th International Seminar on Elastomers (Kurume, Japan). **1990**, 333.
6. Ito, M. *Material life*, **1995**, *7*, 195.
7. Seguchi, T.; Morita, Y. *Radiation resistance of plastics and elastomer, Polymer Handbook*, **1998**, VI 583.

Chapter 8

Rubber Aging Study: Real Time with "Ideal" Storage

Thomas W. Wilson III

Taiwan Country Innovation Team, Nike Inc., 447 Wen Hsin Road, Sec. 3, 28th Floor, Taichung 40667, Taiwan

Anecdotal evidence suggests that rubber outsoles change over time leading to consumer perceptions of decreased performance. The purpose of this ageing study was two fold. First, the physical properties of a standard rubber compound were evaluated over time to quantify changes. Second, simple formula and process adjustments were made to see if it was possible to produce a rubber product that: 1) exhibited acceptable or improved properties, and 2) minimized property changes over time. The results show that reducing the sulfur level by as much as 30% from what is typically used in production leads to improved properties with reduced changes; i.e. more consistency, over time.

From previous accelerated and real time ageing studies, it is known that rubber compounds exhibit complex property changes over time (*1,2*). Oftentimes, this can lead to less than desirable characteristics in the rubber, such as increased stiffness, embrittlement, poor abrasion characteristics, and others. In thin latex rubber products, it is common practice to under cure the rubber. As the product ages, certain properties will tend to improve for a while before starting a decline. For example, latex rubber condoms are stored in hermetically sealed packages, which limit exposure to oxygen, ozone and UV; therefore, their ageing characteristics are more predictable and less pronounced than tires or footwear outsoles, since they can establish a three to five year shelf-life (*3*).

It is hypothesized that improved ageing characteristics of rubber compounds could be facilitated by reducing the amount of sulfur and/or under curing the

© 2008 American Chemical Society

rubber. The following study examines this hypothesis over the time span of one year's storage in a controlled laboratory environment.

Experimental

A production batch of an outsole compound was divided into four equal portions. The only formula difference between each portion was the amount of sulfur and <0.15% pigment for differentiation and tracking. The standard amount of sulfur, based on the current formulation, was designated as 100%. The other three portions had the following amounts: 70%, 85% and 115% of the standard amount. Whenever "% sulfur" is referred to, it is always relative to the standard.

The cure times are determined via an Eekon Rheometer. An uncured sample is placed between two heated discs (150°C). As the sample cures, the viscosity increases. The cure condition, e.g. T90, is determined by the time required for the viscosity to increase to 90% of the difference between the minimum and maximum values. Samples cured at T60 and T75 represent various degrees of under curing. Samples cured at T90 and T90+1 (T90 plus one minute) represent optimal curing. To make an adequate matrix of conditions, each of the four portions was cured at two conditions, either T60 and T90, or T75 and T90+1. Current production would be represented by "100% T90+1", as a bold "X" in Table I.

Table I. Cure matrix

%Sulfur/Cure	*T60*	*T75*	*T90*	*T90+1*
115%	X		X	
100%		X		**X**
85%	X		X	
70%		X		X

After pressing, slabs were placed in shoeboxes and delivered to the Nike Taichung Laboratory for storage and testing (hardness, tensile strength, 300% modulus, percent elongation, tear strength and abrasion) at five intervals over one year. Inside one shoebox was a Cytherm® datalogger that measured temperature hourly.

In Polymer Durability and Radiation Effects; Celina, M., et al.;
ACS Symposium Series; American Chemical Society: Washington, DC, 2007.

Results and Discussion

The temperature in the laboratory was fairly constant with an average temperature of 23.9°C and a standard deviation of 2.20°C. There were a few excursions below the lower 3σ limit, but none above. For ageing studies in rubber systems, low temperatures would be less detrimental to properties than high temperatures and are considered of no significance in the present study.

Baseline Conditions

The physical properties immediately after manufacture are designated as the baseline condition. It can be seen from Table II that, at baseline, every condition for every parameter met the Nike specification.

Table II. Physical Properties

% Sulfur	*Cure*	*Hardness (Shore A)*	*Modulus (kg/cm²)*	*Tensile (kg/cm²)*	*Elongation (%)*	*Tear (kg/cm)*	*Abrasion (cc loss)*
70	T75	64.5	51	150	641	59	0.26
70	T90+1	64.0	53	146	617	58	0.28
85	T60	64.5	57	136	558	60	0.26
85	T90	66.0	53	143	600	56	0.27
100	T75	64.5	61	139	554	61	0.25
100	T90+1	64.5	57	121	524	55	0.28
115	T60	65.5	69	113	438	59	0.28
115	T90	67.0	63	112	471	56	0.29
Nike specification		62~68	>35	>110	>400	>35	≤0.3

The two parameters that display similar changes as a function of sulfur content and extent of cure are percent elongation and tensile strength. Generally as tensile strength increases, there is a concurrent decrease in percent elongation. This applies when the primary mode used to increase tensile strength is an increase in crosslink density. It was unexpected to discover that reducing sulfur content and extent of cure, which would be expected to reduce crosslink density,

resulted in an increase in tensile strength. The optimum condition appears to be at ~70% of the standard amount of sulfur and T75. These changes appear more consistent with a decrease in defects than an increase in crosslink density. Alternatively, there may be differences in the ratio of mono-, di- and poly-sulfidic crosslinks.

The 300% modulus is another parameter that is closely related to crosslink density. It followed the expected trend that increases in sulfur content yielded higher moduli.

Abrasion is a complex phenomenon. The optimum condition for abrasion was 100% sulfur and T75 cure; however, the variation among all the conditions was small: 0.25 to 0.29cc.

Tear strength was similar to abrasion with the optimum condition at 100% sulfur and T75. It too was confined to a tight range: 55 to 61kg/cm.

The most surprising result for the baseline conditions was that severe under curing (T60) and wide variations in sulfur content did not produce any "out-of-spec" material. This result was not anticipated, and showed that the specification may not identify poorly formulated and/or processed materials.

Aged Properties

To determine the optimum process condition(s) and formulation that minimize the effects of ageing requires: 1) an acceptable value for the parameter being investigated; and 2) consistency in the parameter as a function of measurements taken over time. The Nike specification is taken as the acceptable value. The percent standard deviation (%SD) is used as a measure of consistency.

The changes in tensile strength at different time points are displayed in Figure 1. It is evident that lower sulfur content yields higher tensile strength. The data is more easily discerned when the five "time points" are averaged and plotted as a single point with error bars (two standard deviations), as in Figure 2. Plotting in this manner focuses on the "consistency" mentioned previously. The sample displaying the highest average tensile strength and lowest %SD is 70% T90+1. The current manufacturing condition, 100% T90+1, had error bars that extended more than 10% below the minimum specification.

It is immediately apparent from the previous figures that the lower sulfur content (70% of standard) provides a high level of consistency and superior tensile strength when compared to the compounds with higher sulfur content. This was apparent at a cure of T90+1 as well as the under cured, T75, sample.

The percent elongation for each condition was similar to the tensile strength in that the lower sulfur content yielded the highest elongation. Again, 70% T90+1 exhibited the lowest %SD. Also, error bars for five of the eight conditions traversed the specification minimum. The preferred condition would be 70% T90+1.

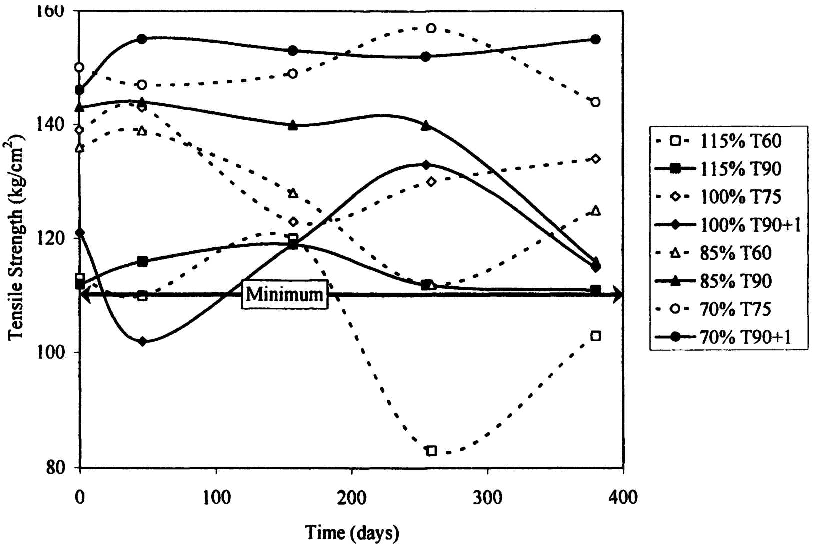

Figure 1. Changes in tensile strength as a function of time.

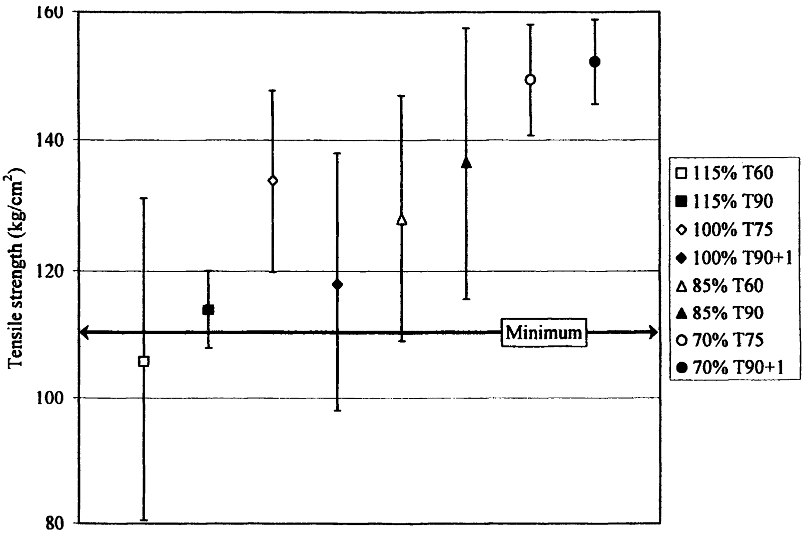

Figure 2. Mean and standard deviation of tensile strength over time (replotting of data from Figure 1).

The 300% modulus was one of the two properties where every condition was within specification and the error bars did not traverse the minimum. It can be seen from Figure 3 that the modulus has a generally downward trend as a sulfur content decreased, consistent with a lower crosslink density.

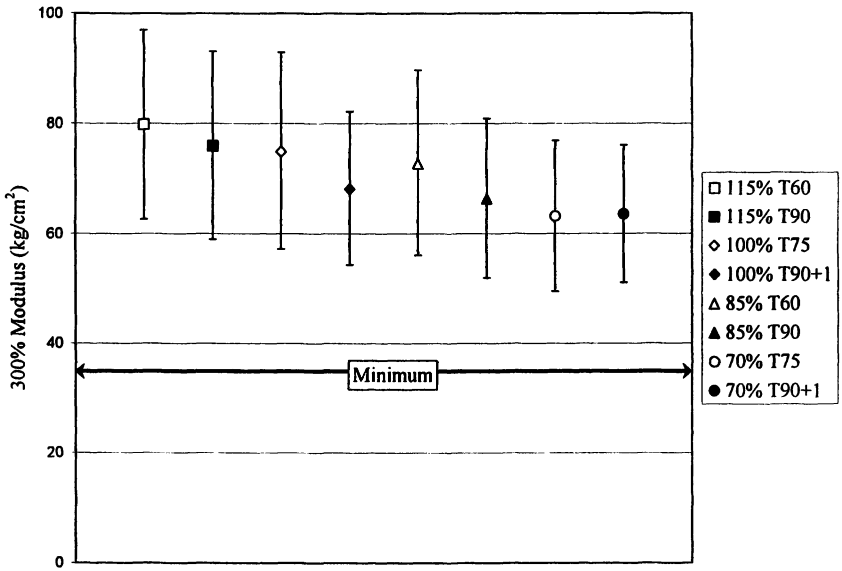

Figure 3. Mean and standard deviation of moduli over time.

The average abrasion ranged between 0.304 and 0.257 with the lower sulfur content providing the better performance. However, only in one case, 70% T75, did the error bars not traverse the maximum. Consistency over time varied with no defining trends.

Tear strength for all conditions was above the specification and the error bars did not traverse the minimum. There was no real trend with sulfur content or extent of cure.

Hardness tends to increase with age in rubber compounds due to further curing at residual carbon-carbon double bonds via rearrangement of poly-sulfidic crosslinks. At the start of the study, every condition was within the specification range. After one year, every condition was above the maximum specification of 68, with a range of 70.5 to 73.5. The lowest sulfur content reduced the average and final hardness by ~3 points when compared to the highest sulfur content, as shown in Figure 4. Since hardness is anecdotally perceived to be an inverse measure of traction by consumers, lower sulfur content could be a marketing advantage.

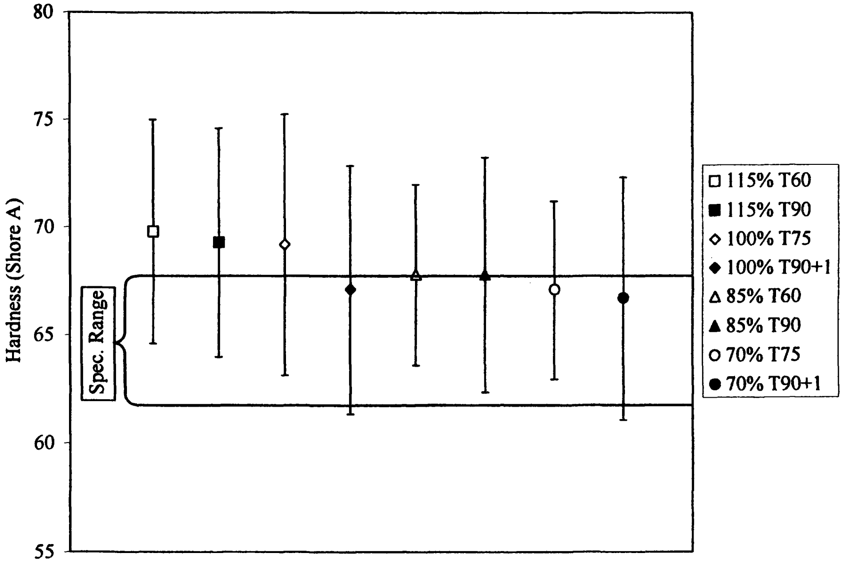

Figure 4. Mean and standard deviation of hardness over time

Sulfur Bonds

The sum of the changes in physical properties indicates that different sulfur contents produced different network morphologies. It is well known that sulfur cured rubber compounds contain mono-, di- and poly-sulfidic bonds. Mono-sulfidic bonds have the highest bond energy and are the least flexible. Poly-sulfidic bonds are the most flexible, but are subject to breakage and rearrangement. The rearrangement increases tensile strength and elongation, but adversely affects compression set. To quantify the changes, samples were submitted to a contract laboratory for sulfur bond analysis. As the sulfur content increased, the sulfur bond ratios, especially mono- and di- changed:

- 70% T90+1 mono/di/poly = 11/26/63
- 100% T90+1 mono/di/poly = 14/22/64
- 115% T90 mono/di/poly = 15/20/65.

As sulfur content increased, the change in sulfur bond ratios exhibit a transition from a "semi-efficient", or lower sulfur/accelerator ratio, to a "conventional",or higher sulfur/accelerator ratio, cure system (*4*). Overall, the

changes appear small, but when the total amount of sulfur is taken into account, the differences are substantial, as noted in Table III.

Table III. Molar Ratios of Sulfur Bonds

% sulfur	*cure*	*mono-*	*di-*	*Poly-*
70%	T90+1	1.0	2.2	5.5
100%	T90+1	1.7	2.8	8.1
115%	T90	2.2	2.9	9.4

The large difference in mono-sulfidic bonds is the main contributor to increased network stiffness with increased sulfur concentration. Mono-sulfidic bonds also have the highest bond energy of the three. The large difference in poly-sulfidic bonds is a probable contributor to poor network ageing at the higher sulfur concentration (*5*).

Summary

The final properties after one year of ageing in an "ideal" storage condition show how much a rubber compound changes. These changes indicate that rubber is a very dynamic system with many factors influencing its properties over time.

The results strongly indicate that at least a 30% reduction in sulfur would enhance stability (consistency over time) and improve certain properties, perhaps throughout the lifetime of the product.

Conclusions

Lowering the sulfur content by 30% showed a definite advantage with respect to performance and consistency. Under curing does not show a distinct, consistent advantage in making a more stable, acceptably performing product. This may be due to competing reactions with oxygen and other factors.

Acknowledgements

The support of the Feng Tay RDC Division #2 in supplying materials, compounding the rubber, and pressing samples; and the support of the Nike Taichung Laboratory for the physical testing are gratefully acknowledged.

References

1. Baldwin, J.M.; Bauer, D. R.; Hurley, P. D. *Rubber Chem. Technol.* **2005**, *78*, 754-766.
2. Baldwin, J.M.; Bauer, D. R.; Hurley, P. D. *Rubber Chem. Technol.* **2005**, *78*, 336-353.
3. *Annual Book of ASTM Standards;* Standard D3492-03; American Society for Testing and Materials; Philadelphia, PA, 2005; Vol. 09.02
4. Chung, B. et al. *Rubber World* **2002**, *227(2),* 36-42.
5. Hertz, D. L. *Elastomerics* **1984**, *116(11)*, 1721-1727.

Chapter 9

Characterization of Biodegradable Polymers: (I) Biodegradation of Poly(vinyl alcohol) under Aerobic and Aqueous Conditions

Jianzhong Lou, Keith Schimmel, Pfumai Kuzviwanza, Dana Warren, and Jizhong Yan

Department of Chemical and Mechanical Engineering, North Carolina Agricultural and Technical State University, 618 McNair, Greensboro, NC 27411

Biodegradation experiments were conducted according to ASTM D5271 to determine the rate of biodegradation of poly(vinyl alcohol), under aerobic and aqueous condition, in an activated sludge, using an oxygen respirometer. The percent of polymer biodegraded was estimated from the measured biochemical oxygen demand (BOD) divided by the theoretical oxygen demand (ThOD). The impact of temperature and polymer concentration on the total oxygen uptake, ultimate biochemical oxygen demand (UBOD), and percent degradation of polymer was evaluated. The experiments showed that the increase in the polymer concentration, not the temperature, caused the increase in the rate and percent of polymer biodegradation.

© 2008 American Chemical Society

Polymers (plastics, rubbers, fibers, coatings, adhesives, and composites, etc.) continue to play an important role in the nation's economy as one of the largest sectors of the chemical industry (*1*). Polymers have displaced metals, glasses, ceramics and wood in many products, especially in the area of packaging. Commodity plastics like polyethylene (PE), polypropylene (PP), polystyrene (PS) and polyvinyl chloride (PVC) in variety of forms such as films, flexible bags and rigid containers have revolutionized the packaging industry. However, once these materials are discarded, they persist in the environment without being degraded thus giving rise to many ecological and environmental problems. The 1996 U. S. EPA Report showed that over 19 million tons of plastics alone, not to include other types of polymers, which may remain in the environment for decades, were dumped annually as municipal solid waste(*2*). Of particular concern are polymers used in a single-use, disposable applications such as baby diapers and food packagings. The high molecular weight, covalently bonded polymer molecules are not readily broken down by the waste management infrastructures such as composting. This results in an irreversible buildup of "die-hard" trash that may cause scarring of landscapes, fouling of beaches, and a serious hazard to marine species. With increasing environmental awareness, the shortage of landfill space and emission concerns, the plastic industry is pushing to design and engineer products that are biodegradable. The plastics of today are manufactured with minimal consideration for their ultimate disposability or recycylability. Hence, authorities are pressuring the industry to review its product design and engineering due to mounting concerns over their environmental impact. No longer will it be sufficient to simply specify the required strength, dimensions, cost and preferred appearance of a plastic product or package. Today's engineer designing such a product must take into account where the package will end up after its useful existence (*3*). This requires that recyclability or biodegradability features be incorporated into the materials, while still retaining performance characteristics. In addition, after the material's intended use it must end up in appropriate infrastructures that use these recyclability or biodegradability attributes (*4*).

Biodegradable polymers offer one of the potential solutions to the environmental problem of polymers. They constitute a loosely defined family of polymers that are designed to degrade through action of living organisms and offer a possible alternative to traditional non-biodegradable polymers where recycling is unpractical or not economical. Interest in biodegradable plastics is being revived by new technologies developed by major companies, such as Bayer, DuPont, and Dow Cargill. Recently, Dow Chemical and Cargill (Dow Chemical is out now) created a joint venture in Blair, Nebraska to become the largest biodegradable polylactide (PLA) producer with annual capacity of 140,000 metric tons. Biodegradable polymers have a wide range of potential applications in markets currently dominated by traditional petroleum-derived plastics. These markets include the packaging industry, farming and also in

specialized bio-medical applications. However, the main constraint on the use of biodegradable polymers is the difference in the price of these polymers compared to bulk produced petroleum based plastics (despite the recent run-up in oil price, petroleum-derived polymers are still less costly than agriculturally-derived biodegradable polymers). The challenge lies in finding applications that would consume large quantities of these materials to lead to price reductions and allowing biodegradable polymers to compete economically in the market. In addition, engineers are faced with an enormous challenge to design materials that exhibit structural and functional stability during storage and use, yet are susceptible to microbial and environmental degradation upon disposal, without severe consequences to the environment.

Biodegradable polymers may be classified as natural and synthetic biodegradable polymers. Cellulose and starch are examples of natural polymers that are produced by all living organisms. They are readily biodegradable through hydrolysis followed by oxidation with the aid of enzymes. Among the synthetic polymers, aliphatic polyesters are generally known to be susceptible to biological attack. Important examples of synthetic biodegradable polymers of industrial scale include poly(vinyl alcohol) (PVOH) and poly(lactic acid) (PLA). The biodegradation of polymeric material follows four-stage kinetics of slow enzyme-catalytic oxidation of organic materials. The first stage of attack by the microorganisms is attachment to the polymer sample. Attachment creates a tiny ecosystem for the microbe to act on the material, usually through enzymes, to break the material down into nutritional requirements for the microbes. The second stage of the biodegradation process is fragmentation of the material. The third stage is disintegration. The material is reduced to powders. Finally, the polymer is reduced to carbon dioxide, water, and minerals. Knowledge of the biodegradability of a polymer is an important aspect of their environmental behavior because a biodegradable substance is expected to cause less ecological problems in the long term than a persistent one.

Our research program on biodegradable polymers consists of the respirometric characterization of biodegradation of polymers, as reported in this paper, and mechanical, thermal-analytical and chromatographic characterization which will be reported later.

For respirometric characterization, the first step is the determination of ready biodegradability. According OECD (Organisation for Economic Co-operation and Development: Paris, France) Test 301F guidelines (*5*), a substance is considered readily biodegradable if it reaches 60% ThOD in a 10-day window within the 28-day test period. The window begins when 10% of ThOD is obtained and must end before day 28 of the test. In this paper, we report the biodegradation of poly(vinyl alcohol) (PVOH) (*6*) in an aqueous environment and investigate the influence of temperature and polymer concentration on the total oxygen uptake, ultimate BOD and percent degradation of PVOH. A series of test were conducted using Test Method D5271 of the American Society of

Testing and Materials (*7*). This method indicates the extent and rate of biodegradation of plastic materials by aerobic microorganisms in an aqueous environment and is performed using a respirometer. The test method is used to determine the ultimate biodegradation which is the complete utilization of a test material by microorganisms resulting in the production of carbon dioxide, water, mineral salts and new microbial cellular constituents (biomass) in contrast to a primary biodegradation which is only the change of the identity of the test material (*8*). The percent of polymer that is biodegraded is calculated by comparing the biochemical oxygen demand (BOD) with the theoretical oxygen demand (ThOD).

Experimental

PVOH Sample. The PVOH utilized in the activated sludge tests was a research grade from Aldrich Chemical Company, Inc. of Milwaukee, Wisconsin (*6*). The PVOH has an average molecular weight of 9,000-10,000 and a degree of hydrolysis of 80%. The PVOH has a low viscosity of about 5.8 cps in a four percent aqueous solution at 20 °C as stated by the supplier. The test material was added to designated reactors at mass loadings of 100 mg and 200 mg PVOH on a dry weight basis.

Sludge. As a source of inoculum, activated sludge microorganisms were obtained from the North Buffalo Wastewater Treatment Facility. This wastewater treatment plant was fed with predominantly municipal sewage and industrial wastewater.

Sludge Preparation. The sludge was settled and the total suspsended solids were determined using the glass fiber filter method. The inoculum concentration was determined to be 2,532 mg/L of mixed liquid suspended solids (MLSS). However, due to the large biomass concentration and high oxygen uptake rate of the sample, the sludge was diluted to the inoculum concentrations given in the different OECD and ISO protocols (*5*). The sample was diluted in a two-liter conical flask using the prepared nutrient-mineral-buffer (NMB) solution to give a final test medium inoculum concentration of 500 mg/L of mixed liquid suspended solids (MLSS).

Nutrient-Mineral-Buffer (NMB) Solution. Table 1 lists the composition of the nutrient-mineral-buffer (NMB) stock solution used as recommend by ASTM 5271. A trace element solution was also added in order to support biological growth. These solutions were used for all biodegradation tests. Each compound in column one was dissolved in distilled water and diluted to 1L at the concentrations listed in column two. The test medium was formed by adding the volumes listed in column three to 1 L of high-quality reagent water and adjusting the pH to pH 7.0 ± 0.1 with HCl and NaOH. Approximately 400 mL of the test

medium/buffer stock solution was added to each reactor at the beginning of each test.

Table 1. Nutrient-Mineral-Buffer (NMB) Stock Solution

Compound(1)	*Concentration(2)*	*in 1L Test Medium(3)*
Ammonium Sulfate, $(NH_4)_2SO_4$	20.00 g/L	10 mL
Calcium Chloride, $CaCl_2$	27.50 g/L	1 mL
Ferric Chloride, $FeCl_3.6H_2O$	0.25 g/L	1 mL
Magnesium Sulfate, $MgSO_4.7H_2O$	22.50 g/L	1 mL
Allylthiourea, $CH_2CHCH_2NHCSNH_2$	2.00 g/L	20 mL
Phosphate Buffer:		20 mL
KH_2HPO_4	8.5 g/L	
K_2HPO_4	21.75 g/L	
$Na_2HPO_4.7H_2O$	33.4 g/L	
NH_4Cl	1.7 g/L	
Trace Element Solution:		2 mL
$FeSO_4.7H_2O$	200 mg/L	
$ZnSO_4.7H_2O$	10 mg/L	
H_3BO_3	10 mg/L	
$CoCl_2.6H_2O$	10 mg/L	
$MnSO_4.H_2O$	4 mg/L	
$Na_2MoO_4.2H_2O$	3 mg/L	
$NiCl_2.6H_2O$	2 mg/L	

Respirometric Setup. All tests were performed with two 8-cell Model AER-200 respirometer systems manufactured by Challenge Environmental Systems, Inc.(Fayettville, AR). The AER-200 respirometer uses the WINDOWS™ 2000 operating system and CHALLENGE™ data acquisition software.

Results and Discussion

The results of the respirometric tests are presented in Figures 1 and 2 for 35 °C and 25 °C experiment, respectively. Oxygen uptake data registered by the respirometer was used to monitor biological activity in the reactors. The control represents the oxygen consumption due to endogenous respiration of the microbial cells at the absence of the polymer substrate. The effects of the

polymer substrate concentration and temperature on the total oxygen uptake are readily seen. At 35°C, the cumulative oxygen uptake over the test period was 545mg O_2/L for the 0.4g PVOH sample and 381 mg O_2/L for the 0.2g PVOH sample. At 25°C, the associated total oxygen uptake ranged from 510mg O_2 /L to 790mg O_2/L for the 0.2g and 0.4g sample respectively. The result suggests that increasing the concentration of PVOH will provide more carbon for microbial growth consequently increasing the rate of reaction and biological activity of the microorganisms. Hence, the total oxygen uptake increases with increasing polymer substrate concentration. Respirometric curves for the samples examined at different temperatures have different shapes and differing intensity of biodegradation. At 35°C, the action of the microorganisms causing the PVOH degradation is initially faster for the first 10 days then biological activity slows down. The lower oxygen uptakes show that the microorganisms had not acclimated to PVOH biodegradation. At 25°C, the total oxygen uptake is greatest. This increase in biological activity is mainly attributed to the fact that the microorganisms were better acclimated to the degradation of PVOH at 25°C. This suggests that the biodegradation of PVOH is optimum at 25°C.

When interpreting the BOD curves (Figures 3 and 4), it is essential to know the respiration due to the biomass itself, called the endogenous respiration. In biodegradation tests, it is important to determine endogenous respiration because the measured respiration data from the test assays with the test substance have to be corrected by these blank values. The concept is then to subtract this

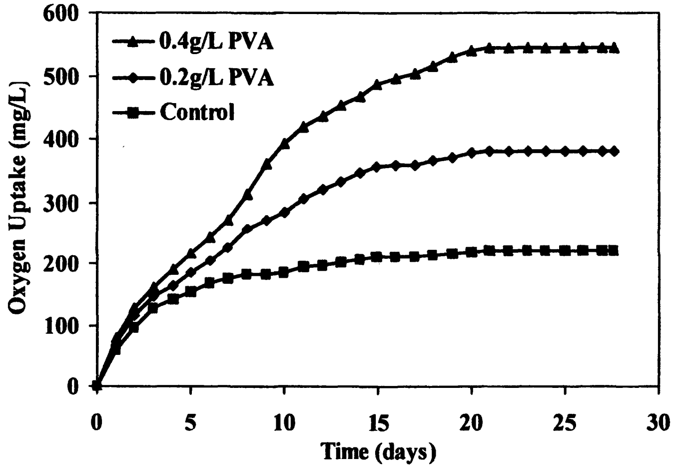

Figure 1. Cumulative Oxygen Uptake for 0.4g PVOH, 0.2g PVOH and Control Sample at 35 °C

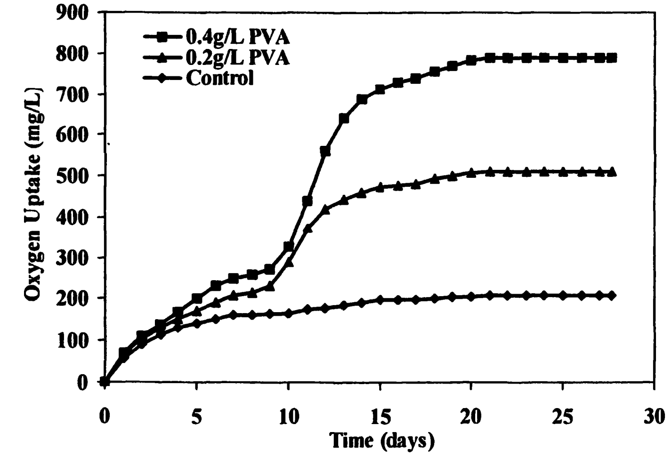

Figure 2. Cumulative Oxygen Uptake for 0.4g PVOH, 0.2g PVOH and Control Sample at 25 °C

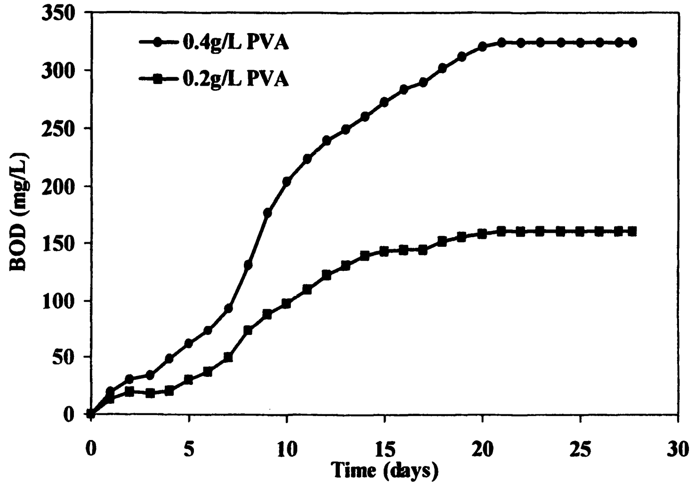

Figure 3. BOD Curves at 35 °C

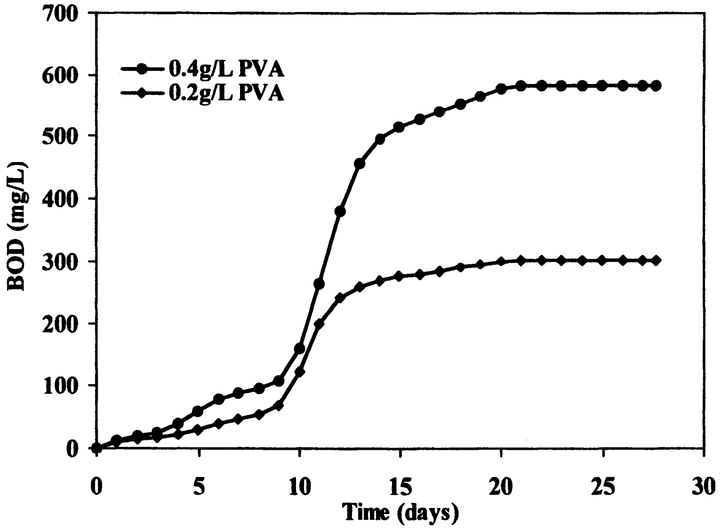

Figure 4. BOD Curves at 25 °C

respiration from the measured respiration in order to determine the true substrate respiration.

Respirometric results to show the effects of temperature and substrate concentration on the ultimate BOD and percent degradation of PVOH are summarized in Table 2.

Table 2. Summary of Respirometric Results

Temp. (oC)	*Test Duration (days)*	*Amount (g)*	*UBOD (mg/L)*	*Percent Degraded*
25	28	0.2	301.62	83.1
25	28	0.4	581.11	79.9
35	28	0.2	160.54	44.2
35	28	0.4	323.86	44.6

As seen from Table 2 and Figures 3 and 4, the ultimate BOD increases with increasing polymer concentration at 35°C and 25°C. The tests confirm that the greater the amount of carbon available for the microorganisms, the greater the biological activity in the reactors, consequently, the higher the ultimate BOD.

The low ultimate BOD values of 160.54 mg/L and 323.86 mg/L at 35°C were probably attributed to the microorganisms not being acclimated to the aqueous environment. As a consequence, the conditions present in the reactors are not good for optimal microbial activity. In addition, the presence of volatile organics in the activated sludge may affect the oxygen uptake rates at higher temperatures. The degrees of biodegradation of PVOH were 44.2-44.6% based on ThOD at 35°C (Table 2, Figure 5). The course of the degradation of the curves at different concentrations is comparable. The curves indicate a lag phase (day 0 to 6), where the adaptation of the microorganisms to PVOH occurs, a degradation phase (day 6 to 19), in which the microorganisms use the PVOH as food and grow, and a plateau phase (day 19 to the end of the test at day 28), in which degradation has ended. However, the degrees of degradation at the end of the test do not exceed the limit value of 60% that is required by the standard to prove the validity of the test. The reason for the low degradation was probably that the microorganisms and enzymes responsible for the degradation of PVOH are ineffective at 35°C. On the other hand, the degrees of biodegradation of PVOH were 79.9-83.1% based on ThOD at 25°C (Figure 6). The curves indicate a lag phase (day 0 to 6), a degradation phase (day 6 to 15) and a plateau phase (day 15 to 28). The test exceeds the limit value of 60% thus proving the ready biodegradability of PVOH in an aqueous environment at an optimum temperature of 25°C.

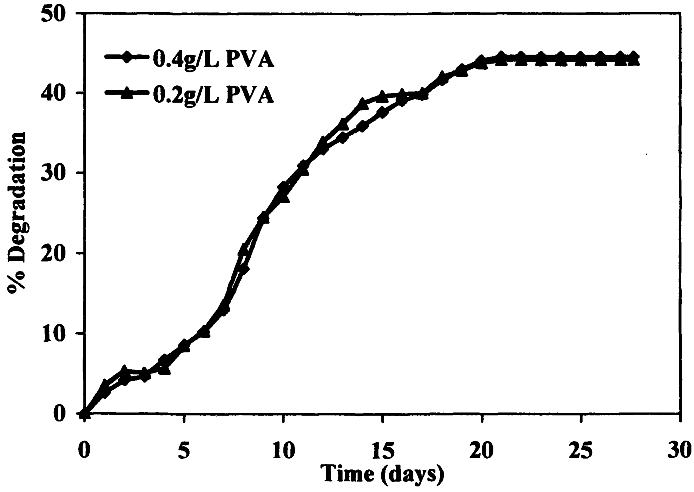

Figure 5. Extent of biodegradation at 35 °C

In Polymer Durability and Radiation Effects; Celina, M., et al.;
ACS Symposium Series; American Chemical Society: Washington, DC, 2007.

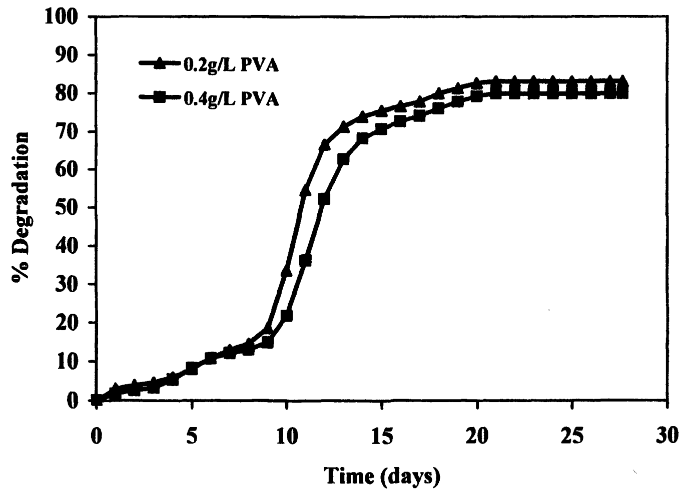

Figure 6. Extent of biodegradation at 25 °C

Conclusion

This paper presents evidence that PVOH can be degraded by cultures derived from activated sludge. The biodegradation testing simulates environmentally realistic conditions and thus we can extrapolate results to natural environments. Results indicate that increasing the concentration of PVOH will increase its bioconversion thus increasing the total oxygen uptake, UBOD, and percent degradation. This may also indicate that PVOH is nontoxic and noninhibitory to activated sludge microorganisms. However no marked improvement in the percent degradation was observed when temperature was increased. This clearly indicates the influence of temperature on biological reactions. Hence, it shows that it is important to adjust the inoculum to the test temperature carefully by an adaptation period.

References

1. *SPI Report: Overview of Plastics Indusrty;* Society of the Plastics Industry, Inc.: Washington, DC, 2001.
2. Franklin Associates, Ltd. *Characterization of municipal solid waste in United States,* U.S. Environmental Protection Agency Municipal and

Industrial Solid Waste Division Office of Solid Waste: Washington, DC, 1996, Report No. EPA530-R-97-015, p. 8.

3. Mohanty, A. K.; Misra, M.; Hinrichsen, G. *Macromol. Mater. Eng.* **2000**, 276/277, 1-24.
4. Narayan, R.; Barenberg, S. A.; Barash, J. L.; Redpath, A. E. *Degradable Materials: Perspectives, Issues, and Opportunities,* CRC Press, New York, New York, 1990.
5. *OECD Guidelines for testing of chemicals: Paris 301 F Manometric respirometry test.* Organisation for Economic Co-operation and Development: Paris, France, 1993.
6. *Aldrich Catalog: Polyvinyl alcohol, 80% hydrolyzed.* Aldrich Chemical Company, Inc.: Milwaukee, Wisconsin, 2005.
7. *Annual Book of ASTM Standards;* Standard D5271-02; American Society for Testing and Materials. Villanova, PA, 1993; Vol. 08.03.
8. Pagga, U.; Reuschenbach P.; Strotman, U. *Water Research* **2003**, 37, pp 1571-1582.

Chapter 10

Degradation of Nylon 6,6 and Glass Fiber Reinforced Nylon 6,6 by Aqueous Solutions of Ethylene Glycol and Calcium Chloride

John Hee Hong[1], D. Manjula Dhevi[2], Jong Soon Lee[2,3], and Kap Jin Kim[2,3,*]

[1]Advanced Technology Center, Corporate Research and Development Division, Hyundai-Kia Motors, Yongin-si, Gyeonggi-do 449–912, South Korea
[2]Department of Advanced Polymer and Fiber Materials, College of Environment and Applied Chemistry, Kyung Hee University, Yongin-si, Gyeonggi-do 446–701, South Korea
[3]Intelligent Textile System Research Center, Seoul National University, Seoul 151–744, South Korea
[*]Corresponding author: email: kjkim@khu.ac.kr, telephone: +82–31–201–2518, fax: +82–31-202–9484

Glass fiber reinforced nylon 6,6 (GFNY66) composites widely used for automotive applications are highly deteriorated when contacted repeatedly with aqueous solutions of ethylene glycol (EG) and calcium chloride resulting in reduced molecular weight, disruption of intra- and intermolecular hydrogen bonding and interfacial failure between glass fiber and nylon 6,6 (NY66) matrix. Hence, it is important to understand clearly the degradation and hydrogen bond breaking mechanism of NY66 and interfacial failure mechanism in GFNY66 in order to improve the mechanical properties of recycled NY66. From ATR-IR spectrum of aq. EG and aq. calcium chloride ($CaCl_2$) treated NY66 specimens, the breakage of intra- and intermolecular hydrogen bonding has been noticed from the shifting of carbonyl stretching band towards lower frequency. The mechanical properties of aq. $CaCl_2$ treated NY66 has been found to be better than that of aq. EG treated NY66 due to

© 2008 American Chemical Society

lesser reduction in molecular weight for aq. $CaCl_2$ treated NY66 specimens. Among all the specimens, aq. EG treated GFNY66 exhibited pronounced deterioration in mechanical properties, which is associated with more contribution of interfacial failure between glass fiber and NY66.

Introduction

Nylons are semicrystalline thermoplastic polymers with good mechanical, thermal and chemical properties. As an important engineering thermoplastic material, almost 35% of total nylons produced are used in automobile industry. Among the several types of commercial nylons used in this industry, nylon 6,6 is widely used in tire cords and various types of automobile parts such as radiator end tank, intake manifold, engine cover, and timing belt cover (*1,2*). Unreinforced nylon 6,6 (NY66) is typically used in hose and wire restrainers, dipstick caps and liners for sheathed cables. Glass fiber reinforced NY66 (GFNY66) is commonly used in brake fluid reservoirs and fuel tubing. NY66 is also commonly reinforced or blended with other materials in order to produce exterior body components for automobiles (*3*). During winter driving in Northern and Southern part of Earth, NY66 containing automotive parts undergoes deterioration in mechanical properties not only under prolonged exposure with cooling liquid (mixture of ethylene glycol (EG) and water) used for radiator end tank in automobiles but also when exposed to salt splash conditions.

Degradation of polymers directly deteriorates their mechanical properties. In particular, the chemical and physical mechanisms of nylon degradation have been studied extensively for decades (*4-9*) and a few studies were also focused on nylon 6 degradation by EG (*10, 11*). Huczkowski et al. studied the glycolysis of nylon 6 in boiling EG with/without catalyst leading to the formation of oligoamides with amino- and hydroxyl endgroups (*10*). Hommez and Goethals studied the degradation of nylon 6 by EG in the presence of phosphoric acid at 250°C leading to a mixture of low molecular weight compounds with free carboxylic acid endgroups and carboxylic acids esterified with EG (*11*). More and Donald studied the effect of metal halides on the deformation mechanism of thin films of nylon by soaking of nylon 6 and NY66 films in saline solutions (*12, 13*). In their study, salt treatment modifies intermolecular bonding, strengthening it in the process and stiffens the polymer chains.

However, from the results of nylon 6 degradation by EG, it is not easy to predict the degradation mechanism of NY66, since, the major products of glycolyzed nylon 6 are EG derivatives of ε-caprolactam and linear oligomers whose chemical structures are basically different from those of NY66 oligomers. In our previous paper, in order to elucidate the degradation mechanism of NY66

by EG clearly, we first studied the degradation of its model compound, N,N-hexamethylenebis(hexamide) by EG and the results were correlated with the degradation mechanism of NY66 by EG (*14*). Our previous results indicate that the amide group of NY66 can be degraded by EG resulting in the presence of degradation products having β-hydroxyethylester group, bis(β-hydroxyethyl)adipate, and δ-valerolactone as proved by FT-IR and GC-MS. From GPC data, as the glycolysis time of NY66 increased, both the number average and weight average molecular weights decreased indicating that the main chain of NY66 was broken into low molecular weight compounds during glycolysis (*14*).

In this paper, our aim is to study the degradation mechanism of NY66 and GFNY66 by aq. solutions of EG and calcium chloride ($CaCl_2$) using ATR-IR, GPC and mechanical studies.

Experimental

Materials

Specimens of nylon 6,6 (NY66) and glass fiber(30 wt%) reinforced nylon 6,6 (GFNY66) for tensile strength and notched impact strength as per ASTM standards were received from DESCO, Korea. Dry methylene chloride (CH_2Cl_2) and dry triflouroaceticanhydride (TFAA) from Mallinckrodt-AR and Acros Organics respectively, Ethylene glycol (EG) and anhydrous calcium chloride ($CaCl_2$) from Samchun Chemicals were used as received.

Immersion of Specimens in aq. EG/aq. $CaCl_2$ Solution

NY66 and GFNY66 specimens of both test types were immersed in aq. EG solution (50/50 v/v ratio) heated at 108°C as well as in 15 wt% aq. $CaCl_2$ solution at room temperature (20°C) and at 70°C for a period of 312 h, 600 h and 1000 h. The treated specimens were characterized by ATR-IR, GPC, tensile and impact tests.

Pretreatment for GPC Measurement

NY66 specimens immersed in different solutions were used for GPC analysis. Before pretreatment for GPC measurement, EG present in the immersed sample must be removed, because it will react with TFAA to give substituted trifluoro ester of ethylene glycol (trifluoro-3-ol-propinoate). Hence, the immersed samples were first treated with distilled water by Sohxlet

extraction for at least 20 cycles to remove EG. The samples were air-dried overnight and then in a vacuum oven for overnight at 90°C to remove moisture.

Since, NY66 and its glycolyzed products and also aq. $CaCl_2$ treated samples cannot be dissolved in the common solvent, terahydrofuran (THF) which is usually used for GPC measurement, NY66 and its immersed samples were modified via triflouroacetylation (*15*) as shown in Figure 1.

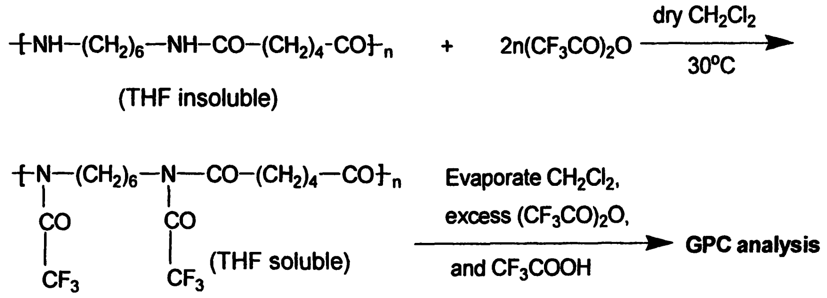

Figure 1. Modification of NY66 via triflouroacetylation to render it soluble in THF for GPC analysis.

56.5 mg of the sample was added to a narrow cylindrical flask and purged with N_2 continuously through an inlet. 1.6 ml of dry CH_2Cl_2 was added to the flask followed by the addition of a three-fold molar excess of TFAA and stirred using magnetic stirrer at 30°C. The reaction was allowed to run until the sample dissolved completely. The trifluoroacetylated sample was then isolated by evaporating CH_2Cl_2, excess TFAA, and trifluoroacetic acid (TFA) under vaccum. 1 ml of dry CH_2Cl_2 was again added to the acetylated sample in order to dissolve it in dry THF to prepare GPC samples. Samples for GPC had to be run within a few hours after sample preparation, otherwise, the dissolved polymer may be precipitated out from the GPC solution through hydrolysis by accidentally absorbed moisture after more than 24 hours.

Characterization

Perkin Elmer Spectra 2000 spectrometer equipped with Durascope ATR (Sens IR Co.) at a resolution 2 cm^{-1} with 12 scans was used for measuring the ATR-IR spectra.

Mechanical tests were carried out in a laboratory where the temperature was maintained at 25°C using a Universal Testing Machine, LR-50 K (LLOYD Instrument, England) at a crosshead speed of 50 mm/min and 98 mm as gauge length. Stress at break, strain at break, work of rupture, and initial modulus were determined as per ASTM standards. Izod notched impact test specimens were

used for the impact test using Impact Tester (Testing Machine Inc. USA, TMI 43-02). At least three tests were carried out for all the specimens and the results were arithmetically averaged. Thickness and width of each specimen were noted and also used for the measurements.

M616LC System (Waters, U.S.A) instrument was used for GPC analysis and three types of the column (Waters HR 0.5, 3, and 4) were used in series. Five standard mono-disperse polystyrene samples having different molecular weights of 511, 6890, 7200, 420000, and 178000 were used for calibration. The solvent used for GPC was THF.

Results and Discussion

ATR-IR Studies

ATR-IR spectra for NY66 specimens treated in aq. EG solution at 108°C as a function of treating times exhibited an increase in i.r. absorption at 3305 cm^{-1} due to the intake of EG as shown in Figure 2a. Absorbed EG is expected to form complexation with the amide portion of NY66 matrix. The $\nu_{as}CH_2$ band at 2929 cm^{-1} is shifted towards higher frequency and a new peak at 2874 cm^{-1} is observed due to the absorption of EG as shown in Figure 2b. However, the presence of ester band at around 1740 cm^{-1} cannot be detected because of its low concentration. The shift of amide-I band at 1640 cm^{-1} to lower frequency may be attributed to the distruption of intra- and intermolecular H-bonding between amides followed by the formation of new H-bonding between amide and hydroxyl group of absorbed EG. The band at 1273 cm^{-1} was shifted towards higher frequency due to absorption of EG and a new shoulder at 1263 cm^{-1} and a new band at 1224 cm^{-1} appeared due to C-O band of absorbed EG (Figures are not shown here).

From ATR-IR spectral data (Figure 2c) of NY66 specimens treated with 15 wt% aq. $CaCl_2$ solution at 70°C, the shift in i.r. amide-I band at around 1640cm^{-1} to lower frequency for immersed samples indicate the disruption of intra- and intermolecular hydrogen bonding of NY66 followed by the formation of carbonyl oxygen-Ca^{+2} dative bond in NY66 matrix as shown in Figure 3. Complexation of hydrogen of NH with Cl^- as shown in Figure 3 decreases the peak intensity of amide-II band associated with decrease in concentration of amide-II bond.

GPC Studies

Figure 4a shows the changes in average molecular weights as a function of treating time when NY66 is treated with aq. EG solution (50/50 v/v) at 108°C.

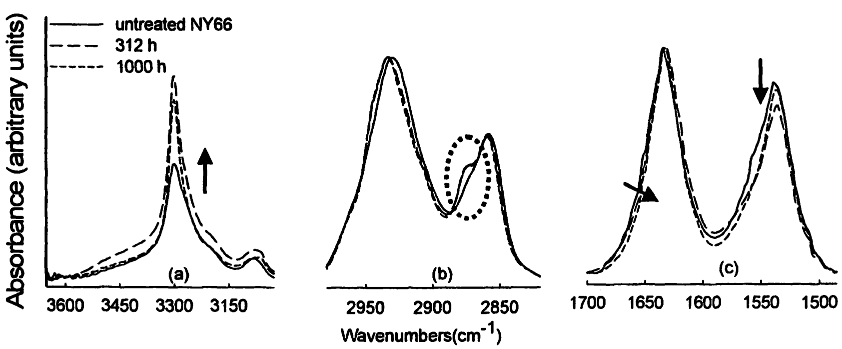

Figure 2. ATR-IR absorption spectra of NY66 treated at different periods of immersion in (a) & (b) aq. EG at 108°C, and (c) aq. $CaCl_2$ at 70°C.

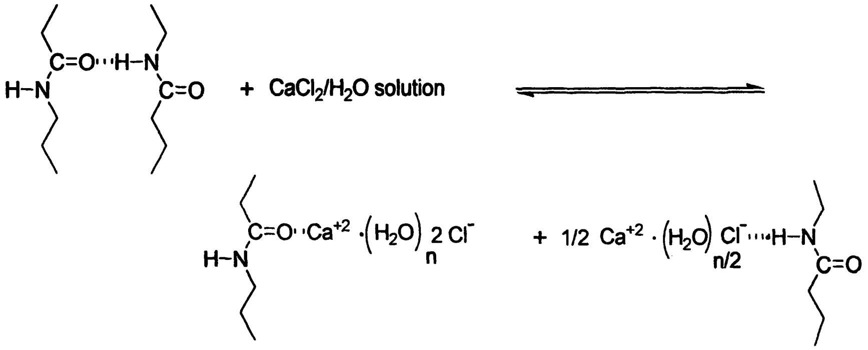

Figure 3. Complexation of amide portion of NY66 with aq. $CaCl_2$ solution.

As the treating time increases, the number average molecular weight (M_n) as well as and weight average molecular weight (M_w) decrease. Up to 312 h, the percentage of reduction in M_n and M_w is considerably more than that for 600 h and 1000 h treated specimens. The M_n of 1000 h treated specimen declined to 5000 compared to M_n=15000 for untreated specimen. The M_w of 1000 h treated specimen declined to 14000 compared to M_w=32000 for untreated specimen. From this data, the number average reduction is found to be 1/3 while the weight average reduction is 1/2 after treatment with aq. EG at 108°C for 1000 h, which indicates that chain scission of NY66 has taken place through hydrolysis and glycolysis.

From GPC data as shown in Figure 4b, the decrease in molecular weight for NY66 specimens treated with aq. $CaCl_2$ solution at 70°C is much less in comparision to that of NY66 treated with aq. EG at 108°C. M_n and M_w for untreated NY66 are 14831 and 31674, respectively, while for aq. $CaCl_2$ treated NY66 sample (70°C, 1000 h), they are 13715 and 29740, respectively. This less reduction in M_n and M_w for aq. $CaCl_2$ solution treated specimens suggests that there is no significant chemical degradation, but only the breakage of intra- and intermolecular H-bonding in nylon matrix as already proved from ATR-IR shifting in amide-I band to lower frequency.

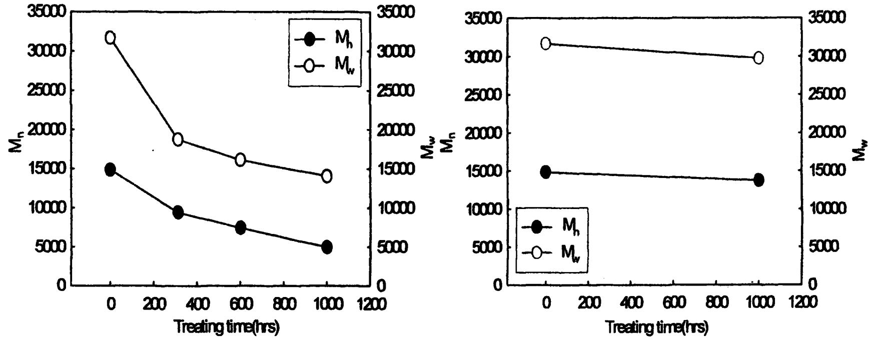

Figure 4. Changes in average molecular weight as a function of treating time for NY66 treated with (a) aq. EG at 108°C and (b) aq. $CaCl_2$ (15 wt%) at 70°C.

Mechanical Studies

With aq. EG solution at 108°C

From mechanical measurements of NY66 and GFNY66 treated with aq. EG solution at 108°C, the relative reduction ratio in stress at break for treated GFNY66 is more than that of treated NY66 due to more contribution of interfacial failure between glasss fiber and NY66 than that of breakage of intra-

and intermolecular H-bonding followed by newly formed H-bonding between the absorbed EG and amide portion of NY66 matrix. The decrease in stress at break for treated GFNY66 specimen for 312, 600 and 1000 h almost remains the same as shown in Figure 5a. Longer duration of immersion in aq. EG solution is not necessary for the experiment to be conducted because the interface between NY66 matrix and glass fiber can be destroyed even within a short duration of time. Decrease in stress at break for treated NY66 is also due to decrease in molecular weight indicating that the degradation has occurred as a result of absorption of EG into NY66 matrix as proven by GPC.

Strain at break for untreated NY66 is 19.27 % while for untreated GFNY66, it is decreased to 6.6 % with the addition of 30 wt% glass fiber. In NY66, the chains are almost extended during stretching whereas, for GFNY66, the chain orientation is more or less restricted due to interfacial force between glass fiber and NY66 matrix and exhibit less elongation than NY66 specimens. After treatment with aq. EG solution, the strain at break is rather increased for treated NY66 even after high reduction in molecular weight due to breakage of intra- and intermolecular hydrogen bonding in NY66 by absorbed EG, whereas for treated GFNY66, it is nearly unchanged (Figures are not shown here). Work of rupture is increased for treated NY66 due to larger contribution of much increased strain at break than that of decreased stress at break, whereas, for treated GFNY66, it is decreased due to larger contribution of decreasing stress at break than nearly unchanged strain at break (Figures are not shown here).

Izod impact strength as shown in Figure 5b is increased for both treated NY66 and GFNY66 due to newly formed hydrogen bonding of hydroxyl group of EG with the amide portion, but for treated GFNY66, it is less than treated NY66 due to only 70 wt % of NY66 matrix in it. Hence more energy is required to break the notched treated specimens when compared to that of untreated one.

Initial modulus has declined for both treated NY66 and treated GFNY66 because the absorbed EG disrupts the intra- and inter molecular hydrogen bonding existed within NY66 matrix followed by the formation of hydrogen bonding of hydroxyl group of absorbed EG with the amide portion of NY66 matrix (Figures are not shown here).

Thickness and width of the treated tensile specimens were increased when compared to that of untreated specimen for both NY66 and GFNY66 due to the complex formation of EG with NY66 matrix but the increase is less for treated GFNY66 specimens in comparison to that of treated NY66 specimens because of the presence of only 70 wt % of NY66 in GFNY66.

With aq. $CaCl_2$ at 20°C/70°C

Mechanical data of NY66 and GFNY66 samples treated with aq. $CaCl_2$ (20°C/70°C) for different time intervals are shown in Figure 6a. The decline in

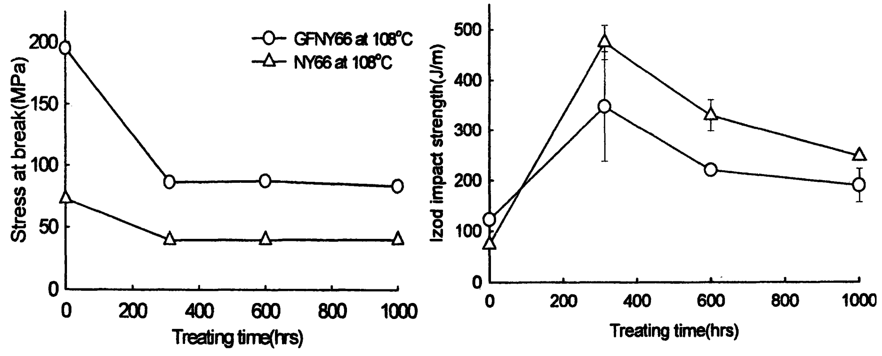

Figure 5. (a) Stress at break and (b) Izod impact strength as a function of treating time when NY66 and GFNY66 are treated with aq. EG at 108 °C.

stress at break for 312 hours treated GFNY66 is more than that of treated NY66. The deterioration in mechanical properties is more pronounced in the heating case (70°C) than that of at room temperature (20°C). Since molecular weight reduction is negligibly small after aq. $CaCl_2$ treatment as shown in Figure 4b, the highly reduced stress at break for treated GFNY66 is associated mainly with interfacial failure between glass and nylon matrix caused by the absorbed $CaCl_2$. The absorbed calcium ions which have two vacant orbital, would also form a coordinate bond with one lone pair of oxygen of the amide in nylon matrix and the chloride ions will form a H-bond with the hydrogen of the amide portion in the nylon matrix as shown in Figure 3. This results in increased strain at break (Figure is not shown here). Strain at break for treated NY66 is found to be more when compared to that of treated GFNY66. This is more pronounced in the heating case than that at room temperature.

Work of rupture for treated NY66 is increased due to highly increased strain at break, whereas it is decreased for treated GFNY66 due to decreased stress at break resulting from interfacial failure caused by the absorbed $CaCl_2$. The thickness and width of treated tensile specimens are increased for both NY66 and GFNY66 due to the penetration of salt solution into NY66 matrix leading to the formation of complexation with the amide portion of NY66 and the increase in thickness is well pronounced for samples treated at 70°C. Izod impact strength is increased for both treated NY66 and GFNY66 as shown in Figure 6b.

Initial modulus is declined for both treated NY66 and GFNY66 but less pronounced in the case of GFNY66 due to its reinforcement with 30% glass fiber. The decrease in initial modulus for both types is due to the disruption of H-bonding between the amide portions of NY66 matrix by the absorbed calcium ions thereby forming a complexation as shown in Figure 3.

Thickness and width of the treated impact strength specimens were increased when compared to that of untreated specimen for both NY66 and

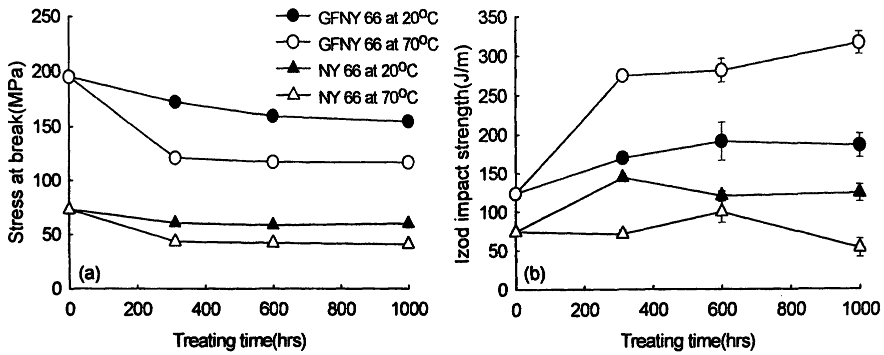

Figure 6. (a) Stress at break and (b) Izod impact strength as a function of treating time when NY66 and GFNY66 specimens are treated with aq. $CaCl_2$ ($20^oC/70^oC$) solution.

GFNY66 due to the penetration of salt solution into NY66 matrix. The increase in thickness and width of specimens is more in the case of NY66 treated specimens than that of GFNY66 treated specimens due to similar reason as mentioned for aq. EG treated samples.

Conclusions

In this paper, we have studied the degradation and hydrogen bond breaking mechanism in NY66 and interfacial failure mechanism in GFNY66 specimens by immersing them in aq. EG (108°C) as well as in aq. $CaCl_2$ (20 °C/70°C) for different time intervals and characterized them using ATR-IR, GPC, and mechanical measurements. ATR-IR spectral data of treated NY66 and GFNY66 samples showed the shifting of C=O band at 1640 cm^{-1} to lower frequency due to the distruption of intra- and intermolecular hydrogen bonding between amides resulting in reduced molecular weight from GPC studies. However, the lesser reduction in molecular weight for aq. $CaCl_2$ treated NY66 samples compared to aq. EG treated NY66 samples resulted in their better mechanical peoperties. Among all the specimens, aq. EG treated GFNY66 exhibited pronounced deterioration in mechanical properties, which is associated with more contribution of molecular weight reduction. Interfacial failure between glass fiber and NY66 and the distruption of intra- and intermolecular H-bonding between amide portions of NY66 matrix also contribute to the deterioration in mechanical properties.

Acknowledgement

This study was supported by Next Generation Vehicle Technology Co., Korea.

References

1. Kohan, M. I. In *Nylon Plastics Handbook*; Kohan, M. I., Ed.; Hanser Gardner: New York, 1995; pp 6-8.
2. Lann, P.L.; Derevjanik, T.S.; Snyder, J.W.; Ward Jr, W.C. *Thermochim. Acta* **2000**, *357*, 225-230.
3. Barineau, J. M. In *Nylon Plastics Handbook;* Kohan, M. I., Ed.; Hanser Gardner: New York, 1995; pp 515-516.
4. Dunn, P.; Sansom, G. F. *J. Appl. Polym. Sci.* **1969**, *13*, 1641-1655.
5. Dunn, P.; Sansom, G. F. *J. Appl. Polym. Sci.* **1969**, *13*, 1657-1672.
6. Mitomo, H.; Kuriyama, I. *Polymer* **1982**, *23*, 1377-1380.
7. Igarashi, M.; DeVries, K. L. *Polymer*, **1983**, *24*, 769-782.
8. Rigal, A. T.; Patterson, G. H.; Pistillo, W. R.; Scharf, C. R.; Ward, W. C. *Thermochim. Acta* **1993**, *226*, 363-368.
9. Bernstein, R.; K.; Gillen, K. T. *Polym. Degrad. Stab.* **2005**, *88*, 480-488.
10. Huczkowski, P.; Kapko, J.; Olesiak, R. *Polymer* **1978**, *19*, 77-80.
11. Hommez, B.; Goethals, E.J. *J. Macromol. Sci. Pure Appl. Chem.* **1998**, *A35*, 1489-505.
12. More, A. P.; Donald, A. M. *Polymer* **1992**, *33*, 4081-4086.
13. More, A. P.; Donald, A. M. *Polymer* **1993**, *34*, 5093-5098.
14. Kim, K. J.; Dhevi, D. M.; Lee, J. S.; Cho, Y. D.; Choe, E. K. *Polym. Degrad. Stab.* **2006**, *91*, 1545-1555.
15. Jacobi, E.; Schuttenberg, H.; Schulz, R.C. *Makromol. Chem. Rapid Commun.* **1980**, *1*, 397-402.

Chapter 11

Aspects of the Radiation Chemistry of Some Transparent Polyimides

David J. T. Hill

Department of Chemistry, The University of Queensland, Brisbane 4072, Australia

The sensitivities of a series of transparent polyimides to simulated space conditions for GEO and LEO have been assessed. The effects of UV, VUV, atomic and molecular oxygen, gamma and electron beam radiation on the polymers have been reviewed. The changes in the visible spectra, the radicals formed, the changes in the surfaces of polyimide films under vacuum and in the presence of oxygen and, in the case of high-energy irradiation, the structural changes in the polyimide have been considered.

Aromatic polyimides are well recognized to have excellent chemical stability, so they have found applications in extremely harsh and corrosive environments. For example, they are used as insulators in nuclear facilities and as thermal blankets on spacecraft where the materials may be exposed to high-energy radiation in the presence of oxygen. The best known of the commercial polyimides is Kapton, which is marketed by Du Pont. The chemical structure of Kapton is shown in Figure 1, along with that of Ultem, another commercial polyimide marketed by General Electric.

In Kapton and Ultem the carbonyl groups of the imides are directly attached to phenyl rings and they are strongly electron withdrawing, so the adjacent aromatic groups tend become positively charged. On the other hand, the nitrogen atoms in the imides are electron donating, so the aromatic groups attached to these atoms tend to become negatively charged. Where the two imide rings in the polyimide repeat units are attached to the same aromatic ring,

 © 2008 American Chemical Society

as in Kapton, the charge separation along the polymer chain can be significant. Then strong donor-acceptor complexes may be formed between adjacent polymer chains (*1*). These donor-acceptor complexes in the case of Kapton absorb visible radiation, as shown in Figure 2, and are responsible for its intense brown colour.

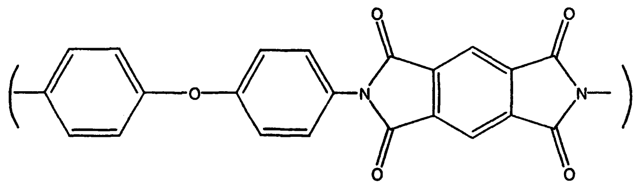

Kapton

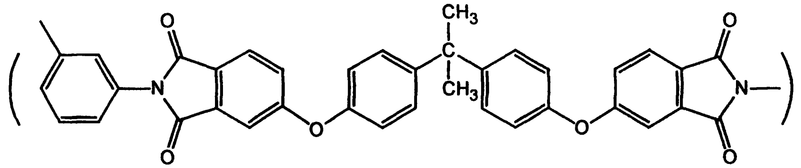

Ultem

Figure 1. Chemical structures for Kapton and Ultem.

Ultem on the other hand has the imide groups attached to different phenyl rings in the repeat unit, so the charge separation in Ultem is lower than in Kapton. In addition, because of the kinked nature of the repeat units in Ultem, adjacent chains are unable to approach one another as closely as they can in Kapton. So in Ultem donor-acceptor complex formation is not as efficient as in Kapton, and Ultem absorbs less strongly in the visible region, as can be seen in Figure 2.

In space the solar energy maximum emission from the sun occurs at approximately 550 nm (*2*). Thus for some space applications, polymers are required that have a high transmittance at 550 nm, so there is a need for polyimides more transparent than Kapton throughout the visible region.

Several polyimides with low absorption at 550 nm have been prepared by St Clair (*1,3*) by utilizing dianhydride monomers with the anhydride units on different phenyl rings and with bulky electron withdrawing groups on the phenyl rings in the diamine units so as to reduce charge separation. They have also incorporated meta linkages between phenyl rings to generate chain kinks to

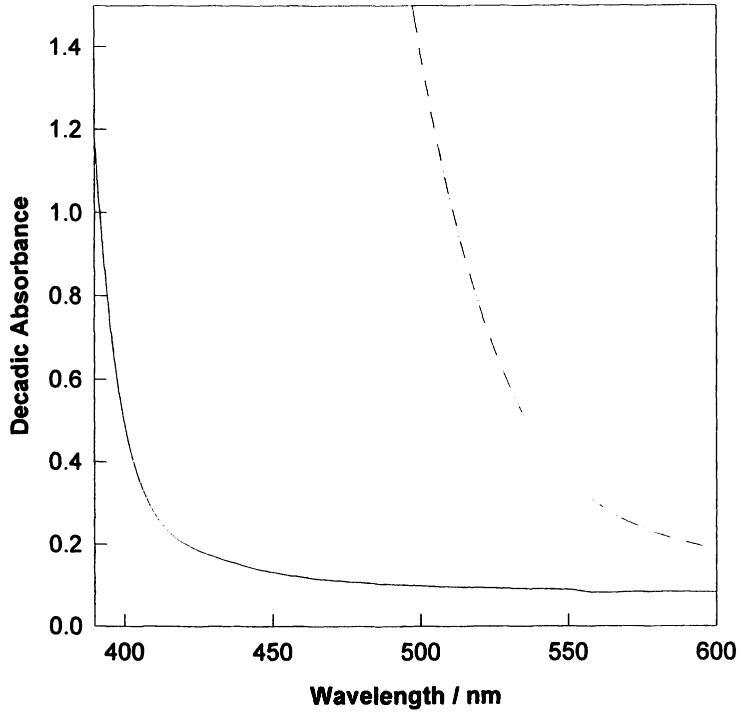

Figure 2. The visible spectrum of Kapton –·· – and Ultem ——.

minimize chain alignment and hence disrupt donor-acceptor complex formation. Some examples of the use of these principles are demonstrated in the polyimides shown in Figure 3 that have excellent transparency, particularly at 550 nm.

In geosynchronous earth orbits (GEO) a space vehicle is exposed to intense UV and VUV radiation from the sun, as well as high-energy cosmic radiation and the electron fields which surround the earth. Depending on the location of a space vehicle, the dose rates of the high-energy radiation can range from approximately 0.5 to 2 MGy per year (*4*). In low earth orbits (LEO) the dose rates for high-energy radiation are lower, being of the order of approximately 0.5 kGy per year, but there is a high atomic oxygen flux (*5*), as well as the cosmic and UV and VUV radiation in the range 100 – 400 nm. The atomic oxygen flux impacting the surface of a spacecraft depends on its altitude and orientation. For example, the leading surface of a spacecraft experiences a higher oxygen atom flux than does the trailing surface. The velocity of the spacecraft as well as the angle of incidence determines the impact energies of the oxygen atoms.

ODPA/ODA

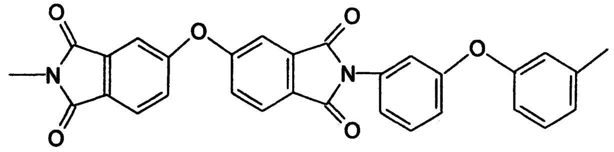

ODPA/DAB

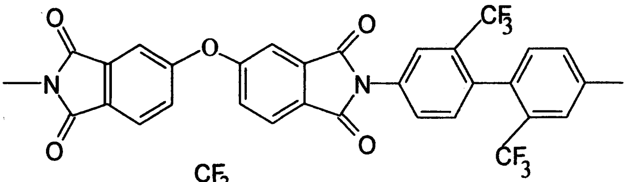

6FDA/ODA

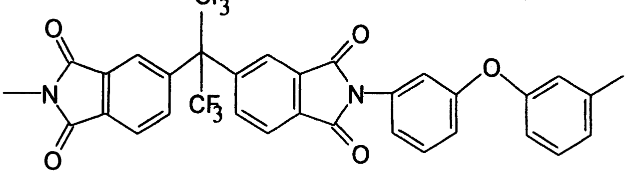

6FDA/DAB

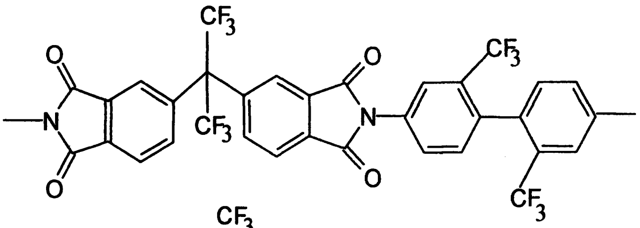

6FDA/PDA

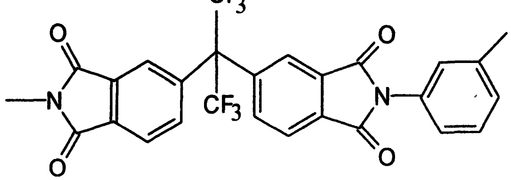

ODPA/6FODA

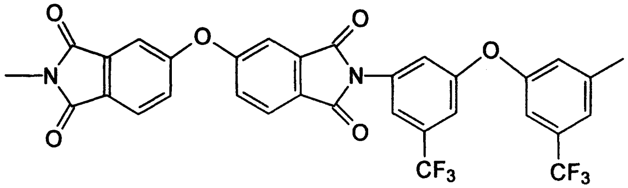

Figure 3. Chemical structures of some transparent polyimides.

In addition, the spacecraft in GEO and LEO experience fluctuating temperatures as they pass through the dark and light regions of their orbits. These temperatures can range from below 200 K to above 400 K.

So, the polymers used in space, and particularly those used on the outer surfaces of space vehicles, must be able to withstand extremely harsh environments. Therefore, before any polymer is used in a space, it is important to assess its sensitivity to space conditions. We have previously reported on the sensitivity of several transparent polyimides to conditions that are similar to those found in GEO and LEO (*6-13*). In this paper some of the results of these studies are reviewed using examples from the series of polymers presented in Figure 3.

Experimental

Samples

The polyimides shown in Figure 3 were prepared at the NASA-Langley Laboratory by Dr John Connell and are all very pale yellow in colour. Typical visible spectra of ≈50 μm films of some polyimides are presented in Figure 4 as examples. The glass transition temperatures, Tg, of the polyimides are high, all being above 450 K.

UV Photolysis

The UV photolysis studies were performed under vacuum or in air using an unfiltered high-pressure mercury/xenon lamp purchased from Oriel. The films were located 30 cm from the lamp and separated from it by a heat filter. The output from the lamp was 9.1 mW cm^{-2}.

VUV Photolysis

The VUV radiation and oxygen atom flux were generated in an oxygen plasma powered by a radio-frequency source (*14*). The charged species in the plasma were eliminated using an earthed grid and VUV only, atomic and molecular oxygen only or VUV as well as atomic and molecular oxygen could be made incident on a sample via an appropriate choice of the protective baffle.

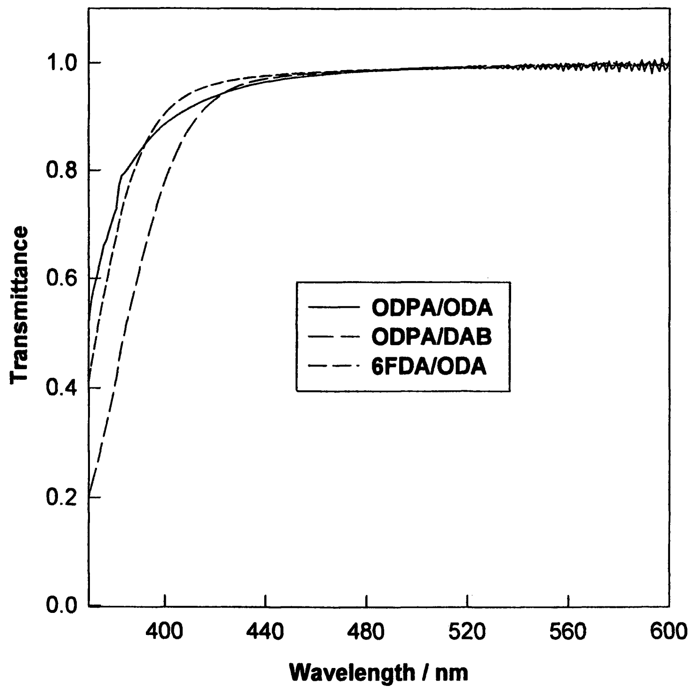

Figure 4. Visible transmission spectra of some transparent polyimides.

γ-Radiolysis

The samples were irradiated under vacuum or in air at the desired temperature using ^{60}Co gamma radiation (Nordian Gammacell-220) at a dose rate of approximately 7 kGy h^{-1}.

Electron Beam Radiolysis

The samples were irradiated at the Japan Atomic Energy Research Establishment (JAERI) in Takasaki, Japan using an electron accelerator producing electrons with an energy of 1 MeV and a current of 4 mA. During radiolysis the films were maintained at a constant temperature in a custom made apparatus (*15*).

Results and Discussion

UV Radiolysis of the Polyimides

Because of the high concentrations of phenyl rings in the aromatic polyimides, they all absorb UV wavelengths very strongly (see Figure 4). Consequently, most of the energy absorbed at these wavelengths is deposited in the surface regions of the films that are exposed directly to the radiation. Following UV photolysis under vacuum, all of the polyimides exhibited small red shifts in the absorption spectrum below 450 nm, but remained completely transparent above 500 nm. The observed red shifts are probably a result of the formation of surface radicals and other chemical chromophores (*16*). For photolysis in the presence of oxygen, oxidized polymer species could also contribute to the small red shifts near 400 nm.

Narrow singlets with a g-value of 2.004 and a width of 0.8 mT (6) characterized the ESR spectra of the radicals formed on UV photolysis of the polyimides under vacuum at room temperature. The narrow singlets suggest that the unpaired electron densities are delocalized over the aromatic groups along

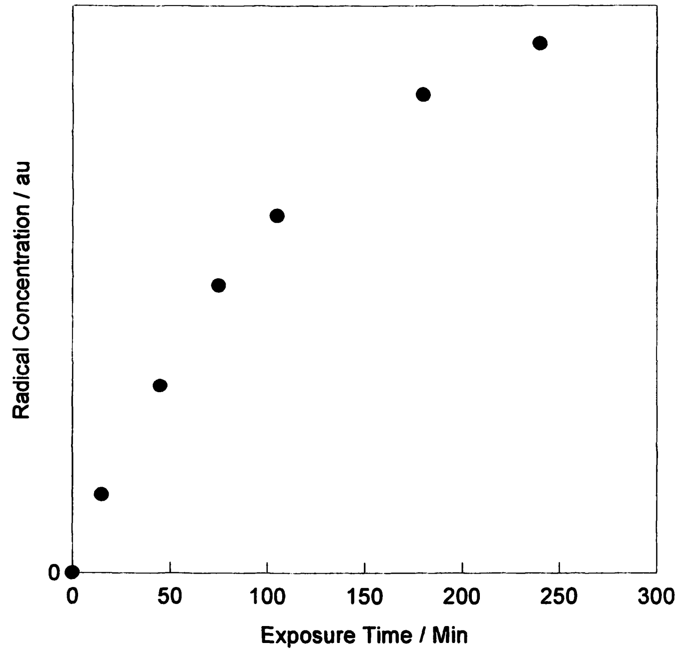

Figure 5. Radical concentration versus UV exposure time in oxygen for 6FDA/PDA.

the polymer chains. If the photolysis occurs in the presence of oxygen, the ESR spectra of the radicals are broader singlets centred at g = 2.005 with a line width of 1.4 mT (*6*). These broader spectra are indicative of the presence of oxygen-centred peroxy and alkoxy radicals, as well as carbon-centred radicals. These alkoxy radicals can be formed as a result of phenyl ring opening during photo-oxidation, as reported by Clough et al. (*17*) for polystyrene. Clough et al. proposed that the ring-opening reactions occur via the formation of complexes between oxygen and the phenyl rings. A similar mechanism could apply in the case of the UV photo-oxidation of aromatic polyimides.

On photolysis in the presence of oxygen, the radical concentration begins to plateau at longer exposure times (see Figure 5 for 6FDA/PDA). This indicates that either stable photo-oxidized surfaces are formed on the films during exposure, that radical combination reactions begin to occur, or, more likely, that

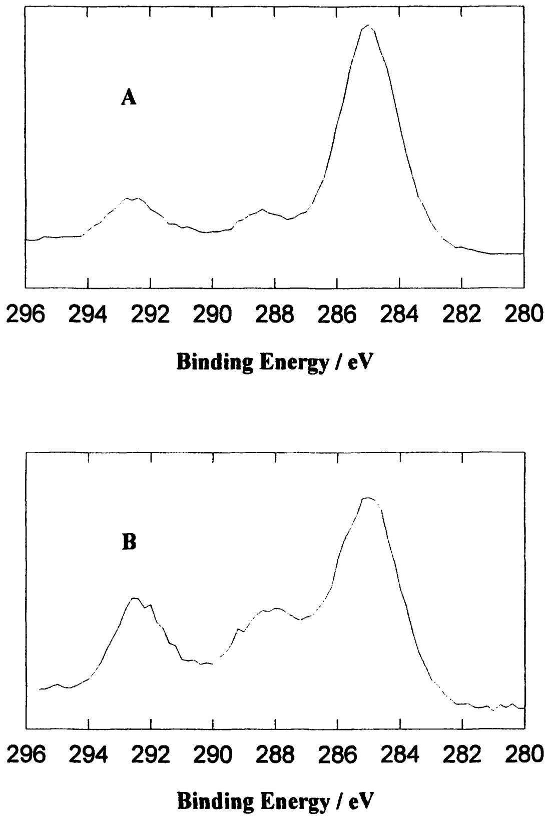

Figure 6. XPS C1s spectra for 6FDA/DAB film surface (A) before exposure to UV in the presence of oxygen and (B) after exposure in the presence of oxygen.

degradation results in the ablation of the surface layer with the formation of volatile products and the loss of some radical species. The latter explanation is supported by FT-IR spectral evidence (*18*) that indicates a decrease in the absorption peak intensities during photolysis of films in the presence of oxygen.

The photo-oxidation of the surfaces of the films in the presence of oxygen was also confirmed by XPS studies (*6*). The oxidation is clearly evident for a 6FDA/DAB film in the two C1s spectra shown in Figure 6. The spectra show an increase in the intensity of the C-O and C=O peaks at 286-289.5 eV relative to that for the C-C peak at 285 eV and the C-F peak at 292.5 eV. These spectra were obtained for the surface of the film directly exposed to the radiation. Photolysis of other polyimide films in the presence of oxygen yielded similar results.

On exposure, the O1s/C1s ratios in the surface layers of the films, obtained from simulation of the spectra, rapidly increase initially with exposure time and then plateau to essentially constant values, see example for 6FDA/DAB in Figure 7. This observation of a plateau in the ratio is consistent with the ablation of the surface layers of the film during photo-oxidation.

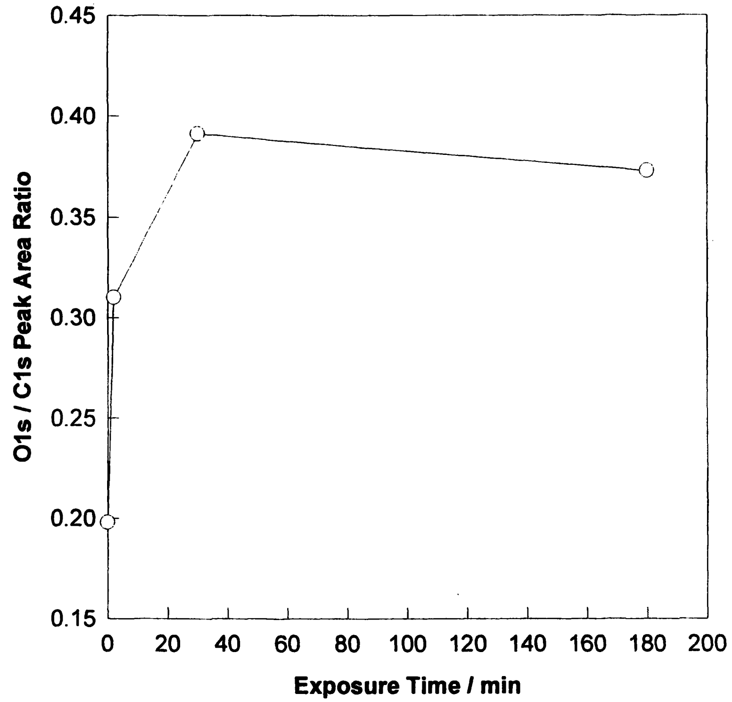

Figure 7. XPS O1s/C1s ratio for 6FDA/DAB exposure to UV in the presence of oxygen at various times. The line is to guide the eye.

In Polymer Durability and Radiation Effects; Celina, M., et al.;
ACS Symposium Series; American Chemical Society: Washington, DC, 2007.

VUV Radiolysis of the Polyimides

The UV wavelengths incident on any space vehicle extend below those incident at the surface of the earth and well into the VUV region, where the Lyman-α emission of atomic hydrogen from the sun is at 121 nm. At these short wavelengths sigma bonds contribute to the energy absorption process. In order to examine the effects of short wavelengths on the polyimide films they were exposed to the VUV radiation generated by an oxygen plasma (*7*). The VUV emission spectrum from the plasma does not exactly mirror the VUV spectrum in space, but some of the emission from the oxygen plasma occurs at 130 nm, which is close to the wavelength of the Lyman-α emission of hydrogen.

At the short VUV wavelengths of the oxygen plasma, all of the polyimide films will have a very high absorbance, and these energies will produce excited sigma states in the surface molecules of the exposed films that will lead to bond breakdown and molecular degradation.

After exposure of the polyimide films for up to 180 minutes to just the VUV radiation from the oxygen plasma, XPS analyses of the surfaces of the films were essentially unchanged (*7*), see Figure 8. However, since the film does absorb the incident radiation, with consequent molecular degradation, ablation of the surface degradation products must occur, leaving a "clean" surface.

If in addition to the VUV radiation of the oxygen plasma, the polyimide films are exposed to the neutral oxygen atoms and molecules present in the plasma, significant changes are observed in the compositions of the surface layers of the films. This is evident in the C1s XPS of the exposed surface of a 6FDA/ODA film, as demonstrated in Figure 9. The spectrum shows evidence for substantial carbon oxidation of the surface, as was observed for UV exposure in the presence of oxygen, but to a much greater extent. There was also evidence in the N1s XPS of the films exposed to atomic oxygen for the formation $-NO_2$ substituted products which appear in the spectrum at 408 eV, see Figure 10 for ODPA/ODA. These products were not observed for the films exposed to UV in the presence of oxygen.

Exposure of the polyimide films to the neutral oxygen atoms and molecules in the plasma in the absence of any VUV radiation also resulted in oxidation of the surface layers of the films. However, the rate of oxidation was less than that when the VUV component of the plasma was present (see Figure 8). This difference is indicative of a synergistic effect of the short wavelength radiation in the polyimide oxidation process.

γ- and e-Beam Radiolysis of the Polyimides

Both high-energy γ- and e-beam radiation are capable of forming anions, cations, excited electronic states and neutral radicals when they interact with a polymer (*19*). Thus high-energy radiation differs from UV radiation in that ions

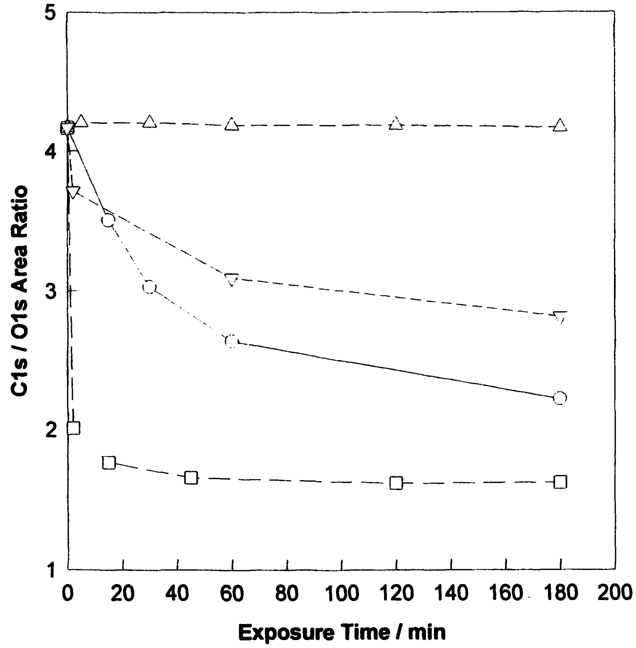

Figure 8. Dependence of the XPS C1s/O1s surface atom ratio on exposure time for 6FDA/PDA. VUV alone (Δ); VUV + atomic oxygen (□); atomic oxygen

are formed in the matrix as well as excited electronic states. Anion and cation radicals are unstable at ambient temperature, but anion radicals may be stable at 77 K. Cation radicals decay to a cation and neutral radical below 77 K. Neutral radicals may also undergo secondary reactions forming new structures.

Radical formation in the polyimides on γ-radiolysis under vacuum has been investigated by ESR spectroscopy. At 77 K the radical spectra of the irradiated polyimides are composed principally of two partially overlapping singlets (*8,9*), one of which decays when the temperature is raised to ≈200 K. This component has been assigned to anion radicals formed at 77 K by trapping of thermalized electrons in the polymer matrix. The other singlet has been assigned to neutral radicals with the free electron delocalized over several units of the polymer chain. These radicals are thus similar to the radicals formed on UV photolysis. Other minor radical components are also sometimes evident in the spectra, for example in that of Ultem that has been irradiated at 77 K (*9*).

The G-values for radical formation on vacuum radiolysis of some polyimides at 77 K are given in Table I. These radical yields provide an assessment of the relative radiation sensitivities of the polyimides. The results show that Kapton is the most radiation resistant (lowest G-value) of the polyimides, but that the stabilities of the other transparent polyimides are also

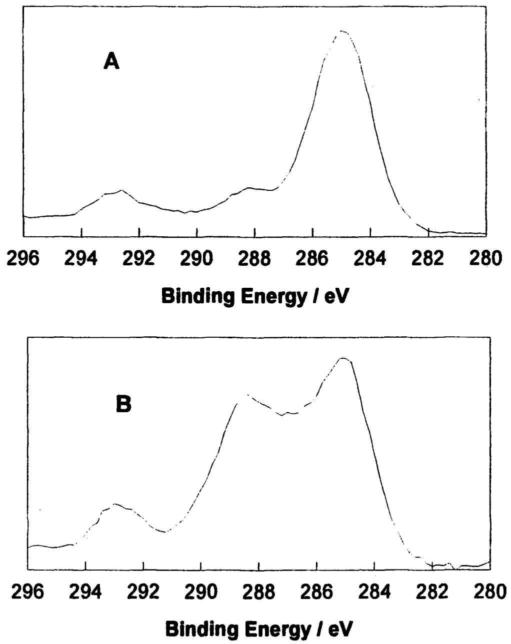

Figure 9. Typical XPS C1s spectra of the surface of a 6FDA/ODA film. (A) before exposure (B) after exposure to VUV plus atomic and molecular oxygen.

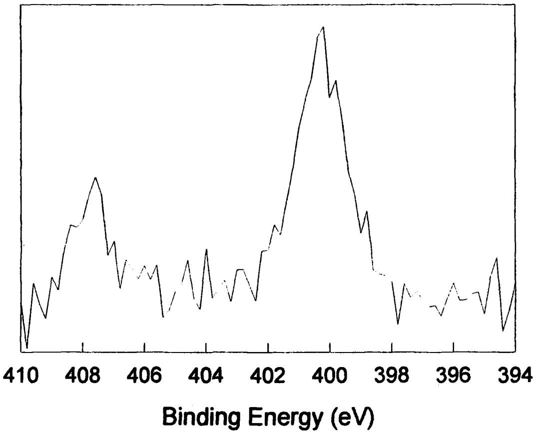

Figure 10. Typical XPS N1s spectrum of ODPA/ODA after exposure to atomic oxygen.

Table I. G-values for radical formation on γ-radiolysis at 77 K under vacuum.

Polyimide	*G-value x 10^2*
Kapton	1.7
Ultem	2.0
ODPA/ODA	3.2
ODPA/DAB	4.7
6FDA/ODA	6.2
6FDA/DAB	7.2

very high relative to other polymers (e.g. polyethylene has a G-value of ≈2.5 at 77 K (*20*)). The radiation stabilities of the aromatic polyimides can be attributed to their high concentration of aromatic groups. These groups are capable of degrading absorbed energy to heat, thereby minimizing the extent of bond scission reactions.

Following high-energy radiolysis new chemical structures are formed in a polymer. Kapton and many of the other polyimides have been reported to undergo nett chain scission (*11*) on radiolysis. On the other hand, Ultem undergoes nett crosslinking (*10*), with a gel dose above 10 MGy. However, the nature of the crosslinks in Ultem has still not been unequivocally identified.

Because the aromatic polyimides are very resistant to degradation by high-energy radiation, any changes in the polymer structure on radiolysis are difficult to observe experimentally. Thus the radiation chemical yields for formation of new structures are difficult to measure. However, Devasahayam et al. have carried out detailed ^{13}C NMR (*13*) and Raman spectroscopy (*18*) studies of the chemical changes in Ultem on radiolysis under vacuum at both room and elevated temperatures. They have identified the para-substituted diphenylether units as the principal sites for radiation damage. This can be seen in the Raman spectra in Figure 11. The most significant difference between the spectrum of the unirradiated film and that of a film irradiated by e-beam in an inert atmosphere at 503 K to a dose of 18.5 MGy occurs at 1200-1300 cm^{-1}. There was a decrease in the relative peak intensities of the irradiated film in this region, which is the finger-print region for the diphenylether units in Ultem. This observation is consistent with degradation at the phenyl ether linkages. Devasahayam et al. also observed a small decrease in the carbonyl peak intensity at ≈1780 cm^{-1}, suggesting that there is also some damage to the imide groups.

Devasahayam et al. (*12*) have also carried out Raman studies of the changes in the functional group concentrations at high dose for several other transparent polyimides. In this study the polyimides were irradiated in an inert atmosphere by e-beam over a range of temperatures from ambient temperature to 503 K. The Raman study indicated that the principal centres for radiation damage in these polyimides were located at the phenyl ether units in the diamine components and at the fluorinated isopropylidine units in the dianhydride components.

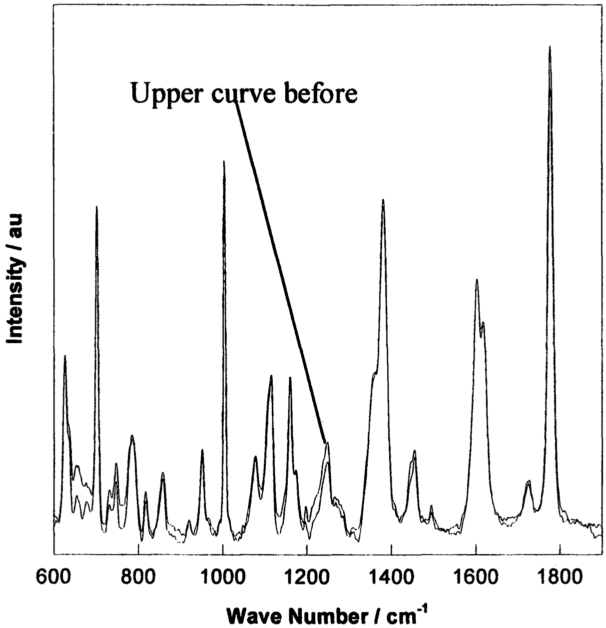

Figure 11. Overlapping FT-IR spectra of an Ultem film obtained before and after e-beam irradiation to a dose of 18.5 MGy at 503 K.

Summary

These studies have demonstrated that the transparent polyimdes are degraded slowly under simulated GEO and LEO conditions. However, while they are less stable than Kapton under the conditions, their stability is very high relative to aliphatic polymers over a wide range of temperatures. The origin of their stability is their high aromatic content and their high Tg. The lower stability of the transparent polyimides relative to Kapton may be attributed to their slightly lower aromatic group concentration. The stability of the polyimides under simulated GEO and LEO conditions was found to be lower at temperatures close to their glass transition temperature.

Acknowledgements

I wish to thank Dr John Connell of NASA Langley Research laboratory for providing the samples of all of the polyimides discussed herein except those of Kapton and Ultem. I also wish to thank all of my other coworkers whose names appear with mine in the reference list.

References

1. St Clair, T.L. In *Polyimides*; Wilson, D.; Stenzenberger, H.D.; Hergenrother, P.M., Eds.; Blackie: New York, 1990; pp 58-78.
2. Ohta, T. *Energy Technology Sources, Systems and Frontier Conversion;* Permagon: Yokohama, Japan, 1994; p12.
3. St. Clair, A.K., St. Clair, T.L., *Polymer High Technology;* ACS Symp. Ser., Washington, D.C., 1987; Vol. 346, 437-444.
4. Tenny, D.R. *NASA Conf. Publ. 3035*. 1988, 25-52.
5. Young, P.; Siochi, E.J. Slemp,W.S. *Irradiation of Polymers*; Clough, R.L., Shalaby, S.W., Eds.; ACS Symp. Ser., Washington, D.C., 1996; Vol. 620, 264-292.
6. Hill, D.J.T.; Rasoul, F.A.; Forsythe, J.S.; O'Donnell, J.H.; Pomery, P.J.; George, G.A.; Young, P.R.; Connell, J.W. *J. Appl. Polym. Sci.* **1995,** *58*, 1847-1856.
7. Rasoul, F.A.; Hill, D.J.T.; Forsythe, J.S.; O'Donnell, J.H.; Pomery, P.J.; George, G.A.; Young, P.R.; Connell, J.W. *J. Appl. Polym. Sci.* **1995,** *58*, 1857-1864.
8. Devasahayam, S.; Hill, D.J.T.; Connell, J.W. *Radiat. Phys. Chem.* **2001,** *62*, 189-194.
9. Devasahayam, S.; Hill, D.J.T.; Connell, J.W. *Radiat. Phys. Chem.* **2002,** *64*, 299-308.
10. Devasahayam, S.; Hill, D.J.T.; Whittaker, A.K. *High Perform. Polym.*, **2003,** *15*, 259-267, 2003.
11. Devasahayam, S.; Hill, D.J.T.; Connell, J.W. *High Perform. Polym..* **2005,** *17*, 547-559.
12. Devasahayam, S.; Hill, D.J.T.; Connell, J.W. *J. Appl. Polym. Sci.* **2006,** *101*, 1575-1582.
13. Brereton, I.; Devasahayam, S.; Hill, D.J.T.; Whittaker, A.K. *Radiat. Phys. Chem.* **2004,** *69*, 65-77.
14. Dai, X.J.; Elms, F.M.; George, G.A. *J. Appl. Polym. Sci.* **2001,** *80*. 1461-1469.
15. Kanazawa, T.; Haruyama, Y; Yotsumoto, K. *Report of the Japan Atomic Energy Research Institute:* JAERI-M 92-062, 1992.
16. Clough, R.L.; Gillen, K.T.; Malone, G.M.; Wallace, J.S. *Radiat. Phys. Chem.,* **1996,** 48, 583-594.
17. Clough, R.L.; Kristiansen, M.; Ogilby, P.R. *Macromolecules*, **1990,** 23, 2698-2704.
18. Devasahayam, S. Ph.D. thesis, The University of Queensland, Brisbane, Australia, 2001.
19. O'Donnell, J.H.; Sangster, D.F. *Principles of Radiation Chemistry:* Edward Arnold: London, 1969, pp 21-24.
20. Hill, D.J.T.; O'Donnell, J.H.; Pomery P.J.; Sangster, D.F. *Polymer Handbook*, 3 ed.; Brandrup, J., Immergut, E.H., Eds.: John Wiley: New York, 1989, pp II 387-397.

Chapter 12

Suppression of the Long-Term Degradation of Polymers by SiO_2 Coatings

Toshitaka Oka[1,3], Mitsuaki Kondo[1], Akihiro Oshima[1], Masakazu Washio[1], Minoru Iwata[2], Hisaaki Kudo[2], Yosuke Katsumura[2], Kenji Ito[3], Yoshinori Kobayashi[3], Takeshi Murakami[4], and Yoshimasa Hama[1]

[1]Advanced Research Institute for Science and Engineering (RISE), Waseda University, Central 5, 1–1–1 Gigashi, Tsukuba 305–8565, Japan
[2]School of Engineering, The University of Tokyo, 7–3–1 Hongo, Bunkyo-ku, Tokyo 113–0033, Japan
[3]National Institute of Advanced Industrial Science and Technology (AIST), Tsukuba, Ibaraki 305-8568, Japan
[4]National Institute of Radiological Sciences (NIRS), 4–9–1, Anagawa, Inage-ku, Chiba-shi 263–8555, Japan

Long-term oxidative degradation of an ion-beam irradiated polymer was studied. Silicon oxide thin layers were deposited on the surfaces of high density polyethylene (HDPE) to suppress the oxygen permeation. HDPE samples irradiated with a C^{6+} ion-beam were stored up to 12 months after the irradiation and the evolution of the chemical structure was followed by micro-Fourier transform infrared (micro-FT-IR) spectroscopy. Silicon oxide layers were found effective to suppress the long-term oxidative degradation of the ion-irradiated polymer.

© 2008 American Chemical Society

Introduction

Irradiated polymers react with the air and their mechanical properties are gradually degraded during long-term storage [1]. We deposited silicon oxide thin layers on the surfaces of polypropylene to effectively suppress the oxygen permeation during the gamma-ray irradiation [2]. The samples were stored up to 6 months after the irradiation. Their chemical structures and mechanical properties were studied with micro-Fourier transform infrared (micro-FT-IR) spectroscopy and tensile tests, respectively. We confirmed that SiO_2 coating could suppress radical-oxygen reactions and hence the long-term degradation of mechanical properties after the irradiation [3].

Irradiated high density polyethylene (HDPE) shows conspicuous self-oxidation that continues for more than 4 years [4]. This paper concerns the depth profile of chemical structures of HDPE coated with SiO_2 after ion-beam irradiation. With ion-beam irradiation, one can introduce an inhomogeneous depth distribution of functional groups due to the variation of the ion energy deposition as a function of depth. We discuss the suppression of long-term oxidative degradation in C^{6+}-irradiated HDPE with SiO_2 gas barrier coating.

Experimental

Sample and SiO_2 deposition

Additive free HDPE (Japan Polyethylene Corporation, Japan) was used. The density and thickness of the sample were 0.953 g/cm^3 and 2 mm, respectively.

Both surfaces of the samples were coated with SiO_2 thin layers by a magnetron sputtering system (ANELVA, Japan) under argon plasma. Radio-frequency was 13.56 MHz and the discharge power was 300 W. Thicknesses of SiO_2 layers were 0, 60 and 120 nm. The samples with these SiO_2 layers are hereafter called A, B and C, respectively. With SiO_2 deposited under the same condition, oxygen permeation through 1 mm thick polypropylene was decreased from 50 cm^3 m^{-2} day^{-1} to 1 cm^3 m^{-2} day^{-1} [2].

Irradiation

Ion beam irradiations were carried out at Heavy Ion Medical Accelerator in Chiba (HIMAC) in air at room temperature. The ion-beam irradiation condition is detailed in Table I.

Table I. Ion-beam irradiation condition.

Ion	*Energy MeV/u*	*Beam current μA*	*Fluence ions/cm²*	*Range μm*
C^{6+}	6	120	$6.72x10^{12}$	166

Range of the ion beam was calculated with SRIM-2003 [5].

Measurements

Micro-Fourier transform infrared (FT-IR) spectroscopy was employed to examine the chemical structures by observing absorption bands at 1716 cm^{-1} (carbonyl group), 964 cm^{-1} (*trans*-vinylene) and 910 cm^{-1} (end-vinyl). After 2 months from the irradiation, samples were sliced into 100-150 μm films along the direction of ion-beam penetration and the FT-IR spectra were measured as a function of depth from the surface [6]. We obtained the net absorbance ΔAbs. for the three bands for carbonyl group, *trans*-vinylene and end-vinyl at each depth by subtraction of the measured spectrum from that of the unirradiated sample. Sliced samples were stored in the dark at room temperature. They were repeatedly measured after 4, 6 and 12 months from the irradiation to observe the effect of long-term storage.

Results

Trans-vinylene

Figure 1 shows the depth profiles of irradiation-induced absorption of *trans*-vinylene for samples A, B and C, which were measured after 2 months from the irradiation. The peak of the profile was continuously shifted to deeper depths with increasing SiO_2 thickness. The depth profiles were unchanged as a function of storage time after the irradiation (data not shown).

Carbonyl group

Figure 2 shows depth profiles of carbonyl group absorbance after 2 months from the irradiation. The profile of uncoated sample A was similar to the depth profile of the absorbed dose or the Bragg curve [4]. The uncoated sample as well as the sample with 60 nm SiO_2 (B) had clear peaks around 110 μm, which is supposed to be the projected range. On the other hand, the absorbance of the sample with 120 nm SiO_2 (C) gradually decreased with increasing depth. The absorbance around 110 μm is higher in the order of A>B>C. In contrast, the

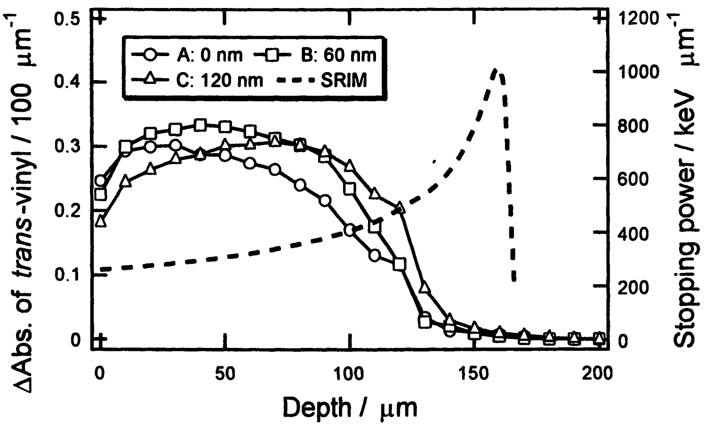

Figure 1. Depth profile of trans-vinylene absorbance, 2 months from the irradiation. Dotted line represents the depth profile of stopping power calculated with SRIM-2003.

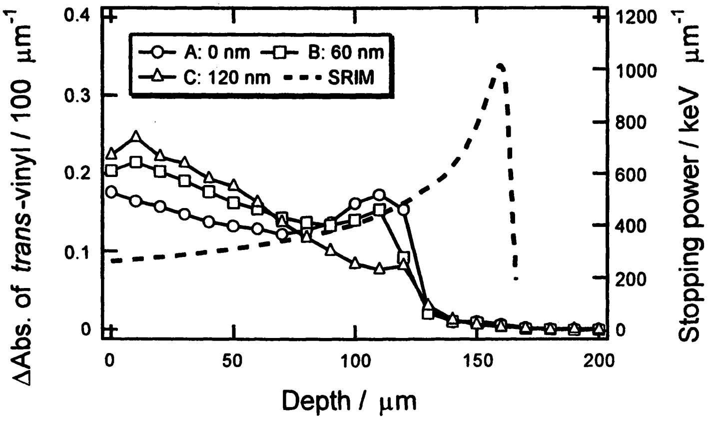

Figure 2. Depth profiles of carbonyl absorbance, 2 months from the irradiation. Dotted line represents the depth profile of stopping power calculated with SRIM-2003.

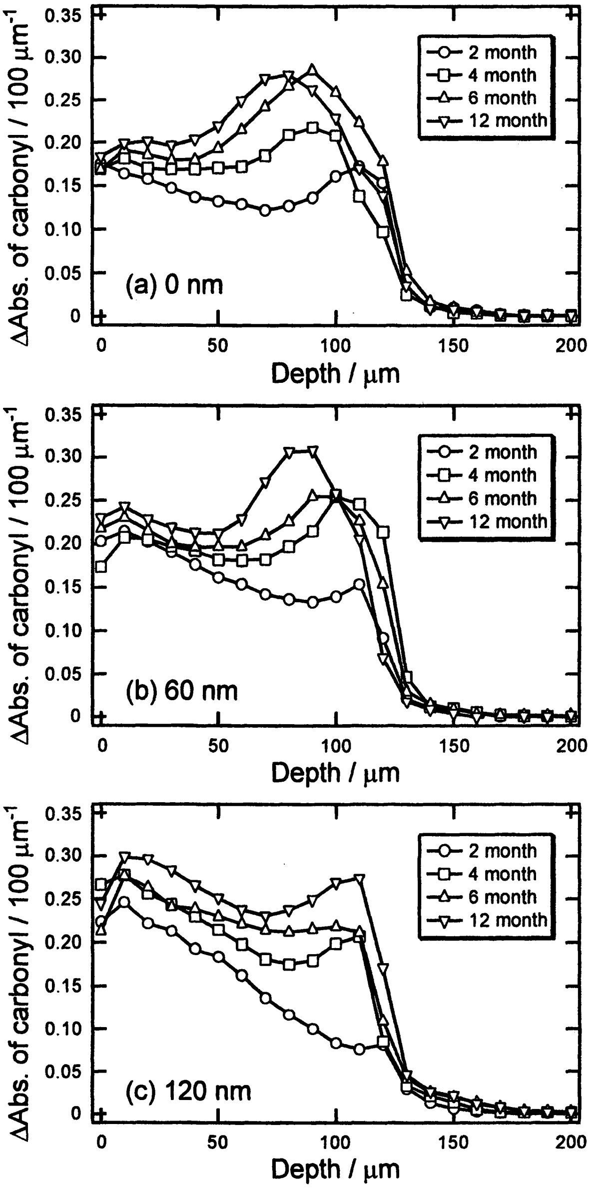

Figure 3. Depth profiles of carbonyl absorbance, 2, 4, 6 and 12 months from the irradiation. Thickness of the SiO_2 layers are (a) 0 nm, (b) 60 nm and (c) 120 nm.

absorbance in the shallow region from the surface to 80 μm is reversed and higher in the order of C>B>A.

Figure 3 presents depth profiles of carbonyl absorbance for samples A, B and C, measured after 2, 4, 6 and 12 months from the irradiation. The peaks near the supposed projected range intensified with increase in storage time. From the data we see oxidation progressed even after 12 months from the irradiation.

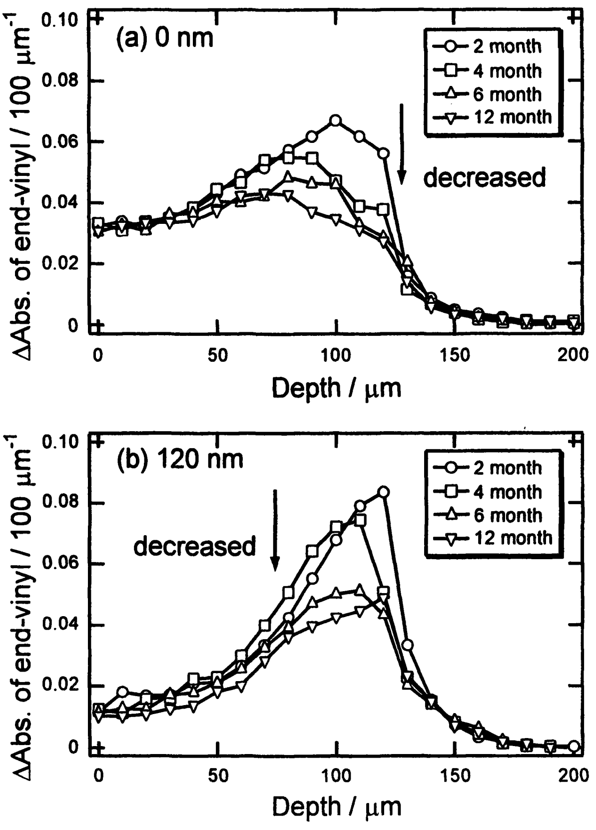

Figure 4. Depth profiles of end-vinyl absorbance of (a) sample A and (b) sample C. Absorbance decreases with time.

End-vinyl

Plots of end-vinyl absorbance for samples A and C are shown in Figure 4. In contrast with the carbonyl group, end-vinyl absorbance decreases during long-term storage. The absorbance of uncoated sample A was higher than sample C

with 120 nm SiO_2 coating in the shallow region. In the photolysis of polyethylene, end-vinyl increases with the formation of carbonyl groups by the Norrish type reaction [7], which is opposite to our present observation.

Discussion

Effect of ion-beam irradiation

It is well known that the predominant free radicals produced by ionizing radiation in HDPE are alkyl and allyl radicals [8]. The alkyl radical is unstable and disappears at room temperature, whereas the allyl radical is stable in vacuum at room temperature [4]. In our case, both radicals may act as a trigger to form *trans*-vinylene, end-vinyl, hydroperoxide and the carbonyl group.

The absorbance of each functional group in the shallow region is affected by SiO_2 coating. The absorbance of *trans*-vinylene and end-vinyl is decreased in SiO_2 coated samples (B and C). The trend of the absorbance of the carbonyl group is opposite to *trans*-vinylene and end-vinyl (Table II). These results suggest that the radicals in each sample disappear differently in the shallow region. During the SiO_2 deposition, the samples are exposed to argon plasma, thereby the crystalline region near the surface is damaged and made amorphous. Radicals disappear rapidly in the amorphous region by reaction with oxygen molecules and tend to form carbonyl groups or hydroperoxides. This results in reduction of *trans*-vinylene originating from the radicals in samples B and C.

In contrast with the results in the shallow region, the absorbance of the carbonyl group near the projected range is lower in SiO_2 coated samples. The crystalline structure is not damaged by plasma in the deeper region, and the oxygen permeation in B and C is suppressed by the SiO_2 layer. Radicals form *trans*-vinylene and end-vinyl, so that carbonyl formation is reduced in B and C.

Table II. Absorbance in the shallow region.

	Sample A	*Sample B*	*Sample C*
trans-vinylene	high	medium	low
end-vinyl	high	medium	low
carbonyl group	low	medium	high

Long-term Oxidative Degradation

As shown in Figure 3, different oxidation rates were observed between uncoated and coated samples. The radicals react with oxygen permeated from

the surface during the long-term storage and form carbonyl groups. The depth profile of the carbonyl group becomes similar to that of absorbed dose with increasing storage time [4].

The oxidation of HDPE during long-term storage is mainly due to the hemolytic decomposition process of hydroperoxide. Hydroperoxide undergoes thermolysis or photolysis, producing radicals by the following processes [4,9-10],

$$ROOH \rightarrow RO^{\bullet} + O^{\bullet}H \text{ (thermolysis, photolysis)}$$
$$2\,ROOH \rightarrow RO^{\bullet} + RO_2^{\bullet} + H_2O \text{ (thermolysis).}$$

The radicals produced in these reactions attack the polymer main chain, and react with oxygen to form new carbonyl groups. They may form new hydroperoxide, which initiates a new oxidative process as mentioned above. SiO_2 coating could reduce these oxidative reactions during long-term storage, especially in sample C with the thickest SiO_2.

Summary

Effect of 6 MeV/u C^{6+} ion-beam irradiation on the long-term oxidation of HDPE coated with SiO_2 was investigated. The irradiated samples were stored for 2, 4, 6 and 12 months, in air, in the dark, at room temperature. After the storage, the changes of the chemical structures were measured with micro-FT-IR. The SiO_2 barrier coating was effective to suppress the radical-oxygen reaction and the oxidative degradation. Our observation is consistent with a model that permeated oxygen gradually forms new carbonyl groups during long-term storage after ion-beam irradiation of HDPE in air. We observed the decrease of end-vinyl during long-term storage, which may be specific to ion-beam irradiation.

Acknowledgment

The authors would like to acknowledge Dr. Masayuki Ito (Waseda University) for his enlightening suggestions. The ion-beam irradiation was supported by the Research Project with Heavy Ions at NIRS-HIMAC.

References

1. Oka, T.; Hama, Y. *Res. Chem. Intermed.* **2005**, *31*, 661-668.
2. Kobayashi, Y.; Zheng, W.; Ito, K.; Yu, R.; Hirata, K.; Togashi, H.; Sato, K.; Oka, T.; Hama, Y. *Radioisotopes* **2003**, *52*, 449-455.

3. Oka, T.; Hama, Y.; Ito, K.; Kobayashi, Y. *Nucl. Instrum. Methods Phys. Res. Sect. B-Beam Interact. Mater. Atoms* **2005**, *236*, 420-424.
4. Hama, Y.; Oka, T.; Uchiyama, J.; Kanbe, H.; Nabeta, K.; Yatagai, F. *Radiat. Phys. Chem.* **2001**, *62*, 133-139.
5. Ziegler, J. F.; Biersack, J. P.; Littmark, U. In *The Stopping and Range of Ions in Solids*; Pergamon, 1985.
6. Oka, T.; Kanbe, H.; Yatagai, F.; Hama, Y. *Nucl. Instrum. Methods Phys. Res. Sect. B-Beam Interact. Mater. Atoms* **2003**, *208*, 181-184.
7. Stark, N. M.; Matuana, L. M. *Polym. Degrad. Stab.* **2004**, *86*, 1-9.
8. Dole, M. In *The Radiation Chemistry of Macromolecules*; Dole, M., Ed.; Academic: New York, 1972.
9. Kamiya, Y.; Niki, E. In *Degradation and Stabilization of Polymers*; Jellinek, H. H. G. Ed.; A Series of Comprehensive Reviews; Elsevier, 1983; Vol. 1, Chapter 7.
10. Hagiwara, M; Kagiya, T. In *Degradation and Stabilization of Polymers*; Jellinek, H. H. G. Ed.; A Series of Comprehensive Reviews; Elsevier, 1983; Vol. 1, Chapter 8.

Chapter 13

Comparisons of Polyhedral Oligomeric Silsesquioxane Polyimides as Space-Survivable Materials

Sandra J. Tomczak[1,*], Vandana Vij[2], Timothy K. Minton[3], Amy L. Brunsvold[3], Darrell Marchant[1], Michael E. Wright[4], Brian J. Petteys[4], Andrew J. Guenthner[4], Gregory R. Yandek[2], and Joseph M. Mabry[1]

[1]AFRL/PRSM, Materials Applications Branch, Air Force Research Laboratory, 10 East Saturn Boulevard, Building 8451, Edwards Air Force Base, CA 93524
[2]ERC Incorporated, Materials Applications Branch, Air Force Research Laboratory, 10 East Saturn Boulevard, Building 8451, Edwards Air Force Base, CA 93524
[3]Department of Chemistry and Biochemistry, Montana State University, 108 Gaines Hall, Bozeman, MT 59717
[4]Research and Engineering Sciences Department, Chemistry Division, NAVAIR-U.S. Navy, China Lake, CA 93555–6100
[*]Corresponding author: email: sandra.tomczak@edwards.af.mil

Kapton® is used extensively in spacecraft thermal blankets, solar arrays, and space inflatable structures. Atomic oxygen (AO) in low Earth orbit (LEO) causes severe degradation of Kapton®. SiO_2 coatings impart remarkable oxidation resistance to Kapton®, yet imperfections in the SiO_2 application process and micrometeoroid / debris impact in orbit damage the SiO_2 coating leading to Kapton® erosion. Polyhedral oligomeric silsesquioxane (POSS) is a silicon and oxygen cage-like structure surrounded by organic groups which can be polymerizable. POSS-diamine was polymerized to form POSS-Kapton® polyimide, which is self-passivating by the formation of a silica layer upon exposure to AO. Evidence of a SiO_2 passivation layer has been shown by X-Ray Photoelectron Spectroscopy studies on AO exposed 3.5, 7.0,

 © 2008 American Chemical Society

and 8.75 weight % Si_8O_{11} main chain (MC)-POSS-PI samples with erosion yields of 3.7, 0.98, and 0.3 percent, respectively, of the erosion yield for Kapton H® at a fluence of 8.5 x 10^{20} O atoms cm^{-2}. The self-passivation of POSS-Kapton®-PIs has also been demonstrated by monitoring a 1 micron deep scratch in MC-POSS-PI after exposure to AO. A study of the effect of temperature on the AO erosion of POSS-Kapton® samples showed that although the erosion of MC-POSS-PIs increased with temperature, they erode significantly less than their no-POSS analogous at elevated temperatures. Physical property characterization of POSS-PIs exposed to AO, and samples flown in LEO on the Materials International Space Station Experiment (MISSE), provide evidence that POSS-PIs are a potential Kapton® replacement material.

Introduction

Kapton® polyimide is used extensively on spacecraft in flexible substrates for lightweight, high-power solar arrays because of its inherent strength, temperature stability, excellent insulation properties, UV stability and IR transparency. It is also used in conjunction with Teflon FEP in multilayer insulation blankets for thermal control insulation because of its superior optical properties, including low solar absorptance. In these multilayer insulation blankets, aluminium (or gold) is typically applied to Kapton® due to its low emissivity [1].

It has been well established through LEO space flight experiments [2-5] and ground-based simulations of atomic oxygen (AO) in LEO [6-10], that polymeric materials undergo severe degradation as a result of this aggressive environment encountered in LEO. In this high vacuum environment, materials are subjected to solar radiation, thermal cycling which can range from -50 °C to 150 °C, bombardment by low and high-energy charged particles, as well as high incident fluxes of AO [11]. These harsh conditions necessitate the design of space-survivable materials.

AO in LEO impacts materials with a collision energy of 4.5-6 eV [12-14]. This O-atom translational energy is enough to overcome many reaction barriers and facilitates the degradation of Kapton®. The silicon-oxygen bond energy is 8 eV, and this bond is intact after AO exposure. For this reason, Kapton® is typically coated with silica to impart resistance to AO. Imperfections in the silica layer created during the deposition process, or during flight, lead to uncoated Kapton® which erodes readily in the presence of AO. Damaged aluminium coatings on Kapton® have been shown by de Groh et al, to lead to trapped AO in the Kapton® matrix. This AO can ricochet in the trapped spaces

before reacting, thereby burrowing out cavities, causing increased material erosion [2].

The nanodispersion of Si and O throughout the polyimide polymer matrix leads to the formation of a protective silica layer on the polyimide surface when the material reacts with AO [15]. Our data indicates that upon AO exposure, the organic material in the polymer surface erodes, while the atomic oxygen reacts with the nanodispersed POSS to form a silica layer. Therefore, when POSS is copolymerized to form POSS-PI, it imparts remarkable AO resistance, and does so with minor effects in the storage modulus, glass transition temperature, and coefficient of thermal expansion [15].

Evidence for the formation of a protective silica layer on the surface of POSS-PIs upon exposure to AO was found in X-Ray Photoelectron Spectroscopy (XPS) studies of POSS-PIs flown on MISSE1, and in separate studies of POSS-PIs exposed to AO in a ground-based facility. To directly compare the effect of AO on Kapton H®, SiO_2 coated Kapton HN®, and 8.75 weight % Si_8O_{11} cage "main-chain" POSS-polyimide (8.75 wt % Si_8O_{11} MC-POSS-PI), these materials were exposed to AO, scratched, and exposed to a second equivalent AO fluence. The erosion of the three materials, inside and outside of the scratched area, was monitored by stylus surface profilometry. The results of this study indicate that a silica layer is formed upon exposure of POSS-PIs to AO, and after scratching this layer, a new silica layer forms in the scratched area during AO exposure. Physical property characterizations and the effects of an approximately four year flight of POSS-PIs on the International Space Station will be presented.

Experimental

Synthesis of POSS-Polyimide Copolymers

Polyimides with the same chemical formula as Kapton® were synthesized by condensation polymerization of 4,4′-oxydianiline (ODA) and pyromellitic dianhydride (PMDA) in an N,N′-dimethylacetamide (DMAc) solvent [15, 16]. A POSS dianiline monomer (Figure 1) with two 1-(4-aminophenyl)-pendant groups and eight cyclopentyl pendant groups was synthesized using a procedure described by Feher et al. in 2003 [17]. Using this monomer, POSS-polyimide random copolymers were synthesized as shown in Figure 1 with POSS monomer loadings corresponding to 0, 5, 10, 20, and 25 wt% [18], which correspond to Si_8O_{11} cage loadings of 0, 1.75, 3.5, 7.0, and 8.75 wt %. "Side-chain"-POSS (SC-POSS) monomer was synthesized by Wright, et al. [19] from which 3.5, 7.0 wt % Si_8O_{12} cage SC-POSS-PIs were synthesized in the same manner as described above. All poly(amic acids) were cured to POSS-PIs as previously reported [18].

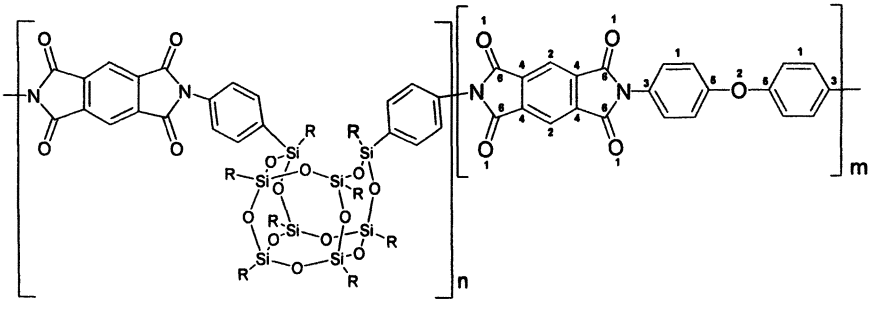

Figure 1. The structure of MC-POSS-Polyimide. R = cyclopentyl.

Exposure of POSS-Polyimides to Low Earth Orbit

POSS-PIs containing 0, 1.75, and 3.5 wt % Si_8O_{11}, were flown in LEO at about 370 km (~230 miles) on the International Space Station for nearly 4 years as part of the Materials International Space Station Experiment 1 (MISSE1). The circular samples were exposed to all aspects of the LEO environment including AO and UV light, except the outer ring of the samples which was covered by the sample holder. The step height difference between this masked outer ring and the neighbouring exposed sample area was measured in twelve places by profilometry. The surface atomic composition of the samples was determined by XPS.

AO Exposure of POSS-Polyimides

Ground-based POSS-PI sample exposures to AO were performed with a pulsed AO beam, operating at a repetition rate of 2 Hz and containing hyperthermal O-atoms that were generated by combining oxygen with 7 Joules per pulse CO_2 from a laser-detonation source [20-23]. The hyperthermal beam contains neutral O-atoms and molecular oxygen, with an ionic component of 0.01%. The mole fraction of AO in the beam was above 70 % and, for some exposures, above 90 %. Kinetic energies of the fast O-atoms in the beam can range from 2 to 15 eV, with the average being about 5.2 eV. Prior to exposure, samples were covered with a stainless steel mesh disk in order to mask areas and achieve AO exposed and unexposed areas. The O-atom fluence was on the order of 10^{20} O-atoms cm^{-2} for all experiments. All samples in this work were handled in ambient air after exposure and prior to etch depth determination by profilometry, surface topography, and surface chemistry measurements [24].

Surface Characterization of Scratched POSS-Polyimides

Multiple samples of Kapton H®, 8.75 % Si_8O_{11} MC-POSS PI, and silica-coated Kapton HN® (provided by Astral Technology Unlimited, Inc. Lot No. 00625-007, with a 130 nm SiO_2 coating) were exposed to hyperthermal AO. The beam was produced by the laser detonation source previously described [24, 25]. Three samples of each type were exposed to 100k pulses of the beam, along with a Kapton H® standard. After the first exposure, the etch depths of the screened samples were measured. A set of unscreened samples underwent surface morphology measurements. The third set of samples was scratched. For each sample, one approximately 40 µm wide and 1µm deep scratch was made with a diamond-tipped scribe, and two approximately 20 µm wide and 1µm deep scratches were made with a razor blade. All scratches were measured by profilometry (with a 5µm radius probe tip) in several places. Screens were placed over the scratched samples and these samples were exposed to additional 100k shots of the hyperthermal AO beam. After removal of the samples from the chamber, profilometry was used to measure step height differences between exposed and unexposed areas and to profile each scratch in AO exposed and unexposed areas.

XPS data was obtained with the use of non-monochromatized Mg Kα radiation (1253.6 eV) and a hemispherical CLAM 2 (VG Microtech) analyzer. Scanning electron microscopy (SEM) was performed using an ISI CL6 operating at 15 keV equipped with a Kevex X-ray detector, as previously reported [18].

Physical Properties Characterization of POSS-Polyimides

Polyimide samples were analyzed by a DMTA V from TA Instruments using a 5 °C/min temperature ramp from room temperature to 500 °C and a tensile geometry [18].

Measurements of the coefficient of thermal expansion (CTE) were taken on a thermo mechanical analyzer (TMA 2940) from TA Instruments with a film fiber attachment, in a nitrogen atmosphere. The cured films were cut into 15mm by 3mm samples, the force applied was 0.05N & 0.10 N, and the sample was heated at 5 °C/min. The CTE was calculated as $\alpha = (\Delta L \times K)/(L \times \Delta T)$ where L = length, K = a cell constant, T = temperature °C. Test variability was +/- 2.306 ppm/ °C based on five Kapton H® tests.

The Effect of Temperature on The Erosion of POSS-Polyimides by a Hyperthermal O-Atom Beam.

The erosion of 0 wt %, 3.5 wt % and 7.0 wt % Si_8O_{11} POSS-polyimides exposed to a hyperthermal O-atom beam has been studied at 25 °C, 100 °C, 150

°C, 220 °C, and 300 °C. Two samples of each type of material were exposed simultaneously. One of each sample type was covered with a screen during exposure. Each exposure was to 50,000 pulses of the hyperthermal O-atom beam, and included a "screened" Kapton H® reference sample. The O-atom fluence was on the order of 10^{20} O-atoms cm^{-2}. The nominal O-atom translational energy of each exposure was 5.2 eV, and the O/O_2 ratio in the beam was 0.65:0.35. For the 25 °C exposure, the films (which were not cast on substrates) were placed in the sample holder. For the higher temperature exposures, the films were cast on germanium discs that were in contact with a controlled heating block during the exposures, and were equilibrated to the desired temperature.

Results and Discussion

The AO exposure of 0, 3.5, 7.0, 8.75 wt % Si_8O_{11} MC-POSS-PI (POSS "R" group is cyclopentyl) films was carried out in a simulated LEO environment where films of these materials were etched by exposure to a hyperthermal O-atom beam [2]. The difference in etch depth between the eroded and stainless steel screen-protected areas of the samples, made it possible to calculate an AO reaction efficiency (R_e) or erosion rate of the material for a given AO flux.

The AO reaction efficiency of the Kapton H® reference sample was used to calculate the Kapton® equivalent fluence and erosion yields of each sample exposure. For various exposures, the step heights (or etch depths) of POSS-PI films were plotted as a function of the step height of the Kapton H® film [18, 26]. The derivative functions indicated that the 3.5 and 7.0 wt % Si_8O_{11} POSS polyimide films reached erosions rates of 3.7 and 0.98%, respectively, of the erosion rate for Kapton H® after 395,000 beam pulses (8.47 x 10^{20} atoms cm-^{2}) [9, 10]. 8.75 wt% Si_8O_{11} MC-POSS-PI samples had an erosion rate that was 0.3 percent of the erosion rate for Kapton H®, and 1/3 of 7.0 wt % POSS-PI at a fluence of 8.5×10^{20} atoms cm^{-2}. These results support the formation of a passivating silica layer that is a result of the nano-dispersed POSS moieties reacting with AO.

A "self-passivation test" was carried out to better assess the protective silica layer formation witnessed by XPS of POSS-PIs. Kapton H®, SiO_2 coated Kapton HN®, and 8.75 wt % Si_8O_{11} MC-POSS-PI were exposed to equivalent AO fluences. The etch depth of the Kapton H® after the initial exposure was 7.0 ± 0.2 µm, indicating an O-atom fluence of 2.3 x 10^{20} O atoms cm^{-2}. This sample appeared significantly roughened after exposure. The etch depth of 0.26 ± 0.15 µm of the 8.75 wt % Si_8O_{11} MC-POSS-PI film was difficult to measure since the overall etch depth was not much greater than the slight roughness caused by the exposure. For the SiO_2 coated Kapton HN® the etch depth was below the practical measurement limit of the profilometer and the sample surface appeared unaffected.

SEM images of Kapton H®, SiO_2-coated Kapton HN®, and 8.75 wt % Si_8O_{11} MC-POSS-PI that were AO-exposed, scratched, and underwent a second exposure to 2.3 x 10^{20} O atoms cm^{-2} are shown in Figure 2. For the SEM image of Kapton H®, the exposed region is in the left side of the image and has a more roughened surface with a deepened scratched area. The etch depth of the Kapton H® sample outside of the scratch was about 5.5 µm. The scratch was 20 µm wide and 1µm deep unexposed and 1.4 µm deep relative to the neighboring eroded surface after the second exposure. The top of the SiO_2-coated Kapton HN® image was exposed to AO and only had erosion in the scratched area with unaffected neighboring silica-coated Kapton HN®, demonstrating the effects of damage to silica coatings on Kapton®. Here the unexposed scratch was 20 µm wide and 1µm deep and the exposed scratch was 8 µm deep relative to the neighboring exposed surface, amounting to 7 µm of erosion in the scratch. 8.75 wt % Si_8O_{11} MC-POSS-PI was exposed to AO in the darkened upper right area in Figure 2c. A difference in step height between exposed and unexposed unscratched areas of the 8.75 wt % Si_8O_{11} MC-POSS-PI was < 200nm and is not visible by microscopy. In Figure 2c, the scratch was 35 µm wide and 1.4 µm deep unexposed and about 1.8 µm deep after AO exposure. This result indicates that 8.75 wt % Si_8O_{11} MC-POSS-PI experienced about 400 nm of erosion inside the scratch during AO exposure. In comparison, Kapton H® eroded about 5 µm inside and outside the scratch, plus Kapton H® eroded an additional 0.200 µm in the scratch during exposure. In all instances, the scratched regions apparently eroded slightly more than the unscratched exposed areas. This may be explained by the undercutting effect described above, where the O-atoms are focused deeper into the polymer matrix by scattering from the sidewalls of the scratches. These results are summarized in Table 1.

The results of the study of the effect of temperature on AO erosion of POSS-polyimides are given in Tables 2 and 3 below. The results in Table 1 show that polyimide and POSS-PIs experience increasing erosion with increasing temperature. It is interesting to note that the erosion of Kapton H® (Tg = 400 °C) decreases at 300 °C which is the final cure temperature for Kapton® polyimide. For each temperature, the etch-depths of the POSS-PIs (Table 2) divided by the etch depth of Kapton H® are given in Table 3. The erosion of the 0 wt % POSS-PI exhibited the strongest temperature dependence, with the etch depth increasing by a factor of about 3.6 from 25 °C to 300 °C. The 3.5 wt % and 7.0 wt % Si_8O_{11} POSS-PIs showed less temperature dependence in their erosion. The etch depths of these samples increase by factors of 2.2 and 2.4, respectively, with the increase from 25 °C to 300 °C, and with the uncertainty in the measurements, these factors might be considered the same.

The results show that although POSS-PIs have increased erosion with temperature, they do erode less than their no-POSS analogous at elevated temperatures. In most cases, except at 200 °C, a doubling of the POSS content from 3.5 wt % to 7.0 wt % Si_8O_{11}, causes the etch depth to decrease by about

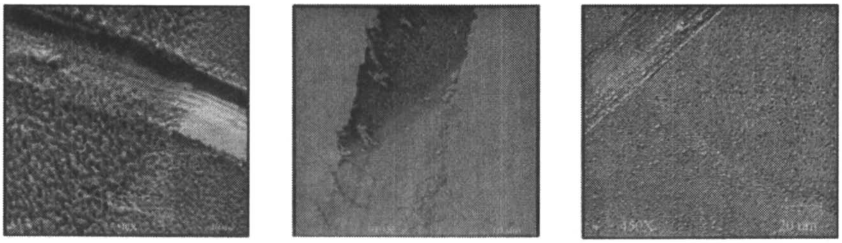

(a.) (b.) (c.)

Figure 2. SEM images of results from a self-passivation experiment. (a.) Kapton H®, (b.) SiO_2 coated Kapton HN® (Provided by Astral Industries Inc.), and (c.) 8.75 wt % Si_8O_{11} cage MC-POSS-PI. Samples were exposed to 2.3 x 10^{20} atoms/cm^2, scratched, covered by a wire screen and exposed again to 2.3 x 10^{20} atoms/cm^2. The area covered by the wire screen was (a.) the right side, (b.) the bottom portion, and (c.) the left side.

half. The O-atom fluences used in this study are at least half of those used in other work with these materials. It has been seen that at higher O-atom fluences, at room temperature, there is an increasing difference in the erosion of polyimide and POSS-PI. This is because the erosion of polyimide increases linearly with fluence while the erosion of POSS-polyimide increases by approximately the square root of the fluence [18, 26]. Hence, it is expected that the higher fluence exposures, at elevated temperatures, may reveal a more marked reduction in erosion yields for the POSS-polyimides compared to the erosion yields for the polyimide and Kapton H® films.

The physical properties of POSS-PIs were evaluated by DMTA at Edwards Air Force Research Laboratory and have been discussed previously [15]. The glass transition temperatures (Tg) were as follows: 420 °C for 0 % POSS-PI, 394 °C for 3.5 % Si_8O_{11} MC-POSS-PI, 390 °C for 7 % Si_8O_{11} MC-POSS-PI, 383 °C for 8.75 % Si_8O_{11} MC-POSS-PI. The 7 % Si_8O_{11} MC-POSS-PI exhibited a tan δ peak very similar in intensity and breadth to the 0 % POSS-I peak, while the 3.5 and 8.75 wt % Si_8O_{11} MC-POSS-PI tan δ peaks were slightly greater than half the height, and of similar width, to the 0 and 7 wt % POSS samples [18]. This unique behavior of the 7 wt % Si_8O_{11} MC-POSS-PI may be from similar chain packing to the 0 % POSS-PI sample. A side-chain POSS (SC-POSS) monomer has been synthesized by Wright et al. [19] and was readily copolymerized to form POSS-PIs with POSS as a pendant group. In an AO exposure with a total fluence of 3.53 x 10^{20} O atoms/cm^{-2}, 7 % Si_8O_{12} SC-POSS-PI had an erosion yield that was 3.3 % of Kapton H®. In a previous AO exposure study total fluence of 4.10 x 10^{20} O atoms/cm^{-2}, 7 % Si_8O_{11} MC-POSS-PI had an erosion yield that was 3.8 % of Kapton H®. These results indicate that MC- and SC-POSS-PIs have approximately equal AO resistance. DMTA

Table 1. Self-Passivation Experiment Erosion Depths

Material	*Kapton H®*	*SiO_2-coated Kapton HN® with Aluminum under-coating*	*8.75 wt % Si_8O_{11} MC-POSS PI*
After 1st exposure.	5.5 μm	~ 0 μm	0.200 μm
After 2ndexposure. Outside of scratch.	5 μm	~ 0 μm	~ 0 μm
After 2nd exposure. Inside of scratch.	5 μm	7 μm	~ 0.400 μm

Table 2. The etch depths for polyimide, 3.5 wt % and 7.0 wt % Si_8O_{11} POSS-polyimides, and Kapton H® after exposure to a hyperthermal O-atom beam at five temperatures.

Sample Temperature	*0% POSS-Polyimide (μm)*	*3.5 wt % Si_8O_{11} POSS-PI (μm)*	*7.0 wt % Si_8O_{11} POSS-PI (μm)*	*Kapton H® (μm)*
300 °C	10.37 ± 0.47	1.24 ± 0.17	0.67 ± 0.16	3.14 ± 0.13
220 °C	7.47 ± 0.37	0.94 ± 0.21	0.78 ± 0.08	3.46 ± 0.20
150 °C	5.36 ± 0.23	1.02 ± 0.11	0.41 ± 0.07	3.59 ± 0.11
100 °C	4.09 ± 0.38	0.82 ± 0.07	0.43 ± 0.06	3.55 ± 0.11
25 °C	3.17 ± 0.24	0.63 ± 0.08	0.30 ± 0.08	3.50 ± 0.12

Table 3. The ratio of etch depths for polyimide, and 3.5 wt % and 7.0 wt % Si_8O_{11} POSS-polyimides to Kapton H® after exposure to a hyperthermal O-atom beam at five temperatures.

Sample Temperature	*0% POSS-PI/ Kapton H® (μm)*	*3.5 wt % Si_8O_{11} POSS-PI/ Kapton H® (μm)*	*7.0 wt % Si_8O_{11} POSS-PI/ Kapton H® (μm)*
300 °C	3.30 ± 0.20	0.40 ± 0.06	0.21 ± 0.05
220 °C	2.16 ± 0.16	0.27 ± 0.06	0.23 ± 0.03
150 °C	1.49 ± 0.08	0.28 ± 0.03	0.11 ± 0.02
100 °C	1.15 ± 0.11	0.23 ± 0.02	0.12 ± 0.02
25 °C	0.91 ± 0.08	0.18 ± 0.02	0.086 ± 0.02

measurements taken at Michigan State University (consistently 20 °C less than those taken at Edwards AFB due to instrumentation) have shown that the Tg of 7 wt % Si_8O_{12} SC-POSS-PI is 400 °C, and decreases to 378 °C after exposure to $2.3x10^{20}$ oxygen atoms cm^{-2}. The tan δ peaks for this material were slightly more intense and broader than commercial Kapton H®.

The sudden temperature changes experienced by materials in the LEO environment make the coefficient of thermal expansion (CTE) a highly important material property. In order for POSS-PIs to be a drop-in replacement for Kapton®, it is necessary that the new material have predictable CTEs with similar values to Kapton®. The CTE values for several samples are shown in Table 4. The addition of POSS slightly increases the CTE, and a slight decrease is seen after exposure of the SC-POSS-PI to AO. Mismatches in the CTEs between polymeric materials and their coatings lead to cracks, crazing, and mechanical material failure. The CTE of fused silica is about 0.55 (μm/m°C) [27, 28] and the CTE of the silica passivation layer formed on POSS-PIs in the presence of AO is expected to be close to that of silica in value. This mismatch between the silica passivation layer and the underlying POSS-PI is likely to cause cracks in the silica. The self-passivating properties of the POSS-PIs described above result in the formation of a silica passivation layer in the areas where cracks or damage have occurred, once again protecting the underlying POSS-PI.

Table 4. Coefficients of Thermal Expansion for POSS polyimide films.

Sample	**CTE (μm/m°C)**
Kapton H®	30.25
0% POSS-PI	33.11
7 % Si_8O_{11} MC-POSS-PI	33.5
8.75 % Si_8O_{11} MC-POSS-PI	35
7 % Si_8O_{12} SC-POSS-PI	35.86
7 % Si_8O_{12} SC-POSS-PI exposed to AO†	33.64

*Test variability based on 5 Kapton H® tests = ± 2.306 ppm/°C.

†$2.3x10^{20}$ oxygen atoms cm^{-2}

MC-POSS-PI films were recently retrieved from the Materials International Space Station Experiment after being flown in LEO for 3.9 years on a sample holder that was exposed to all aspects (AO, UV) of the LEO environment. These films included a 0, 1.75, and 3.5 wt % Si_8O_{11} MC-POSS-PIs. All films were adhered to an aluminum substrate before flight. The innermost portion of the circular samples experienced greater erosion than the portion furthest from the center of the samples. The outer portion neighbors the edges that were covered by an aluminum mask throughout the flight and remained unexposed to

the space environment. The step heights from the unexposed (masked) area and the neighboring exposed outer portion of samples, with original thicknesses of roughly 30 μm, were measured. It was found that a 32.55 ± 0.87 μm thick 0% POSS-PI film completely eroded. 1.75 % MC-POSS-PI showed some survival with a step height of 5.79 ± 1.31 μm between the exposed outer portion and the masked area, although the inner portion of this sample completely eroded. 3.5 % MC-POSS-PI film remained throughout with a step height of 2.12 ± 0.34 μm from the outer portion and the unexposed area, and an inner region that experienced greater erosion causing thinner areas of the film. It was determined by XPS that the atomic percentages of the top 10 nm of the films were 34 % Si, 59 % O, and 7 % C for both the 1.75 and 3.5 wt% Si_8O_{11} MC-POSS-PI samples.

Conclusion

The incorporation of POSS nanostructures into polyimides has been shown to significantly extend the lifetime of these materials in LEO. Studies on the effect of a hyperthermal O-atom beam on POSS-PIs have shown the improved oxidation resistance imparted to polyimides by the addition of POSS. XPS data of both the AO-exposed and space-flown POSS-PI materials indicated that the improved oxidation resistance of these materials is due to a rapidly formed silica layer upon exposure of POSS-polymers to high incident fluxes of atomic oxygen.

A study of the response of scratched materials to AO showed that if a Kapton H® surface is scratched, the scratched material will erode at roughly the same rate as undamaged Kapton H®. A SiO_2 coating of 130 nm protected underlying polyimide from AO attack, but after the coating was compromised, the exposed polymer eroded (during AO exposure) at approximately the same rate that uncoated Kapton® eroded. The 8.75 wt % Si_8O_{11} MC-POSS-PI experienced only 1 - 2 % the erosion yield of Kapton H® that was exposed to an equivalent amount of AO. This is presumably due to a silica layer formed on the surface of the material during AO exposure. When this layer was removed by a scratch, newly AO-exposed material had the same low erosion yield, indicating that a silica passivating layer formed in the scratched area.

It was found that the incorporation of POSS slightly reduces the glass transition temperature (Tg) of Kapton® polyimide, however, the Tg values of POSS-PIs are well above the temperatures experienced by materials in LEO. The CTE of POSS-PIs is similar to the CTE of commercial Kapton H®. A new SC-POSS monomer imparts about the same AO resistance to polyimides as the MC-POSS monomer. The modulus, Tg, and CTE of SC-POSS-PIs were determined before and after exposure to atomic oxygen, and are comparable to the values of these properties for Kapton H®.

POSS-polyimide samples flew on the International Space Station for nearly

4 years and showed space-survivability in LEO, with a film of the 3.5 wt % Si_8O_{11} POSS-polyimide remaining.

Acknowledgements

The authors would like to thank 2nd Lt. Laura Moody for performing DMTA and CTE measurements. We thank Dr. Andre Lee of Michigan State University for carrying out DMTA studies. We gratefully acknowledge Dr. Rene Gonzalez for his previous work with POSS-polymer synthesis, AO exposure, and XPS analysis. We appreciate Mrs. Marietta Fernandez for her work on SEM images and Dr. Timothy Haddad for his assistance in synthetic chemistry. We thank Astral Technologies Unlimited, Inc. for the kind donation of silica-coated Kapton HN®. Dr. Shawn Phillips of Edwards AFB is acknowledged for the initial suggestion of the "self-passivation" (scratch) test presented in this work. This work was financially supported by Defense Advanced Research Projects Agency (DARPA), the Air Force Office of Scientific Research (Grant No. F49620-01-1-0276), and the Air Force Office of Scientific Research through a Multiple University Research Initiative (Grant No. F49620-01-100335).

References

1. Karam, R. D. in *Satellite Thermal Control for Systems Engineers, Progress in Astronautics and Aeronautics*, Zarchan, P., Ed.; American Institute of Astronautics and Aeronautics, Inc.: Reston, VA, 1998, Vol. 181, pp 153-157.
2. de Groh, K. K.; Banks, B. A.; Demko, R. in *Techniques for Measuring Low Earth Orbital Atomic Oxygen Erosion of Polymers*, TM-2002-211479; NASA Center for Aerospace Information, Handover, MD, 2002, pp 1-13.
3. Koontz, S. L.; Leger, L. J.; Visentine, J. T.; Hunton, D. E.; Cross, J. B.; Hakes, C. L. *J. of Spacecraft and Rockets*, **1995**, *32*, 483-495.
4. de Groh, K. K.; Banks, B. A. *J. of Spacecraft and Rockets*, **1994**, *31*, 656-664.
5. Banks, B. A.; Rutledge, S. K.; de Groh, K. K.; Mirtich, M. J.; Gebauer, L.; Olle, R.; Hill, C. M. *Proc. 5th Int. Symp. on Materials in a Space Environment*, Cannes-Mandelieu, France, **1991**, p. 137.
6. Tennyson, R. C. *Surface and Coatings Technology*, **1994**, *68/69*, 519- 527.
7. Gilman, J.W.; Schlitzer, D. S.; Lichtenhan, J. D. *J. Appl. Polym. Sci.*, **1996**, *60*, 591-596.
8. Gonzalez, R. I.; Phillips, S. H.; Hoflund, G. B. *J. of Spacecraft and Rockets*, **2000**, *37*, 463-467.

9. Minton, T. K.; Garton, D. J. In *Advanced Series in Physical Chemistry: Chemical Dynamics in Extreme Environments*, Dressler, R. A., Ed.; World Scientific: Singapore, 2001, pp. 420-489.
10. Dooling, D.; Finckenor, M. M. *Material Selection Guidelines to Limit Atomic Oxygen Effects on Spacecraft Surfaces, NASA/T,* **1999**, 209-260.
11. Grobner, J.; Kerr, J. B. *J. of Geophysical Research-Atmospheres*, **2001**, *106*, 7211 - 7217.
12. Champion, K.S.W.; Cole, A.E.; Kantor, A.J.; In *Standard and Reference Atmospheres, Handbook of Geophysics and the Space Environment*, Jursa, A.S., Ed.; Air Force Geophysics Laboratory, United States Air Force; Nat. Tech. Info. Serv.: Springfield, VA. 1985, Ch. 14, pp. 1-43.
13. Hedin, A. E., *J. of Geophysical Research-Space Physics*, **1983**, *88*, 170-188.
14. Koontz, S. L.; Leger, L. J.; Rickman, S. L.; Hakes, C. L.; Bui, D. T.; Hunton, D. E.; Cross, J. B. *J. of Spacecraft and Rockets*, **1995**, *32*, 475-482.
15. Tomczak, S. J.; Marchant, D.; Svejda, S.; Minton, T. K.; Brunsvold, A. L.; Gouzman, I.; Grossman, E.; Schatz, G. C.; Troya, D.; Sun, L. P.; Gonzalez, R. I. in *Materials for Space Applications, Mater. Res. Soc. Symp. Proc.*, Chipara, M.; Edwards, D. L.; Benson, R. S.; Phillips, S. Eds.; MRS Warrendale, PA., 2005; *851*, pp 395-406.
16. Mather, P. T.; Jeon, H. G.; Romo-Uribe, A.; Haddad, T. S.; Lichtenhan, J. D. *Macromolecules*, **1999**, *32*, 1194-1203.
17. Wright, M. E.; Schorzman, D. A.; Feher, F.J.; Jin, R. Z. *Chem. of Materials*, **2003**, *15*, 264-268.
18. Wright, M. E.; Petteys, B. J.; Guenthner, A. J.; Yandek, G. R.; Tomczak, S. J.; Minton, T. K.; Brunsvold, A. Publication in progress.
19. Feher, F. J.; Nguyen, F.; Soulivong, D.; Ziller, J. W. *Chemical Communications*, **1999**, *17*, 1705-1706.
20. Feher, F. J.; Terroba, R.; Ziller, J. W. *Chem. Comm.*, **1999**, *22*, 2309-2310.
21. Feher, F. J.; Soulivong, D.; Eklund, A. G. *Chem. Comm.*, **1998**, *3*, 399-400.
22. Blanski, R. L.; Phillips, S. H.; Chaffee, K.; Lichtenhan, J. D.; Lee, A.; Geng, H. P. *Polymer Preprints*, **2000**, *41(1)*, 585-586.
23. Amy L. Brunsvold, Timothy K. Minton, Irina Gouzman, Eitan Grossman, and Rene Gonzalez *High Perform Polym*, **2004**, *16*, 303-318.
24. Gonzalez, R. I. Ph.D. thesis, University of Florida, Gainesville, FL, 2002.
25. Phillips, S. H.; Haddad, T. S.; Tomczak, S. J. *Cur. Opin. Solid State Mat. Sci.* **2004**, *8*, 21-29.
26. Tomczak, S.J.; Vij, V.; Marchant, D.; Minton, T. K.; Brunsvold, A. L.; Wright, M. E.; Petteys, B. J.; Guenthner, A. J. *Proc. SPIE*, **2006**, *6308*, 630804.
27. White, G. K. *J. Phys. D: Appl. Phys.* **1973**, *6*, 2070-2078.
28. Optical Components.com.

Chapter 14

Effects of Simulated Space Environments on Piezoelectric Vinylidene Fluoride-Based Polymers

Tim R. Dargaville[1-3], Roger L. Clough[1], and Mathew Celina[1,2,*]

[1]Sandia National Laboratories, Albuquerque, NM 87185
[2]Under contract to SNL
[3]Current address: School of Physical and Chemical Sciences, Queensland University of Technology, Brisbane 4001, Australia

Piezoelectric polymers based on polyvinylidene fluoride (PVDF) are of interest as adaptive materials for large aperture space-based telescopes. In this study, two piezoelectric polymers, PVDF and P(VDF-TrFE), were exposed to conditions simulating the thermal, radiative and atomic oxygen conditions of low Earth orbit. The degradation pathways were governed by a combination of chemical and physical degradation processes with the molecular changes primarily induced via radiative damage, and physical damage from temperature and atomic oxygen exposure, as evident from depoling, loss of orientation and surface erosion. The piezoelectric responsiveness of each polymer was strongly dependent on exposure temperature. Radiation and atomic oxygen exposure caused physical and chemical degradation, which would ultimately cause terminal damage of thin films, but did not adversely affect the piezoelectric properties.

© 2008 American Chemical Society

High performance polymers have been recognized as a key component in the emerging technology of exceptionally large-area spacecraft, such as solar sails, arrays and large telescope mirrors. The intrinsic low density, functionality, processibility and flexibility of certain polymers make them attractive considering the storage and weight limitations of launch vehicles. Unfortunately, the hostile environment of space is extremely damaging to organic polymers, often severely restricting their performance and lifetimes (*1-5*). This is especially concerning given the great cost in launching the spacecraft into orbit and possible limitations on the duration or success of missions.

Thin film piezoelectric polymers have the potential to be used in revolutionary large diameter film-based primary mirror adaptive optics for low Earth orbit (LEO) based telescopes. Using piezoelectric polymers has the advantage of incorporating the actuation mechanism directly into the thin film such that any mirror shape changes can be adjusted in real time. This allows for correction/compensation of misalignment errors, temperature fluctuations and even focus shifting (*6*). To achieve maximum weight savings, a mirror made from a piezoelectric polymer may not have any protective shielding, and could therefore be exposed to atomic oxygen (AO), vacuum ultraviolet (VUV) radiation, and the temperature extremes of LEO. We are interested in examining how piezoelectric polymers based on the vinylidene fluoride backbone will perform in LEO conditions with the overall materials selection and performance requirements having been previously considered (*7,8*).

In this paper we have addressed the issue of piezoelectric performance of PVDF and copolymers of vinylidene fluoride and trifluoroethylene (P(VDF-TrFE)) over temperature ranges simulating the LEO environment, and examined the effects of radiation (gamma and vacuum ultraviolet) and atomic oxygen.

Experimental

The polymers used were poled piezoelectric films 30 ± 2 μm PVDF from MSI and 28 ± 2 μm P(VDF-TrFE) from Ktech Corp. The details of the temperature annealing and AO/VUV experiments have been reported elsewhere (*9-11*).

Results and Discussion

Effects of Temperature

It is generally accepted that commercial PVDF devices should not be used above 80°C due to deterioration of the piezoelectric performance. In LEO the

temperature of the material may exceed 80°C if it has full sun exposure and a low emittance to absorbance ratio. With this in mind, we exposed films of piezoelectric PVDF and P(VDF-TrFE) to elevated temperatures and then measured the residual piezoelectric response via the d_{33} piezoelectric coefficient. In Figure 1 the d_{33} coefficient is plotted against the annealing temperature for the PVDF homopolymer and for 20 and 30 % TrFE copolymers. Included in these plots are the respective DSC traces. The loss in the d_{33} of the homopolymer above 80°C does not correspond with any significant transition in the DSC; instead we propose that the loss in piezoelectric response is due to thermal contraction (as evidenced by a decrease in the film area (*9*)) of the highly stretched films causing concomitant randomization of the dipoles. The two TrFE copolymers exhibit gradual decreases in their d_{33} coefficients at low annealing temperature followed by a rapid reduction at 100 and 125°C for the 30 and 20 % TrFE copolymers, respectively. The DSC traces indicate that the loss in d_{33} coefficient corresponds with the Curie transition (T_c; the point at which the crystalline phase changes from the polar form to the non-polar form). Clearly the copolymer with 20 % TrFE content is superior in temperature performance to the 30 % TrFE copolymer.

It is noteworthy to mention that the d_{33} loss profiles in Figure 1 are independent of annealing time beyond several hours. For example, the PVDF homopolymer has the same d_{33} coefficient after annealing at 120°C for one day as it does after 1 year. This is very encouraging since even with a limited piezoelectric response, the materials will still deform when an electric field is applied, although the magnitude of the deformation per unit field will be less than before heat exposure.

In LEO the temperatures a material experiences in the Earth's shadow may be as low as minus 100°C (*4*). To examine the performance of the PVDF homopolymer and 20 % copolymer at sub-ambient temperatures we measured the remanent polarization (P_r; the polarization with no electric field applied) which was extracted from D-E hysteresis loops. These results are plotted in Figure 2. When cooled, the homopolymer experienced a drop in P_r at higher temperature compared with the TrFE copolymer. Instead of a loss of polarization, as observed during thermal annealing, the diminished P_r at low temperature can be attributed to an increased energy barrier for dipole switching resulting in lower observed polarization due to changes of molecular mobility and T_g as a function of temperature.

To confirm that the results from d_{33} and remanent polarization measurements translate into bimorph performance across a wide temperature range, small rectangular bimorphs were fabricated to mimic small sections of a thin film telescope mirror. An electric field was applied to the bimorphs and the maximum deflection measured. This deflection was converted to d_{31} (the piezoelectric response in the plane parallel to the deflection) (*12*) and plotted (Figure 3) between -95 and +80°C. Superimposed on the plots are the moduli of

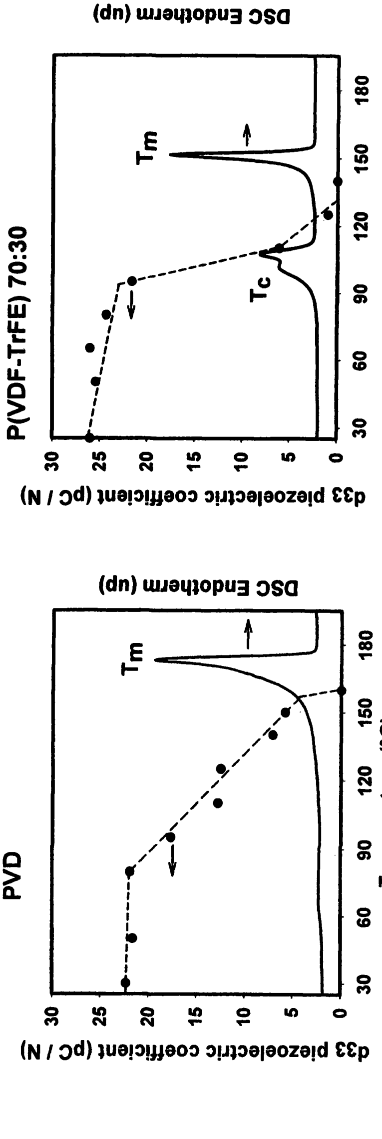
P(VDF-TrFE) 70:30
DSC Endotherm (up)
Tm
Tc
d33 piezoelectric coefficient (pC / N)
Temperature (°C)
PVD
DSC Endotherm (up)
Tm
d33 piezoelectric coefficient (pC / N)
Temperature (°C)

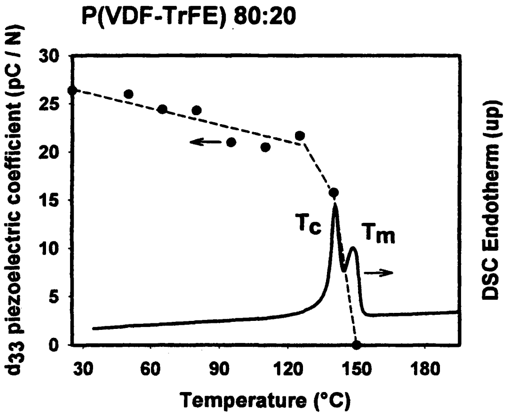

Figure 1. Loss in the d_{33} piezoelectric coefficient as a function of annealing temperature correlated with DSC endotherms for the PVDF homopolymer and two TrFE copolymers.

the two non-annealed materials measured using differential mechanical analysis (DMA). The magnitude of the bimorph deflection over the temperature range studied clearly depends on the modulus of the material. Below the glass transition temperature the bimorphs stiffen and the deflection decreases, while at high temperature any thermal depoling is compensated by the softening of the materials and results in greater deflection. A similar correlation between the d_{31} coefficient (determined from the polarization when a stress was applied) and the modulus for PVDF was reported by Wang (*13*). The TrFE copolymer has a much less pronounced glass transition at approximately -30°C and as a result, has improved low temperature deflection (and higher P_r (Figure 2)) compared with the homopolymer. The bimorphs were also annealed at 110 and 140°C and the deflection measured. The resulting loss in deflection potential agrees well with the d_{33} annealing experiments, i.e. the copolymer can withstand higher temperatures without depoling.

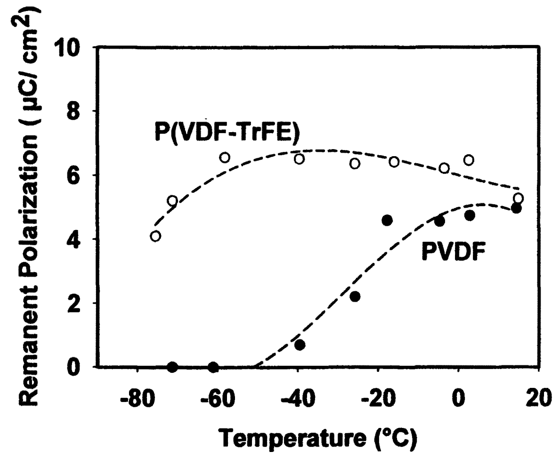

Figure 2. Remanent polarization of PVDF and $P(VDF_{80}\text{-}TrFE_{20})$ as a function of temperature.

Effects of Vacuum UV Irradiation and Atomic Oxygen

In addition to the large thermal extremes in LEO, materials may also be exposed to atomic oxygen (AO) and the full solar spectrum, which extends into the highly energetic vacuum UV range (115 – 200 nm). The high flux of atomic oxygen (AO), (approximately 10^{15} atoms/cm^2-s with an orbital speed of 8 km/s) formed by photodissociation of the small concentration of residual molecular oxygen in LEO, will cause surface pitting and erosion, while the VUV exposure may induce deleterious radiation events (*5*).

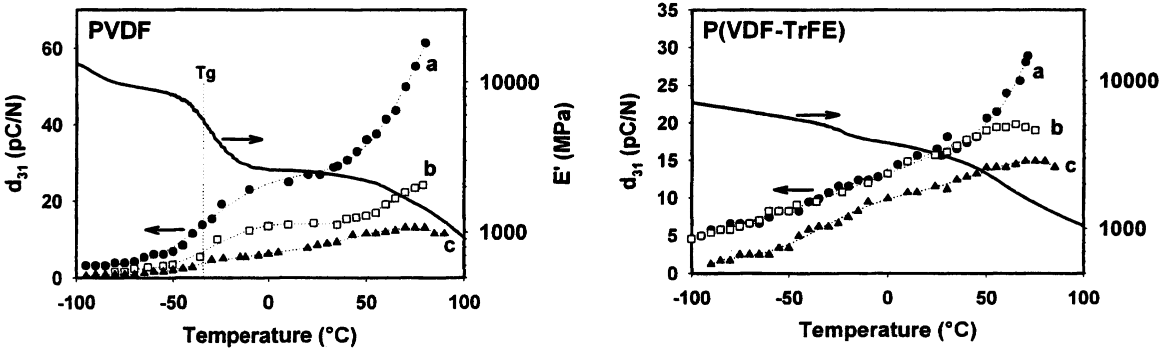

Figure 3. Effect of temperature on d_{31} coefficients and storage moduli (E') of a PVDF homopolymer bimorph and a P(VDF_{80}-$TrFE_{20}$) bimorph. a) unannealed; b) annealed 24 hrs at 110 °C; c) annealed 24 hrs at 140 °C.

Vinylidene fluoride polymers are known to undergo net crosslinking when exposed to ionizing radiation (*14-16*). It was therefore not surprising that when exposed to gamma irradiation both PVDF and P(VDF-TrFE) films formed significant insoluble components, as indicated in the sol-gel plots of Figure 4A. It was unexpected, however, that when exposed to VUV radiation, the TrFE copolymer crosslinked extensively while the homopolymer did not (Figure 4B). To understand these observations it is useful to consider the differences between gamma and VUV irradiation. Photochemistry involves absorption of photons of specific energies by particular chromophores with the material creating an excited state, and is thus much more specific compared to gamma irradiation. The probability of a photochemical event occurring depends on the overlap of the emission spectrum of the source and the absorption spectrum of the specimen. Although the absorbance spectra for the two materials studied were not available below 200 nm, we can assume that they will strongly absorb in this range as the energies in the VUV spectrum (<200 nm) are absorbed by $\sigma \rightarrow \sigma^*$ transitions which are present in all materials. Possibly the most important difference between gamma irradiation and VUV irradiation is the penetration depth. Gamma photons have sufficient energy to penetrate deeply into polymers, while VUV photons are usually absorbed in a thin surface layer due to the absorbance by σ bonds (*17*). We propose that the highly energetic short wavelength photons (<170 nm (*18*)) are absorbed in the surface layers of both polymers causing surface crosslinking. The differences in the absorbance characteristics of the two polymers arises from the fate of the longer, less energetic but deeply penetrating photons. We propose that the PVDF homopolymer absorbs the shorter wavelengths in the top few micrometers causing crosslinking, while the longer wavelengths are harmlessly dissipated by the polymer. In the copolymer the shorter wavelengths are also absorbed at the surface and the longer wavelengths, which penetrate into the bulk, interact with the comonomer units generating radicals, which combine to form crosslinking sites and lead to material degradation. The reason for the higher absorbance by the copolymer may be due to disruption of the CH_2 CF_2 alternation by the CHF groups as hypothesized by French et al. (*19*).

The effects of combined AO plasma and VUV radiation on PVDF and P(VDF-TrFE) were also studied. AO can cause surface erosion of polymers by physical sputtering and surface oxidation (*5*). PVDF and P(VDF-TrFE) were no exception with significant erosion rates between 2.5 and 2.8 x 10^{24} cm^3 / AO atom observed. These rates place them at the more sensitive end of the scale of erosion yields for polymers (*5*). Scanning electron microscopy (SEM) was used to examine the changes in the surface texture before and after exposure to AO/VUV (Figure 5). The AO component appears to have caused surface roughening, and in the case of the PVDF homopolymer the highly oriented structure is pronounced. The homopolymer films used in this study were highly stretched in order to render them piezoelectric, whereas the TrFE copolymer

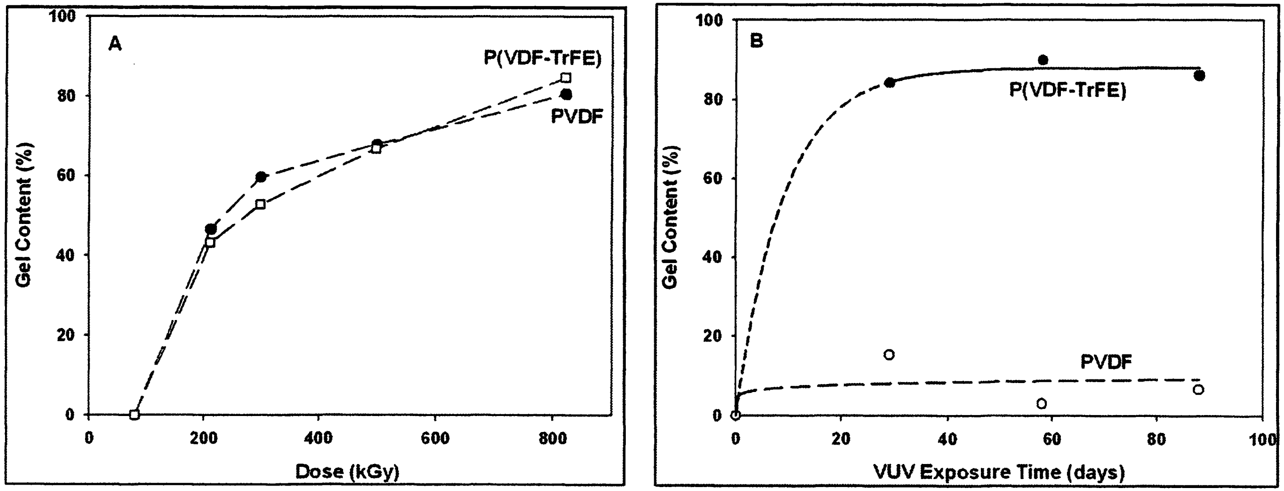

Figure 4. Gel content of PVDF and P(VDF_{70}-$TrFE_{30}$) exposed to (A) gamma radiation, and (B) VUV radiation.

films have the advantage that they do not require stretching to obtain piezoelectricity (*20*).

Despite the changes to the physical properties caused by VUV or combined AO/VUV exposure, little change in the piezoelectric response for either polymer was observed, i.e. the polymers may suffer significant radiation and surface reactions but these reactions affect the piezoelectric properties very little. Considering that the piezoelectric properties originate largely from the bulk crystalline domains, it is reasonable that surface changes due to erosion, or crosslinking of the amorphous regions by radiation, do not impact greatly on the crystalline polar domains, and hence the piezoelectric response. It should be noted that Zhang and co-workers (*21*) found that copolymers with high TrFE content can change from being piezoelectric to electrostrictive by exposure to radiation, however, in our case the TrFE content is much less than what was studied by Zhang.

Conclusions

For piezoelectric polymers based on the vinylidene fluoride backbone to be used as spacecraft materials they must be durable to extreme temperatures and the highly radiative environment of space. In this broad study we have simulated the temperature, radiation and AO conditions found in LEO and examined the effects they have on piezoelectric films of PVDF and P(VDF-TrFE). Loss in the piezoelectric properties after exposure to high temperatures appears to be linked to film contraction and the Curie transition for the PVDF and TrFE copolymer films, respectively. At sub-ambient temperatures, the piezoelectric performance is governed by the glass transition, which is more subtle in the copolymer and hence gives the copolymer greater flexibility and piezoelectric response at low temperature. The results from experiments measuring primary piezoelectric indicators such as d_{33} and remanent polarization, agreed well with the deflection of bimorphs made from each polymer.

When exposed to gamma radiation both polymers had almost identical gel formation, so it was surprising that when treated with VUV radiation the response of each polymer was dramatically different. The homopolymer showed signs of surface crosslinking with little change to the bulk, while the TrFE copolymer had a degree of crosslinking consistent with VUV radiation initiated events throughout the film. VUV radiation damage is considerably more selective than gamma and is dependent on the absorption characteristics of the polymers. We propose that the PVDF homopolymer absorbs the shorter wavelengths in the top few micrometers causing crosslinking, while the longer wavelengths are harmlessly dissipated by the polymer. In the copolymer the shorter wavelengths are also absorbed at the surface and the longer wavelengths, which penetrate into the bulk, interact with the comonomer units generating

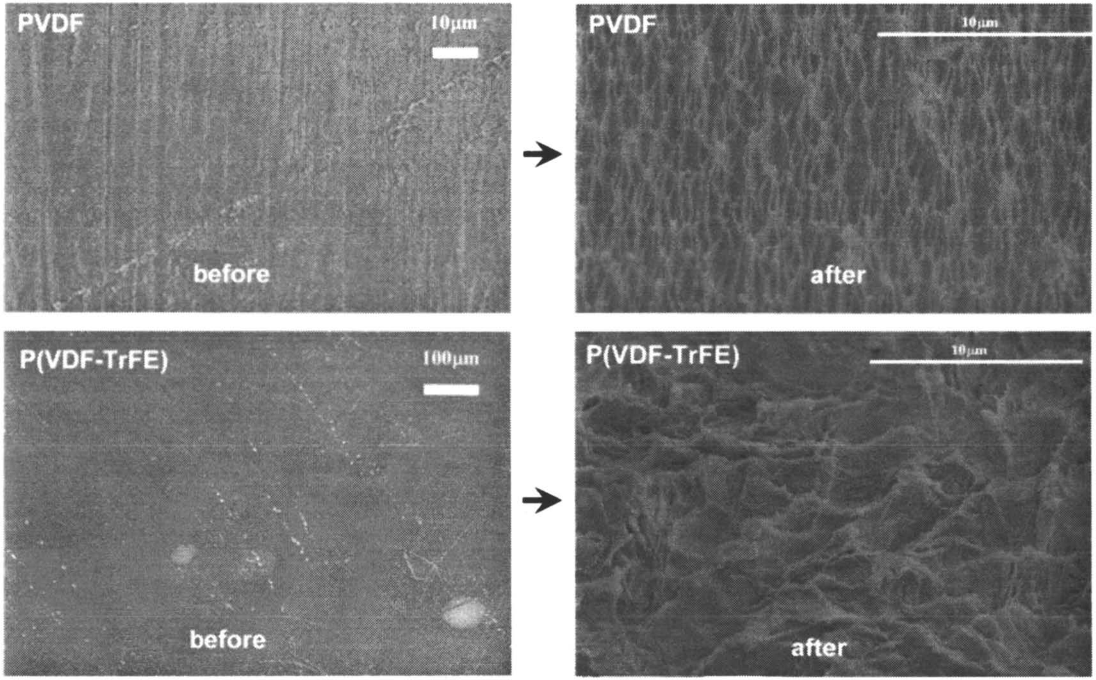

Figure 5. Surface SEM images of PVDF and P(VDF-TrFE) before and after exposure to AO/VUV.

radicals, which combine to form crosslinking sites and lead to material degradation. This demonstrates that gamma radiation cannot be used as a reliable avenue to predict VUV radiation degradation in these polymers.

The effects of simultaneous AO/VUV exposure of the two vinylidene fluoride based polymers were also examined. In both cases significant weight loss and surface erosion resulted from AO attack. Erosion yields were 2.8×10^{-24} cm^3/atom for PVDF and 2.5×10^{-24} cm^3/atom for P(VDF-TrFE), consistent with previous literature data for similar materials. The film orientation of PVDF samples was reflected in the surface topology features after exposure, while the less orientated P(VDF-TrFE) samples had less regular surface patterning after exposure. Significantly, neither AO nor VUV irradiation dramatically altered the piezoelectric properties and we propose that these materials should perform satisfactorily under moderate LEO conditions.

Acknowlegements

Sandia is a multiprogram laboratory operated by Sandia Corporation, a Lockheed Martin Company, for the United States Department of Energy's National Nuclear Security Administration under Contract DE-AC04-94AL85000. The authors express their appreciation to Gary Zender, Deborah Waters, Bruce Banks, Julie Elliot and Roger Assink for technical assistance and useful discussions.

References

1. Young, P. R.; Siochi, E. J.; Slemp, W. S. *Polym. Prepr.* **1994**, *35*, 916-917.
2. Rasoul, F. A.; Hill, D. J. T.; George, G. A.; O'Donnell, J. H. *Polym. Advan. Technol.* **1998**, *9*, 24-30.
3. Dursch, H. W.; Pippin, H. G. In *Materials Degradation in Low Earth Orbit (LEO)*; Srinivasan, V.; Banks, B. Ed.; The Minerals, Metals & Materials Society: Warrendale, 1990, p 207-218.
4. Dever, J. A.; de Groh, K. K.; Banks, B. A.; Townsend, J. A. *High Perform. Polym.* **1999**, *11*, 123-140.
5. Banks, B. A. In *Modern Fluoropolymers*; Scheirs, J., Ed.; John Wiley & Sons: Chichester, 1997, p 103-113.
6. Martin, J. W.; Redmond, J. M.; Barney, P. S.; Henson, T. D.; Wehlburg, J. C.; Main, J. A. J. *Intel. Mat. Syst. Str.* **2000**, *11*, 744-757.
7. Celina, M.; Dargaville, T. R.; Chaplya, P. M.; Clough, R. L. *High Perform. Polym.* **2005**, *17*, 575-592.

8. Celina, M. C.; Dargaville, T. R.; Chaplya, P. M.; Clough, R. L. *Mat. Res. Soc. Sym. Proc.* **2005**, *851*, 449-460.
9. Dargaville, T. R.; Celina, M.; Chaplya, P. M. *J. Polym. Sci., Part B Polym. Phys.* **2005**, *43*, 1310-1320.
10. Dargaville, T. R.; Celina, M.; Martin, J. W.; Banks, B. A. *J. Polym. Sci., Part B Polym. Phys.* **2005**, *43*, 2503-2513.
11. Dargaville, T. R.; Elliott, J. M.; Celina, M. *J. Polym. Sci., Part B Polym. Phys., submitted*
12. Uchino, K. Ferroelectric Devices; Marcel Dekker Inc.: New York, 2000.
13. Wang, T. T. *Ferroelectrics* **1982**, *41*, 213-223.
14. Lyons, B.J. *Radiat. Phys. Chem.* **1995**, *45*, 159-174.
15. Forsythe, J. S.; Hill, D. J. T. *Prog. Polym. Sci.* **2000**, *25*, 101-136.
16. Dargaville, T. R.; Celina, M.; Clough, R. L. *Radiat Phys Chem* **2006**, *75*, 432-442.
17. Clough, R. L. In *Encyclopedia of Polymer Science and Engineering*; John Wiley & Sons, Inc., 1988; Vol. 13, pp 667-708.
18. Dever, J. A.; Mccracken, C. A. *High Perform. Polym.* **2004**, *16*, 289-301.
19. French, R. H.; Wheland, R. C.; Qiu, W.; Lemon, M. F.; Zhang, E.; Gordon, J.; Petrov, V.; Cherstkov, V. F.; Delaygina, N. I. J. *Fluorine Chem.* **2003**, *122*, 63-80.
20. Tashiro, K. In *Ferroelectric Polymers*; Nalwa, H. S., Ed.; M. Dekkar, Inc.: New York, 1995.
21. Bharti, V.; Xu, H. S.; Shanthi, G.; Zhang, Q. M.; Liang, K. *J. Appl. Phys.* **2000**, *87*, 452-461.

Chapter 15

Pulse Radiolysis Study on Aqueous Solutions of Polysaccharide Derivatives

Seiichi Saiki[1], Yusa Muroya[2], Hisaaki Kudo[2], Yosuke Katsumura[1], Naotsugu Nagasawa[3], and Fumio Yoshii[3]

[1]Department of Nuclear Engineering and Management, School of Engineering, The University of Tokyo, Tokyo, Japan
[2]Nuclear Professional School, School of Engineering, The University of Tokyo, Tokyo, Japan
[3]Takasaki Advanced Radiation Research Institute, Japan Atomic Energy Agency, Takasaki, Japan

Irradiated polysaccharides generally degrades, but some kinds of polysaccharide derivatives in an aqueous solution, for example carboxymethyl cellulose/chitin/chitosan etc, become crosslinked and form hydrogels in the case of concentrated solution. By irradiating polymer solutions, polymer radicals are produced by the reaction of polymer chains with water decompositions, OH radical and hydrated electron etc, and then the crosslinking takes place by the reaction of polymer radicals with each other. To study the early process of the gelation of polysaccharide derivatives by ionizing irradiation, we evaluated the reactivity of the reaction of polymer chains with OH radical, hydrated electron and with inorganic, sulphate or carbonate radicals by pulse radiolysis technique.

 © 2008 American Chemical Society

Introduction

Recently pollution with unbiodegradable waste, for example a large amount of synthetic plastic consumed in a daily life, has become a problem. To use biodegradable materials is one means of reducing the environmental burden. One of biodegradable materials is polysaccharides, for example cellulose, chitin/chitosan, starch, alginate etc, and are expected as harmless materials for the environment. Especially, cellulose is famous as main component of plants and trees, and is the most abundant polysaccharide on earth. Structure of cellulose is described as a copolymer consisting of glucose units linked by β1-4 glycosidic bond. As fiber, pulp and wood, cellulose is applied for building materials, paper, clothes and many tools used in a daily life etc, and has been indispensable in a human life. Chitin is a main component of shell of crab and shrimp and is the second abundant natural polymer after cellulose. Structure of chitin is described as a copolymer consisting of glycosamine and N-acetylglucosamine units linked by β1-4 glycosidic bond. Chitosan is generally obtained by deacetylation of chitin. These polysaccharides have characteristics of biocompatibility and biodegradability, and chitin and chitosan have antimicrobial and antifungal activities*(1)*. Nowadays, with progress for modification technique of these polymer, cellulose, chitin and chitosan can have been applied for more fields, agriculture and pharmacy, biotechnology, biomedical materials etc*(2,3)*. For instance, cellulose and chitin have poor water-solubility and chitosan can be water-soluble only in an acidic solution, however carboxymethylated derivatives become water-soluble and have applied for cosmetics and food industry*(4)*. One of a modification method of polymers is a radiation technology. Not using a chemical, it is an advantage for the radiation technology that a harmful waste fluid doesn't come out from modifying process in the environment. The irradiation to polymers induces two effects for polymers. One is "scission", which lowers moleculer weight, and the other is "crosslinking" and "grafting" etc, which higher moleculer weight. Generally, it is known that the irradiation to polysaccharides of natural polymer induces chain scission reactions*(5,6,7)*. It has been reported that the irradiated chitosan and alginate have a better anti-bacterial activity than the unirradiated and that can have been applied as a plant growth promoter and as a protectant of plants. *(8,9,10,11)*

Recently, it has been reported that polysaccharide derivatives on a concentrated aqueous solution can be hydrogeled by ionizing irradiation. For instance, carboxymethyl cellulose*(12,13)*, hydroxypropyl cellulose*(14)*, hydroxypropylmethyl cellulose*(15)*, carboxymethyl chitin/chitosan*(16)*, and carboxymethyl starch*(17)*, and so on. These hydrogels consisiting of polysaccharides have also biodegradability as well as unirradiated, and some kinds of these hydrogels have various characteristics depending on a variety of

substituents. For instance, carboxymethyl chitosan hydrogel has antibacterial activity*(18)*.

Hydrogels are polymer networks crosslinked by hydrophilic polymer and can absorb water in their own structure. For their high water-absorbing property and good biocompatibility, applications of hydorgels have been studied on many fields, especially on biomedical field*(19,20,21,22)*. Radiation technology is advantageous for produce of hydrogels as biomedical material, because sterilization and crosslinking can take place simultaneously. Synthetic polymer hydrogel produced by radiation technology have been studied and applied for biomedical material*(23)*. The study concerning the radiation-induced crosslinking reaction of synthetic polymer such as poly (vinyl alcohol), poly (vinyl methyl ether), etc, have been reported*(24,25,26)*. In the case of polysaccharides, though the hydrogel property has been reported *(12,13,14,15,16,17)*, reports concerning the gelation mechanism of polysaccharides are a little*(27,28)*.

In this report, focusing to carboxymethyl chitin/chitosan and carboxymethyl cellulose, we studied the reactivity of water radiolysis products with polymer chains using the pulse radiolysis method as the first step to clarify early gelation process of polymer radicals related to crosslinking.

Experimental

Materials

Carboxymethyl chitin/chitosan was obtained from the Kouyou Chemical Co., and carboxymethyl cellulose was obtained from the Daicel industry Co. Structures of two repeating units of these polysaccharide derivatives are shown in *Figure 1* (carboxymethyl chitin/chitosan (left), carboxymethyl cellulose (right)). As the important indicator of polymer property, DS and DDA are showed on Table I. DS shows the average degree of substitution per one monomer unit. The upper bound of DS of carboxymethyl chitin/chitosan is 2, and of carboxymethyl cellulose is 3. DDA means the degree of deacetylation of carboxymethyl chitin/chitosan and shows average percentage amino group substituted for acetyl group of one polymer chain.

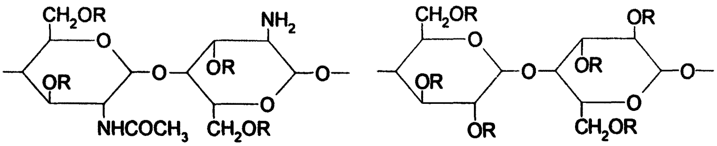

Figure 1. Structure of carboxymethyl chitin/chitosan (left)and carboxymethyl cellulose (right)

Table I. Property of polysaccharide derivatives

Polymer	*DS*	*DDA*
Carboxymethyl chitin	0.64	26.8
Carboxymethyl chitosan	0.54	61.8
Carboxymethyl cellulose	2.2	-

Note : Units of DDA is percent (%)

Pulse Radiolysis

Pulse radiolysis system is showed in *Figure 2.* Electron beam is from S Band LINAC (Energy 35MeV and pulse width 10 ns, Nuclear Professional School, School of Engineering, The University of Tokyo, Japan possesses) and Xe lamp is used as analysis light. The intensity of transmitted light was converted into an electric signal with the PIN-photodiode, and data processing of the absorbance was done by PC. The quartz cell of 2cm in the optical path length was used for the sample cell. The absorbance defined as equation (1). The value is determined from the ratio of the intensity of transmitted light to incident light, and is proportional to the concentration of solute absorbing light at measured wavelength. By following the decay of the absorbance, kinetics of intermediates can be measured.

$$Absorbance \equiv \log(I_0/I) = \varepsilon c \ell \quad (1)$$

I_0 : intensity of incident light I : intensity of transmitted light
ε : absorption coefficient [$M^{-1}s^{-1}$] c : concentration of solute absorbing light [M]
ℓ : optical path length [cm]

In this experiment, the rate constants of the reactions of hydrated electron and OH radical, generated by irradiation to water, with polymer chains were measured by the pulse radiolysis method. The rate constants could be related to the generation rate of polymer radicals which are involved in crosslinking reaction.

In addition, the rate constants of the reactions of inorganic radical, sulphate radical and carbonate radical, with polymer chains were also measured. Sulphate radical is generated from $K_2S_2O_8$, and carbonate radical is from Na_2CO_3 or $NaHCO_3$. It has been reported that hydrogels generated under the presence of inorganic radicals have different character*(29)*and inorganic radicals attack a specific part of the sugar chain unit*(30)*, so it is interesting from physical properties viewpoint and fundamental science viewpoint to irradiate a polymer solution under inorganic solute existence. At the experiments about inorganic radical, the pH of the solutions was adjusted with $HClO_4$ and NaOH. The

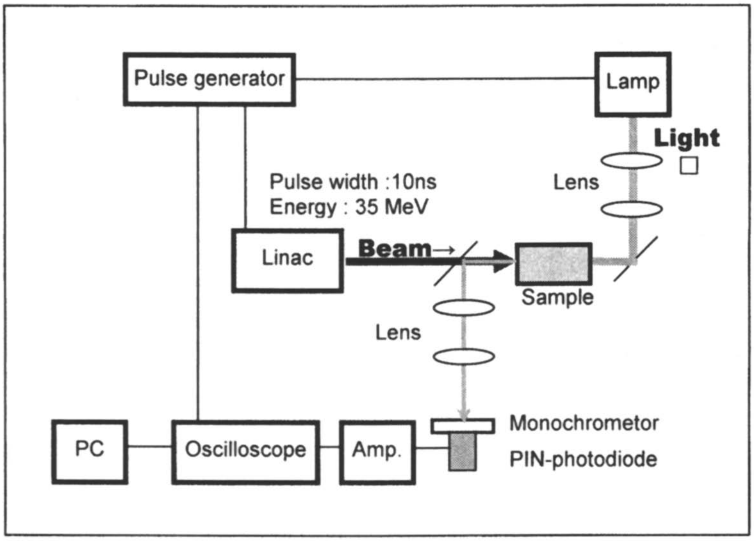

Figure 2. Pulse radiolysis system

radicals generated by irradiation and the ion dissociated from $HClO_4$ and NaOH don't influence measurement data and the absorbance.

Results and Discussion

When polymer solution is irradiated, water chiefly absorbs the energy of the radiation, and water decomposition, which is hydrated electron, OH radical, and hydrogen atom, proton, etc, are generated in the solution[reaction (2)]. These radicals having a high reactivity cause various chemical reactions in the solution.

In a polymer solution, it is assumed that the radicals such as hydrated electron and OH radical produce some polymer radicals which cause crosslinking reactions[reaction (3)(4)].

$$H_2O \xrightarrow[\text{radiation}]{\text{ionizing}} e^-_{aq}, {}^\bullet OH, {}^\bullet H, H^+, OH^-, H_2O_2, etc \qquad (2)$$

$$e^-_{aq}, {}^\bullet OH, etc + polymer \rightarrow polymer^\bullet + products \qquad (3)$$

$$polymer^\bullet + polymer^\bullet \rightarrow crosslinked \quad polymer \qquad (4)$$

Rate Constants of the Reaction of the Radicals of Water Decomposition with Polymer Chains

Hydrated electron

Evaluating the reactivity of hydrated electron with polymer chains[reaction (5)], it is necessary to reduce the effect of the reaction of OH radical. So, *tert*-butanol was added to a polymer solution as scavenger of OH radical[reaction (6)]. *Tert*-butanol radical produced by reaction (6) doesn't influence chemical reactions and absorbance data. Experiments were carried out under argon saturation for removal of oxygen, because oxygen reacts with hydrated electron and hydrated electron diminishes rapidly [reaction (7)].

Figure 3 is the result of pulse radiolysis experiment about the reaction of hydrated electron with polymer chains(0 or 30 mM carboxymethyl chitosan solution with 0.3 M *tert*-butanol under Ar saturation), and shows the decay of the absorbance as a function of time. This absorbance was measured at wavelength 720 nm, which is the absorption peak of hydrated electron. As seen in *Figure 3*, the absorbance increases immediately after the irradiation, and attenuates afterwards. This means that hydrated electron is generated immediately after irradiation and diminishes gradually by some reactions of hydrated electron. Compared the absorbance decay of polymer solution with the decay of solution without polymer, the decay of polymer solution is faster than without polymer, so it is obvious that hydrated electron reacts with polymer chains. The decay curve can be fitted by pseudo first-order decay. The pseudo first-order decay is shown by equation (8). From estimating the slope of the pseudo first-order decay rate of the absorbance at 720 nm against polymer concentration, the rate constant of the reaction of hydrated electron with polymer chains can be calculated (*Figure 4*). The rate constants of the reaction of hydrated electron with CM-chitin and CM-chitosan was determined as 1.1×10^7 and $1.4 \times 10^7 [M^{-1}s^{-1}]$. These values are almost the same with the value of carboxymethyl cellulose*(28)*.

$$e_{aq}^{-} + polymer \rightarrow polymer^{\bullet} + products \tag{5}$$

$$^{\bullet}OH + tert\text{BuOH} \rightarrow OH^{-} + tert\text{BuOH}^{\bullet} \tag{6}$$

$$e_{aq}^{-} + O_2 \rightarrow O^{\bullet -} + O^{2-} \tag{7}$$

$$[A] = [A]_0 \cdot e^{-k[B]t} \tag{8}$$

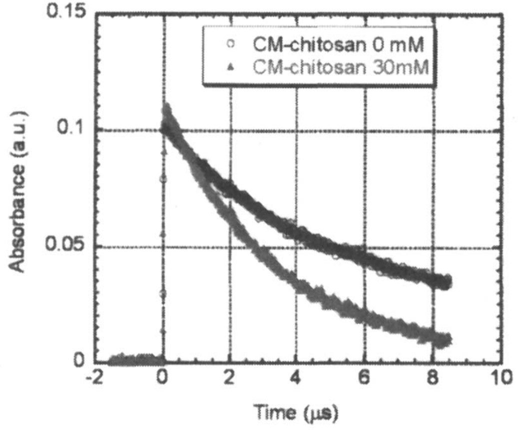

Figure 3. Time profile of the absorbance at 720 nm.

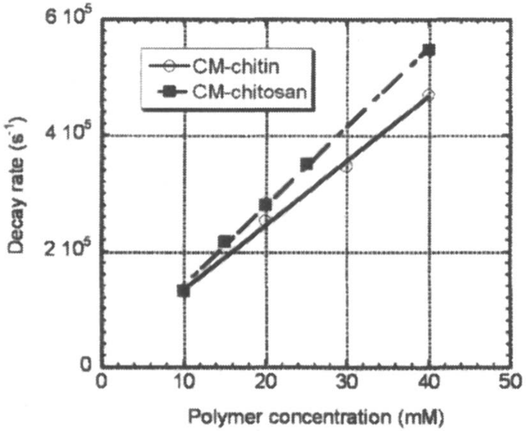

Figure 4. Plot of the pseudo first-order decay rate of hydrated electron against polymer concentration.

In Polymer Durability and Radiation Effects; Celina, M., et al.;
ACS Symposium Series; American Chemical Society: Washington, DC, 2007.

OH radical

The experiments evaluating the reactivity of the reaction of OH radical with polymer chains were performed under N_2O saturation for reducing the influence of hydrated electron and oxygen. N_2O reacts with hydrated electron and produces OH radical[reaction (9)]. To measure the rate constants of OH radical with polymer chains, a competition method is suitable. An absorption peak of OH radical is at UV region and the absorption coefficient is very low, so it is difficult to observe OH radical directly. In this experiment, KSCN and KI were used as a competitor scavenger. OH radical reacts with SCN^- or I^- and generates $(SCN)_2^{\bullet -}$ or $(I)_2^{\bullet -}$, which has a strong absorbtion peak at wavelength 472 nm and 380 nm [reaction (10)(11) and (12)(13)]. Irradiating the polymer solution under KSCN or KI existence, OH radical reacts with both polymer chains and a competitor scavenger. Reaction (15) shows the equation between the change of the absorbance of $(SCN)_2^{\bullet -}$ or $(I)_2^{\bullet -}$ and the ratio of both reaction rates. *A* means the absorbance of $(SCN)_2^{\bullet -}$ at 472 nm or $(I)_2^{\bullet -}$ at 380 nm of the polymer solution, and A_0 means the absorbance of the solution without polymer. Concentration of scavenger was fixed at 2 mM, and the rate constant of the reaction of OH radical with $SCN^{\bullet}$ and $I^{\bullet}$ are both $1.1 \times 10^{10} [M^{-1}s^{-1}]$*(31)*. So, measuring the change of the absorbance of $(SCN)_2^{\bullet -}$ or $(I)_2^{\bullet -}$, the rate constant of the reaction of OH radical with polymer chains can be calculated from equation (15).

Figure 5 shows time profile of absorabance at 472 nm by pulse radiolysis (0 or 30mM carboxymethyl chitosan solution with 2 mM KSCN under N_2O saturation). As seen in *Figure 5*, the absorbance without polymer is obviously lower than a polymer solution. So, it was confirmed that OH radical reacts with polymer chains. *Figure 6* shows the relation between the change of the absorbance of $(SCN)_2^{\bullet -}$ or $(I)_2^{\bullet -}$ and the ratio of both reaction rate. The slope of the plot means the rate constants of the reaction of OH radical with polymer chains. The vertical axis is left-term of equation (15) and the horizontal axis is right-term of equation (15) except for $k_{OH+polymer}$. From the slope, the rate constants of the reaction of OH radical with CM-chitin and CM-chitosan was determined as 1.4×10^9 and $1.7 \times 10^9 [M^{-1}s^{-1}]$ using KSCN and as 9.3×10^8 and $1.1 \times 10^9 [M^{-1}s^{-1}]$ using KI. Compared the rate constants of the reaction of hydrated electron and OH radical, the value of OH radical is almost 100 times as high as that of hydrated electron. The rate constants using KSCN is higher than using KI in both case of CM-chitin and CM-chitosan. This is assumed that SCN^- accumulates around $-NH_3^+$, amino group.

$$e_{aq}^- + N_2O \xrightarrow{H_2O} {}^{\bullet}OH + OH^- + N_2 \qquad (9)$$

$$^{\bullet}OH + SCN^{-} \rightarrow OH^{-} + SCN^{\bullet} \quad (10)$$

$$SCN^{\bullet} + SCN^{-} \rightarrow (SCN)_2^{\bullet -} \quad (11)$$

$$^{\bullet}OH + I^{-} \rightarrow OH^{-} + I^{\bullet} \quad (12)$$

$$I^{\bullet} + I^{-} \rightarrow (I)_2^{\bullet -} \quad (13)$$

$$^{\bullet}OH + polymer \rightarrow OH^{-} + polymer^{\bullet} \quad (14)$$

$$\frac{A_0}{A_1} - 1 = \frac{k_{OH+polymer} \times [polymer]}{k_{OH+scavenger} \times [scavenger]} \quad (15)$$

Rate Constants of the Reaction of Inorganic Radical with Polymer Chains

Sulphate radical

Sulphate radicals are produced by the reaction of sulphate acid ion with hydrated electron and hydrogen atom[reaction (16)(17)]. From the yields of water decomposition, most of sulphate radicals are produced by reaction (16). Sulphate radical have an absorption peak at 455 nm and the absorption coefficient is high(16000[$M^{-1}cm^{-1}$] *(32)*), so we can measure an absorbance decay of sulphate radical directly. The absorbance at 455 nm decays following by pseudo first-order and the decay is faster under higher concentration. So, we confirmed the reaction of sulphate radical with polymer chains[reaction (18)]. The rate constants of the reaction of sulphate radical with polymer chains were calculated from estimating the slope of the pseudo first-order decay rate of the absorbance at 455 nm against polymer concentration as well as the case of hydrated electron. As seen in ***Figure** 7*, the rate constants with CM-chitin and CM-chitosan, CM-cellulose at natural pH are 4.8×10^7(pH 8.8), 9.0×10^7(pH 9.3) and 1.7×10^7(pH 5.4) [$M^{-1}s^{-1}$]. These values are lower than that of OH radical. It shows that OH radical is more oxidative than sulphate radical.

This experiment was done at various pH, but at lower pH than 6, CM-chitin and CM-chitosan solutions become white-clouded and were unable to be

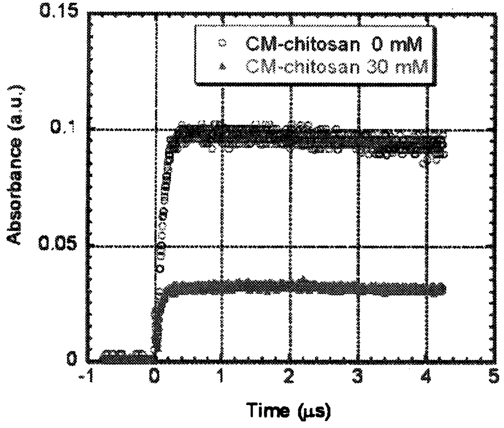

Figure 5. Time profile of the absorbance at 472 nm.

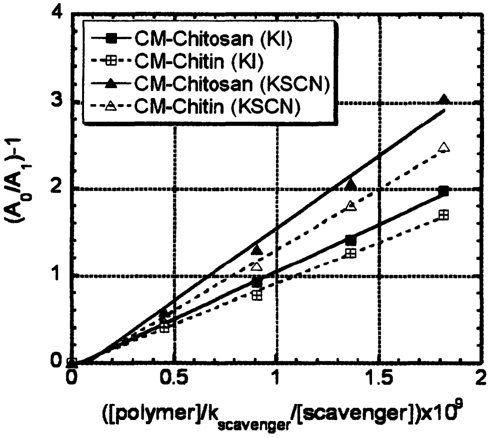

Figure 6. Competition kinetics of polymer and SCN^-, I^- by reaction with OH.

measured because light doesn't transmit through the sample cell. It can be assumed that $-NH_3^+$ and $-COO^-$ are coexistent at less than pH 6 and polymer aggregates in the solution. The reactivity of sulphate radical with polymer chains have little pH dependency because the rate constants are almost constant at every pH solution measuring the data. At around pH 11, the rate constants are a little lower. It can be thought that this is because of the influence of the reaction of sulphate radical with OH^-.

$$e_{aq}^- + S_2O_8^- \rightarrow SO_4^{\bullet-} + SO_4^{2-} \quad (16)$$

$$^\bullet H + S_2O_8^- \rightarrow SO_4^{\bullet-} + HSO_4^- \quad (17)$$

$$SO_4^{\bullet-} + polymer \rightarrow HSO_4^- + polymer^\bullet \quad (18)$$

Carbonate radical

Carbonate radical is generated by the reaction of OH radical with carbonate ion and bicarbonate ion [reaction (19)(20)], so this experiment was done under N_2O saturation[reaction (9)]. Carbonate radical has an absorption peak at 600 nm. As well as hydrated electron and sulphate radical, the rate constant of the reaction of carbonate radical with polymer chains[reaction (21)] can be calculated from estimating the slope of the pseudo first-order decay rate of the absorbance at 600 nm against polymer concentration. Then, the rate constants with CM-chitin and CM-chitosan, CM-cellulose were determined as $(3.9\sim6.4)\times10^5[M^{-1}s^{-1}]$(*Figure 8*). These values are lower than the value of OH radical and sulphate radical, and so this shows carbonate radical is less oxidative than OH radical and sulphate radical. Focusing the rate constants of CM-chitosan, the value at around pH 9.5 is lower than over pH 10. This is because of pKa of amino group, protonation and unprotonation. For a weak reactivity of carbonate radicals, it can be assumed that carbonate radical have a selectivity attacking polymer chains.

$$^\bullet OH + HCO_3^- \rightarrow CO_3^{\bullet-} + H_2O \quad (19)$$

$$^\bullet OH + CO_3^{2-} \rightarrow CO_3^{\bullet-} + OH^- \quad (20)$$

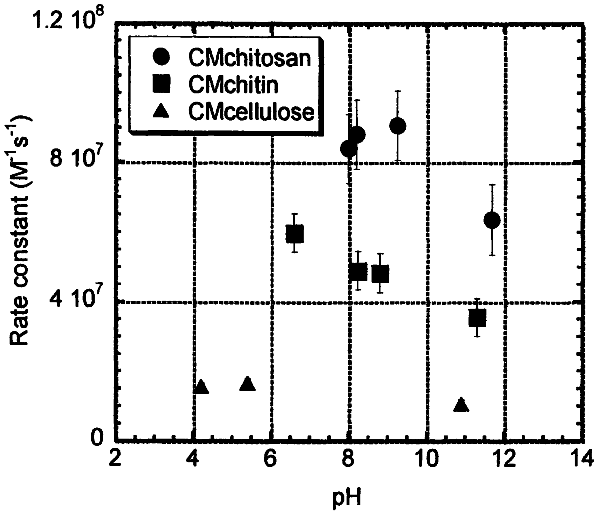

Figure 7. Rate constants of the reaction of sulphate radical with polymer chains.

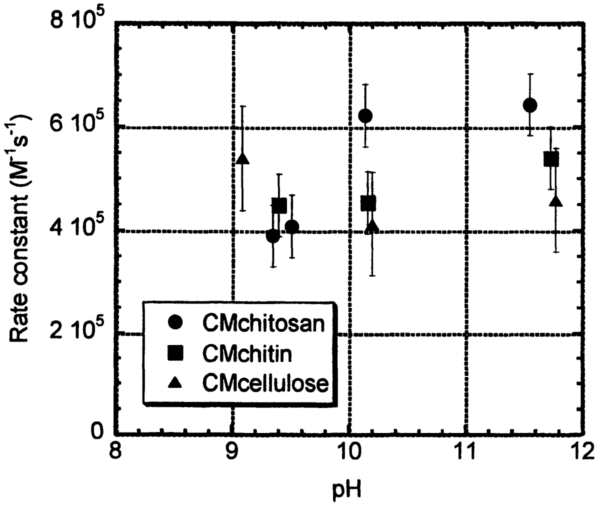

Figure 8. Rate constants of the reaction of carbonate radical with polymer chains.

$$CO_3^{\bullet -} + polymer \rightarrow HCO_3^- + polymer^\bullet \qquad (21)$$

Conclusions

We confirmed that OH radical and hydrated electron, water decomposition, sulphate radical and carbonate radical, inorganic radical, attack carboxymethyl chitin / chitosan and CM-cellulose. OH radical at a rate constant of $1.4x10^9$ and $1.7x10^9[M^{-1}s^{-1}]$ using KSCN and $9.3x10^8$ and $1.1x10^9[M^{-1}s^{-1}]$ using KI, and hydrated electron at a rate constant of $1.1x10^7$ and $1.4x10^7[M^{-1}s^{-1}]$ reacts with CM-chitin and CM-chitosan. The rate constant of OH radical is about 100 times as high as that of hydrated electron.

Sulphate and carbonate radical attack polymer chains at a lower rate than OH radical. The rate constants of sulphate radical with CM-chitin, CM-chitosan and CM-cellulose are (3.5□6.0)$x10^7$, (6.3□9.0)$x10^7$ and (1.1□1.7)$x10^7[M^{-1}s^{-1}]$, and of carbonate radical are (4.5 □ 5.4)$x10^5$, (3.9 □ 6.4)$x10^5$ and (4.1 □ 5.4)$x10^5[M^{-1}s^{-1}]$. The reactivity of sulphate radical doesn't depend on pH, but the rate constant of carbonate radical with CM-chitosan is a little lower at pH 9.5 than over pH 10. It can be assumed that carbonate radical have a selectivity attacking polymer chains because of a weak reactivity and that the reactivity is also influenced by the conditions of substituents(amino group), protonation or unprotonation.

References

1. Liu, X. F.; Guan, Y. L.; Yang, D. Z.; Li, Z.; Yao, K. D. *J. Appl. Polym. Sci.* **2001**, *79*, 1324-1335.
2. Saiki, I.; Watanabe, K.; Tokura, S.; Azuma, I. *Chitin Derivatives in Life Science*, 1992, 20-26.
3. Koide, S. S. *Nutrition Research* **1998**, *18(6)*, 1091-1101.
4. Olaru, N.; Olaru, L.; Stoleriu, A.; Timpu, D. *J. Appl. Polym. Sci.* **1998**, *67*, 481-486.
5. Charlesby, A. *J. Polym. Sci.* **1955**, *15*, 263-270.
6. *CRC Handbook of Radiation Chemistry* Tabata, Y.; Ito, S.; Tagawa, S. Eds., CRC Press, Boca Raton, FL, 1991, pp XIV 742, Table XIV. 15.
7. Leonhardt, J.; Arnold, G.; Baer, M.; Langguth, H.; Gey, M.; Huebert, S. *Radiat. Phys. Chem.* **1985**, *25*, 887-892.
8. Matsuhashi, S.; Kume, T. *J. Sci. Food Agric.* **1997**, *73*, 237-241.
9. Hien, N. Q.; Nagasawa, N.; Tham, L. X.; Yoshii, F.; Dong, V. H.; Mitomo, H.; Makuuchi, K.; Kume, T. *Radiat. Phys. Chem.* **2000**, *59*, 97-101.

10. Kume, T.; Takehisa, M. *Effect of gamma-irradiation on chitosan. Proc. 2nd. Int. Conf. on Chitin/Chitosan,* Sapporo, Japan, 1982, pp 66-70.
11. Tham, L. X.; Nagasawa, N.; Matsuhashi, S.; Ishioka, N. S.; Ito, T.; Kume, T. *Radiat. Phys. Chem.* **2001**, *61*, 171-175.
12. Fei, B.; Wach, R. A.; Mitomo, H.; Yoshii, F.; Kume, T. *J. Appl. Polym. Sci.* **2000**, *78*, 278-283.
13. Wach, R. A.; Mitomo, H.; Yoshii, F.; Kume, T. *J. Appl. Polym. Sci.* **2001**, *81*, 3030-3037.
14. Wach, R.A.; Mitomo, H.; Yoshii, F.; Kume, T. *Macromol. Mater. Eng.* **2002**, *287*, 285-295.
15. Pekel, N.; Yoshii, F.; Kume, T.; Guven, O. *Carbohydrate Polymers* **2004**, *55*, 139-147.
16. Zhao, L.; Mitomo, H.; Nagasawa, N.; Yoshii, F.; Kume, T. *Carbohydrate Polymers* **2003**, *51*, 169-175.
17. Nagasawa, N.; Yagi, T.; Kume, T.; Yoshii, F. *Carbohydrate Polymers* **2004**, *58,* 109-113.
18. Yoshii,F.; Zhao, L.; Wach, R. A.; Nagasawa, N.; Mitomo, H.; Kume, T. *Nucl. Instr. Meth. Phys. Res. B.* **2003**, *208*, 320-324.
19. Kaetsu, I. *Radiat. Phys. Chem* **1981**, *18*, 343-356.
20. Peppas, N. A. *Hydrogels in Medicine and Pharmacy* CRC Press: Boca Raton, FL, 1986.
21. Rosiak, J. .M.; Ulanski, P.; Rzeznicki, A. *Nucl. Instr. Meth. Phys. Res. B* **1995**, *105*, 335-339.
22. Rosiak, J. M.; Ulanski, P.; Pajewski, L. A.; Yoshii, F.; Makuuchi, K. *Radiat. Phys. Chem.* **1995,** *46*, 161-168.
23. Rosiak, J. M.; Yoshii, F. *Nucl. Instr. Meth. Phys. Res. B* **1999**, *151*, 56-64.
24. Janik, I.; Rosiak, J. M. *Radiat. Phys. Chem.* **2002**, *63*, 529-532.
25. Ulanski, P.; Bothe, E.; Rosiak, J. M.; von Sonntag, C. *Macromol. Chem. Phys.* **1994**, *195*, 1443-1461.
26. Janik, I.; Kasprzak, E.; Al-Zier, A.; Rosiak, J. M. *Nucl. Instr. Meth. Phys. Res. B* **2003**, *208*, 374-379.
27. Wach, R. A.; Mitomo, H.; Nagasawa, N.; Yoshii, F. *Radiat. Phys. Chem.* **2003**, *68*, 771-779.
28. Wach, R. A.; Kudoh, H.; Zhai, M.; Nagasawa, N.; Muroya, Y.; Yoshii, F.; Katsumura, Y. *Polyme* **2004**, *45*, 8165-8171.
29. Kaplan, H.; Guner, A. *J. Appl. Polym. Sci.* **2000**, *78*, 994-1000.
30. Al-Assaf, S.; Navaratnam, S.; Parsons,B. J.; Phillips, G. O. *Free Radical Biology & Medicine.* **2006**, *40*, 2018-2027.
31. Buxton, G. V.; Greenstock, C. L.; Helman, W. P.; Ross, A. B. *J. Phys. Chem. Ref. Data* **1988**, *17*, 513-886.
32. Chawla, O. P.; Fessenden, R. W. *J. Phys. Chem.* **1975**, *79*, 2693-2700.

Chapter 16

Specialized Light Curing Resin Systems for Fabrication of Inflatable Rigidizable Structures

Andrea E. Hoyt Haight, Larry A. Harrah, and Ronald E. Allred

Adherent Technologies, Inc., 11208 Cochiti SE, Albuquerque, NM 87123

Inflatable structures that become rigid after reaching the required shape are a promising approach various structures including large space-deployed craft, such as antennas and solar sails and unmanned aerial vehicles (UAVs). A need exists for a controlled, clean rigidization technology to harden inflatable spacecraft after they have achieved the required shape. Adherent Technologies is addressing that need through the development of a family of radiation (ultraviolet [UV] and visible light) curable resins for structural composite matrices termed Ridigization on Command™ (ROC). These resins are being formulated to cure in low-temperature conditions with varying kinetics at low power inputs with various illumination schemes.

Introduction

Over the past ten years, Adherent Technologies, Inc. has been extensively involved in the development of light curing materials for inflatable space structures. These structures cover a wide range of sizes, from small wing structures for unmanned aerial vehicles (UAVs) for defense applications to huge support structures (~25-meter diameter) for space-based communications satellites. Within these various application scenarios are a wide range of cure requirements. For example, wings for UAVs need to exhibit a "snap cure", curing within a few seconds of exposure to the initiating light, whereas the

 © 2008 American Chemical Society

support structure application cure rate is less critical, but lower temperatures are likely to be encountered. Additional requirements relating to strucutral weight and power required must also be considered.

During the course of these programs, Adherent Technologies has investigated two primary classes of resins for these applications. These include photoinitiated cationic curing epoxy resins, which feature a "living polymerization" as well as fast curing free-radical resin formulations. Regardless of the application scenario, a thorough understanding of these systems and the ability to predict their cure behavior under a variety of conditions is required if they are to find any real applications in space or military applications.

This paper discusses our analyses of two such specialized resin systems and the development of models that will allow us to predict the time required to cure given a particular set of light intensity and temperature conditions.

Experimental Methods

Kinetics Experiments

Data for kinetics modeling was collected using a Perkin-Elmer Diamond Differential Scanning Calorimeter (DSC). Two slightly different experimental configurations were used, depending upon the resin system under consideration.

Cationic Epoxy Resin Systems

For the cationic epoxy resin systems, exposure of the resin to light from blue (470nm) and green (530nm) LEDs was required. The choice between these LEDs depended upon the sensitizer dye selected for activation. To cure the samples in the DSC cell, a Teflon holder was made for the two pairs of blue and green LEDs that would be placed over both the sample and the reference sides of the DSC head (Figure 1). The blue/green LED wires were hooked up to a dc power supply that would allow us to set the output as current limiting. A visible light intensity meter (UVP Multi-Sense® MS-100 Meter with MS-155 Visible Light Probe) was used to match the intensity of the LED illumination in the DSC cell as closely as possible with that to be employed in the final application.

Two different types of DSC kinetics experiments were then conducted, one to evaluate the effects of system temperature, and the other to evaluate the effect of light intensity on the cure behavior; light intensity was adjusted by changing the settings on the light source power supply.

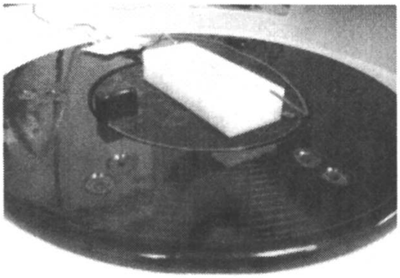

Figure 1. DSC sample head with LEDs mounted in Teflon support block.

Free Radical Resin Systems

The cure of the free radical resin systems was conducted using high intensity UV LEDs. To ensure safety of the analysis system and to improve reproducibility of the data, our DSC system was modified further with respect to the experiments described above. Ideally, the modified system would be flexible to evaluation of many different light sources (1), and such that the light sources could be positioned reproducibly relative to the sample pans in the instrument (2).

The system was modified to accommodate a dual light guide system. The light guides selected were 5-mm diameter liquid light guides. The large diameter ensures that the sample received the highest possible intensity and the liquid filler eliminated any orientation effects that might observed with optical fiber light guides. The modified system is shown in Figure 2.

Experiments were again conducted to look at the temperature dependence of the cure rate for these systems. The primary light source employed for these experiments was a Nichia NCCU001E high power (100mW) UV LED with an emission maximum at 380nm.

(a) (b)

Figure 2. Modification of differential scanning calorimeter for photocure kinetics analysis. (a) Dual light guides inserted through instrument cover and (b) light guide output into sample compartment

Polymerization Reaction Mechanism Kinetics and Modeling

The polymerization reactions induced by light activation are appropriate for resin curing in a large variety of applications in a great span of environments. For this reason it is of major importance that prediction of their behavior in this variety of application be possible and accurate. We have examined the kinetics of these curing reactions and have attempted to predictively model their behavior. In our studies we examined two quite different initiation and curing reactions: cationicaly cured epoxy formulations and free radical curing acrylates. In both cases we have directed our attention to the photochemical initiation of the curing reaction.

Mechanistically these two cases are quite different. For cationically cured epoxies, the initiator moiety (cation) cannot directly terminate the cure propagation but species created *in association* with the initiation step (anions) may carry the seeds of the termination process. For free radical initiation and propagation cures, the initiator can also function as a chain terminator. Thus the kinetics and mechanisms in the two case are quite different. We will discuss the two cases separately.

Cationic Curing Mechanisms and Modeling

In our studies we have used diaryliodonium salts of the non-covalently bonding anion, hexafluoroantimonate, as photo-activator. The photoactivation of these salts leads to the dissociation of the diaryliodonium cation into aryl radicals and an iodoaryl radical ion, the initial cationic initiator moiety. These salts absorb light only below about 380nm with strong absorption occurring only below 340nm. In order for these materials to be used at more accessible wavelengths, a sensitizer dye is added. The photo-excited form of this dye transfers its excitation energy to the diaryliodonium cation, eventually resulting in the generation of the initiator moiety similar to that achieved from direct photo-excitation of the diaryliodonium salt. The efficiency of this sensitization process suggests that it is not a direct energy transfer process from the dye singlet excited state (typically with a lifetime less that 3 nanoseconds) but may involve the substantially longer lived triplet followed by energy or charge transfer to the iodonium. Singlet excitation transfer would require proximity of the acceptor molecule within the donor lifetime, not a likely process in a diffusion controlled environment such as might be expected in a relatively viscous resin system. Nevertheless, the production of the initiator moiety following the absorption of light is expected to be fast compared to the chemical processes that follow.

Following photochemical production of the initiator moiety from the iodonium salt, sequential reaction with monomer moieties proceeds until exhaustion of available monomer. This "living" polymerization process should be characterized by the following expressions:

Initiation
$$\frac{\partial C_{ch}}{\partial t} = k_I \cdot I \cdot C_{ep} \quad (1)$$

Propagation
$$-\frac{\partial C_{ep}}{\partial t} = k_p C_{ep} \int_0^t k_I \cdot I \cdot C_{ep} \partial t \quad (2)$$

where C_{ep} is the concentration of polymerizable groups, C_{ch} is the concentration of propagating chains, I is the light intensity, k_I is the initiation rate constant and k_P is the chain propagation rate constant. k_I contains the quantum efficiency for active species formation and thus will depend upon excitation light wavelength and temperature as well as the concentration of both activator and sensitizer. For our experiments, activator and sensitizer concentrations were held constant.

In our calculations, we used finite difference estimation to model the shapes of the polymerization exotherms. We assumed that the temperature variation is primarily a result of the diffusion limited nature of both the initiation and propagation processes with an activation energy of roughly 42kJ/mole. Since both the initiation and propagation reactions would be expected to result in the same exotherm per reaction step, no distinction was made between their effect. Thus the calculated exotherm is a relative quantity. k_i and k_p were used as relative quantities to obtain these curves and absolute values were not derived. The photochemical step in initiation was calculated based upon the measured light intensity and the fraction of light absorbed in our sample thickness; a quantum efficiency of roughly 0.5 was assumed for the creation of the initiator specie from the absorbed light. Agreement between the calculation and experiment was judged based upon the ability to reproduce the shapes, light intensity behavior and reaction progression with variation in temperature.

In these studies, the reactions were followed using Differential Scanning Calorimetry (DSC) to measure the reaction exotherm. From data obtained in our experiments, we estimate that the response time of our instrument is roughly 3-4 seconds with our average sample weight (depending of course, on sample weight, density and thermal conductivity). Most of our studies were using sampling rates of 1 second.

Using these equations, we calculated typical DSC curves expected for several temperatures. The calculated curves are shown in Figure 3 below.

The variation with time at the various effective temperatures agrees well with our experimental observations. Our experimental data gave a mean thermal activation energy of 37.95 ± 2.27 kJ/Mole for polymerization. The model also predicts well the dependence on initiating light intensity. As can be seen from Equation (2) above, the dependence on light intensity is predicted to be linear. Figure 4 shows the experimental result of varying light intensity at constant temperature.

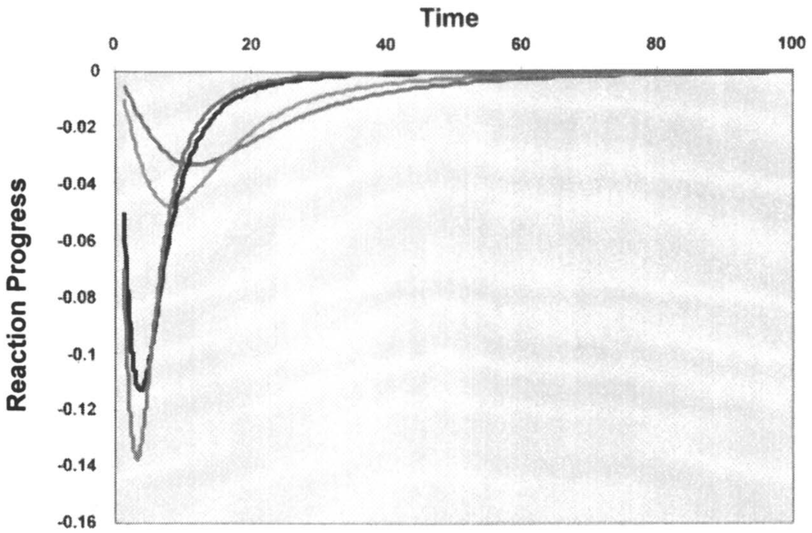

Figure 3. Calculated DSC curves using the simple living polymer model at several temperatures.

In Figure 4 above, a small feature is observed in the experimental data near the onset of reaction. The magnitude of this feature varied from run to run and is attributed to two factors, unbalance between illumination on the sample and reference pans in the DSC and an exotherm associated with the initiator production reaction between the sensitizer and activator. It is not very reproducable but is most probably an extremely fast reaction temporally unresolved by the instrumentation.

Note that there is generally excellent agreement between the experimental data of Figure 4 and shapes of the calculated curves shown in Figure 3. Consequently, this model does afford a reliable predictive tool for this particular photoinitiated cationic epoxy system. The general applicability of the model to other cationic epoxy formulations has not yet been verified.

Free Radical Curing Mechanisms

The free radical cure of acrylate resins is expected to be far more mechanistically complex than the cationic case described above since the free radical initiator can also function as a chain terminator in the system. It can also recombine to give the original activator structure. Furthermore, each of these reactions will give different size exotherms per reaction unit. For example, the formation of a single carbon-carbon bond from radical recombination gives an

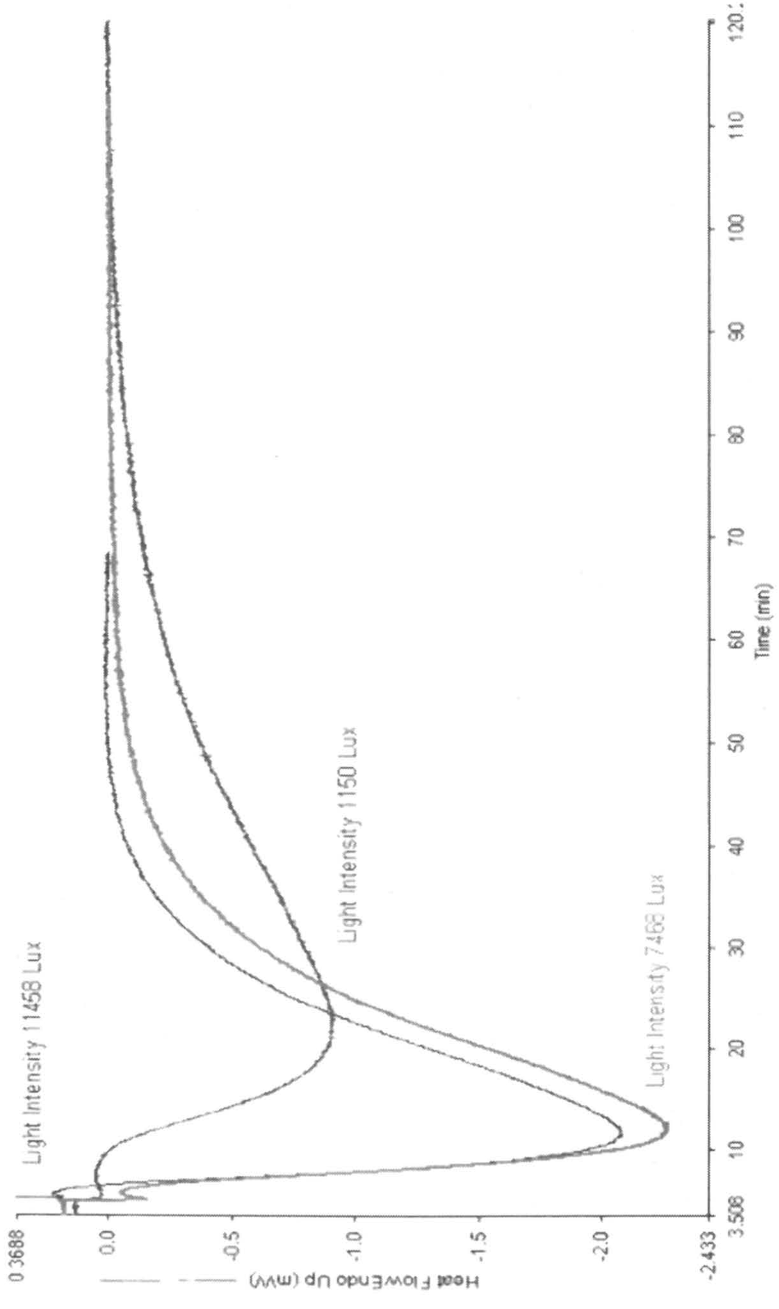

***Figure 4**. Light intensity effects on reaction exotherm at constant temperature and wavelength.*

exotherm of approximately 245 kJ/mole, radical addition to a carbon-carbon double bond about 72 kJ/mole. Propagation would release then approximately 72 kJ/mole while termination gives 245 kJ/mole. Initiator recombination should also result in 245 kJ/mole. We note that in the initial production of radical initiators, the 245 kJ/mole is supplied by the initiating photon.

Our application in an inflatable wing required a very fast, "snap" cure. Therefore, our resins were formulated from urethane based polyacrylates for their known fast curing rates (*1*). These resins are internally hydrogen bonded giving a prepatterned distribution of reactive moieties which may require little or no diffusion (either translational or rotational) to place them in a reactive orientation. This factor does result in much faster propagation and a tendency for formation of isotactic triads (*2*). In addition to using this general resin family, a significant portion of multifunctional resin base (hexafunctional) was employed. The presence of several reactive moieties on each resin molecule further complicates any mechanism of propagation between chains or intrachain. In simple hydrogen bonded acrylates, a phenomenon known as the "gel effect" results in an apparent acceleration of chain propagation as the chain length increases (2,*3*). The "gel effect" has been attributed to inhibition of chain recombination as the chains lengthen. This effect has not been specifically reported in these more complex polacrylates but may well be present in our systems. Our experiments utilized activators derived from aromatic ketones which are cleaved photochemically and absorb in the near UV portion of the spectrum.

As expected, the reaction exothems from our experiments with polyfunctional urethane acrylate systems are much more complex than those found with the cationic epoxy polymerizations. Figure 5 shows results from our aliphatic triacrylate DSC runs at three temperatures under continuous illumination.

The kinetic complexity of the system is evident. At the two higher temperatures, the exotherm consists of two, and perhaps more processes in the total exotherm, while at the lower temperature only one peak is evident. The initial peak is moving to longer times as the temperature is lowered and most probably the longer time peak is shifting slightly and becoming broader. It is likely that the two (or more) processes are coalescing at the low temperature. It is significant that the center of the exotherm is not apparently affected by temperature.

In hopes of isolating the several phenomena involved, we carried out a "flash" excitation by illuminating for only 5 seconds and comparing that result to continuous illumination. The result of this experiment is shown in Figure 6.

Surprisingly the two methods of excitation gave very similar results. The slight shift in start times are most probably the result of timing error in hand starting the exposures at 1 minute. The rise times for the first process are nearly identical but the overall width and exotherm is greater for the continuous illumination. These data suggest that the 5 second illumination is sufficient to

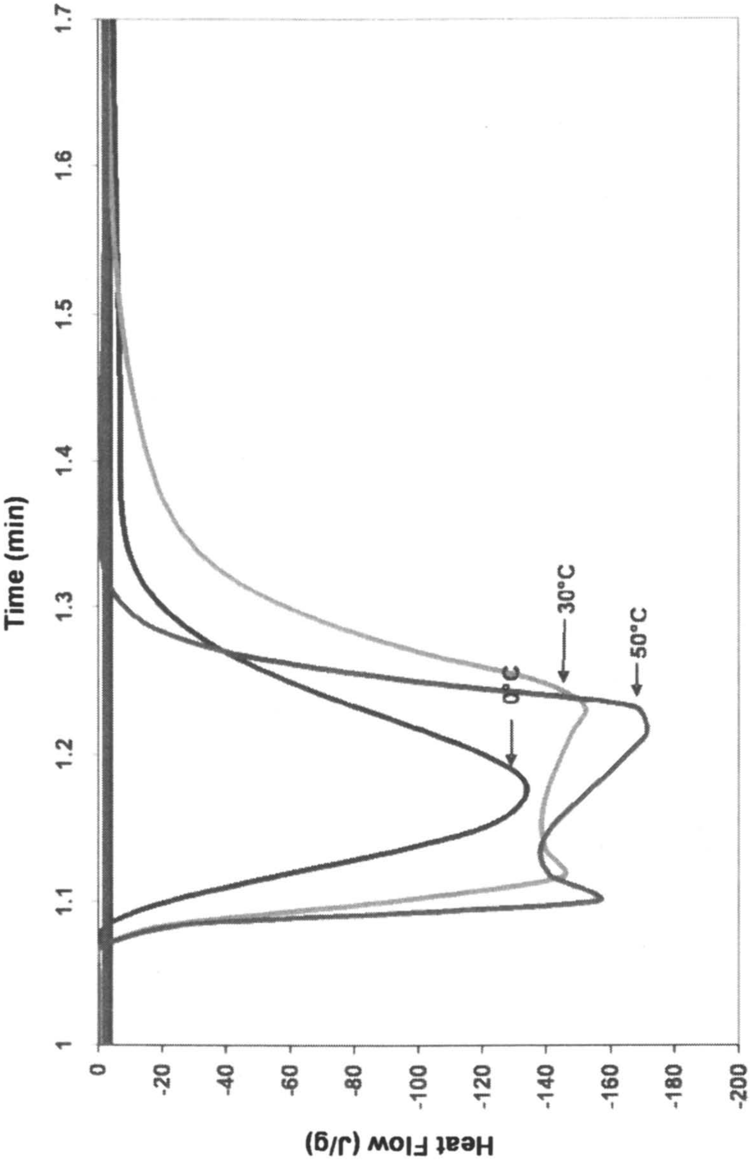

Figure 5. DSC exothems from photo-initiated aliphatic urethane triacrylate resin at 0°, 30°, and 50° C.

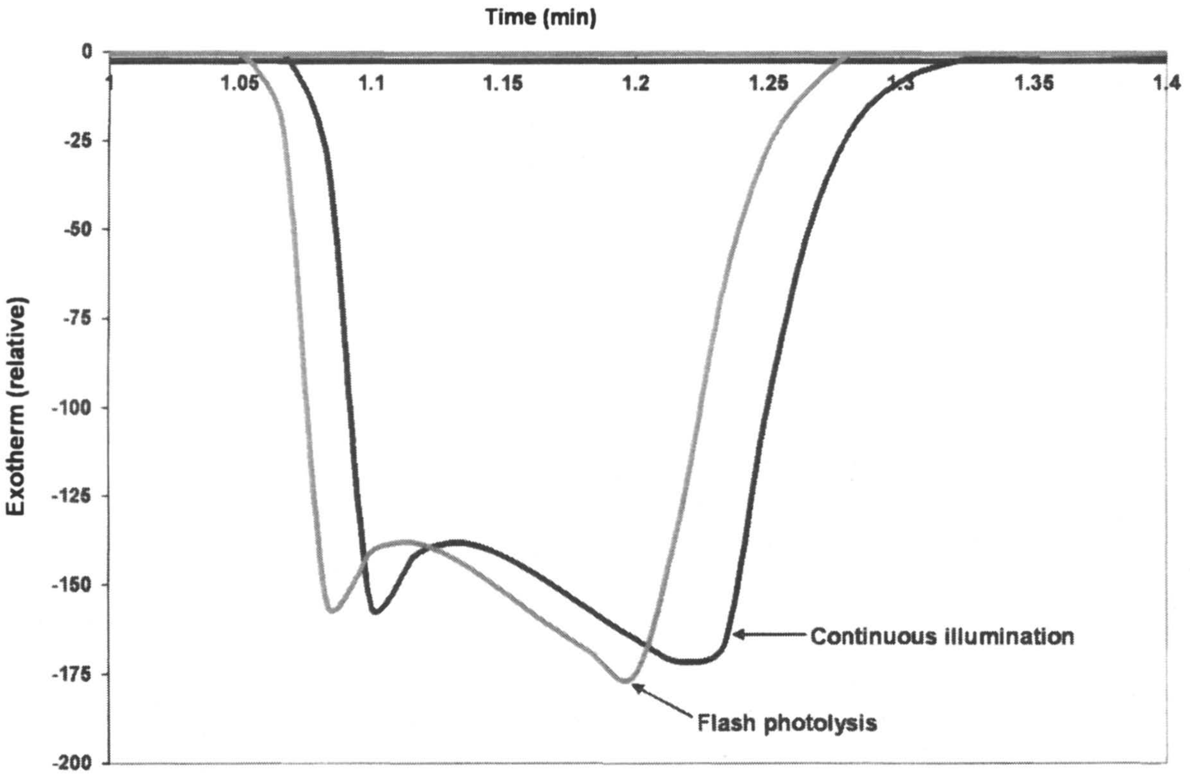

Figure 6. Flash illumination (black) and continuous illumination (gray) DSC curves for aliphatic urethane triacrylate at 50 °C.

complete the resin cure and the end, additional exotherm in the continuous case, results from initiator termination of chains after exhaustion of monomer moieties. A curious feature is the continuous rise in exotherm from about 7 seconds, to the maximum at 12 seconds into the run for the "flash" excitation. This must result from an acceleration of the propagation reaction in the flash illumination case beyond the time where illumination has ceased. The abrupt fall of the exotherm after (presumably) the monomer is exhausted further indicates propagation acceleration. We note that the rise duration exceeds our estimate of the thermal response time of our experiment (3-4 seconds).

From these two experiments, we can conclude that a five second illumination at the high light intensity used here is sufficient to effect complete cure. We also suggest that the propagation acceleration observed, if real, cannot result from a process which involves limiting chain recombination; the rise continues after no additional chains are initiated. In combination with the temperature behavior of continuously illuminated samples, we conclude as well that the two maxima result from two distinct populations of "monomer" moieties with different propagation velocities.

We speculate that the two populations are those with rigid positioning by the hydrogen bonding network and those in more flexible sites. Of course the two populations could involve the end and more centrally located acrylate moieties but this distinction should require that a 2:1 ratio exist between the populations here. It is not obvious that a 2:1 ratio exists for the integrated intensities.

Both populations should exhibit a positive temperature dependence for the propagation rate but the more rigid sites may show a rate increase as the system density increases at lower temperature. It is possible that for the "rigid" sites these factors cancel. The previous observation that the center of the combined exotherm appears not to shift with temperature seems to confirm a general low or zero overall activation energy for chain propagation.

The shift in the first maximum towards longer times at low temperatures does indicate that these processes have the higher activation energy and are probably the "free" sites. The second maximum then represents the more rigid set.

The aromatic urethane hexaacrylates making up the remainder of the formulation behave in a nearly analogous fashion as shown in Figure 7.

In the Figure 7, the features noted in the aliphatic triacrylate thermograms are apparent in these resin cures as well. An additional maximum is evident in these curing curves at times around 1.5 minutes for the resolved exotherms at 30 and 50° C. A long tail appears on the exotherm from the 0° run as well. This difference between the aliphatic and aromatic resins most probably indicates the presence of an additional distinct "monomer" population in the aromatic structures. We note that the ratio between the first two populations' exotherms is nearly the same for the triacrylates and hexaacrylates thus confirming our supposition that the distinction between these groups is not between the interior and terminal acrylate moieties.

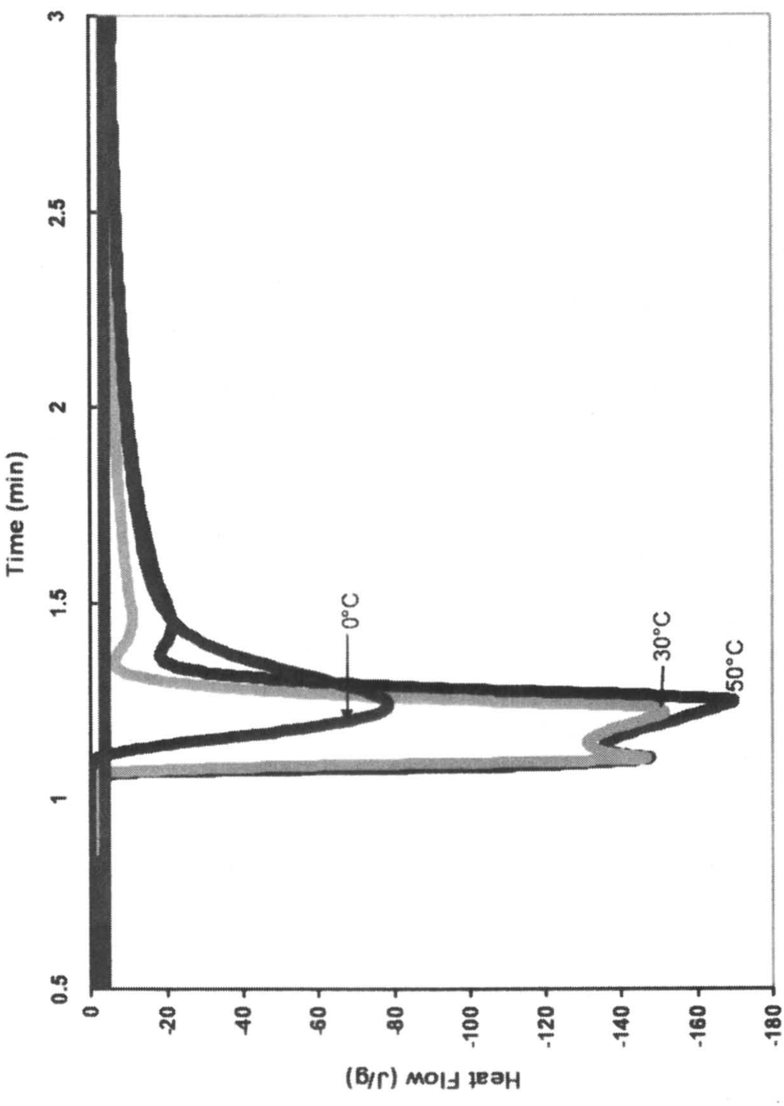

Figure 7. Aromatic urethane hexacrylate photocures at 0°C (dark gray), 30°C (light grey), and 50°C (black).

In the aromatic resin results, the center of the exotherm does appear to move to longer times for the 0° C run. However the initial exotherm rise is also delayed (timing error?). Our observation of nearly no temperature dependence for the cure from the triacrylates may be appropriate for these last resins as well.

Many of the observations we have made on these data involve features barely more extended than our estimate of instrument response time. Conclusions reached from these data and observations are therefore quite tentative but do provide guidance on more definitive experiments that will be required to resolve the mechanistically complex curing of these resins. It seems quite likely that the apparent acceleration of the propagation reaction is real and requires further study. The nature of the two or three distinct populations needs resolution as does the origin of the observed acceleration.

We have carried out some preliminary mathematical modeling of these cures based on our tentative conclusions on the mechanistic complexity. The results do not mirror the experiments well. In particular, it is difficult to explain the apparent sequential nature of the third maximum from the aromatic hexaacrylate resin cures. This third maximum appears even in flash excitation although less prominent than with continuous illumination. In Figure 8 we show the latter part of the cure exotherm with flash excitation illustrating this third maximum. Interestingly this third maximum occurs later in the flash excitation (at ~ 2 minutes) than with continuous excitation (1.45 minutes).

This third "population" must only be initiated after other populations have completed their action and these last reactions are initiated by the precursor reaction terminations. The nature of this process is unclear.

Our results and conclusions need much further study to resolve. Experiments on simpler systems need be made to isolate the various phenomena or determine their origin. In particular, time-resolved thermal analyses need to be performed on monoacrylate urethane resins and on polyacrylate, non-hydrogen bonded resins to more fully understand the mechanistic variety observed.

Conclusions

In general, it was shown that the behavior of specialized visible light curing cationic epoxy resins under different temperature and light intensity conditions could be successfully modeled. Modeling proved much more complicated for the acrylate-based systems likely due in part to the internal hydrogen bonding between adjacent chains in the uncured system and due to the complex nature of the formulation, which consisted of trifunctional aliphatic and hexafunctional aromatic components. Additional work is underway to provide a better understanding of the curing mechanisms in these systems so that a robust predictive model can be developed.

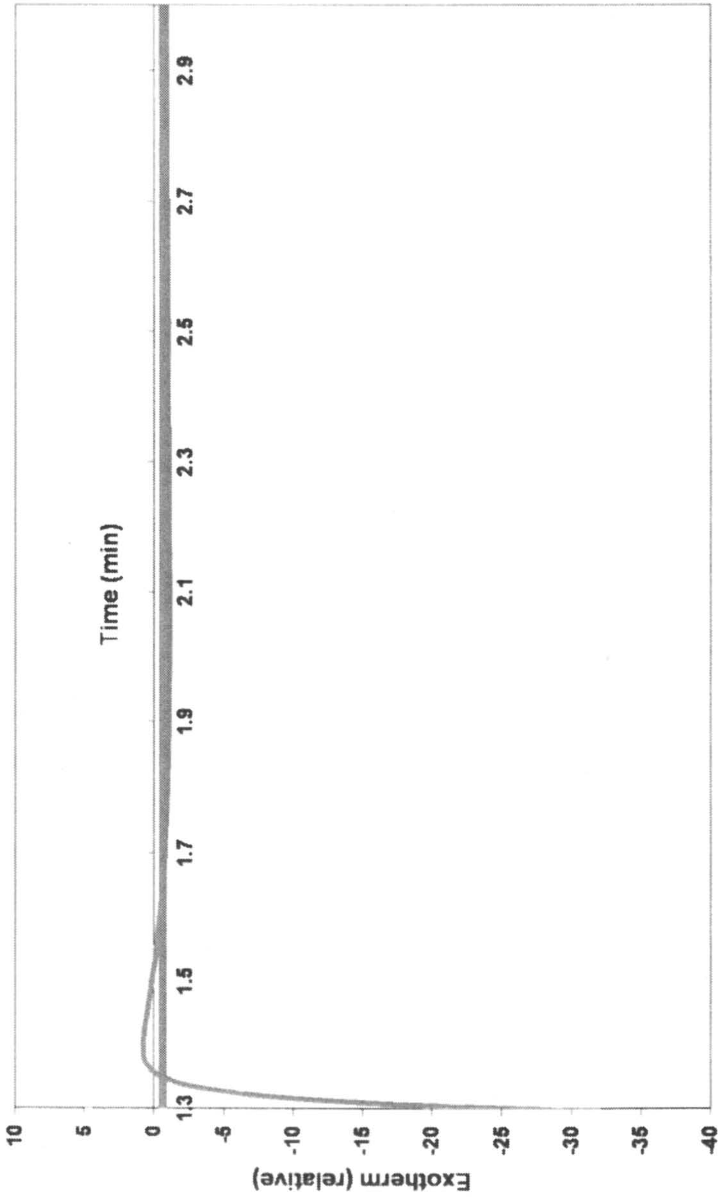

Figure 8. Aromatic urethane hexaacrylate cure exotherm from 5 second flash excitation at 50° C.

References

1. Jansen, J. F. G. A.; Dias, A. A.; Dorschu, M.; Coussens, B. *Macromolecules* **2003**, *36*, 3861-3873.
2. O'Neil, G. A; Wisnudel M. B.; Torkelson, J. M. *Macromolecules* **1996**, *29*, 7477-7490.

Chapter 17

Radiation Target Analyses of Plasmid DNA

T. J. Anchordoquy[1], M. D. C. Molina[1], and E. S. Kempner[2]

[1]School of Pharmacy, University of Colorado Health Sciences Center, Denver, CO 80262

[2]Office of Science and Technology, National Institute of Arthritis, Musculoskeletal and Skin Diseases, National Institutes of Health, Bethesda, MD 20892

Frozen solutions of high molecular weight circular DNA were irradiated with high-energy electrons. Molecules that survived the radiation exposure were detected by structural and functional techniques and were analyzed using radiation target theory. Radiation damage (as a loss of function) was not observed in a distant portion in the same chain, indicating a lack of energy transfer along the DNA polynucleotide. The results complement the same phenomena observed in RNA but are in contrast to the observations in proteins.

Effects of ionizing radiation on DNA have been widely studied for many years (1), although previous radiation target analyses were only reported before well-defined preparations and advanced techniques became available. It was reported that radiation damage in RNA occurred only locally in that molecule (2), in distinction with the well-established spread of radiation damage throughout polypeptides (3).

Gamma rays and high-energy electrons ionize atoms at random along their trajectories; the chance of an interaction being dependent on the number of atoms in the molecule. In each interaction, large amounts of energy are transferred to the target, resulting in excitations and covalent bond breakage. These direct effects of radiation dominate in frozen or dried materials. Because of the randomness, the undamaged (surviving) molecules decrease exponentially

U.S. government work. Published 2008 American Chemical Society.

with radiation exposure; the rate of this exponential is directly proportional to the mass of the target molecules.

A circular form of DNA (plasmid) encoding the gene for green fluorescent protein (GFP) was used in the present experiments. The DNA structure in plasmids is the classical double-helix form in which two strands of DNA interact via hydrogen bonds and base-stacking interactions. The GFP plasmid contains 5030 base pairs (bp) of total mass 3300 kDa. When produced in bacteria, the circular double-stranded plasmid is highly coiled into a compact "supercoiled" form (Figure 1). A single break in the backbone of either of the two DNA

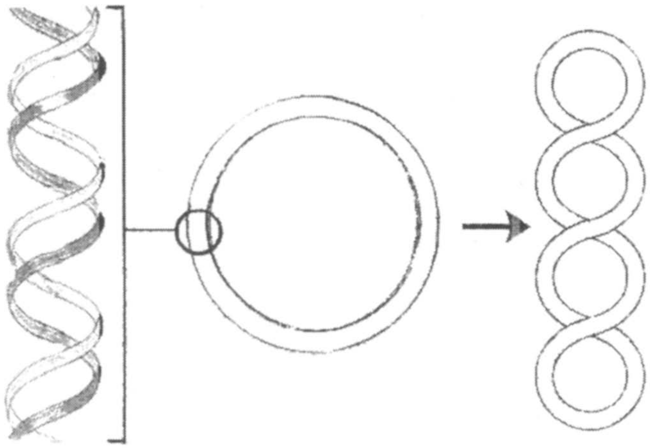

Figure 1. The two strands of the classical DNA double helix (left) are circularized (center) and twisted into a supercoiled form (right) when produced in bacteria.

strands causes the double-stranded molecule to unwind its supercoils and assume a relaxed, open-circular form. If a second break occurs in the other DNA strand nearby the location of the first break, the resulting double-strand break will cause the circular form to be converted to a linear form. These three forms have very different hydrodynamic properties and can readily be separated by agarose gel electrophoresis. In addition to a physical separation and quantification of the different plasmid forms, the biological activity of the plasmid can be assessed by introducing irradiated DNA into cells and monitoring the levels of GFP expression. These results revealed that in a single direct radiation interaction, damage is confined to a limited region of the DNA molecule.

Several earlier radiation studies of plasmid DNA have appeared, but only two concerned the direct actions of ionizing radiation; both used very low energy electrons. Hieda et al. (4) studied radiation interactions directly with the phosphorus atom; in spite of the large number of orbital electrons, phosphorus ionizations were not unusually effective in radiation damage. Boudaiffa et al. (5) showed that electrons with energies typical of secondary electrons could cause single-, double- and multiple-strand breaks in DNA.

Materials and Methods

The plasmid encoding green fluorescent protein (pGreen Lantern-1) was originally obtained from Gibco-BRL (Carlsbad CA). The plasmid was propagated in *E. coli*, and purified by Aldevron Custom Plasmid Purification (Fargo ND). The plasmid was dissolved at a concentration of 3 mg/mL in sterile 2.5 mM Tris-HCl pH 8.5. Plasmid samples (20 uL) were frozen on dry ice in 2 mL glass ampules and sealed with an oxygen-gas flame. Sealed, frozen samples were shipped and held at –80 C before and after irradiation at -135 C (6) with 13 MeV electrons from a linear accelerator at the Armed Forces Radiobiology Research Institute (Bethesda MD) or at the National Institutes of Standards and Technology (Gaithersburg MD).

Assays:

Conversion of supercoiled plasmids to the open circle and linear forms were monitored by subjecting samples to 0.9% agarose gel electrophoresis (7). Unirradiated plasmid ranging from 100 to 1000 ng was included on each gel with irradiated samples in order to create a standard curve. After migration, gels were stained with ethidium bromide and quantified by fluorometric image analysis using a Fluor-S MultiImager and Quantity One software (Biorad, Hercules CA). Aliquots of irradiated plasmid containing 2 ug DNA were diluted in water and mixed with 8.4 uL of 10 mM polyethylenimine (pH 7) to facilitate delivery to African green monkey kidney cells (COS-7) as previously described (8). After 4 h the media was replaced with fresh media and cells were grown at 37 C for approximately 40 h. After harvesting and washing, cells were analyzed for green fluorescent protein expression using a Coulter Epics XL glow cytometer (Hialeah FL). Fluorescence was monitored at 525 nm from 5000 cells per sample, and triplicate transfections were measured per sample.

Results

The supercoiled forms of the plasmid were rapidly lost by small doses of ionizing radiation. The amount of open-circle forms rose simultaneously, reached a maximum and then slowly decayed with increasing radiation exposure. Linear forms did not appear until higher doses were obtained; the amounts of these rose and reached a plateau.

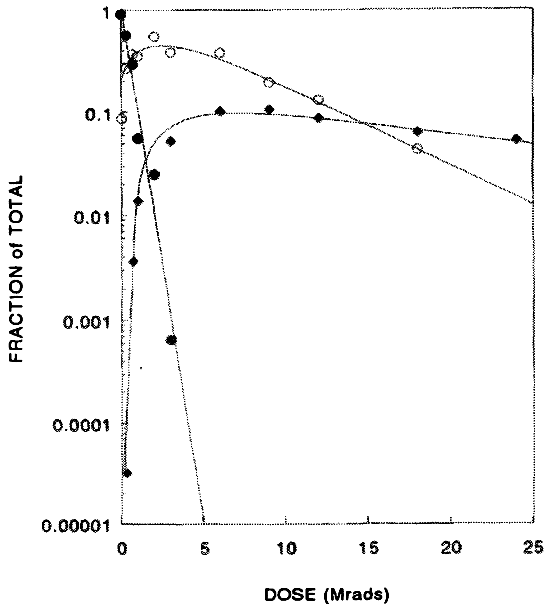

Figure 2. Surviving forms of GFP-plasmid after exposure of the frozen supercoiled plasmid to various doses of ionizing radiation. Supercoiled (solid circles), open circle (open circles) and linear forms (solid diaminds) are shown. Normalized to total DNA originally present.

Radiation target theory predicts an exponential loss of molecules as a function of radiation exposure; the rate of this loss is directly proportional to the mass of the molecule. The supercoiled form was observed to decay in this manner. The double-stranded GFP plasmid has a mass of 3300 kDa. In three independent experiments, the amount of supercoiled DNA decreased exponentially with radiation dose (Fig. 2), yielding a target size of 3059 kDa (Table 1), indicating that a single radiation interaction anywhere in the plasmid

results in disappearance of that molecule from the supercoiled population. By itself, this does not indicate whether there are one or more product types.

The plasmid preparations used in these studies contained some level (<20%) of open circle forms prior to irradiation; their number increased after low doses of radiation as they are produced from damaged supercoiled molecules. The increase in open circle forms ceases on exhaustion of the supply of parent supercoiled molecules. Further radiation exposure resulted in damage to the open circle molecules revealed as an exponential decrease in open circle forms (Fig. 2). Analysis of the amount of open circle forms is described by the difference of two exponentials – one due to the production and the other due to the destruction of the open circle form. The complexity of these curves presents difficulties in resolving the two exponential components (9) since only some of the data points are used in each fit. Combining data from several experiments increases the number of data points, enabling more accurate target determinations.

Table I. Target Sizes (in kDa) of Irradiated GFP Plasmid

Assay		*Production*	*Destruction*
Supercoiled	3059		
Open circle		1936	140
Linear form		242	
Transfection	1067		

Data from three combined experiments.

The rise and fall of the open circle form were resolved as the difference of two exponentials, leading to target sizes of 1936 and 140 kDa, respectively (Table I). Since the open circle form is expected to arise from a single polymer cleavage in one DNA chain, the anticipated target size is 1650 kDa. Considering the experimental errors, the present value is reasonable. Open circle forms ultimately decayed at higher doses, yielding a target size of 140 kDa (~424 bases). In this study it can be concluded that destruction of the open circle requires an ionization somewhere in the mass of 140 kDa out of a total mass of 3300 kDa.

The linear form is expected to arise when an open circle molecule suffers a polymer cleavage in the intact strand, 'close to' the preexisting break in the

opposite strand. It could also arise directly from the supercoiled form provided the initial radiation interaction caused nearby cleavages in both strands. The present experiments showed a rise of linear forms to a plateau; no decrease in amount of linear forms was seen in this range of radiation exposures (Fig. 2). The appearance of linear forms was related to damage in a mass of 242 kDa (Table 1).

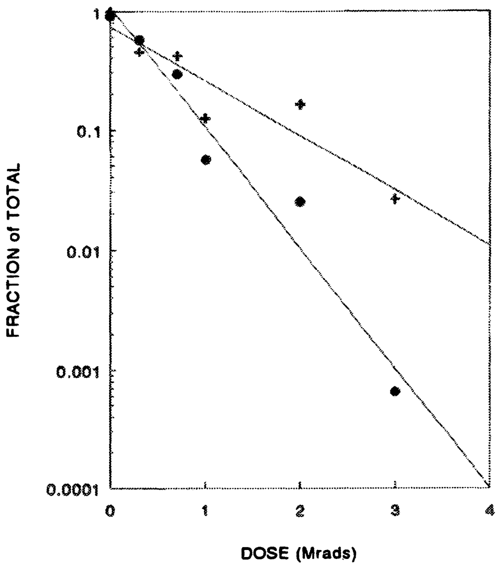

Figure 3. Surviving GFP expression in COS-7 cells transfected with irradiated GFP plasmids. Supercoiled molecules (solid circles) and transfected GFP function (crosses) are shown. Note dose scale expanded from Figure 2.

These structural analyses are complemented by transfection analyses from the same irradiated samples. In each experiment the amount of transfection was reduced by radiation exposure to a level of 1 to 9% of the control. Further exposure did not reduce this level. The transfection assay has a 'background' value due to intrinsic cell fluorescence which is independent of radiation damage. Similar phenomena have been reported in irradiation of enzymes in which there was a small non-enzymatic reaction producing the same product. As in those cases, this component could be subtracted from all samples, giving a simple exponential decrease in transfection activity (Fig. 3). In three experiments the target size associated with transfection activity was 1067 +/- 155 kDa, considerably smaller than the 3300 kDa total mass (Table I).

Discussion

A simple exponential decrease of measured properties as a function of radiation dose indicates that the effect is due to a single radiation interaction. Radiation target theory predicts that the rate of this decrease is directly proportional to the mass of the structure responsible for that property. Thus the disappearance of supercoiled plasmids is caused by a single radiation interaction anywhere in a mass of 3059 kDa – close to the known mass of the entire molecule. This result does not indicate the fate(s) of the 'hit' supercoiled DNA molecules.

Assays of the open circle and linear forms showed a complex relationship with radiation exposure. These results are similar to observations in another plasmid after exposure to extremely low energy X-rays (4). There was an initial dramatic increase in both forms up to a maximum that (in open circles) then decreased exponentially, or (in linear forms) remained constant. The initial rise has been observed in other systems (10, 11) in which irradiation of some larger structure released a product (or removed the inhibition of the molecule) being assayed. The initial rate of increase can be analyzed to yield the mass of the 'parent' structure. A final decrease in function or structure is due to radiation destruction of the measured material. In the present study, open circle forms display this complex response in which the eventual decrease is then due to the destruction of existing open circle forms. Target analysis treats this situation as the difference of two exponentials (9, 10). Since only some of the experimental points are used to resolve each component, increased error arises in the calculated target mass. The linear form molecules showed no decrease at higher doses; these data were fit with a [1-exp(-x)] type curve which also introduces significant uncertainty in the target size.

A 'nick' (breakage of a covalent bond in the polymer backbone of a single strand) in supercoiled DNA causes the molecule to unwind into an open circle form (12). In the current studies the initial rise in the amount of open circle forms occurred at a rate expected from the mass of one chain of this DNA, just as predicted. Further radiation exposure causes a decrease of open circle molecules at a rate expected from a ~140 kDa structure. As with the supercoil form, this results only means that a radiation interaction in this mass alters the structure so that the molecule no longer moves on electrophoresis as an open circle molecule. At least some of these altered molecules are expected to change to the linear form because of nearby breaks in the opposite strand. The target size of ~140 kDa should be interpreted as a segment of the open circle in which a radiation interaction deposits energy which eventually leads to scission of a backbone bond in the intact chain, nearby the original break in the opposite chain. This radiation-sensitive mass depends on two factors: the distance from the site of the radiation interaction that the energy can travel before it causes a bond scission and, secondly, how near the existing opposite-strand break must be

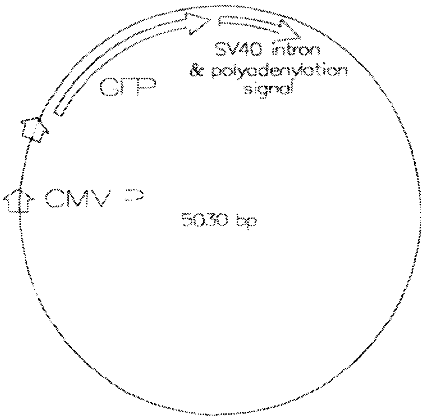

Figure 4. Map of the GFP plasmid.

in order to rupture the open circle. This target mass is clearly much smaller than one strand of the DNA.

Linear forms only appear after exposure of supercoiled and open circle molecules to ionizing radiation. The rise of linear forms results in a target size of 242 kDa; the 140 kDa target for loss of open circles is similar, considering the inherent errors in these determinations. In general, these structural target sizes are consistent with expectations from biochemical and molecular biological studies. Determination of the radiation sensitivity of biological function, via transfection, adds a useful dimension to these results.

Transfection and expression of the GFP protein decreased exponentially in irradiated samples, but at a slower rate than the loss of supercoiled forms. This resulted in a target size considerably smaller than the size of the DNA molecule, only about one-third the mass. The map of this plasmid (Fig. 4) shows that the segment of the plasmid directly involved in transfection activity (which includes the CMV promoter, GFP gene, SV40 intron and polyadenylation signal) has a calculated mass of 1067.880 kDa.

The target size observed for transfection, 1067 kDa, is extremely close to this value. This result has important ramifications: radiation damage elsewhere in the plasmid DNA does not affect transfection activity, so clearly there cannot have been any radiation damage (sufficient to cause covalent bond breakage) to the active fragment. Thus it can be concluded that in DNA there is at most only negligible transfer of radiation energy along the polymer chain. This is precisely what was observed in ribozymal RNA (2), but totally different from observations in proteins. It was suggested that the restriction in energy transfer was due to the presence of sugar rings in the polymer backbone that are thought to limit radiation damage in oligosaccharides (13); the deoxyribose content of DNA is consistent with this idea.

Acknowledgements

The work was supported in part by the Office of Science and Technology, National Institute of Arthritis and Musculoskeletal and Skin Diseases.

References

1. *Effects of Ionizing Radiation on DNA;* Huttermann, J.; Kohnlein, W.; Teoule R., Eds. Springer Verlag: Berlin, 1978.
2. Bernstein, S. L.; Kempner, E. Proc. Natl. Acad. Sci. (US) **1996**, *93*, 6410-6414.
3. Kempner, E. S. *Analyt. Biochem.* **1999**, *276*, 113-123.
4. Hieda, K.; Hirono, T.; Azami, A.; Suzuki, M.; Furusawa, Y.; Maezawa, H.; Usami, N.; Yokoya, A.; Kobayashi, K. *Int. Jour. Radiat. Biol.* **1996**, *70*, 437-445.
5. Boudaiffa, B.; Hunting, D.; Cloutier, P.; Huels, M. A..; Sanche, L. *Int. Jour. Radiat. Biol.* **2000**, *76*, 1209-1221.
6. Harmon, J. T.; Nielsen, T. B.; Kempner, E. S.; *Meth. Enzymol.* **1985**, *117*, 65-94.
7. Molina, M. C.; Armstrong, T. K.; Zhang, Y.; Patel, M. M.; Lentz, Y. K.; Anchordoquy, T. J. *Jour. Pharm. Sci.* **2004**, *93*, 2259-2273.
8. Molina, M. C.; Allison, S. D.; Anchordoquy, T. J. *Jour. Pharm. Sci.* **2001**, *90*, :1445-1455.
9. Kempner, E. S. *Bull. Math. Biol.* **1995**, *57*, 883-898.
10. Harmon, J. T.; Kahn, C. R.; Kempner, E. S.; Schlegel, W. *Jour. Biol. Chem.* **1980**, *255*, 3412-3419.
11. Vessey, D. A.; Kempner, E. S. *Jour. Biol. Chem.* **1989**, *264*, 6334-6338.
12. Nelson, D. L.; Cox, M. M. *Lehninger Principles of Biochemistry;*. fourth edition. WH Freeman and Company, NY,. 2005
13. von Sonntag, C. *Adv. Carbohydr. Chem. Biochem.* **1980**, *37*, 7-77.

Chapter 18

Chemical and Radiation Cross-Linking of Polytetrafluoroethylene by Containing Fluorinated Compound

Akihiro Oshima and Masakazu Washio

Advanced Research Institute for Science and Engineering, Waseda University, 3–4–1 Okubo, Shinjuku, Tokyo 169–8555, Japan

The thermo-chemical-induced crosslinking of polytetrafluoroethylene (PTFE) has been demonstrated by using fluorinated-compound without any other catalyst materials. The heat-treatment for PTFE containing the various amount of fluorinated-compound was carried out at 350 °C ± 5 °C for 30 minutes. After treatment, the various measurements and analysis were performed. By the solid-state ^{19}F-NMR spectroscopy, the new signal appeared at −188 ppm, which is assigned to the fluorine signal of >CF– group (Y-type crosslinking site). The obtained materials showed good mechanical properties and lower crystallinity, which were confirmed by tensile and flexural tests, and DSC analysis, compared with PTFE. Hence, the obtained material is confirmed to be crosslinked through thermal chemical reaction with decomposion of fluorinated-compound. The chemical-radiation synergetic crosslinking of PTFE (SX-PTFE) was carried out. By ^{19}F-NMR spectroscopy, several new peaks were appeared at – 85 ppm, – 89 ppm, – 110 ppm, – 114 ppm and – 188 ppm, respectively. The peaks at – 83 ppm and – 89 ppm correspond to $-CF_3$ were assigned to the fluorine signals of chain end group in amorphous and branching chain end group, respectively. The peaks at −110 ppm and −114 ppm were assigned to the fluorine signals of Y-type crosslinking site and hexafluoropropylene, respectively. The signal at −188

© 2008 American Chemical Society

ppm is assigned to the fluorine signal of >CF– group. The peak intensity was higher than chemical-crosslinking and radiation-crosslinking. The mechanical properties of the SX-PTFE composite were much improved. The wettability of the obtained materials was the same as that of PTFE. That is, wettability of obtained materials hold the original property.

Introduction

It is well known that polytetrafluoroethylene (PTFE) has the excellent characteristics of heat resistance, solvent resistance, high frictional properties and electrical insulation, compared with those of other hydrocarbon polymers. It has been believed for many years that crosslinking of PTFE takes place neither in ordered state, nor in disordered state in solid. Namely, since PTFE molecules have a helical coil structure in the crystalline state, even in amorphous phase below the melting point, free radicals formed in the solid state are restricted by the steric hindrance of molecular chain to react with radicals formed in neighboring molecules. Though PTFE has been extremely sensitive to ionizing radiation leading to main chain scission, it has been found that the crosslinked PTFE has been produced by irradiation under specific conditions, that is, at 340 °C ± 10 °C under oxygen-free atmosphere [1-6]. The obtained crosslinked PTFE shows remarkable improvements in radiation resistance, mechanical properties, frictional properties and light transparency due to decreasing of crystalline components, compared with those of non-crosslinked PTFE [7-10].

According to our solid-state ^{19}F- and ^{13}C-NMR spectroscopy, FT-IR spectroscopy, electron spectroscopy for chemical analysis (ESCA), it has been made clear that Y-type and modified Y-type (Y'-type) crosslinking structures are formed in PTFE by its molten state irradiation [6, 10, 11]. In addition, it has been found that the various sorts of double bonds structure excluding crosslinking site are produced. Y-type crosslinking through recombination of alkyl radical and methylene (end-chain) type radical can be easily expected by probability of combinations for both radicals in its molten state.

From the above mentioned reaction mechanism of radiation-crosslinking, if the thermo-chemical induced-radicals will be produced in the molten state of PTFE, it may be thought that the thermo-chemical induced-crosslinking will be able to take place.

In present study, thermo-chemical-induced crosslinking of PTFE has been demonstrated by using fluorinated-compound without any other catalyst materials. Characterization of crosslinked PTFE, which was obtained by radiation and chemical crosslinking, has been studied by various measurement techniques, such as thermal analysis (DSC, TGA), mechanical test, solid-state ^{19}F-NMR spectroscopy, and so on.

Experimental

Materials and Crosslinking Treatments

The materials for the experiments were an aqueous dispersion PTFE (FLUON® XAD - 911; average diameter of particles: 0.25 μm, concentration: 60 wt%, Mn: 1.4×10^6, viscosity at 25 °C: 20 mPa·s, Asahi-Glass Fluoropolymers Co. Ltd.), and fluorinated-compound such as fluorinated-pitch (Rinoves® P N-7-M; average diameter of particles: 1.2 μm, atom ratio of F/C: 1.6, Mn: 2.0×10^3, Osaka Gas Chemicals Co. Ltd.) [12, 13]. And also the plane-woven carbon fabric (TORAYCA® T-300, #C06142, TORAY Industries, Inc.) was used for the mechanical tests such as the tensile and the flexural tests.

The polymer-blend dispersions of PTFE and fluorinated-pitch with various concentration of fluorinated-pitch have been coated on stainless steel (SUS-304). The various coated polymer-blend were heat-treated at 350 °C ± 5 °C for 30 minutes. Further, samples were subjected to EB irradiation with a 200keV from EB accelerator (CURETRON®, NHV Corporation) up to 1000 kGy at 330 °C ± 3 °C in nitrogen gas atmosphere.

For mechanical test such as tensile test and flexural test, the impregnation of polymer-blend to the carbon fiber was carried out several soakings of the fiber in the polymer-blend dispersion consists of PTFE (98.2 wt%) and fluorinated-pitch (1.8 wt%). A sheet of chemical crosslinked pre-forming sample was prepared under the pressure at around 20 MPa and then heat-treated at 350 °C ± 5 °C for 30 minutes. Samples were irradiated by EB up to 1000 kGy at 335 °C ± 3 °C in nitrogen gas atmosphere.

Laminate panels were fabricated by means of compression molding in its molten state from a sheet of pre-forming by lay-up of sixth plys before and after thermo-chemical treatment and EB irradiation, respectively.

Measurements

Differential scanning calorimetric analysis (DSC: Perkin Elmer: PYRIS Diamond DSC) and thermogravimetric analysis (TGA: SHIMADZU TGA-50H) were performed. Melting and crystallization temperatures, and heat of melting (ΔHm) and heat of crystallization (ΔHc) of irradiated specimens were measured by DSC under nitrogen atmosphere. The heating and the cooling rate of specimen were 20 °C /min. Thermal decomposition temperatures were measured by TGA under nitrogen atmosphere. The heating rate was 10 °C /min.

SEM photographs were taken by an S-2500CX (Hitachi Co. Ltd.). The voltage was set at 25 kV and the current was set at 10 mA.

Solid-state ^{19}F-NMR measurements were performed on a JEOL CMX-400 spectrometer (fluorine frequency, 376 MHz) operating at 9.4 T with Doty Ultrasonic CP/MAS probe at 150 °C. The magic-angle spinning rate was set to 12 kHz and 15 kHz to avoid overlaps of CF_3 and CF signals with spinning sidebands of the internal $-CF_2-$ signal, respectively. ^{19}F chemical shifts were expressed as relative values to the $-CF_2-$ fluorine resonance of PTFE as an external resonance at −124.0 ppm from $CFCl_3$. The spectrum in a region around the internal CF_2 signal was simulated using the Alice program provided by JEOL in order to obtain the detailed information.

Tensile test with the direction of 45 ° for plane-woven carbon fabric was carried out at the crosshead speed of 20 mm/min using ASTM-D1822L type dumb-bell shape specimen. The three-point bending test of laminate panels was carried out at ambient temperature using an INSTRON (type 4302). The specimen was cut to $^{L}64$ mm×$^{W}10$ mm×$^{T}1.5$ mm, and beam-span length of bending test was 32 times the specimens' thickness. The crosshead speed was 2 mm/min.

Wettability of obtained materials was determined by measuring the contact angle between various solvent droplets (0.05 ml) and surfaces at five different points of each sample surface and the measured values of contact angle were averaged.

Results and Discussion

Chemical Crosslinking of PTFE using Fluorinated-Pitch

Figure 1 shows SEM photographs of each powder of PTFE and fluorinated-pitch. For PTFE, the average particles sizes were few μm caused by co-aggregation of sub-micron size fine particles. In the case of fluorinated-pitch, it was found a similar structure to graphite fluoride $(CF)_n$, that size was about 1 μm or 2 μm.

The heat-treatment for PTFE containing the various amount of fluorinated-pitch [PTFE / fluorinated-pitch polymer-blend: PTFE / FP] was carried out at 350 °C ± 5 °C for 30min. Figure 2 shows the thermal properties of heat-treated PTFE with fluorinated-pitch. The melting and the crystallization temperatures shift to lower temperatures by addition of fluorinated-pitch. And also, the heat of crystallization (ΔHc) decreased with increasing of amount of fluorinated-pitch.

The present experimental results show that the changes of thermal properties of PTFE with fluorinated-pitch after heat–treatment at around 350 °C in the molten state are completely different from those of PTFE non-additive fluorinated-pitch. The changes and the behavior of thermal properties in the

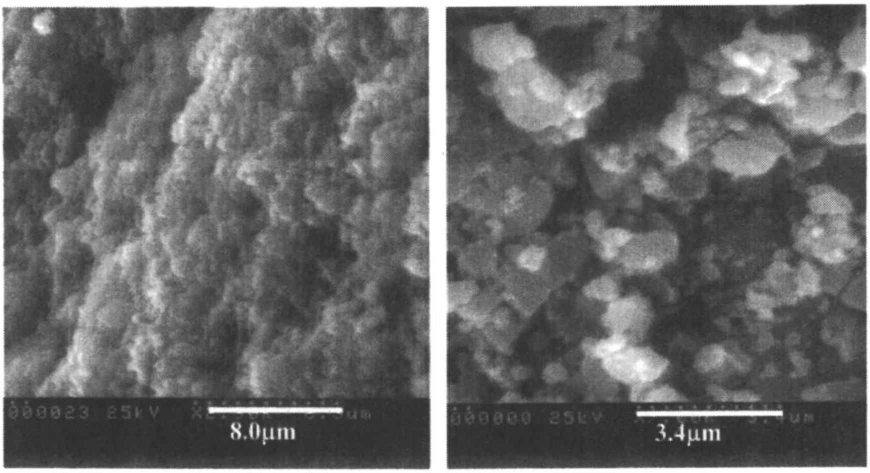

Polytetrafluoroethylene (PTFE) ***Fluorinated-pitch***

Figure 1 SEM photographs of PTFE (left) and fluorinated-pitch (right).

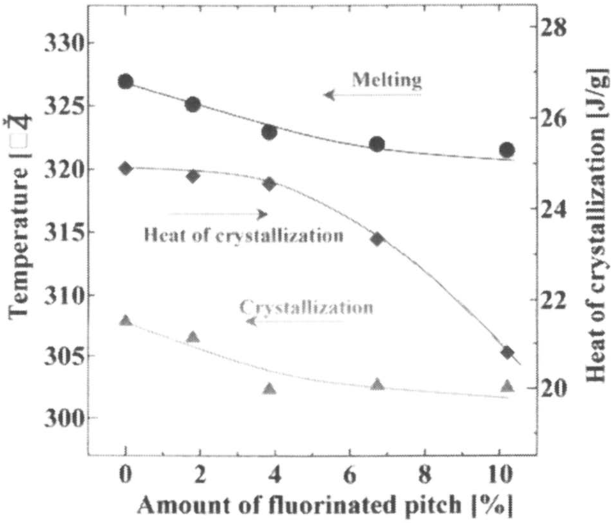

Figure 2 The thermal properties of heat-treated PTFE with fluorinated-pitch as functions of amount of fluorinated-pitch.

molten state strongly suggest the network formation by the thermo-chemical induced-crosslinking in PTFE. Especially, increase in amount of fluorinated-pitch indicates the increase of network density in PTFE molecules.

The crosslinking between PTFE polymer chains and fluorinated-pitch should prevent crystallization of molecules from the molten state. When the crosslinking density is low, the molecules with rather long chain between crosslinking points might crystallize, where the crystal size would be small and also the ratio of crystalline against amorphous parts would decrease. The DSC results are well explained by above model.

By the solid-state ^{19}F-MAS-NMR spectroscopy for PTFE, an intense peak at – 124 ppm was observed. This intense peak was straightforwardly assigned to fluorine signal of internal CF_2 (int–CF_2–). This is indicating that the PTFE used in this experiment has a completely linear chemical structure without crosslinking. The solid-state ^{19}F NMR spectrum of heat-treated PTFE with fluorinated-pitch (1.8 wt% additive) is shown in figure 3. The new signal was observed besides the intense peak at – 124 ppm. The new signal, which appeared at – 188 ppm, was due to the changed chemical structures. The signal is assigned to fluorine signal of >CF– group, which represents crosslinking sites in the polymer chain. Thus, the obtained material is confirmed to be crosslinked through thermo-chemical reaction.

Figure 4 shows the TGA curves of fluorinated-pitch, PTFE and heat-treated PTFE with fluorinated-pitch (1.8 wt% additive). For the fluorinated-pitch, there are mainly two separated steps degradation pattern in the TGA curves. The first degradation step began at 200 °C and ended at 311 °C, and the second degradation step began at 362 °C and ended at 520 °C. It may be thought that the first step should be attributed to the degradation of cyclohexane ring structure with perfluoro-methylene, and the second step should be attributed to the degradation of the fluorinated-pitch matrix. For PTFE, it began to degrade at 460 °C and ended at 620 °C [10, 14].

In the case of heat-treated PTFE with fluorinated-pitch, there are mainly two separated steps of degradation pattern as shown in figure 4. The first step began at 423 °C and ended at 607 °C, and the second step began at 642 °C and ended at 733 °C. It may be considered that the first step should be attributed to the degradation of PTFE matrix, and the second step should be attributed to the degradation of the PTFE and fluorinated-pitch combined matrix. Moreover, the inflection point of first degradation step of heat-treated PTFE with fluorinated-pitch was higher than that of PTFE. Thus, it will be suggested that the thermal durability was improved due to network formation in PTFE and fluorinated-pitch combined matrix.

The first degradation step of fluorinated-pitch should be induced crosslinking reaction in PTFE molecules. That is, the crosslinking would be occurred in PTFE molecules through thermal chemical reaction with decomposion of fluorinated-pitch without EB irradiation.

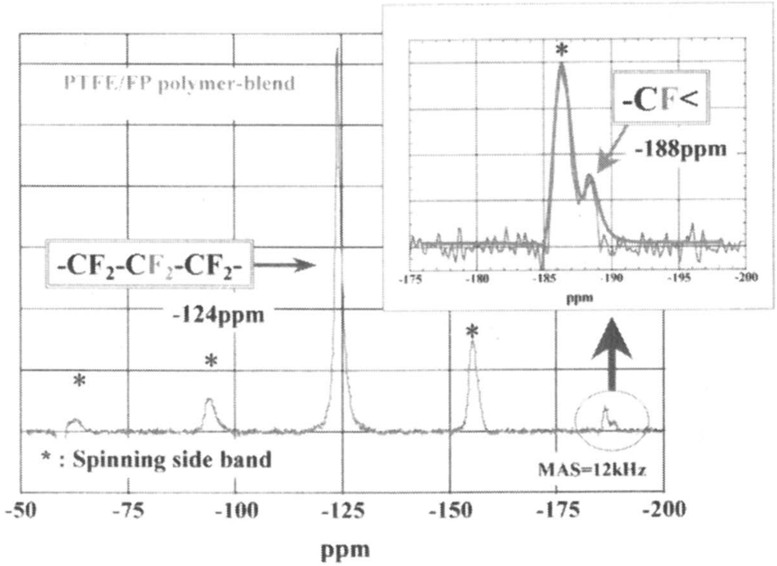

Figure 3 The solid-state ^{19}F NMR spectrum of heat-treated PTFE (98.2 wt%) with fluorinated-pitch (1.8 wt%). The magic angle spinning frequency is 12 kHz. The measurement temperature is at 150 °C.

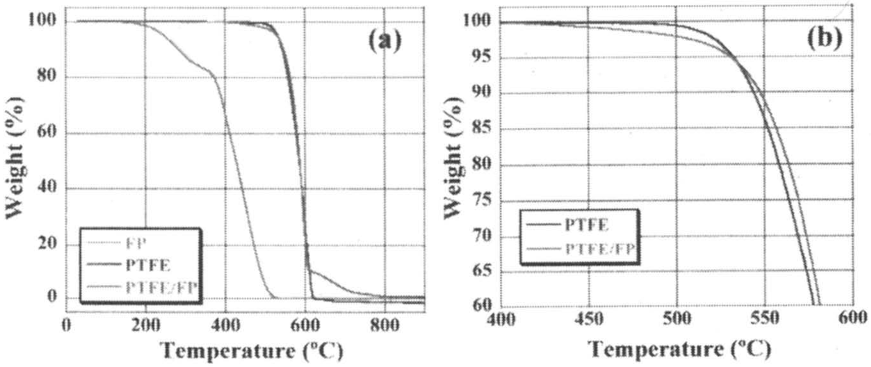

Figure 4 The TGA curves of fluorinated-pitch, PTFE and heat-treated PTFE with fluorinated-pitch (1.8 wt% additive: PTFE/FP). (a) Temperature range of 0 °C to 900 °C, (b) Temperature range of 400 °C to 600 °C.

In Polymer Durability and Radiation Effects; Celina, M., et al.;
ACS Symposium Series; American Chemical Society: Washington, DC, 2007.

It could be considered that the reaction kinetics of thermo-chemical crosslinking of PTFE with fluorinated-pitch was as follows; the fluorinated-pitch consists of the fluorinated cyclohexane ring structure with perfluoro-methylene. The fluorinated cyclohexane ring structures were broken along with the induced fluorine radicals (F·) due to decomposition above 200 °C. The produced fluorine radicals reacted with each other, and then, fluorine gases (F_2) were evaporated. Moreover, the fluorine radicals became attacking to PTFE molecules. As the results, the thermo-chemical induced alkyl radicals and chain end radicals will be produced on PTFE molecules in the molten state. The alkyl radicals and chain end radicals reacted with each other, and also, the fluorinated-polymer fragment from decomposition of fluorinated-pitch may be combined with PTFE main chain radicals to generate long branches. Thus, the thermo-chemical induced-crosslinking would be able to take place.

Table I shows the mechanical properties of the carbon fiber-reinforced PTFE (PTFE composite; non-crosslinked) and the carbon fiber-reinforced PTFE with fluorinated-pitch (PTFE / FP composite; thermo-chemical crosslinked). For the tensile test with a direction of 45 ° for plane-woven carbon fabric, the tensile strength of the PTFE / FP composite was about 2.3 times higher than that of the non-crosslinked PTFE composite. Moreover, the Young's modulus of the crosslinked composite was about 2.6 times higher than that of the PTFE composite. The tensile strength and Young's modulus are results of 0 ° or 90 ° direction for the fabric reflected the carbon fiber strength and the modulus.

For the three-point bending test of the sixth plys laminate panels, the flexural strength of the PTFE / FP composite was about 2.9 times higher than that of the PTFE composite. Moreover, the flexural modulus of the PTFE / FP

Table I. The tensile and flexural properties of the carbon fiber-reinforced PTFE and the carbon fiber-reinforced PTFE with fluorinated-pitch. Volume of carbon fiber was 54.3 %

	*Tensile properties (direction of 45 °)**		*Flexural properties***	
	Strength (MPa)	*Young's modulus (MPa)*	*Strength (MPa)*	*Flexural modulus (GPa)*
PTFE composite	11.7	138	42.6	8.30
PTFE / FP composite	26.8	357	121.9	15.9

*: One-ply sheet, **: Sixth plys laminated panel

composite was about 1.9 times higher than that of the PTFE composite. It was found that the mechanical properties of PTFE / FP composite was improved by thermo-chemical crosslinking.

Synergistic Crosslinking of PTFE

The synergistic crosslinking was carried out, that is, EB-crosslinking treatment was performed after thermo-chemical crosslinking treatment of PTFE with fluorinated-pitch (1.8 wt% additive). The thermal properties of obtained crosslinked PTFE were examined by DSC analysis shown in Table II. The melting and the crystallization temperatures of radiation-crosslinked PTFE (RX-PTFE), thermo-chemical-crosslinked PTFE (CX-PTFE), synergetic-crosslinked PTFE (thermo-chemical and radiation; SX-PTFE) shift to lower temperatures, compared with PTFE.

The heat of crystallization (ΔHc) of reference materials *i.e.*, PTFE and CX-PTFE are 24.9 kJ / kg and 24.7 kJ / kg, respectively. The ΔHc of RX-PTFE and SX-PTFE are 35.5 kJ / kg and 33.0 kJ / kg, respectively. The ΔHc of SX-PTFE was lower than that of RX-PTFE, *i.e.*, the crystallinity of SX-PTFE was smaller than that of RX-PTFE. The ΔHc of RX-PTFE and SX-PTFE were higher than those of PTFE and CX-PTFE. It would be caused by low EB dose that the main chain scission would take place in PTFE and then crystallized. In the case of high EB dose, the ΔHc of RX-PTFE and SX-PTFE were smaller than initial value.

These results may indicate that the chain scission would occur like the case of EB-crosslinking process of PTFE [3, 6, 10] in CX-PTFE matrix and the crosslinking reaction would be taken place by recombination between EB-induced alkyl and methylene types radicals.

From the solid-state ^{19}F-MAS-NMR spectroscopy for synergetic-crosslinked PTFE (SX-PTFE; EB dose: 100 kGy), the new signals were observed besides the

Table II. The thermal properties of obtained samples; PTFE, radiation-crosslinked PTFE (RX-PTFE), thermo-chemical-crosslinked PTFE (CX-PTFE), synergetic-crosslinked PTFE (thermo-chemical and radiation; SX-PTFE)

	Melting temperature (℃)	*Crystallization temperature (℃)*	*Heat of crystallization (ΔHc) (kJ / kg)*
PTFE	326.9	307.7	24.9
CX-PTFE	325.1	306.4	24.7
RX-PTFE*	317.1	289.8	35.5
SX-PTFE*	314.2	287.7	33.0

*: EB dose for crosslinking was 100 kGy.

intense peak at – 124 ppm (int–CF_2–). For SX-PTFE, the several new peaks appeared at – 83 ppm, – 89 ppm, – 110 ppm, – 114 ppm and – 188 ppm, respectively. The signal in a range from – 100 to – 130 ppm corresponds to –CF_2–, as assigned by previous papers [6, 10, 16]. The small peaks at – 110 ppm and – 114 ppm have different chemical shifts from the int–CF_2– in the crystalline state (– 124 ppm), corresponding to the various kinds of –CF_2– groups with high dimensional structures by network formation in the PTFE matrix. The signals at – 110 ppm and – 114 ppm were assigned to the fluorine signals of Y-type crosslinking site and hexafluoropropylene (HFP), respectively, as previously reported [16]. Further, the peaks at – 83 ppm and – 89 ppm corresponds to –CF_3 were assigned to the fluorine signals of molecular chain end (–CF_3) group in amorphous and branching chain end group including chain end of perfluoroalkylvinylether, respectively, as previously reported [16].

The appearance of a signal at – 188 ppm is assigned to fluorine signal of >CF– group with Y-type crosslinking site in the polymer chain [6, 8, 16]. In the case of SX-PTFE, the peak intensity at – 188 ppm was higher than the thermo-chemical crosslinking (CX-PTFE) and the radiation-crosslinking (RX-PTFE). The increase in intensity of >CF– indicates the number of crosslinking sites in the PTFE with fluorinated-pitch matrix. Thus, the network density of synergetic-crosslinked PTFE (SX-PTFE) was higher than that of the thermo-chemical crosslinking (CX-PTFE) and the radiation-crosslinking (RX-PTFE).

Figure 5 shows the tensile strength and Young's modulus with the direction of 45 ° tensile properties of 1-ply sheet composites consist of plain-woven carbon fiber-reinforced RX-PTFE and carbon-fiber-reinforced SX-PTFE (fluorinated-pitch 1.8 wt% additive) as a function of EB dose. For the carbon fiber-reinforced RX-PTFE, tensile strength increases with increasing dose up to 500 kGy, and then tends to decrease with EB dose, as previously reported [15]. Young's modulus also increases with increasing the EB dose. For SX-PTFE composite, tensile strength and Young's modulus increase with increasing EB dose. Both tensile strength and Young's modulus of SX-PTFE composite were higher than those of RX-PTFE composite. The tensile strengths of SX-PTFE composite and RX-PTFE composite with crosslinking dose of 500 kGy were about 27.3 MPa and 32.2 MPa, respectively. The strength of the SX-PTFE composite was about 1.2 times higher than that of the RX-PTFE composite. In addition, the strength of CX-PTFE composite and RX-PTFE composite with an EB dose of 500 kGy was almost equal.

The Young's modulus of SX-PTFE composite and RX-PTFE composite with crosslinking dose of 500 kGy were about 452 MPa and 500 MPa, respectively. The Young's modulus of SX-PTFE composite was about 1.1 times higher than that of RX-PTFE composite.

By radiation-process of the fabrication, the decomposition gases are evolved from PTFE matrix and the mass decreases with increasing EB dose. The evolved gases will induce the micro defects and vacancies. In the case of RX-PTFE

In Polymer Durability and Radiation Effects; Celina, M., et al.;
ACS Symposium Series; American Chemical Society: Washington, DC, 2007.

composite, the de-lamination between PTFE and the carbon fibers will easily occur, and also RX-PTFE, which is matrix, is easily torn at the defects, *i.e.* poor toughness like as PTFE [17]. On the other hand, for SX-PTFE composite, the toughness of matrix would be improved by addition of fluorinated-pitch.

Table III shows the flexural properties of RX-PTFE composite with an EB dose of 500 kGy and SX-PTFE composite (fluorinated-pitch 1.8 wt% additive) with an EB dose of 500 kGy. For the three-point bending test of the sixth plys laminate panels, the flexural strength of SX-PTFE composite was about 1.1 times higher than that of the RX-PTFE composite. The flexural modulus of SX-PTFE composite was about 1.3 times higher than that of RX-PTFE composite. It was found that the flexural properties of SX-PTFE were improved, compared with RX-PTFE composite.

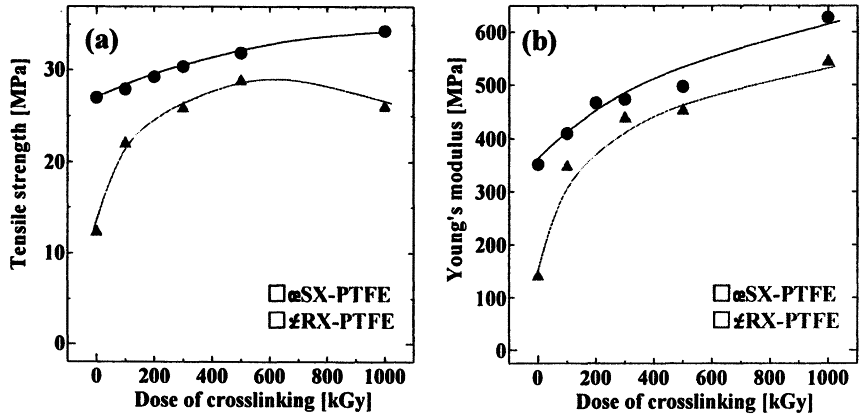

Figure 5 The tensile strength and the Young's modulus with the direction of 45 ° tensile properties of one ply sheet composites consist of plain-woven carbon fiber-reinforced RX-PTFE and the carbon-fiber-reinforced SX-PTFE (fluorinated-pitch 1.8 wt% additive) as a function of EB dose.

Table III. The flexural strength and flexural modulus of the carbon fiber-reinforced RX-PTFE (RX-PTFE composite) and the carbon fiber-reinforced SX-PTFE (SX-PTFE composite). Volume of carbon fiber was 54.3 %, Sixth plys laminated panel.

	Flexural strength (MPa)	*Flexural modulus (GPa)*
RX-PTFE composite	138.2	21.5
SX-PTFE composite	158.3	28.7

Table IV shows the change of contact angle against to various solvents between droplet and surfaces of the obtained materials. The water contact angles of reference materials i.e., PTFE and radiation crosslinked PTFE (RX-PTFE) are 104 ° and 102 °, respectively [15]. The water contact angle of thermo-chemical crosslinked PTFE (CX-PTFE) and synergetic crosslinked PTFE (SX-PTFE) are 109 ° and 107 °, respectively. The contact angle of water hardly changes by radiation, thermo-chemical, and synergetic crosslinking. In addition, the contact angle of other solvents hardly changed, as shown in Table IV. Thus, the wettability of the obtained materials was the same as that of non-crosslinked PTFE, *i.e.*, the wettability of obtained materials hold the original property.

Table IV. The contact angle between droplet and surfaces of obtained samples; PTFE, radiation-crosslinked PTFE (RX-PTFE), thermo-chemical-crosslinked PTFE (CX-PTFE), synergetic-crosslinked PTFE (thermo-chemical and radiation; SX-PTFE)

	Non-treatment	*Radiation*	*Thermo-chemical*	*Thermo-chemical+Radiation*
	PTFE	*RX-PTFE*	*CX-PTFE*	*SX-PTFE*
Water	104 °	102 °	109 °	107 °
Methyl alcohol	53 °	54 °	55 °	54 °
Acetone	78 °	76 °	77 °	78 °
Tetra-hydro-furan(THF)	46 °	45 °	48 °	46 °
Ethylen-glycol	91°	89°	91°	90°

Conclusion

The thermo-chemical-induced crosslinking of PTFE (CX-PTFE) has been demonstrated by using fluorinated-pitch without any other catalyst. By the solid-state ^{19}F-NMR spectroscopy, the new signal appeared at – 188 ppm. The signal is assigned to the fluorine signal of >CF– group, which represents Y-type crosslinking site. The obtained materials showed the good mechanical properties and the lower crystallinity, which were confirmed by tensile and flexural tests, and DSC analysis, compared with PTFE. Thus, the obtained material is confirmed to be crosslinked through thermal chemical reaction with decomposed the fluorinated-pitch.

The chemical-radiation synergetic crosslinking of PTFE (SX-PTFE) was carried out. By ^{19}F-NMR spectroscopy, the several new peaks were appeared at – 83 ppm, – 89 ppm, – 110 ppm, – 114 ppm and – 188 ppm, respectively. The peaks at – 83 ppm and – 89 ppm corresponding to $–CF_3$ were assigned to the

fluorine signals of molecular chain end (–CF_3) group in amorphous and branching chain end group including chain end of perfluoroalkylvinylether, respectively. The signals at – 110 ppm and – 114 ppm were assigned to the fluorine signals of Y-type crosslinking site and hexafluoropropylene (HFP), respectively. The appearance of a signal at – 188 ppm is assigned to the fluorine signal of >CF– group with Y-type crosslinking site. The network density of SX-PTFE was higher than that of CX-PTFE and RX-PTFE.

The mechanical properties of SX-PTFE composite were higher than those of CX-PTFE composite and RX-PTFE composite. The wettability of the obtained materials was the same as that of PTFE, *i.e.*, the wettability of obtained materials holds the original property.

Acknowledgements

The authors acknowledge Prof. Y. Hama of Waseda University for valuable discussions and suggestions throughout this study, as well as Dr. E. Katoh of NIAR for valuable discussions on ^{19}F-NMR spectroscopy and Mr. T. Hyuga of Waseda Uni. for assistance with the ^{19}F-NMR experiments. The authors thank Dr. T. Maeda and Dr. M. Saito of Osaka Gas Chemical Co.Ltd. for kindly supplying fluorinated-pitch. This study was performed by the projects research of RISE, Waseda Uni., "the manufacturing of high functional fluorinated-polymer materials", the research group members are greatfully acknowledged.

References

1. Tabata, Y. *Proc. Taniguchi Conf.*, June **1992**, Sapporo, Japan., pp118-120.
2. Sun, J.; Zhang, Y.; Zhong, X.; Zhu, X. *Radiat. Phys. Chem.* **1994**, *44*, 655.
3. Oshima, A.; Tabata, Y.; Kudoh, H.; Seguchi, T. *Radiat. Phys. Chem.* **1995**, *45*, 269.
4. Tabata, Y.; Oshima, A.; Takashika, K.; Seguchi, T. *Radiat. Phys. Chem.* **1996**, *48*, 563.
5. Tabata, Y.; Oshima, A. *Macromol. Symp.* **1999**, *143*, 337-358.
6. Katoh, E.; Sugisawa, H.; Oshima, A.; Tabata, Y.; Seguchi, T.; Yamazaki, T. *Radiat. Phys. Chem.* **1999**, *54*, 165.
7. Oshima, A.; Ikeda, S.; Seguchi, T.; Tabata, Y. *J. Adv. Sci.* **1997**, *9*, 60-66.
8. Oshima, A.; Ikeda, S.; Seguchi, T.; Tabata, Y. *Radiat. Phys. Chem.* **1997**, *49*, 279.
9. Oshima, A.; Ikeda, S.; Seguchi, T.; Tabata, Y. *Radiat. Phys. Chem.* **1997**, **49**, 581.
10. Oshima, A.; Ikeda, S.; Katoh, E.; Tabata, Y. *Radiat. Phys. Chem.* **2001**, 62, 39-45.

11. Oshima, A., Ikeda, S.; Kudoh, H.; Seguchi, T.; Tabata, Y. *Radiat. Phys. Chem.* **1997**, *50*, 611-615.
12. Maeda, T.; Fujimoto, H.; Yoshikawa, M.; Watanabe, N.; Touhara, H. *J. Fluorine Chem.* **1991**, *54*, 40.
13. Fujimoto, H.; Maeda, T.; Yoshikawa, M.; Watanabe N.; Touhara, H. *J. Fluorine Chem.* **1993**, *60*, 69.
14. Li, J.; Sato, K.; Ichizuri, S.; Asano, S.; Ikeda, S.; Iida, M.; Oshima, A.; Tabata, Y.; Washio, M. *Eur. Polymer J.* **2005**, *41*, 547-555.
15. Oshima, A.; Udagawa, A.; Tanaka, S. *Radiat. Phys. Chem.* **2001**, *62*, 77-81.
16. Oshima, A.; Hyuga, T.; Asano, S.; Mutou, F.; Ichizuri, S.; Li, J.; Miura, T.; Washio, M. *Nucl. Instr. and Meth. B* **2005**, *236*, 172-178.
17. Udagawa, A.; Oshima, A. *Japanese Patent*, Tokugan 2000-155902.

Chapter 19

Polymer Nanostructure Formation by Particle Beams

Shu Seki[1], Satoshi Tsukuda[1], Seiichi Tagawa[1], and Masaki Sugimoto[2]

[1]The Institute of Scientific and Industrial Research, Osaka University, Ibaraki, Osaka 567–0047, Japan
[2]Quantum Beam Science Directorate, Japan Atomic Energy Research Agency, Takasaki, Gumma 370–1292, Japan

High energy charged particle irradiation of polystyrene and polysilane derivatives is shown to cause crosslinking reactions leading to the formation of a polymer gel containing cylindrical nanostructures of regular length and thickness. The deposited energy density in a charged particle track controlled the spatial distribution of crosslinks of polymer molecules. The radial variation in dose along each ion track results in the formation of cylindrical structures with nm-sized radius of the cross-section. These cylindrical structures are well visualized as worm-like structures (nanowires). The similar schema for the formation of the nanowires have been demonstrated for the charged particle irradiation of a variety of polymeric materials including π-conjugated polymers, polymers for hydrogels, and proteins. The present results represent the potential utility of this technique for single-particle fabrication of nano-structures with sub-nanometer spatial resolution.

 © 2008 American Chemical Society

Introduction

The use of high-energy charged particles has extended to many fields in recent years. In medicine, non-homogeneous energy deposition along an ion trajectory (ion track) plays a crucial role in cancer radiotherapy [1], allowing for high spatial selectivity in the depth distribution of the radiation dose. The direct observation and application of ion tracks in media have also attracted interest in materials science, where it is known as nuclear track fabrication [2]. The technique has also been applied to the production of micro- and nano-sized pores in materials through chemical etching of the tracks [3]. The clear correlation between the etched pore and the characteristics of the incident charged particle has been utilized for measurement of the velocity and mass of the incident particles[4], and in particular for the measurement of galactic cosmic rays in space [5].

The radiation sensitivity of polymers, such as *G* values (number of reactions per 100 eV of absorbed dose), have been studied extensively for many polymers and types of radiation. Radiation induced crosslinking of polymers was formulated by Charlesby based on the statistical mechanics of polymer molecules, giving the *G* values for crosslinking (*G(x)*) and chain scission (*G(s)*) [6]. Cherlesby's theory has been extended by many groups to explain reactions in real polymer systems [7], as the initial formulation was based on an ideal polymer system involving a random distribution of molecular sizes and crosslinks and neglecting effects of the solid state structure of the target polymer. Ion beam-induced chemical reactions are an exceptional case in that the spatial distribution of the deposited energy by incident ions is non-homogeneous [8,9]. The specific properties of ion beams have been characterized by the linear energy transfer (LET), given by the energy deposition of an incident particle per unit length, and the effects of LET on the yield of chemical reactions in a medium, particularly crosslinking reactions in polymeric materials, have been investigated extensively [10].

The ion track radius is also an important parameter in such reactions, reflecting the local spatial distribution of energy deposited by an incident ion and influencing the character of subsequent chemical reactions [8-12]. We recently reported on main-chain scission and crosslinking reactions in a variety of polymer systems and proposed chemical core sizes in ion tracks based on discussion of the non-homogeneous spatial distribution of reactions [9-15]. Intra-track crosslinking reactions are also of interest with respect to the potential for the direct formation of nano-structured materials, and materials exhibiting these reactions have been successfully visualized in recent years [11,13]. However, despite the extensive experimental and theoretical study undertaken to date, many factors in the relationship between the ion track structure and the chemical core radius remain unclear. This paper proposes a new formulation that determines the chemical core radius in an ion track based on the initial

distribution of deposited energy, the efficiency of the chemical reactions, and the molecular structure of the target polymer materials.

Energy Distribution in an Ion Track

A charged particle penetrating into the polymer medium can release active intermediates at high density within a limited area along the track of a single ion, giving a non-homogeneous spatial distribution of chemical reactive intermediates. Ion irradiation at low fluence without overlapping between ion tracks produces single ion events in the target materials. In polystyrene, which is one of the most typical polymeric materials subjected to crosslinking reaction upon irradiation, only the molecules within an ion tracks are crosslinked with small chemical effects outside the ion track. The crosslinking reactions result in the formation of a cylindrical nanowire structure in thin films. The non-crosslinked area outside ion tracks can be removed by development with solvent (cyclohexane), utilizing the change in solubility due to the gelation of polystyrene. The nanowires formed by ion bombardment can therefore be completely isolated on the substrate.

These cylindrical chemical cores of the nanowires based on polystyrene (PS) can be visualized by atomic force microscopy (AFM), as shown in Fig. 1. In this section , polystyrenes with a variety of molecular weight were used as the target polymer materials, represented as PS*n* where the molecular weight increases from 2.1×10^3 to 1.1×10^6 with increasing number of *n* from 1 to 8. is the After the development procedure, the nanowires lie prostrate on the substrate surface, and are overlapped giving the entangled structures in some cases as shown in Fig. 1(c). It should be noted that the range of incident particle in the polymer media were set far longer than the thickness of the polymer films in all cases, thus all incident particles were passing through the polymer films and stopped in the substrates. The length of the nanowires reflects the thickness of the original polystyrene film, whereas the thickness (cross-section) of the nanowires increases with the molecular weight of the polystyrene. The average molecular size of the polymer is therefore a primary factor determining the thickness of the nanowires. However, the nanowire thickness also increased with the linear energy transfer (LET) of the ion beam, as the high-LET 500 MeV $^{197}Au^{31+}$ beam produced thicker wires than those prepared using the low-LET 400 MeV $^{84}Kr^{18+}$ beam.

The radii of the nanowires were determined by AFM as r_1 and r_2 which were defined as the half-width at half-maximum and the half height of the AFM traces of the nanowire cross-section, respectively. The values of r_1 and r_2 are typically observed as 11.3 and 3.4 nm for the nanowires based on PS1. The ration of r_1/r_2 showed considerable increase with the molecular weight of the polymers. The values of r_2 were much lower than r_1, showing that the nanowires formed an

elliptical cross-section due to sagging onto the substrate surface after development. Assuming that the nanowire cross-section is a simple ellipse, the nominal radius r is defined as follows to facilitate discussion of the distribution of deposited energy and crosslinking reactions on an ion track [16].

$$r = \sqrt{r_1 \times r_2} \quad (1)$$

The value of r increased with molecular weight of the polymer and LET of the ion beam, as shown in Table 1.

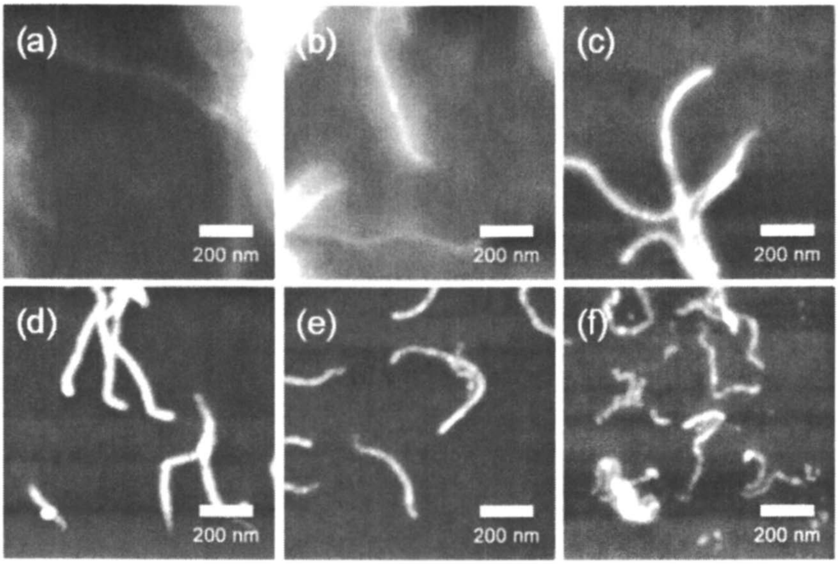

Figure 1. AFM micrographs of nanowires based on polystyrene (PS) showing the variation in size with molecular weight and the type of ion beam. The nanowires were formed by 450 MeV $^{129}Xe^{23+}$ beam irradiation to (a) a PS8 (M_n = 1.1 × 10^6) (b) a PS7 (M_n = 6.8 × 10^5) and (c) a PS4 (M_n = 1.2 × 10^5) thin films at 1.0 × 10^9 ions/cm^2. The nanowires were also formed by (a) 500 MeV $^{179}Au^{31+}$, (b) 450 MeV $^{129}Xe^{23+}$ and (c) 400 MeV $^{84}Kr^{18+}$ beams irradiation to PS3 (M_n = 5.15 × 10^4) thin films at (d) 5.1 × 10^8, (e) 6.9 × 10^8, and (f) 1.1 × 10^9 ions/cm^2.

At the center core of the ion track, the deposited energy density is greater than in the outer penumbra region. It is expected that the distribution of crosslinking points in an ion track will reflect the radial energy density, and that the number of crosslinking points in the core will be much larger than in the penumbra. For example, the core of nanowires formed in a polysilane derivative has been shown to have a three-dimensional Si-C structure [9,11].

According to this hypothesis, the following formulae have been proposed to describe the coaxial energy in an ion track [8]:

$$\rho_{\mathrm{p}}(r) = \frac{LET}{2}\left[2\pi R^2 \ln\left(\frac{e^{1/2} r_{\mathrm{p}}}{r_{\mathrm{c}}}\right)\right]^{-1} ; r_{\mathrm{c}} < R \leq r_{\mathrm{p}} \qquad (2)$$

Here, ρ_{p} is the deposited energy density in the penumbra area, and r_{c} and r_{p} are the radii of core and penumbra areas.

The nominal radius r is much larger than the core size suggested by theoretical considerations [8]. For example, the theoretical physical core size(r_{c}) for a 500 MeV Au ion beam is 0.74 nm, whereas r obtained for this ion beam in the present experiments is 6.2–27.6 nm. The radial margins of the nanowires therefore lie in the penumbra area, where crosslinking occurs by energy deposition from secondary electrons. It is expected that the polymers form a gel in this region, with one crosslinking point per polymer chain at the outer radial boundary. The deposited energy density (ρ_{cr}) at r is therefore adopted as the critical energy density of gelation for polystyrene. Polymer gelation requires the introduction of at least one crosslink per polymer molecule. Assuming a contribution solely from the crosslinking reactions in the chemical core, ρ_{cr} is given by

$$\rho_{\mathrm{cr}} = \frac{100\rho A}{G(x)mk} \qquad (3)$$

where ρ is the density of polymers, m is the molecular weight of the monomer unit, A is Avogadro's number, k is the degree of polymerization, and $G(x)$ is the efficiency of crosslinking reactions induced by irradiation (number of reactions per 100 eV energy absorbed). The deposited energy densities ρ_{cr} for the 500 MeV Au and 450 MeV Xe ion beams were estimated for polystyrene films of various molecular weights (mk) using Eq. (3) with the parameter of $G(x)$, ρ, and m as 0.38 $(100\ \mathrm{eV})^{-1}$, 1.08 g/cm^3, and 104 g/mol, respectively [16]. The value of $G(x)$ was determined from the geration dose upon irradiation of PS1. The results are listed in Table 1, and estimated ρ_{cr} variation regard to M_n is in good agreement between these two heavy ion beams. Although the nominal radii of nanowires formed by exposure to the two beams differed for the same polymer weight, the deposited energy densities at the radial margin were almost identical, and decreased with increasing polymer weight. Thus, the higher-LET ion beam (500 MeV Au) maintains elevated energy densities to a greater radial distance compared to the lower-LET ion beam (450 MeV Xe), while the energy density required to induce gelation by crosslinking increases with the molecular weight of the polymer.

Substitution of ρ_{cr} for $\rho_p(r)$ in Eq. (2) gives the radius of the "theoretical chemical core" r', as follows [9].

$$r'^2 = \frac{LET \cdot G(x)mk}{400\rho\pi A}\left[\ln\left(\frac{e^{1/2}r_p}{r_c}\right)\right]^{-1} \tag{4}$$

The experimental nominal radius (r) and theoretical chemical core radius (r') are summarized in the table 1. These values are in good agreement for thicker nanowires, but the experimental values are much larger for thinner nanowires. This can be attributed to variations in the efficiency of energy leakage from the core to the penumbra area, and the size of molecules with respect to the wire diameter. The ion track model employed in the present paper is highly simplified, treating the deposited energy density in the core region as constant values. In reality, however, the energy density in the penumbra increases close to the boundary with the core, which will affect the efficiency of energy leakage from the core in a radius-dependent manner. The effect of relative molecular size can be seen in the shapes of the nanowires, where wires formed in low molecular weight polymer are worm-like, whereas those in high molecular weight films are rod-like. These effects of energy leakage and the shape and size of polymer chains must be considered in discussion of the deposited energy density.

Table 1. Sizes of Polystyrene Nanowires

	r and r' (nm)		ρ_{cr} (eV/nm^3)	
Entry	*500 MeV* $^{197}Au^{31+}$	*450 MeV* $^{129}Xe^{23+}$	*500 MeV* $^{197}Au^{31+}$	*450 MeV* $^{129}Xe^{23+}$
PS1	6.2(1.4)[a]	-	4.2	-
PS2	6.9(2.9)	-	3.4	-
PS3	10.7(6.8)	8.1(5.8)	1.4	1.73
PS4	12.0(10.2)	10.8(8.6)	1.1	0.99
PS5	14.4(13.0)	12.1(11.1)	0.78	0.79
PS6	18.4(17.8)	17.0(15.0)	0.48	0.40
PS7	26.0(24.7)	20.1(20.8)	0.24	0.29
PS8	27.6(31.4)	21.4(26.4)	0.21	0.25

[a]Values in the parenthesis are r' estimated by eq. 4; PS: polystyrene, PS1 (M_n = 2.1 × 10^3), PS2 (M_n = 9.0× 10^3), PS3 (M_n = 5.1 × 10^4), PS4 (M_n = 1.2 × 10^5), PS5 (M_n = 1.9 × 10^5), PS6 (M_n = 3.5 × 10^5), PS7 (M_n = 6.8 × 10^5), PS8 (M_n = 1.1 × 10^6)

Precise Size Control of Nanowires

The nanowires produced by charged particle irradiation into polymeric thin films have their ultra-small dimension of cross-section of which radius ranges from ~1 to a few tens nm. One of the primary factor determining the radius of the nanowire is the "size" of molecules, which is often quantified in terms of "molecular weight" of the target polymer materials [9,11,13-16]. However, polymeric materials generally show a distribution of the molecular weight, and the length of their chains can not be determined discretely. Flexibility of the polymer backbone is also important to consider the global configuration of the molecules, hence the "size" of the molecules. Statistical modeling of the global configuration of polymer molecules have been vigorously performed, and the scaling law has been successfully developed to analyze the chain configuration [17]. Several important properties of the polymeric materials show quantitative correlation with the flexibility of their backbone. Gyration radius of polymer molecules represents the "size" of the molecule in condensed phase, and has been well interpreted by the scaling law on the basis of flexible chain model.

The polymers used in the present study have relatively "flexible" backbones, providing sufficient modeling accuracy based on the scaling law in their molecular weight ranges. For instance, persistence length (average length of "rod-like" units in the polymer chain) of polystyrene has been measured as ~ 1 nm in a typical solution or in the amorphous phase, thus the gyration radius of the molecule with 100 monomer units is expected to be less than 10 nm [18]. The small radius of the polymer molecules is, however, almost equivalent to the size of the nanowires produced by the present technique. This suggests that the contribution from the chain configuration is required for precise analysis of the radial size of the nanowires. In the present section, Si backbone conjugated polymers, polysilanes, were chosen as target polymer materials [19]. Backbone conformation of the polysilane derivatives has been well investigated in relation to their strong near-UV optical absorption [19,20], because the absorption attributed to the transition between their backbone conjugated molecular orbitals has been very sensitive to the conformational and vibronic transformation of their main chains [19-23]. Hence, the global conformation of the macromolecules can be predicted by simple spectroscopy of the polymers.

Our group previously reported that radiation induced crosslinking reactions in polysilane derivatives are mainly promoted by side-chain dissociated silyl radicals, and that the predominant reaction is determined by the radical concentration in the ion tracks [14,20,21]. Thus, the distribution of crosslinks in an ion track is expected to obey the equations (2) and (3) given in the previous section, and the crosslinking reaction also gives cylindrical poly(methylphenylsilane) (PMPS)-based nanowires with fairly controlled sizes as shown in Fig. 2. Using the reported value of $G(x)$ = 0.12 derived from

radiation-induced changes in molecular weight [21,24], the non-empirical formulation of Eq. (4) gives the theoretically predicted values of *r*'. The values of *r*' are consistent with the experimental values for polymers with sufficient chain length (PMPS1 and PMPS2), however, a considerable discrepancy occurs between the calculated and experimental results for polymers with shorter chains.

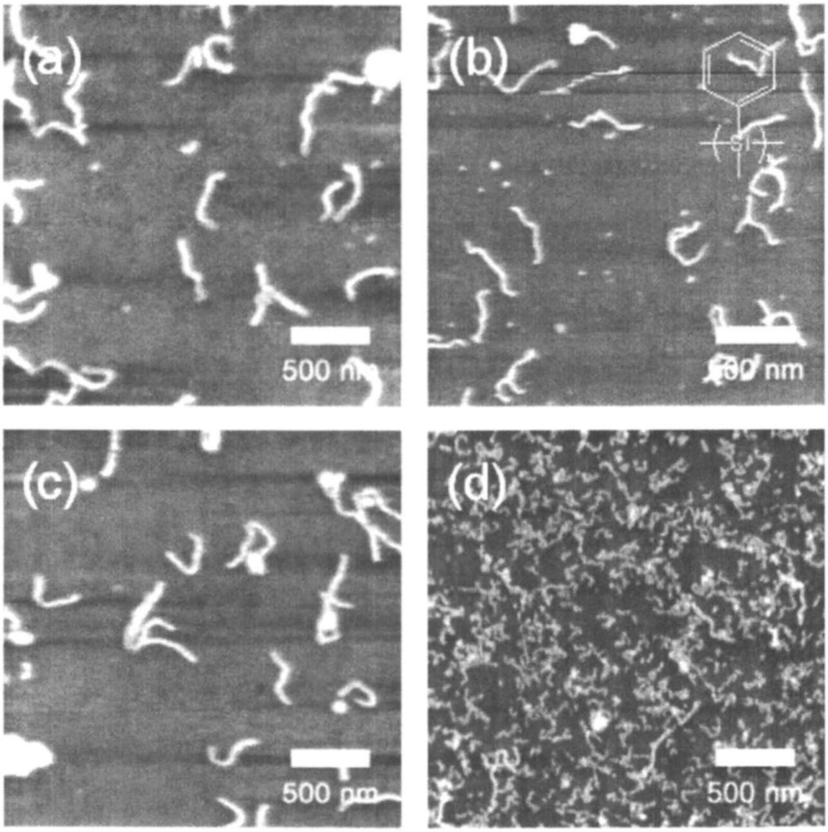

Figure 2. AFM micrographs of nanowires based on poly(methylphenylsilane) (PMPS, Chemical structure is presented in (b) as superimposed one) showing the variation in size with molecular weight and the type of ion beam. The nanowires were formed by 450 MeV $^{129}Xe^{23+}$ beam irradiation to (a) PMPS2 (M_n = (1.1-1.5) × 10^5) (b) PMPS4 (M_n = (4.6-5.2) × 10^3) thin films at 4.7 × 10^8 ions/cm^2. The nanowires were also formed by (c) 450 MeV $^{129}Xe^{23+}$ and (d) 5.1 MeV $^{28}Si^{2+}$ beams irradiation to PMPS3 (M_n = (0.95-1.0) × 10^4) thin films at (c) 4.7 × 10^8 and (d) 5.5 × 10^{10} ions/cm^2.

In Polymer Durability and Radiation Effects; Celina, M., et al.;
ACS Symposium Series; American Chemical Society: Washington, DC, 2007.

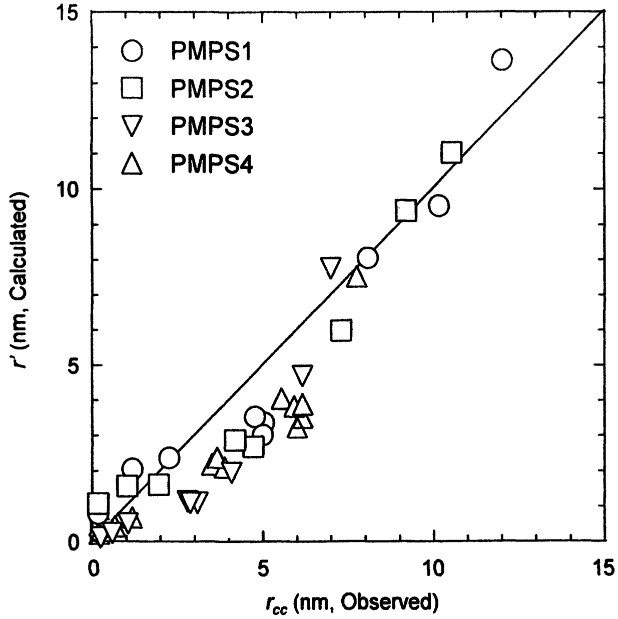

Figure 3. Correlation between chemical core radius (r_{cc}) estimated experimentally by use of Eq. (1) and those (r') theoretically predicted using Eq. (6). Molecular weight of the polysilanes are M_n = 2.6-4.6 × 10^5 (PMPS1), 1.1-1.5 × 10^5 (PMPS2), 0.95-1.0 × 10^4 (PMPS3), and 4.6-5.2 × 10^3 (PMPS4), respectively with small molecular weight distributions (Mw/Mn) less than 1.8.

The global configuration of the polymer molecules depends heavily on the length of the polymer chains, leading to transformation from random coil (long chain) to rod-like (short chain) conformations. The gyration radius (R_g) of a polymer molecule, which determines the size of a molecule spreading in the media, is correlated with this transformation. The following expression was suggested for this correlation between R_g and the degree o fpolymerization (N):

$$R_g = \kappa N^{\alpha} \quad (5),$$

where κ is a constant. The index α depends on the global configuration of the molecules, varying from 0.4 (random coil) to 0.5 (rod-like). The persistence length of a chain has been reported to be 1.1 nm for PMPS [19], and the length of a monomer repeating unit in an Si chain, derived from the Si-Si bond length of 0.2414 nm, is 0.20 nm with a dihedral angle of 114.4° [22]. Based on these structural parameters, the scaling law for a helical worm-like chain model [25] results in an index α of 0.410, 0.419, 0.485, and 0.492 for PMPS1–4,

respectively. Thus, the effective volume of a polymer chain can be simply calculated as $4/3\pi R_g^3$, and the substitution of $mN/\rho A$ in Eq. (4) with the effective volume leads the expression

$$r'^2 = \frac{LET \cdot G(x) N^{3\alpha}}{400\pi\beta} \left[\ln\left(\frac{e^{1/2} r_p}{r_c} \right) \right]^{-1} \quad (6),$$

where β is the effective density parameter of the monomer unit (kg m^{-3}). Based on Eq. (6), the calculated value of r' is plotted again the experimental values (r_{cc}) in Figure 3. All polymers, with a variety of molecular weights, follow a single trend, and the calculated values display good correspondence in the range $r_{cc} > 7$ nm. The underestimate of r_{cc} by Eq. (6) for $r_{cc} < 7$ nm suggests that the initial deposition of energy and the radial dose distribution estimated by Eq. (2) do not account for the radial distribution of chemical intermediates and thus cannot model the concentration of crosslinking in the core of the ion track. The value of *G(x)* increases dramatically with an increase in the density of reactive intermediates. Based on the assumption that *G(x)* is a function of the density of deposited energy, the present results indicate that the yield of the chemical reaction is dependent on the energy density. Crosslinking reactions in ion tracks therefore have potential for not only single-particle fabrication with sub-nanometer-scale spatial resolution for any kind of crosslinking polymer, but also the study of nano-scale distributions of radial dose and chemical yield in an ion track.

Summary

Based on the strong dependence of the chemical yield of crosslinking reactions on the energy density deposited non-homogeneously by high energy single particle, a cylindrical scheme was derived to represent the distribution of crosslinks in an ion track. The cylindrical structures were clearly visualized by AFM as worm-like structures (nanowires) associated with the core of ion tracks, and analyzed quantitatively by the simple model of the transformation of their cross-section into an ellipse. The size of these nanowires determined by the analytical representation was confirmed to match that observed by AFM. The dependence of the size of nanowires on the chain length of the polymer and the LET of incident ions was formulated in terms of the radial variation of dose in ion tracks and the global chain configuration of the polymers, providing a good fit of the experimental results for nanowire with radius of 7 nm or greater. The present results also demonstrate the possibility of single-particle fabrication of nano-structures with sub-nanometer spatial resolution.

Acknowledgement

The authors thank Dr. Y. Kunimi and Dr. K. Maeda of the Institute of Scientific and Industrial Research (ISIR), Osaka University. This work was supported in part by a Grant-in-Aid for Scientific Research from the Japan Society for the Promotion of Science (JSPS).

References

1. Wilson, R. R. *Radiology* **1946**, *47*, 487.
2. *Nuclear Tracks in Solid*, Fleisher, R. L.; Price, P. B.; Walker, R. M., University of California Press, **1975**, Los Angels.
3. Price, P. B.; Walker, R. M. *Nature* **1962**, *196*, 732; Fleischer, R.L.; Price, P.B. *Science* **1963**, *140*, 1221.
4. Bean, C. P.; Doyle, M. V.; Entine, G. *J. Appl. Phys.* **1970**, *41*, 1454.
5. Cartwright, B. G.; Shirk, E. K.; Price, P. B. *Nucl Instr. Meth.* **1978**, *153*, 457.
6. Charlesby, A. *Proc. R. Soc. London Ser.* **1954**, *A222*, 60; Charlesby, A. *Proc. R. Soc. London Ser.* **1954**, *A224*, 120.
7. Saito, O. *J. Phys. Soc. Jpn.* **1958**, *13*, 1451; Inokuti, M. *J. Chem. Phys.* **1960**, *33*, 1607; Zhang, Y. F.; Ge, X. W.; Sun, J. Z. *Radiat. Phys. Chem.* **1990**, *35*, 163; Olejniczak, K.; Rosiak., J.; Charlesby, A. *Radiat. Phys. Chem.* **1991**, *37*, 499.
8. Magee, J. L.; Chatterjee, A. *J. Phys. Chem.* **1980**, *84*, 3529; Chatterjee, A.; Magee, J. L. *J. Phys. Chem.* **1980**, *84*, 3537.
9. Seki, S.; Tsukuda, S.; Maeda, K.; Matsui, Y.; Saeki, A.; Tagawa, S. *Phys. Rev.* **2004**, *B 70*, 144203.
10. LaVerne; J.A. *J. Phys. Chem.* **1996**, *100*, 18757; Seki, S.; Shibata, H.; Ban, H.; Ishigure, K.; Tagawa, S. *Radiat. Phys. Chem.* **1996**, *48*, 539.
11. Seki, S.; Maeda, K.; Tagawa, S.; Kudoh, H.; Sugimoto, M.; Morita, Y.; Shibata, H. *Adv. Mater.* **2001**, *13*, 1663.
12. Seki, S.; Tsukuda, S.; Yoshida, Y.; Kozawa, T.; Tagawa, S.; Sugimoto, M.; Tanaka, S. *Jpn. J. Appl. Phys.* **2003**, *42*, 4159.
13. Tsukuda, S.; Seki, S.; Tagawa, S.; Sugimoto, M.; Idesaki, A.; Tanaka, S.; Ohshima, A. *J. Phys. Chem.* **2004**, *B108*, 3407.
14. Seki, S.; Maeda, K.; Kunimi, Y.; Tagawa, S.; Yoshida, Y.; Kudoh, H.; Sugimoto, M.; Morita, Y.; Seguchi, T.; Iwai, T.; Shibata, H.; Asai, K.; Ishigure, K *J. Phys. Chem.* **1999**, *B103*, 3043
15. Seki, S.; Kanzaki, K.; Yoshida, Y.; Shibata, H.; Asai, K.; Tagawa, S.; Ishigure, K. *Jpn. J. Appl. Phys.* **1997**, *36*, 5361.
16. Tsukuda, S.; Seki, S.; Sugimoto, M.; Tagawa, S. *Appl. Phys. Lett.* **2005**, *87*, 233119.

17. *Statistical Mechanics of Chain Molecules*, Flory, P.J., John Weily & Sons Inc., **1969**, New York.
18. *Polymer Handbook 4th Edition*, Brandrup, J., Immergut, E.H., Grulke, E.A. Eds., Wiley Interscience, **1999**, Hoboken, New Jersey.
19. Seki, S.; Y.; Yoshida, Y.; Tagawa, S.; Asai, K. *Macromolecules* **32** (1999) 1080 ; Seki, S.; Koizumi, Y.; Kawaguchi, T.; Habara, H.; Tagawa, S. *J. Am. Chem. Soc.* **2004**, *126*, 3521.
20. Seki, S.; Cromack, K.R.; Trifunac, A.D.; Yoshida, Y.; Tagawa, S.; Asai, K.; Ishigure, K. *J. Phys. Chem.* **1998**, *B102*, 8367.
21. Seki, S.; Matsui, Y.; Yoshida, Y.; Tagawa, S.; Koe, J.R.; Fujiki, M. *J. Phys. Chem.* **2002**, *B106*, 6849; Seki, S.; Tagawa, S.; Ishigure, K.; Cromack, K.R.; Trifunac. A. D. *Radiat. Phys. Chem.* **1996**, *47*, 217.
22. Koe, J.R.; Powell, D.R.; Buffy, J.J.; Hayase, S.; West, R. *Angew. Chem. Int. Ed.* **1998**, *37*, 1441.
23. Fujiki, M. *J. Am. Chem. Soc.* **1996**, *118*, 7424.
24. Seki, S.; Tsukuda, S.; Maeda, K.; Tagawa, S.; Shibata, H.; Sugimoto, M.; Jimbo, K.; Hashitomi, I.; Koyama, A. *Macromolecules*, **2005**, *38*, 10164.
25. *Helical Wormlike Chains in Polymer Solutions*, Yamakawa, H., Springer, Berlin, 1997; Yamakawa, H.; Abe, F.; Einaga, Y. *Macromolecules* **1994**, *27*, 5704.

Chapter 20

Effects of Protons, Electrons, and UV Radiation on Carbon Nanotubes

Chong Oh Lee[1], Ebrahim Najafi[1], Jae Yong Kim[3], Song-Hee Han[4], Takhee Lee[1], and Kwanwoo Shin[2,*]

[1]Department of Materials Science and Engineering, Gwangju Institute of Science and Technology, Gwangju 500–712, South Korea
[2]Department of Chemistry, Sogang University, Seoul, 121–742, South Korea
[3]Department of Physics, Hanyang University, Seoul 133–791, South Korea
[4]Advanced Photonics Research Institute, Gwangju Institute of Science and Technology, Gwangju 500–712, South Korea

The effects of high energy radiations, including proton, electron and UV, on the physical and chemical properties of carbon nanotubes (CNT) were investigated. The CNTs sheets were irradiated by high energy proton beam of 10 MeV, electron beam of 2 MeV, and UV radiation in ambient environment, and surface functionalization and morphological structures of CNTs before and after high-energy radiations were monitored by X-ray photoelectron spectroscopy, infrared and Raman spectroscopy. When CNTs were irradiated by proton and electron particles, reactions were induced by the transfer of kinetic energy of the bombarding particles while UV-light dissociated adsorbed O_2 molecules into atomic oxygens, leading to the surface oxidation to CNTs. The irradiated CNTs exhibited radiation induced changes, distinct from native properties inherited from the classical synthetic routes.

 © 2008 American Chemical Society

Introduction

Satellites, spacecraft and equipment used in particle accelerators for high energy nuclear physics involve exposure to high energy radiation and thermal cycling. For example, the radiation environment in space and the atmosphere consists of trapped protons and electrons, cosmic radiation and neutrons. Radiation effects cause extensive damage to a space facility, weakening its performance and lifetime, include latchup, interference, degradation, charging, sputtering, erosion and puncture of materials [1]. As summarized in Figure 1, their energies in space and the atmosphere range from several eV to one GeV – equivalent; Solar cosmic rays, with energies of 10^7 to 10^{10} eV, and galactic cosmic rays, with energies of 10^{10} to 10^{15} eV, long-wave infra red (IR) and ultra violet (UV) radiation in ozonized environments. Without appropriate protection, the exposed surface coatings, especially organic thin films, undergo dissociation, abstraction, and additional reactions that lead to severe mechanical damage, eventually resulting in system failure of the underlying electronics. Further, a single source can induce different reactions on a target, depending on its energy level. Therefore, much effort has been made, on the one hand, to develop advanced synthetic routes by utilizing radiation reactions and, on the other, to test radiation resistant coating surfaces, primarily with the aim of preventing degradation reactions.

One of common approaches for strengthening the durability against radiation, is the addition of fillers to the matrix materials. Carbon nanotubes (CNT)s have inspired scientists and engineers to examine a wide range of potential applications [2,3] as exotic filler materials, since the discovery of their extraordinary mechanical, electrical, magnetic and thermal properties [4].

- The elastic modulus is ~ 1 TPa for single-walled nanotubes (SWNT) and ~ 0.3- 1 TPa for multi-walled nanotubes (MWNT).
- The strength is 50-500 GPa for SWNT and 10-60 GPa for MWNT.
- The resistivity is 5-50 μΩcm.
- The thermal conductivity is theoretically as high as 3000 $Wm^{-1}K^{-1}$.
- The thermal expansion is negligible, while thermal stability is more than 700 °C in air and 2800 °C in vacuum.

These properties are mainly originated from the molecular structures of CNTs, which consist of graphene sheets rolled to form hollow cylinders with an extremely high aspect ratio [5]. Moreover, CNTs can be ether metallic or semi-conducting tubes, depending on their diameter and/or chirality [5]. There are two types of CNTs: SWNTs and MWNTs. Details, such as structure, synthesis methods, application and properties, are well documented [4], [5], [6].

As described above, the unique properties of CNTs provide excellent advantages for many applications and much effort has been focused on developing methods that permit the selective and, more importantly, controlled functionalization of CNTs. Furthermore, since several micrometer-long CNT chains are physically entangled and tightly bundled due to their strong van der Waals interaction, CNTs tend to segregate in most solvents [7]. Consequently, an appropriate chemical modification is necessary to disturb the charge balance around CNTs, or to attach the organic moieties, leading to an enhanced solubility in common organic and aqueous solvents [8-11].

One of the promising methods is to introduce various functional groups on their nonreactive surfaces via oxidative processes [12]. Although many studies have addressed the covalent modification of CNTs in an aqueous environment, little attention has been devoted to dry methods. Dry processes support a mild oxidizing environment and, as a result, are usually less effective than wet methods. Furthermore, dry methods require the accurate control of the temperature, atmosphere, and reaction time during the process [13, 14].

In this regard, much research has focused the direct modification of the CNT surface using intense radiation. This has been applied to energetic particles induced chemical and structural modification of CNT and polymer-CNT composites [15, 16, 17]. In particular, proton irradiated graphite shows the induced magnetic ordering [18]. The proton irradiation of CNTs mostly results in morphological damage, such as welding, curves and fractions of small pieces, and chemical modifications forming C-H bonds [15,19,20]. In this chapter, potential methods for the covalent functionalization of CNTs using exposure to high energy irradiation, including accelerated protons, electrons and UV will be presented. Due to the nature of energetic radiation, some unwanted defects are also highly expected, as shown in Figure 1; a proton beam with E ~ keV can cause a sputtering effect while protons with an energy of ~100 MeV, can be adsorbed by CNTs. Hence, the collision of energetic particles with a carbon atom will results in displacement of the atom and a number of primary knock-on atoms which leave the tube or displace other atoms in the CNT [17].

In addition, such radiation may impinge on CNT-containing devices or composites, causing undesirable effects, such as electrical interference, charging, erosion and puncture of the target surface. Since the CNTs are one of the most common fillers mixed into polymeric matrices to strengthen the durability against radiation, the question as to whether the reinforcements are fundamental to structural uniqueness of CNTs or whether they are due to specific interactions of the polymer adjacent to the CNT networks has not been answered. In order to address this issue, which is critical to understand the reinforcement mechanism, we must first investigate the radiation induced properties of CNT surface under various high energy radiations, which are comparable to the aerospace environment. Therefore, we investigated chemical and morphological changes of CNTs due to energetic particles, including protons and electrons, and UV radiation on CNTs.

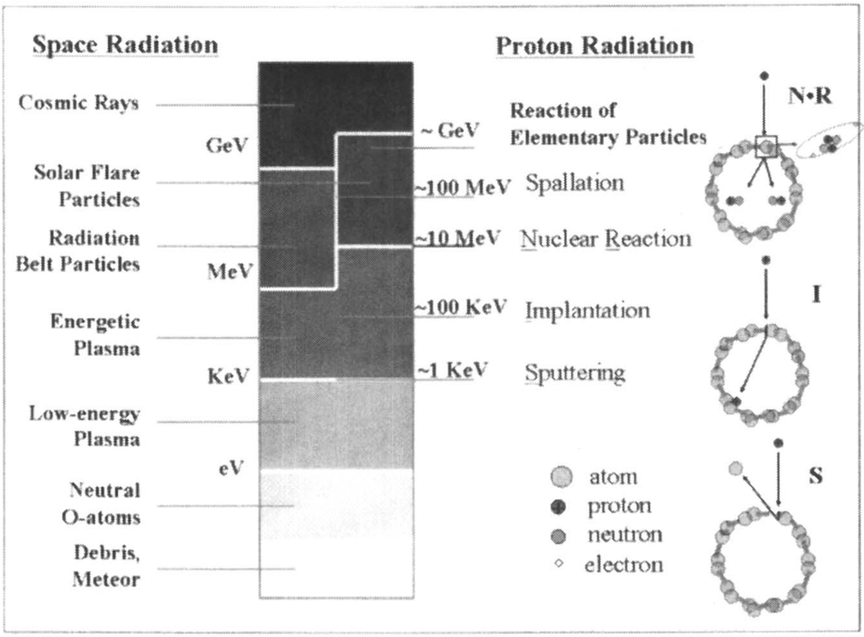

Figure 1. Charged particle energy in a space radiation environment [1] and proton radiation effects.

Experimental

Radiation Sources

Proton radiation was carried out using the MC-50 Cyclotron at the Korea Institute of Radiological and Medical Sciences (KIRAMS) [21]. The proton energy of the MC-50 can be tuned to 38 MeV by cyclotron adjustment and/or an Al energy degrader placed in front of the target [22]. Figure 2a shows its main components. The degrader can control the exit beam energy and the scatterer in the figure also tunes the beam fluence and flux on the target area in Figure 2a. Accelerated protons with energies of 10, 20 and 35.7 MeV were used in this experiment. Detailed conditions, such as radiation energy, dose, and fluence are listed in Table I.

The electron beam were generated from the 2 MeV electron accelerator at the Korea Atomic Energy Research Institute (KAERI). Figure 2b shows a schematic of the electron accelerator. The basic components are as follows: a

300-keV electron gun, a RF bunching cavity, two RF acceleration cavities, a 180-degree bending magnet, and a beam dump [23]. The sample stage was located in the middle between a dump and a kicker magnet. The diameter of the plate of the sample stage was about 20 cm. The nominal kinetic electron energy was 1.5 MeV - 2.0 MeV. The accelerator current was 6 A at peak and 45 mA, on average. Our experiments were performed at an energy of 2 MeV under ambient conditions. The radiation doses were 0, 60, 120, 180 and 240 kGy for each sample. A kilogray (kGy) represents the dose absorbed by the target materials, and is equal to 1×10^3 joule/kg. All experimental conditions are listed in Table I.

Samples for UV/O_3 radiation were also prepared by irradiation with UV in the atmosphere for 60 minutes using a conventional UV/O_3 cleaner (Model # 42-220, Jelight). In order to provide a homogeneous exposure, samples were manually stirred every 10 minutes with a spatula. The UV output of the UV/O_3 generator was 28,000 μWatt per cm^2 at a wavelength of 254 nm.

Materials

The CNTs, both single-walled nanotubes (SWNT) and multi-walled nanotubes (MWNT) prepared by chemical vapor deposition (CVD) and arc-discharge (AD) methods, respectively, were purchased from Iljin Nanotech, Co., Korea. For proton and electron irradiation experiments, CNTs sheets were prepared as shown in Figure 2 by filtration of the CNT solution mixed in dimethylformamide through a cellulose membrane (pore size: 0.45 μm). The thickness of the CNT sheets was approximately 0.5 mm, and they were 47 mm in diameter. After drying in a vacuum oven at 80 °C for 24 hours, CNT sheets (Figure 2) were obtained. These sheets were used in the radiation experiments, and were used for analysis such as SEM, Raman spectroscopy and XPS without any further treatment. For a dispersion test, a CNT powder was used instead of the CNT sheets.

The morphology of the CNTs was examined by a scanning electron microscopy (SEM), transmission electron microscope (TEM), Raman spectroscopy and X-ray photoelectron spectroscopy (XPS). Micro-Raman spectra for CNTs, in powder and/or sheet were collected by a Renishaw Raman microscope (model-Inviareflex) using the 632.8 nm line of 1.5 mW HeNe laser, focused down to a diffraction limited spot size of about 1 μm. The incident laser beam was focused onto the specimen surface through a 50 × objective lens. XPS measurements were performed using a model Multilab ESCA 2000 (VG Co.). The spectrometer is equipped with a non-monochromatic MgK_α X-ray source generating photons with energy of a 1253.6 eV. The system pressure was normally maintained below 10^{-9} Pa. All core level binding energies were referenced to the C1s signal at the binding energy, E_b, of 284.6 eV. The CNT sheets for XPS measurements were mounted on the probe tip by means of double-sided adhesive tape.

Table I. Experimental conditions for proton, electron, and UV radiation

Radiation Source	Facility	Radiation Energy	Radiation Conditions (time/dose /flux)	Sample/Type
Electron	Electron Accelerator (KAERI)	2 MeV	60,120,180,240kGy	SWNT(AD)/Sheet and powder MWNT /Powder
Proton	MC-50 Cyclotron (KIRAMS)	10 MeV	5,10,30,60 min./ 3.83×10^8P/cm^2/sec	SWNT(AD)/ Sheet
UVO	UV/O_3 Generator (Jelight)	28,000 μW/cm^2 (at 254 nm)	0,60,180 min	MWNT(CVD)/ Powder

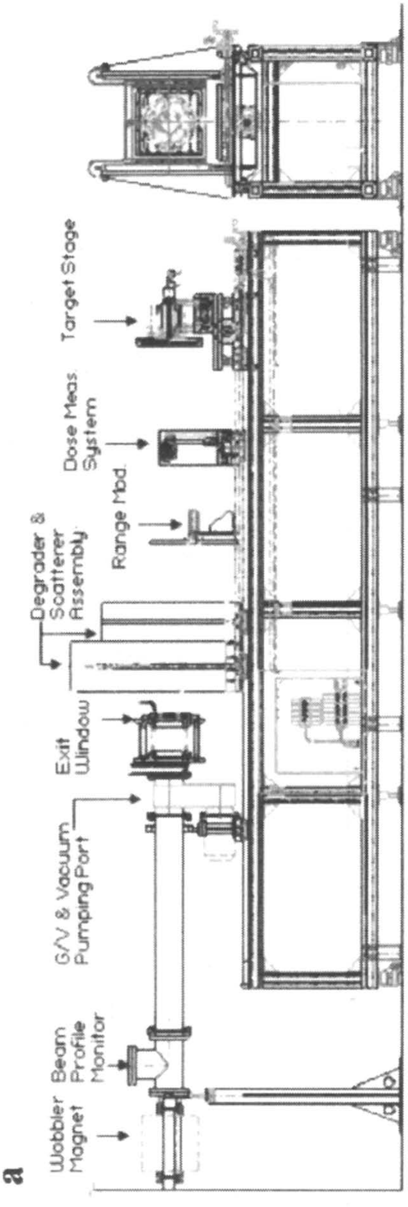
a
Wobbler Magnet
Beam Profile Monitor
G/V & Vacuum Pumping Port
Exit Window
Degrader & Scatterer Assembly
Range Mod.
Dose Meas. System
Target Stage

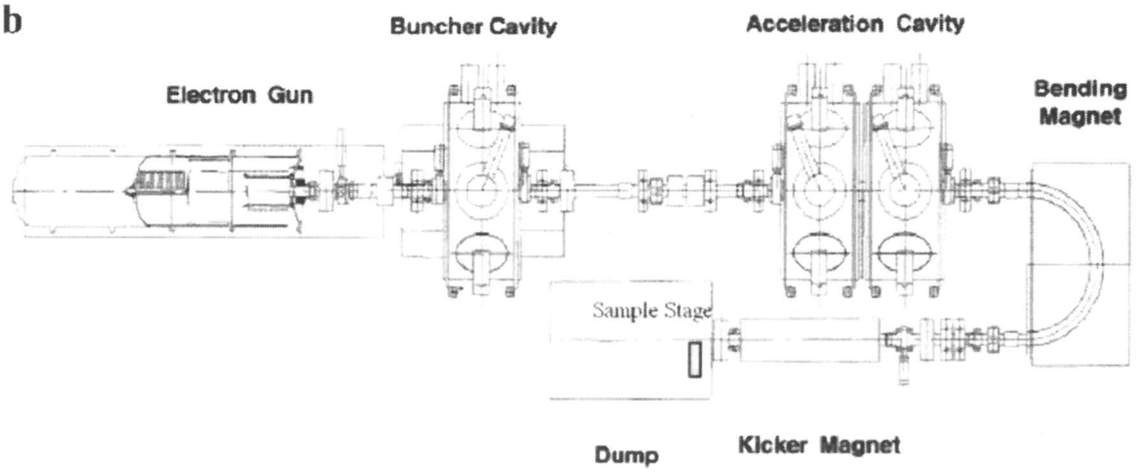

Figure 2. (a) MC-50 Cyclotron setup at the KIRAMS for proton radiation [19] (b) the electron beam accelerator at the KAERI for electron radiation [20].

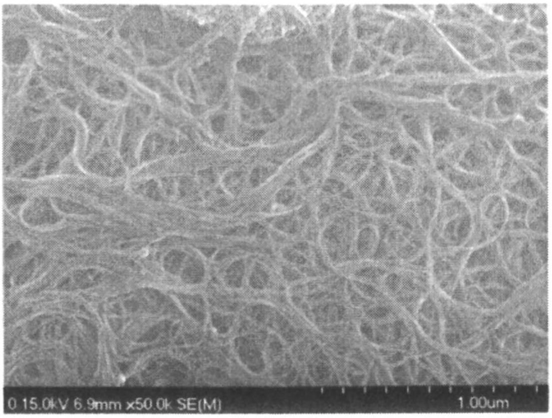

Figure 3. SEM image of SWNT sheets for proton and electron radiation.

Surface modifications by electron, proton and UVO Irradiation

Chemical changes

Since protons and electrons are known to transfer their energy to target materials by direct collision, inducing excitation, ionization and knock-on collision reactions, those types of radiation are often used as a very effective method for modifying the native structures of materials. Reactions on CNTs from proton and electron particles can then be induced by the transfer of kinetic energy of the bombarding particles. In addition, very reactive atomic oxygen is generated when ambient oxygen is dissociated by irradiation at 184.9 nm and ozone at 253.7 nm, thus promoting a degree of oxidative modification of CNTs [26, 27]. Fewer investigations have been devoted to studies of principal radiation effects, which might vary, depending on the radiation sources used and the energies involved.

XPS and FT-IR were used to characterize the modified CNT surfaces. The combined results provided quantitative information on the chemical composition and structure of CNTs. For XPS, when an X-ray beam is directed at the SWNT surface, the energy of the X-ray photon is absorbed by a carbon core electron. The core electron escapes from the atom if the photon energy is sufficiently large. Since CNTs are made up of a hexagonal lattice of carbon atoms analogous to the atomic planes of graphite, one can easily obtain the main peak at 285 eV from C1s. However, the raw material usually contains amorphous carbon and various

oxygen containing groups created at the sidewalls, depending on the synthetic method and degree of functionalization on its surface. Consequently, carbon-based contaminants will appear collectively as several peaks around the binding energy of C1s. Therefore, we focused the peaks near 285 eV to determine whether the proton and electron beam, or UV radiation caused any compositional modification.

Figure 4a is a characteristic XPS profile showing C1s binding energy spectra of *pristine* SWNTs. The carbon peak was fitted by several carbon-based surface functional groups, which are indexed as *1*, *2*, *2'*, *2"* and *3* in the figure. The spectra in Figure 4a clearly indicates that there is a narrow peak (*1*) at 285.6 eV of C1s atoms where SP^2 (C=C) and SP^3 (C-C) are composition sensitive. For example, the 284.4 eV of C=C and the 285.11 ~ 285.5 eV of C-C are characteristic of highly ordered lattice conformations. When an oxygen molecule is adsorbed to carbon atoms, the binding energy can be shifted higher due to the higher electronegativity of the oxygen [25, 26]. Therefore, the peaks (*2, 2'* and *2"*) with higher binding energies at 286.4, 288.6 290.5 eV were assigned; C-O, C=O and COO, respectively, indicating that the carbon nanotubes are partially oxidized for pristine SWNTs. This indicates that the SWNTs used in our experiments contain various oxygen containing groups which were probably produced during their synthesis or purification during the manufacturing process.

The origin of peak (*3*) near 284 eV, clearly separated from the main peak (*1*) at 285.6 eV, is not clearly understood, but probably arises from amorphous carbon regions, existing as carbon impurities together with the SWNTs. We cannot rule out that the origin of the peak might be due to the static charging effect, since the sample was mounted on the probe tip by means of insulating double-sided adhesive tape, which might result in a differential static charging at low binding energy [28]. Since this peak was only observed at the pristine sample and the sample exposed to proton radiation (not at the sample exposed to electron radiation) we believe that this peak is due to the nature of a chemical information of SWNTs, not a peak broadening from a experimental artifact.

We, subsequently compared the results for the same SWNTs irradiated at 2 MeV with electrons and those irradiated at 10 MeV with protons in ambient conditions.

Figure 4b shows the XPS spectrum of the electron beam irradiated SWNTs. The radiation dose for this sample was 60 kGy. As shown in the figure, the small peak (*3* in Figure 4a) near 284 eV has essentially disappeared, indicative of the removal of carbon impurities. The peak from oxidized carbon derivatives (*2*), which may include oxygen containing carbons, remained broad, so a proper deconvolution process could not be performed here. However, the relative concentration of peak *2*, obtained from the peak area, decreased upon electron radiation, implying that any significant oxidation did not occur while the carbon impurities were selectively removed by electron radiation. Overall, the spectrum

shows a main peak from C1s carbon (*1*), which was similar to that in Figure 4a, without any distinct shoulder peaks nearby.

Surprisingly, Figure 4c indicates that a very different reaction due to the collision of protons occurred. Notably, the small peak (*3* in Figure 4a) near 284 eV increased significantly while the intensity from the main peak (*1*) is reduced. The peaks (*2, 2', 2"* and *4*) with higher binding energies at 286 - 290 eV were remained and can be assigned to a variety of oxidative derivatives of carbons. Again, the origin of this peak (*3*) is not fully understood and requires further investigation. We, however, postulate that the 10 MeV proton particles generated new sp^3 bonds on the CNT surfaces, corresponding to oxygen-based functional groups such as carbonyl and phenyl groups (which are responsible for the peaks at the higher binding energy region) and preserved the amorphous region of carbon impurities. Consequently, proton collision ruptured C=C bonds around the SWNT, resulting in a very reactive surface which can be oxidized under ambient conditions. We further confirmed that the proton irradiated SWNTs showed an improved solubility in various polar solvents such as DMF, and the solution was very stable even after a month, while raw SWNTs precipitated after only a few minutes.

Recently, ultraviolet (UV) treatment has been suggested to modify the CNT surface [24,27,28]. In details, it has been theoretically shown that UV light excites ambient oxygen molecules to a spin-singlet state, resulting in a significant reduction in the activation energy for oxygen molecule chemisorption [24]. Cai *et al.* have shown that UV-induced atomic oxygens facilitate the surface oxidation of SWNTs [27]. We, recently demonstrated that UV-ozone treatment under ambient conditions can have a dramatic effect on the nature of the surface oxidation of MWNTs, leading to the production of carboxylic acid, phenol, quinine, ester, pyrone, and ketone functional groups [28], as similar to the SWNTs irradiated by protons. Based on the theoretical calculation [24] together with the experimental results, the oxidation mechanism is suggested as follows; the reduction in the activation energy for O_2 molecule chemisorption onto the CNT surface increases the rate of nanotubes adsorption. Simultaneously, reactive atomic oxygens, which are dissociated from bonded oxygen (physisorbed and/or chemisorbed oxygens onto CNT surface) molecules by UV radiation, can induce oxidative cleavage of the carbon bonding to form oxidative functional groups more effectively, as shown in Figure 5.

Fourier-transform infrared spectroscopy (FT-IR) was carried out to determine the chemical structures and types of functional groups present on MWNTs. A comparison of 60-minute FT-IR spectra of raw and UVO treated CNTs are shown in Figure 6. Several peaks corresponding to bond rotation, vibration, and stretching of various oxygen compounds can be observed. The peaks at 1074 cm^{-1}, 1170 cm^{-1}, 1840 cm^{-1} indicate the presence of ester groups, and the peaks at 1524 cm^{-1}, 1636 cm^{-1}, 3442 cm^{-1} are assigned to the stretching

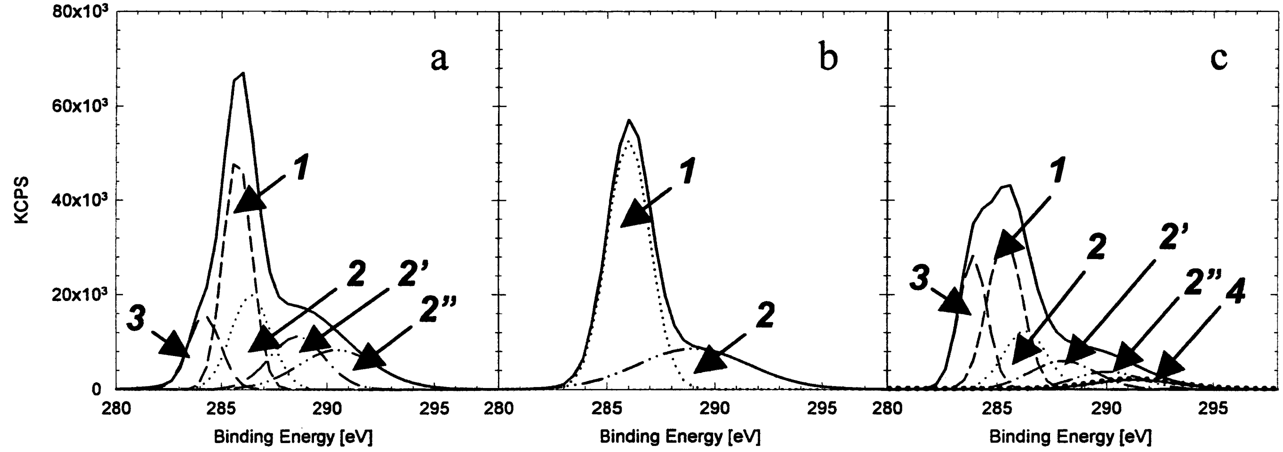

Figure 4. XPS spectra of irradiated SWNT: (a) before, (b) after 2 Mev, electron beam radiation dose of 60 kGy and (c) after 10 Mev, proton beam radiation for 15 minutes.

$$O_2 + h\upsilon : 184.9\ nm \longrightarrow [O] + O_3$$

$$O_3 + h\upsilon : 253.7\ nm \longrightarrow [O$$

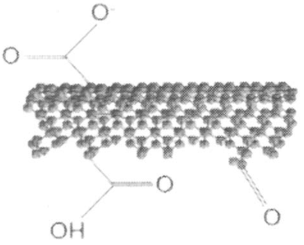

Figure 5. An atomic oxygen is generated when molecular oxygen is dissociated by 184.9 nm and ozone by 253.7 nm, and produces oxygen compounds on the CNT surface.

mode of C=C, C=O of a quinone group, and –OH of a hydroxyl group, respectively [29,30]. Accordingly, the results of Figure 6 illustrate that the UVO treatment of CNTs produced a number of functional groups containing oxygen. Compared to a raw CNT, the dissolution in polar organic solvents (DMF, 1,2-dichlorobenzene and pyridine) was improved by as much as 320%, which is comparable to vigorous acid treatment, without any severe alteration of the aspect ratio of CNTs.

In summary, depending on the nature of sources and conditions, the radiation effects of the CNTs in a relatively short period of time were very different. 1) The effective surface oxidation was observed for the samples exposed to the proton for 15 min and UV-ozone environment in 60 min, and the oxidative functional groups produced by proton and UV-ozone were essentially similar to those produced by acid-based treatment.[31] 2) The electron radiation could remove the carbon impurities, when the operating conditions are carefully optimized. Nevertheless, these radiation methods described above were performed in a form of a dried CNT powder, thus did not produce any harmful chemical byproducts.

Structural Changes

The remarkable structures and properties of carbon nanotubes were reviewed above. Among these, the electrical properties of CNTs have attracted special interest. Depending on the geometrical arrangement of the carbon rings of graphite, CNTs can have either metallic or semiconducting properties. Since electronic properties are strongly related to molecular arrangements, for example, bandgap is inversely related to molecular diameter, the lattice information concerning CNTs should be discussed, as to whether radiation might influence their geometrical structures. Raman spectroscopy normally detects vibration frequencies. Under resonant conditions, the spectra not only provide important

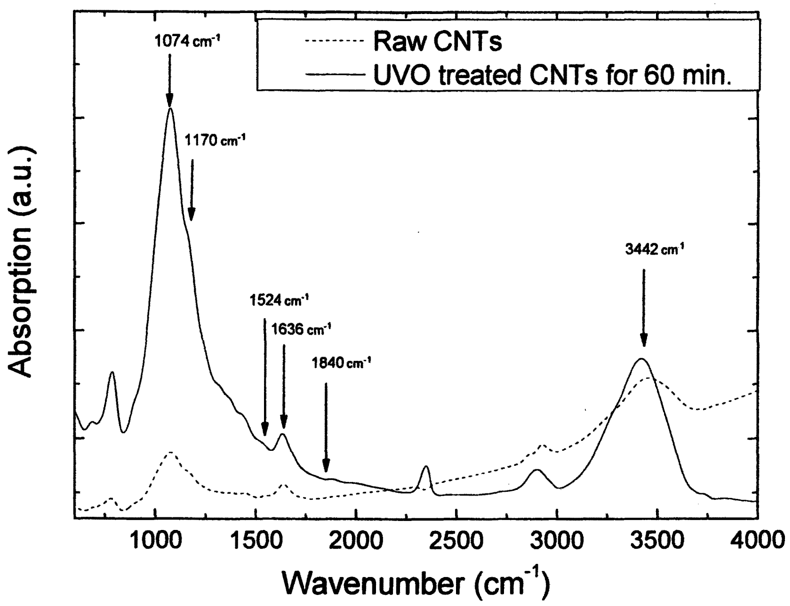

Figure 6. FT-IR spectra obtained from raw MWNT (dotted line) and UVO treated MWNT (line) for 60 min. (Reprinted from Colloids and Surface A: Physicochemical and Engineering Aspects, Najafi et al, 384-385, 373, Copyright(2006), with permission from Elsevier, [29])

information concerning the electronic structure through the strong coupling between electrons and lattice vibrations, but also for this one-dimensional system. In particular, Raman spectra provide information on four important characteristics: radial breathing mode (RBM) associated with the symmetric movement of all carbon atoms in the radial direction, disorder Induced mode (D-band), tangential modes (G-band), second order mode (G'-band).

We first focused on the RBM sections in the 160-300 cm^{-1} region, where the frequency (ω_{RBM}) is inversely proportional to the diameter (d) of individual SWNT and/or bundles by $\omega_{RBM} = C\ (238\ cm^{-1}/nm)/d^{0.93}$ [5,32]. Strong peaks at 169 cm^{-1} and weak peak at 155 cm^{-1} are present in the spectrum of the pristine SWNT (line), indicating that a tube diameter distribution is ranging from 2.0 to 2.2 nm. The principal peaks in the RBM near 150 – 210 cm^{-1} indicate that the pristine SWNTs are largely composed of the semi-conducting tube [32]. Inset to Figure 7 details Raman spectra of SWNTs, that had been irradiated with 2 MeV electrons for various extents of doses. Compared to the peak position for *pristine* SWNTs at ω_{RBM} = 169 cm^{-1}, all of the spectra from electron irradiated SWNTs

show shifts to lower frequencies by 2 ~ 3 cm^{-1}, indicative of geometrical alteration, denoted by a weak change in inter-tubule coupling interactions. We postulate that knock-on atomic displacements due to exposure to electron radiation removes locally attached carbon impurities from SWNT surfaces, causing weaker van der Waals for the SWNTs. This is in agreement with XPS results (removal of the carbon impurities, which do not correspond to the RBM range). Simultaneously, the shoulder at 180 cm^{-1} is dramatically increasing as a function of the radiation dose. The appearance of broad shoulder can be associated with the decrease of the diameter due to the removal of carbon impurities around CNTs. The changes in the Raman spectra after electron irradiation were very different to those in the Raman spectra observed after chemical treatment (i.e. the disappearance of peaks due to the damage by oxidative breaking) [32]. Other characteristic peaks are the D and G Raman bands of SWNTs, which are activated in the 1st-order scattering process of sp^2 carbons by the presence of in-plane substituted hetero-atoms, vacancies, grain boundaries or other defects, and are related to the well-ordered graphite, respectively. Even after a radiation dose of 60, 180 and 240 kGy, no noticeable shift in any peak was observed. However, the ratio of I_G to I_D for pristine SWNT (6.4), decreases by ~ 11 % (5.7 and 5.8 for the samples of 180 and 240 kGy, respectively), indicating that some defects within the SWNT might be produced by the electron radiation.

A series of Raman spectra for SWNT powders exposed to proton radiation are shown in Figure 8. The corresponding frequency regions are selected for the RBM mode range at 100-250 cm^{-1} and the tangential mode range (TM) at 1000-2000 cm^{-1} from the broad frequency in Figure 8a and 8b, respectively. In the figures, no frequency shift at ω_{RBM} = 168.2 cm^{-1} was observed, indicating that the proton radiation does not influence the geometrical structure of a CNT. However, the proton radiation leads to the decrease of all peaks in the RBM section. It can be assumed that the proton radiation destroys the carbon nanotubes, as seen in the chemical treatments with strong acids [33]. The ratio of I_G to I_D was also compared between pristine SWNT and those exposed to proton radiation, and 5.8 for the pristine SWNT decreases to 4.7 for the sample exposed for 10 min, indicative of a significant increase in the number of defects on the SWNT surface.

It, however, should be noted that the trajectory and position of the Bragg peak at a specific energy can be simulated by SRIM code [34], and the samples were deliberately examined in the transmission region where minimal energy transfer between protons and the matrix would be expected. In fact, our recent data clearly indicates that, when MWNTs are exposed to Bragg peak regions, severe structural damage occurs. The TEM images in Figure 9 show that proton radiation induces severe bending, similar to those developed after strong acid treatment in a mixture of nitric acid and sulfuric acid. This bending and shortening was also seen in the cases of electron beam and ion radiation [19,35],

and is possibly due the to radiation-induced defects. Again, these results are in good agreement with the previously described XPS results.

Nonlinear optical properties of exposed CNTs to electron beam

The nonlinear optical (NLO) properties of CNTs have recently attracted substantial interest due to their potential applications in eye protection and as optical sensors in high intensity laser sources. It have been observed that multi-walled carbon nanotubes (MWNTs) possess optical limiting properties with a broadband response covering the visible to the infrared region [36,37]. To assess the potential applications of these CNTs exposed to electron radiation, Z-scan measurements using a Gaussian laser beam (Ti:sapphire laser, wavelength 800 nm with a repetition rate of 1 kHz and with 100 fs pulse width) in a tight focus geometry were performed. The Z-scan is a simple, sensitive single-beam method that takes advantage of the principle of spatial beam distortion to measure both real and imaginary parts of complex nonlinear refractive indices of nonlinear optical materials [38] and measures the normalized transmittance as a function of laser intensity, while the sample is moved through the focal plane of a lens. MWNT powders exposed to 2 MeV electrons were dissolved in dimethylformamide (DMF) and Figure 10 shows the Z-scan results for MWNTs exposed for 0, 120 kGy, and 240 kGy. All of the DMF solutions of the MWNTs exposed to electron radiation possess similar NLO effects within experimental errors and strong effective refractive nonlinearity with a positive sign. This indicates that electron radiation does not affect NLO properties, although surface modification (as described in previous sections) would be expected. The results obtained in the Z-scan measurements shows that it might be possible to use electron radiated CNTs for surface modification with the NLO properties preserved in optical applications.

Summary

We examined the chemical and morphological effects of CNTs before and after high energy radiations, including protons, electrons and UV on CNTs. From XPS, IR and Raman spectra, we found that the CNTs undergo unique changes, depending on the sources, and the conditions. The XPS and Raman spectra indicate that CNT could be oxidized under our proton beam conditions (10 MeV for minutes) as well as UVO environment, while as the electron radiation with an energy of 2 MeV induced the removal of carbon impurities in ambient condition. Irradiated CNTs exhibited radiation induced changes, distinct from the native properties inherited from the classical synthetic routes. If the radiation sources and conditions are carefully controlled, various types of functionalized CNTs for future application may be accessible in the near future.

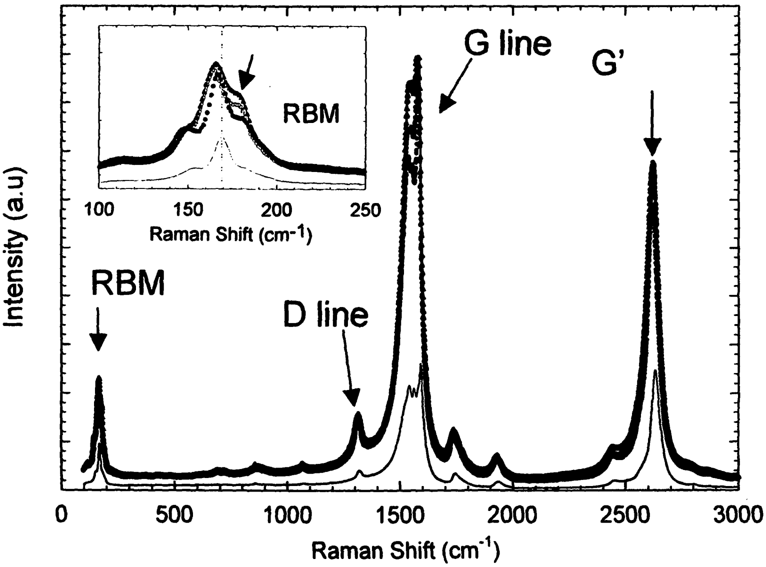

Figure 7. Raman spectrum of SWNT: before (line) and after 2MeV, electron beam radiation dose of 60(closed circles), 180 (open circles) and 240 kGy (closed triangles). Inset: Radial breathing mode (RBM) sections of the Raman spectra.

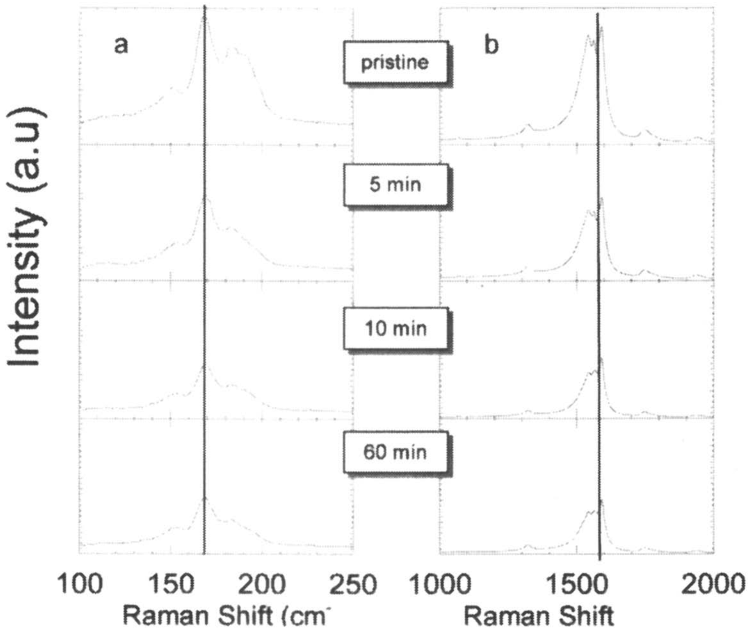

Figure 8. Raman RBM (a) and TM (b) spectrum of SWNT sheet: before and after 10 MeV, proton beam radiation for 5, 10, 30 and 60 minutes.

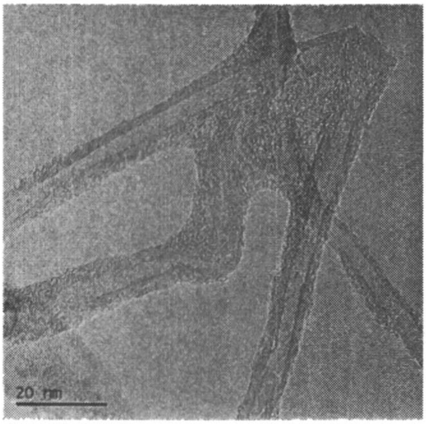

Figure 9. TEM image of MWNT exposed to the Bragg peak regions of a 10 MeV proton beam.

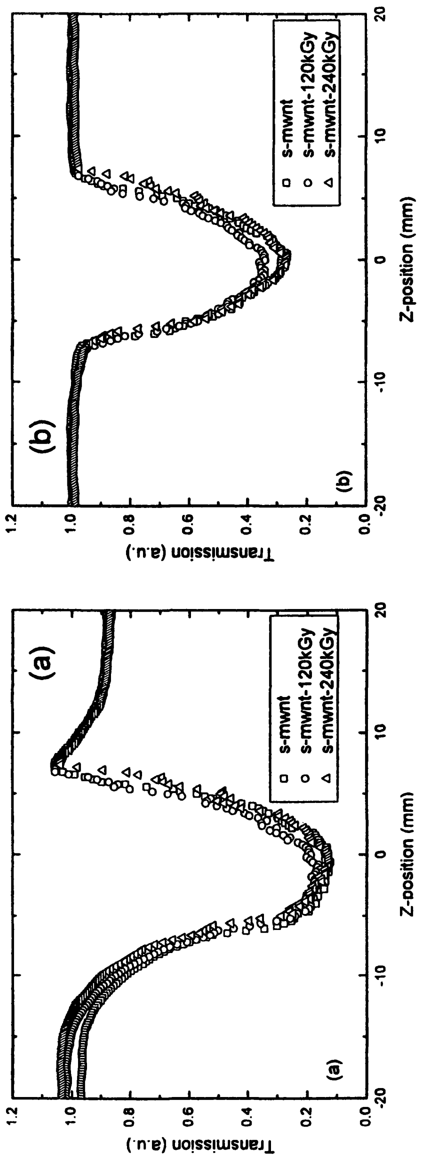

Figure 10. (a) Closed aperture and (b) open aperture Z-scan data for S-MWNTs with different electron radiation dose/DMF solution in 1 mm quartz cell with 800 nm, 100 fs laser pulse.

Acknowledgements

Grateful acknowledgement is made for financial support by a grant (06K1501-01311) from '*Center for Nanostructured Materials Technology*' under '*21st Century Frontier R&D Programs*' and BAERI of the MOST, Korea.

References

1. European Space Agency, Space Environment and Effects Analysis Section. (see, http://www.eas.asu.edu/~holbert/eee460/spacerad.html).
2. Rao, C. N. R.; Govindaraj, A.; Gundiah, G.; Vivekchand, S. R. C. *Chem. Eng. Sci.* **2004**, *59*, 4665-4671.
3. Robertson, J. *Materials Today*, **2004**, *7*, 46-52.
4. Xie, X. L.; Mai, Y.W.; Zhou, X. P. *Mat. Sci. Eng.* **2005**, *49*, 89-112.
5. Belin, T.; Epron, F. *Mat. Sci. Eng.* **2005**, *119*, 105-118.
6. Harris, P. J. F. *Carbon Nanotubes and Related Structures*; Cambridge University Press: Cambridge, 1999.
7. Bahr, J. L.; Mickelson, E.; Bronoikowski, M.; Smalley, E.; Tour, J. *Chem. Com.* **2001**, *2*, 193-194.
8. Murakami, H.; Nomura, T.; Nakashima, N. *Chem. Phys. Lett.* **2003**, *378*, 481-485.
9. Baibarac, M.; Baltog, I.; Godon, C.; Lefrant, S.; Chauvet, O. *Carbon* **2004**, *42*, 3143-3152.
10. Hamwi, A.; Alvergnat, H.; Bonnamy, S.; Béguin, F. *Carbon* **1997**, *35*, 723-728.
11. Qin, S.; Ford, W. T.; Resasco, D. E.; Herrera, J. E. Macromolecules **2004**, *3*, 752-757.
12. Kovtyukhova, N. I.; Mallouk, T. E.; Pan, L.; Dickey, E. C. *J. Am. Chem. Soc.* **2003**, *125*, 9761-9762.
13. Saini, R. K.; Chiang, I. W.; Peng, H.; Smalley, R. E.; Billups, W. E.; Hauge, R. H. *J. Am. Chem. Soc.* **2003**, *125*, 3617-3621.
14. Yudasaka, M.; Ichihashi, T.; Kasuya, D.; Kataura, H.; Iijima, S. *Carbon* **2003**, *1*, 73-1280.
15. Pirlot, C.; Mekhalif, Z.; Fonseca, A.; Nagy, J. B.; Demortier, G.; Delhalle, J. *Chem. Phys. Lett.* **2003**, *372*, 595-602.
16. Neupane, P. P.; Manasreh, M. O.; Weaver, B. D.; Rafaelle, R. P.; Landi, B. J. *Appl. Phys. Lett.* **2005**, *86*, 221908.
17. Krasheninnikov, A. V.; Nordlund, K. *Nucl. Instr. Meth. Phys. Res. B* **2004**, *216*, 355-366.
18. Esquinazi, P.; Spemann, D.; Höhne, R.; Setzer, A.; Han, K.; Butz, T. *Phys. Rev. Lett.* **2003**, *91*, 227201.

19. Basiuk, V. A.; Kobayashi, K.; Kaneko, T.; Negishi, Y.; Basiuk, E. V.; Saniger-Blesa, J. *Nano Letters* **2002**, *2*, 789-791.
20. Khare, B.; Meyyappan, M.; Moore, M. H.; Wilhite, P.; Imanaka, H.; Chen, B. *Nano Letters* **2003**, *3*, 643-646.
21. Chai, J. S.; An, D. H.; Chang, H. S.; Hong, B. H.; Hong, S.; Jung, I. S.; Kang, J.; Kim, J. H.; Kim, Y.; Lee, M. Y.; Suk, J.; Shim, H. H.; Park, C. S.; Yang, T. K. *Proceeding of APAC* **2004**, 67-69.
22. Lee, S. K.; Lee, H. R.; Kim, K. R.; Park, B. S.; Choi, B. H. *Proc. 2005 Particle Accelerator Conference,* 1356-1358.
23. Lee, B. C.; Jeong, Y. U.; Cho, S. O.; Lee, J.; Miginsky, S.; Kulipanov, G. *Nucl. Instr. Meth. Phys. Res. A* **1999**, *429*, 352-357.
24. Grujicic, M.; Cao, G.; Rao, A. M.; Tritt, T. M.; Nayak, S. *Appl. Surf. Sci.* **2003**, *214*, 289-303.
25. Hellgren, N.; Guo, J.; Luo, Y.; Sathe, C.; Agui, A.; Kashtanov, S.; Nordgren, J.; Agren H.; Sundgren, J.-E. *Thin Solid Films* **2005**, *471*, 19-34.
26. Lee, W. H.; Kim, S. J.; Lee, W. J.; Lee, J. G.; Haddon, R. C.; Reucroft, P. J. *Appl. Surf. Sci.* **2001**, *181*, 121-127.
27. Cai, L.; Bahr, J. L.; Yao, Y.; Tour, J. M. *Chem. of Materials* **2002**, *14*, 4235-4241.
28. Okpalugo, T. I. T.; Papakonstantinou, P.; Muarphy, H.; McLaughlin, J.; Brown, N. M. D. *Carbon* **2005**, *43*, 153-161.
29. Najafi, E.; Kim, J.; Han, S.; Shin, K. *Colloids Surf. A: Physicochem. Eng. Aspects* **2006**, *284-285*, 373-378.
30. Socrates, G. *Infrared characteristic group frequencies*; John Wiley & Sons: New York, NY, 1980.
31. Saito, T.; Matsushige K.; Tanaka, K. *Physica B: Condensed Matter* **2002**, *323*, 280-283.
32. Fanning, P. E.; Vannice, M. A. *Carbon* **1993**, *31*, 721-730.
33. Lafi, L.; Cossement, D.; Chahine, R. *Carbon* **2005**, *43*, 1347-1357.
34. Ziegler, J. F.; Biersack, J. P.; Littmark, U. *The Stopping and Range of Ions in Solids*; Pergamon Press: New York, NY, **1985**.
35. Niitsuma, J.; Yuan, X.-L.; Ito, S.; Sekiguchi, T. *Scripta Materialia* **2005**, *53*, 703-705.
36. Chen, P.; Wu, X.; Sun, X.; Lin, J.; Ji, W.; Tan, K. L. *Phys. Rev. Lett.* **1999**, *82*, 2548-2551.
37. Vivien, L.; Anglaret, E.; Riehl, D.; Bacou, F.; Journet, C.; Goze, C.; Andrieux, M.; Brunet, M.; Lafonta, F.; Bernier, P.; Haches, F. *Chem. Phys. Lett.* **1999**, *307*, 317-319.
38. Sheik-Bahae, M.; Said, A. A.; Wei, T. H.; Hagan, D. H.; Van Stryland, E. W. *IEEE J. Quantum Electron.* **1990**, *26*, 760-769.

Chapter 21

Fluoropolymer Outgassing in Micro- and Nanofabrication

Yoshinori Matsui[1,*], Shu Seki[1], Seiichi Tagawa[1,*], Shou Tsuji[2,3], and Toshiro Itani[2]

[1]The Institute of Scientific and Industrial Research, Osaka University, 8–1 Mihogaoka, Ibaraki, Osaka 567–0047, Japan
[2]Semiconductor Leading Edge Technologies, Inc., 16–1 Onogawa, Tsukuba, Ibaraki 305–8569, Japan
[3]Current address: Matsuisita Electric Industrial Company, Ltd., 19 Nishikujo-Kasugacho, Minami-ku, Kyoto, Japan
[*]Corresponding authors

For improved micro- and nano-fabrication, we investigated the outgassing characteristics of fluoropolymers for the semiconductor industry on exposure to 157 nm, and for poly(tetrafluoroethylene) (PTFE) on exposure to a focused ion beam (FIB). The volatiles from these fluoropolymers were observed by *in-situ* quadrupole mass spectrometry. On exposure to 157 nm, side chain scission and the C-F bond play an important role in the outgassing process. Some fluoropolymers produce harmful HF which can damage exposure tools. HF evolution strongly depends on the polymer structure rather than the fluorine content, and can be reduced by optimizing the polymer structure. In contrast, main chain scission plays an important role in the outgassing characteristics of PTFE during FIB exposure. Fluorocarbons close to the upper detection limit of 298 amu were observed, and there is a possibility that some species with masses greater than 298 amu may evolve from the PTFE.

© 2008 American Chemical Society

Introduction

Fluoropolymers have received much attention for applications in various fields because of their excellent properties (1) such as high thermal stability, high chemical stability, low adhesion, biological suitability, low frictional resistance, and transparency at vacuum ultraviolet (VUV) region (2). Because of the sufficient transparency at 157 nm, fluoropolymers are used as a polymer for F_2 and F_2 immersion lithography for semiconductor industry (2). Polymethacrylates containing bi- and/or tri-alicyclic structures, which are major polymers in ArF resist (3), are too absorptive at 157 nm and cannot be used as a polymer in F_2 and F_2 immersion resist (2).

Shortening of exposure wavelength from deep ultraviolet to VUV causes polymer photolysis by direct irradiation, leading to significant amount of resist outgassing. Outgassed species leaving exposed resist film deposit on system lenses and cause optical contamination. Fluorolymer outgassing is therefore a serious problem in F_2 lithography (4 - 8). One of the most important outgassed species is HF which damages exposure tools (4 - 6). On the other hand, it was reported that fluorocarbons does not affect the optical contamination (7). Hydrocarbons such as isobutene is important from the viewpoint of the optical contamination (8). In the case of Polymethacrylates containing bi- and/or tri-alicyclic structures on exposure to 157 nm, outgassed species except for H_2 originate from side chains (4). On exposure to 157nm, scission of side chain plays an important roll in outgassing characteristics of these polymers (4).

Besides the use in F_2 and F_2 immersion lithography, fluoropolymers are used in various fields. Fluoropolymer is one of the candidate for a polymer for MEMS, and fabrication of fluoropolymers by ultra-short pulsed lasers (9), and synchrotron radiations (10) has been studied. Polymer outgassing as well as the micro- and nano-fabrication depends on the polymer radiolysis. It is important for the micro- and nano-fabrication to investigate outgassing characteristics which is obvious outcome in the polymer radiolysis.

In the present study, we investigated outgassing characteristics of fluoropolymers for semiconductor industry on exposure to 157 nm, and also investigated outgassing characteristics of PTFE on exposure to focused ion beam (FIB). Outgassed species from these fluoropolymer were detedted by *in-situ* quadrupole mass spectrometry.

Experimental

Figure 1a shows the experimental set-up for measurement of outgassed species from fluoropolymers on exposure to 157 nm. The exposure source is a LAMBDA PHYSIK OPTex UV excimer laser (Wavelength: 157 nm, Power: 0.8 mJ/pulse, Rep. Rate: 30 Hz, Pulse duration: 5-10 ns FWHM, laser intensity: 2 MW/cm^2) where a vacuum chamber was connected via CaF_2 lens. A PFEIRRER

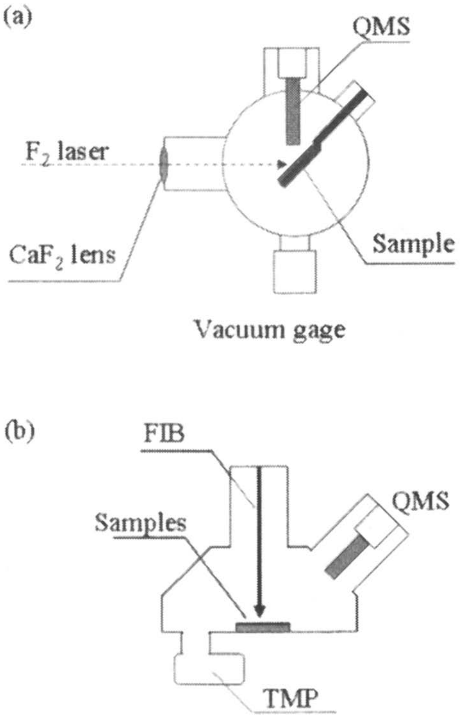

Figure 1. Experimental set-up for measuring outgassed species from (a) fluoropolymers for a resist on exposure to 157 nm, and (b) PTFE on exposure to FIB.

In Polymer Durability and Radiation Effects; Celina, M., et al.;
ACS Symposium Series; American Chemical Society: Washington, DC, 2007.

VACUUM Prisma™ QMS 200 M3 mass spectrometer with a 100 mA, 300 V ionizing source is integrated into the vacuum chamber to examine outgassed species. The QMS is operational at the pressure of ~1 × 10^{-4} torr and scanned over 1-299 amu. The mass spectra of outgassed species were obtained by subtraction of the background mass spectra from the spectra taken with the exposure. The details of the experimental set-up has been described elsewhere (4). Figure 1b shows experimental set-up for measuring outgassed species from PTFE on exposure to FIB, using *in-situ* quadrupole mass spectrometry. Exposure of FIB was carried out by Seiko Instruments Inc. SMI2050 where a PFEIRRER VACUUM Prisma™ QMS 200 M3 mass spectrometer with a 100 mA, 300 V ionizing source is integrated. The details of the experimental set-up has been described elsewhere (11).

Results and Discussion

Outgassed Species from Fluoropolymers for F_2 lithography on Exposure to 157 nm

Outgassed species during 157 nm exposure were observed for two classes of fluorinated backbone-alicyclic-polymers. The former is main-chain fluorinated polymers (TFE-a, TFE-b) and the latter is side-chain fluorinated polymers (FNb) as shown in Figure 2. These polymers were supplied by Semiconductor Leading Edge Technologies, Inc. Fluorine contents of these polymers are 38, 29, and 40 wt%, respectively. Thickness of films of these polymers is ~100 nm. The absorbance of these films is ca. 0.66 ~ 2.7 μm^{-1}. UV and film thickness measurements were performed using a HITACHI VUV-VASE spectroscopic ellipsometer. Figure 3a shows mass spectra of outgassed species from a film of TFE-a during 157 nm exposure. Outgassed species from TFE-a, which has no side chains, include HF (20 amu) that may be one of the most harmful outgassed species to optical elements in exposure tools. As for main-chain fluorinated polymers, HF as well as H_2 evolve from their main chain. H_2O, N_2, and O_2 might be mainly the adsorbates of the vacuum chamber. Figure 3b shows mass spectra of outgassed species from a film of TFE-b containing *tert*-butyl α-fluoroacrylate group. Outgassed species observed in the exposure of the film of TFE-b were H_2 (2 amu), HF (20 amu), N_2 (28 amu), O_2 (32 amu), CO_2 (44 amu), isobutene (56 amu). HF also evolve from this polymer. Some outgassed species such as isobutene evolve from *tert*-butyl α-fluoroacrylate group. Figure 5c shows mass spectra of outgassed species from a film of FNb. In comparison with TFE-a and TFE-b, very small amount of HF was detected. Side-chain fluorinated polymer of FNb produce fluorine-containing outgassed species with high molecular weight instead of HF. It was reported that fluorocarbon does not cause optical contamination (7). In view of outgassing issue, side-chain fluorinated polymer FNb is superior to main-chain fluorinated polymer TFE-b.

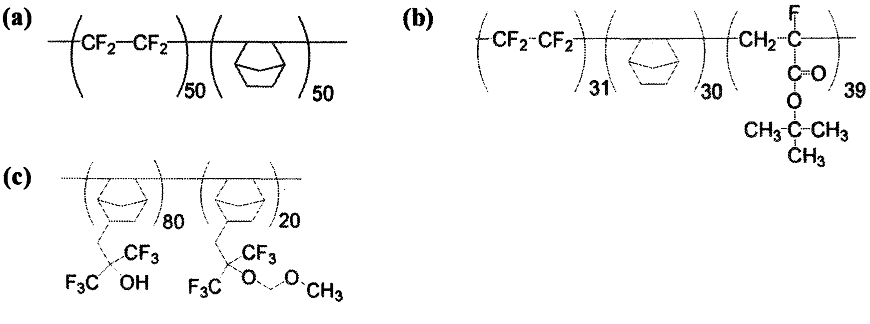

Figure 2. The fluoropolymers employed: (a) TFE-a, (b) TFE-b, (c) FNb.

Outgassed Species from PTFE on Exposure to FIB

Figure 4 shows the mass spectra of outgassed species from FIB irradiated PTFE. There are many mass spectral peaks from 1 amu to 298 amu. The peak located at 69 amu is assigned to CF_3. Other significant peaks are due to fragments of C_xF_y. Outgassed species with the mass-number ~ 298 amu were observed, and it is predicted that outgassed species with mass-number greater than 298 amu evolve from PTFE. Scission of main chain and low boiling point of resulting fluorocarbons (Table 1) are responsible for the outgassed fluorocarbons with high molecular weight.

Table 1. Molecular Weights and Boiling Points of Fluorocarbons.

	Molecular weight	Boiling point [°C] (12)
C_3F_8	188	-36.6
C_4F_{10}	238	-1.9
C_5F_{12}	288	29.2
C_6F_{14}	338	56.6

Conclusions

We focused on outgassing characteristics of fluoropolymers for semiconductor industry on exposure to 157 nm, and also focused on outgassing characteristics of PTFE on exposure to FIB. Outgassed species from these fluoropolymers were observed by *in-situ* quadrupole mass spectrometry.

On exposure to 157 nm, scission of side chain and C-F bond plays an important roll in outgassing characteristics. Some fluoropolymers for semiconductor industry produce harmful outgassed species of HF which

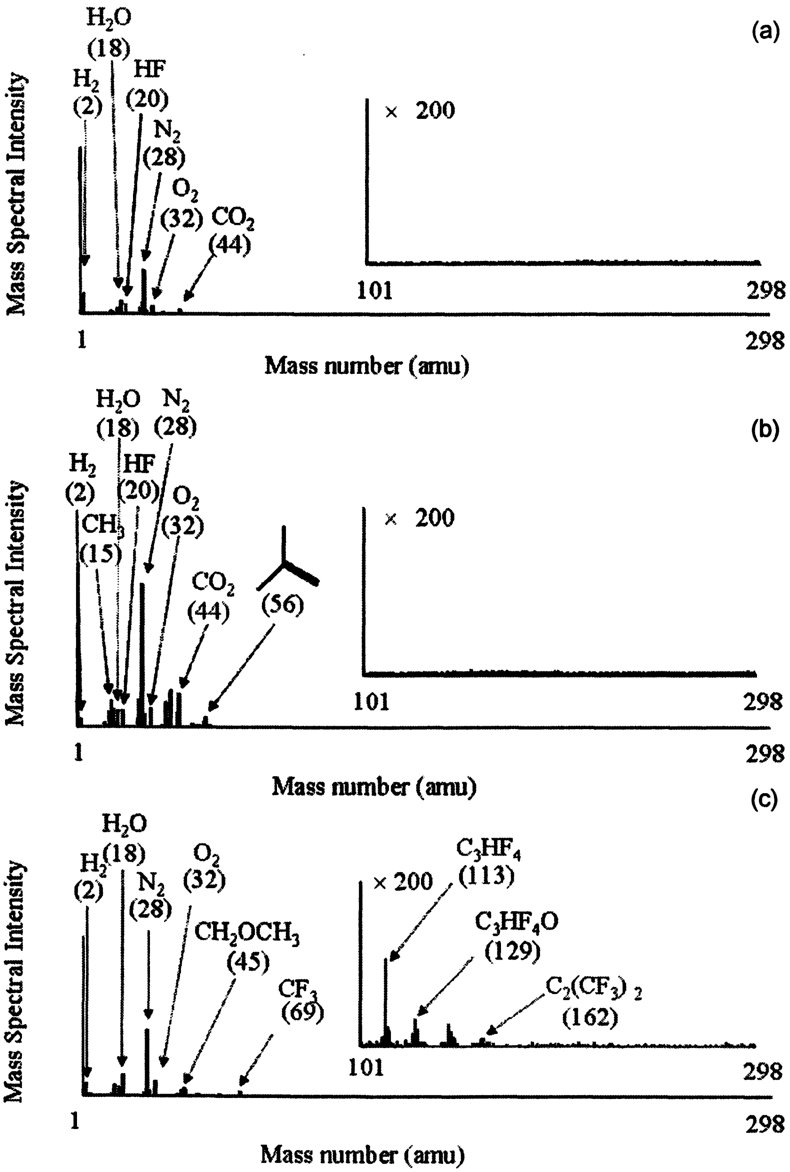

Figure 3. Mass spectra of outgassed species from the 157 nm exposure of films of (a) TFE-a, (b) TFE-b, and (b) FNb.

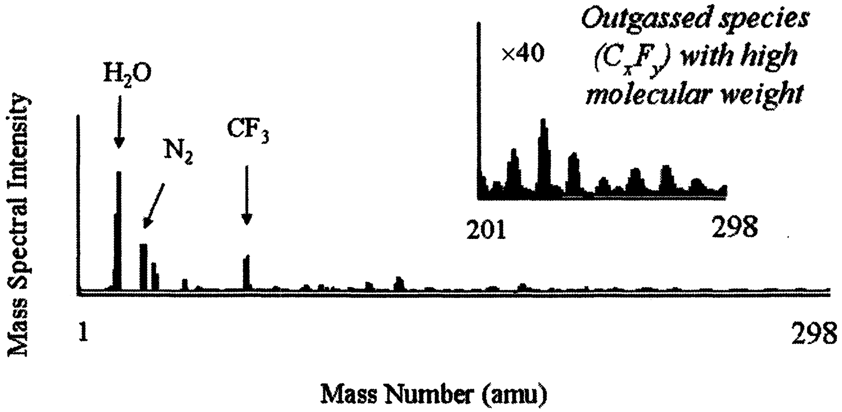

Figure 4. Mass spectra of outgassed species from PTFE on exposure to FIB with a beam current of 1.3 nA.

damages exposure tool. As for main-chain fluorinated polymers with 29~30 wt% fluorine contents, significant amount of HF as well as H_2 evolve from their main chain. On the other hand, very small amount of HF was detected for side-chain fluorinated polymer with 40 wt% fluorine contents. Side-chain fluorinated polymers tend to produce fluorine-containing outgassed species with high molecular weight instead of HF. HF evolution strongly depends on polymer structure rather than fluorine content of the polymers, and can be depressed by optimizing the polymer structure. Except for HF and H_2, other outgassed species are photo-decomposed products of side chains.

On the other hand, fluoropolymer outgassing on exposure to FIB is characterized by main chain scission followed by evolution of flurocarbons with large mass number (~298 amu or more) and with low boiling point.

References

1. Mark, H.; Bikales, N.; Overberger, C.; Menges, G. in: "Encyclopedia of Polymer Science and Engineering", 2nd ed., J. Wiley & Sons, New York, **1964**, Vol. 16, p. 577.
2. Brodsky, C.; Byers, J.; Conley, W.; Hung, R.; Yamada, S.; Patterson, K.; Somervell, M.; Trinque, B.; Tran, H. V.; Cho, S.; Chiba, T.; Lin, S.; Jamieson, A.; Johnson, H.; Heyden, T. V.; Willson, C. G. *J. Vac. Sci. Technol.* **2000**, *B18*, 3396. French, R. H.; Wheland, R. C.; Qiu, W.; Lemon, M. F.; Zhang, E.; Gordon, J.; Petrov, V. A.; Cherstkov, V. F.; Delaygina, N. I. *J. Fluorine Chem.* **2003**, *122*, 63.

3. Takahashi, M.; Takechi, M.; Kaimoto, Y.; Hanyu, I.; Abe, N.; Nozaki, K. *Proc. SPIE*, **1995**, *2438*, 422.
4. Matsui, Y.; Umeda, S.; Seki, S.; Tagawa, S.; Ishikawa, S.; Itani, T. *Jpn. J. Appl. Phys.* **2003**, *42*, 3894.
5. Matsui, Y.; Umeda, S.; Matsui, S.; Seki, S.; Tagawa, S.; Ishikawa, S.; Itani, T. *Proc. SPIE*, **2003**, *5039*, 121.
6. Kunz, R. R. *Proc. SPIE*, **2004**, *5376*, 1.
7. Bloomstein, T. M.; Sedlacek, J. H. C.; Palmacci, S. T.; Hardy, D. E.; Liberman, V.; Rothschild, M. *Proc. SPIE*, **2003**, *5040*, 650.
8. Bloomstein, T. M.; Liberman, V.; Rothschild, M.; Palmacci, S. T.; Hardy, D. E.; Sedlacek, J. H. C. *Proc. SPIE*, **2002**, *4691*, 709
9. Kuper, S.; Stuke, M. *Appl. Phys. Lett.* **1989**, *54*, 4. Kumagai, H.; Midorikawa, K.; Toyoda, K.; Nakamura, S.; Okamoto, T.; Obara, M. *Appl. Phys. Lett.* **1994**, *65*, 1850.
10. Zhang, Y.; Katoh, T.; Washio, M.; Yamada, H.; Hamada, S. *Appl. Phys. Lett.* **1995**, *67*, 872. Yamaguchi, D.; Katoh, T.; Sato, Y.; Ikeda, S.; Hirose, M.; Aoki, Y.; Iida, M.; Oshima, A.; Tabata, Y.; Washio, M. *Macromol. Symp.* **2002**, *181*, 201.
11. Matsui, Y.; Seki, S.; Tagawa, S. *J. Photopolym. Sci. Technol.* **2005**, *18*, 501.
12. Lide, D. R. Handbook of Chemistry and Physics 81st Edition, CRC Press, Boca Raton, London New York, Washington, D. C., **2000-2001**.

Chapter 22

Tailored Nanocomposite Structures for Improved Polymer Performance

Ian MacDonald[1,2], Milena Ginic-Markovic[1], Stephen Clarke[1], Janis Matisons[1], and Dong Yang Wu[2]

[1]School of Chemistry, Physics, and Earth Sciences, Nanomaterials Research Group, Flinders University of South Australia, G.P.O. Box 2100, Adelaide South Australia 5001, Australia
[2]CSIRO Manufacturing & Infrastructure Technology, Melbourne, Australia

The effect of clay, modified with pyridinium cations of systematically increasing chain lengths, on Polyamide 6 based nanocomposites prepared via melt extrusion was investigated. The structure and morphology of the nanocomposites were examined using X-ray diffraction and transmission electron microscopy respectively. It was found that increasing alkyl chain length of the organic modifier leads to a more clay exfoliation which causes an increase in mechanical strength of the resulting nanocomposites. The crystalline structure, obtained by DSC and XRD studies, changes significantly throughout the samples, from the skin layer containing only γ-crystals, to the core region, containing both the α and γ forms. Furthermore, a significant increase in the crystallinity of nanocomposites was noted with increasing alky chain length of clay modifier. The shift in the Si-O band at 1047 cm^{-1}, present in the modified clay, to 1042 cm^{-1}, in the nanocomposite, is indicative of Clay/Matrix interactions.

© 2008 American Chemical Society

Introduction

Polymer clay nanocomposites have, for some time now, been the subject of extensive research into improving the properties of various matrices and clay types. It has been shown repeatedly that with the addition of organically modified clay to a polymer matrix, either *in-situ* (*1*) or by melt compounding (*2*), exfoliation of the clay platelets leads to vast improvements in fire retardation (*3*), gas barrier (*4*) and mechanical properties (*5, 6*) of nanocomposite materials, without significant increases in density or brittleness (*7*). There have been some studies on the effect of clay modification and melt processing conditions on the exfoliation in these nanocomposites as well as various studies focusing on their crystallisation behaviour (*7-10*). Polyamide-6 (PA-6)/montmorillonite (MMT) nanocomposites are the most widely studied polymer/clay system, however a systematic study relating the structure of the clay modification cation to the properties of the composite has yet to be reported.

In order to produce highly exfoliated nanocomposites, the clay used must be modified to change its hydrophilic surface to an organophillic one by an ion exchange reaction with a suitable cationic species. Since the first reported production of PA-6/MMT nanocomposites by researchers at Toyota™ (*11*), the standard modifier has been an ammonium cation with a long alkyl chain. Previous work has shown that use of a cation with less than 12 CH_2 groups in the chain does not produce well exfoliated composites. Other clay modifications include increasing the number of alkyl chains and the use of various end groups, such as COOH (*10*).

The crystallisation behaviour of PA-6/MMT nanocomposites is complicated to analyse because its polymorphic nature produces a monoclinic α and psuedohexagonal γ structure, both of which are affected by the presence of clay particles in the matrix (*9*). The clay particles themselves have been shown to act as nucleating agents, increasing the crystallisation process in some instances while retarding crystal growth in others. Clearly, the cause of these phenomena must be understood so some measure of control can be employed to produce useful nanocomposite materials with desired properties.

To date, there has been few studies on nanocomposites using modifying cations other than ammoniums. Pozgay et al. (*12*) reported the use of hexadecylpyridinium as a modifying cation for use in PP/clay nanocomposites. Pozgays' work compared the exfoliation level in nanocomposites prepared with hexadecylpyridinium modified clay. The journal focused only on the effect of surface coverage of the clay particles by the organic modifier. Their work showed that exfoliation occurs only above a certain gallery spacing determined by the orientation of the organic modifier.

In this work, the effect of alkyl chain length on PA-6/MMT nanocomposites has been studied in a systematic manner and characterised by a range of techniques. The length of the alkyl chain length of the pyridinium cation has

been systematically increased from 8 to 18 and used to produce polymer/clay nanocomposites by melt compounding. The resultant nanocomposites were then characterised by X-Ray Diffraction (XRD), Transmission Electron Microscopy (TEM), Differential Scanning Calorimetry (DSC), PhotoAccoustic InfraRed Spectroscopy (PAIR) and mechanical testing.

Experimental

Materials

Two types of virgin PA-6, F132-E and F223-D, were purchased from DSM Engineering Plastics. Melting and peak decomposition temperatures were determined to be 222°C and 425°C respectively. F132-E is a high viscosity extrusion grade polymer and F223-E a medium/low viscosity injection moulding grade polymer. These polymers are referred to as F132-x and F223-x, where x denotes the additive type. Na^+ Cloisite was purchased from Southern Clay Products and modified by ion-exchange reaction with synthesised pyridinium cations (scheme 1). Cations were synthesised by reaction of pyridine and the appropriate alkyl chloride under reflux conditions. All synthesised structures were confirmed by NMR.

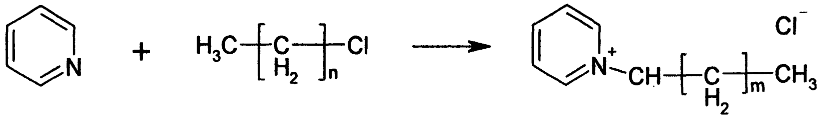

Scheme 1. Synthesis of pyridinium cations

The nanocomposites prepared using modified clay are referred to as oPC, dPC, DdPC, TdPC, HdPC and OdPC denoting increasing alkyl chain length of 8, 10, 12, 14, 16 and 18 respectively and is shown in Table 1. As a reference, a nanocomposite with unmodified clay was also used and denoted UM.

Extruded PA-6 and PA-6 nanocomposites were prepared using a Haake twin-screw extruder with a feed rate of 2kg/hour, barrel temperature of 250°C and screw speed of 150rpm. PA-6 was fed into the extruder using a metered hopper and clay was added separately via a pre-calibrated microfeeder to a level of 3% by weight for each sample. The value of 3% was chosen from previous experiments with clay loading. At this level, excellent improvements in mechanical strength and toughness are obtained without the sample becoming too brittle, which can occur at higher clay loading levels. Clay content was confirmed by weighing remaining MMT ash after ThermoGravimetric analysis.

Samples were then injection moulded into tensile testing bars at 245°C. Before processing, all samples were dried in an oven for at least 24 hours at 65°C.

Table 1. Composite Designations and Alkyl chain Lengths

Clay modification Cation	*Designation*	*Alkyl Chain Length*
None	UM	0
octylpyridinium	oPC	8
decylpyridinium	dPC	10
Dodecylpyridinium	DdPC	12
Tetradecylpyridinium	TdPC	14
Hexadecylpyridinium	HdPC	16
Octadecylpyridinium	OdPC	18

X-Ray Diffraction (XRD)

XRD measurements were performed on a Philips PW1720 with a Co anode running at 40kV and 20mA. Each experiment was conducted from 2.5° to 40° at 0.3°/min on injection-moulded tensile bars both at the skin and the core of each sample, as well as on organoclay powder.

Transmission Electron Microscopy (TEM)

Samples were cut from injection moulded tensile testing bars and ultra thin sections were cut using a cryogenically cooled ultramicrotome. Samples were imaged on a Jeol 1200ex TEM operating at an accelerating voltage of 80kV.

Differential Scanning Calorimetry (DSC)

DSC measurements were performed on a TA Instruments 2190 DSC with temperature and enthalpy calibrations performed using an indium reference. Experiments were performed under a nitrogen atmosphere with a flow rate of 50ml/min. Extruded granules of nanocomposites were heated at 2°C/min to 250°C, held isothermally for 5mins, then cooled to room temperature at 2°C/min. All samples were heated twice, first to examine the properties post extrusion and secondly to examine the preferred crystal structures with slow cooling.

PhotoAccoustic InfraRed Spectroscopy (PAIR)

All experiments were performed on a Nicolet 870 FTIR with a photoaccoustic attachment under a helium atmosphere. Clay samples were dried overnight at 60°C and examined in powder form, allowing five minutes to purge the cell with helium. 10mm PA-6 and nanocomposite discs were cut from tensile specimens and allowed three minutes for the cell to purge. Photoaccoustic spectra were collected at a resolution of $4cm^{-1}$ with a velocity of 0.1581 and 256 scans. All samples were tested in duplicate.

Mechanical Testing

Physical performance of the injection moulded tensile testing bars of nanocomposite materials were performed according to ASTM D638 for tensile properties, and ASTM D790 for flexural tests. Tensile modulus and yield strength were determined using an extensometer at a crosshead speed of 0.51 cm/min. Flexural modulus was determined at a span of 50mm with an applied load rate of 1.3mm/min. The results from the tensile tests were averaged over five samples and the standard deviation found to be within the accepted limits.

Results and Discussion

Nanocomposite Morphology

The structural order of the polyamide 6 nanocomposites was studied by XRD. Figure 1 shows the XRD patterns of PA-6 for the F132-E based nanocomposites containing organically modified clay with alkyl chain lengths from eight to fourteen carbons. Above fourteen carbon units the XRD pattern remains essentially the same so have been omitted from this graph. F223 nanocomposites are not shown as the trends are the same for both materials. The characteristic peak of unmodified clay (not shown) occurs at $2\theta = 8.8°$ and with the increasing alkyl chain lengths in the modified clay, shifts up to a maximum 5.1°, which corresponds to an increase in gallery spacing from 11.6 Å to 17.0 Å (determined through the Bragg equation). From the figure, peak broadening and shift to smaller angles as the length of the alkyl chain on the clay modifier increases, is observed in nanocomposites. This can be ascribed to greater levels of clay exfoliation occurring in the polymer matrix as the observed peaks are related to the spacing between individual platelets.

Pozsgay et al. (*12*) showed, using XRD and TEM, the nanocomposite structure achieved by compounding HdPC modified clay and polypropylene, and

identified increased gallery spacing as an essential prerequisite for exfoliation to occur. With an increase in the organic modifier alkyl chain length , the clay gallery spacing increases, hence, the polymer is able to better move between the individual layers. This results in a greater dispersion of clay nanoparticles and increased range of spacing which is evident on the XRD scans. The more pronounced peaks for oPC, dPC and DdPC indicate a mixed morphology comprising of a decreasing content of intercalated clay tactoids and an increasing content of individual clay particles. From TdPC to OdPC (HdPC and OdPC not shown) the peaks completely disappear and become less pronounced which corresponds to clay-clay platelet spacings of 30Å and higher. Ahmadi et al. (*13*) described the exfoliation process, by showing the XRD shift to lower angles of the characteristic clay peak as the level of exfoliation and dispersion increases, confirming the results described above.

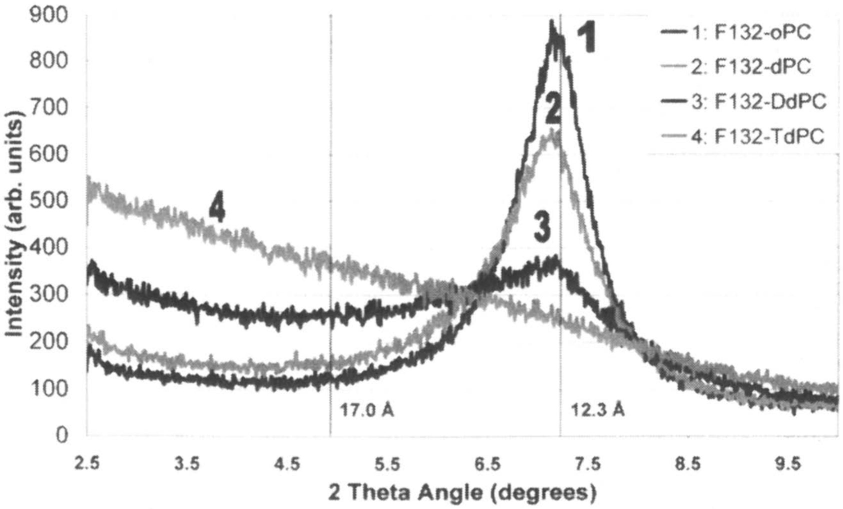

Figure 1. XRD spectra of F132 Nanocomposites oPC, dPC, DdPC and TdPC.

The morphology of the nanocomposites were also determined using TEM. Morgan and Gilman (*14*) described clearly the use of TEM in analysing polymer clay nanocomposites. The TEM images in Figure 2 show the increasing amount of clay exfoliation occurring in UM<dPC<TdPC< OdPC nanocomposites from the F132 grade nylon. Qualitative analysis of a number of images depict decreasing number of large clay tactoids and a more disordered distribution of individual clay layers increasing with the length of the alkyl chain on the organic modifier. This can be ascribed to the larger alkyl chains forcing the clay layers

further apart, reducing the strength of the van der Waal's forces between individual layers and allowing the polymer chains to enter the clay galleries with greater ease and enhance the exfoliation process.

The TEM images and XRD spectra are in good agreement and confirm that cationic pyridinium species can be used for the production of nanocomposites based on both grades of the polyamide. It has been concluded that ready exfoliation of clay layers only occurs with alkyl chain lengths above twelve CH_2 units long.

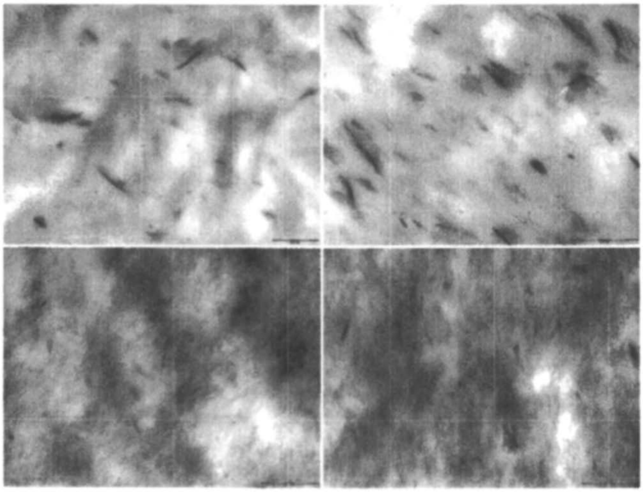

Figure 2. 500nm TEM images of UM, dPC, TdPC and OdPC nanocomposites. Images are sequential from left to right and top to bottom.

Mechanical Properties

Mechanical testing was performed in order to study the effect of the clay modification and dispersion throughout the polymer matrix and hence, determine the performance of the resulting nanocomposite materials. Figure 3 shows the tensile modulus of both grades of nylon (F132-E and F223-D) before and after extrusion as well as the clay/PA-6 nanocomposites. From the figure, it is observed that an increase in the tensile modulus of nanocomposites with increasing alkyl chain length of organically modified clay occurs. Furthermore, F132-x composites show better tensile modulus for the entire range of modified clays. Upon addition of unmodified clay, there is a 5% increase in the modulus of both polymer grades. Following this, the modulus of the modified clay (chain length 8 and 10) containing samples slowly increases to around 15%. A sudden

increase in modulus to 25-30% occurs in nanocomposites DdPC and TdPC with only 3% by weight of modified clay. Comparatively, Huang (*15*) found a 25% increase in modulus was only achievable with the addition of 30% by weight of glass beads to nylon 6.

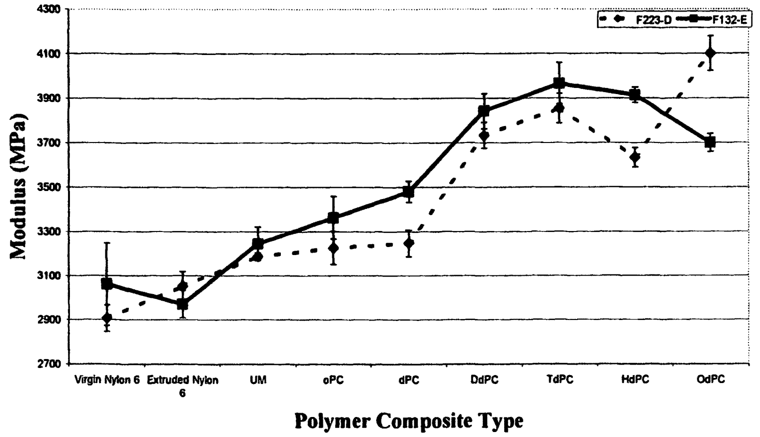

Figure 3. Tensile Modulus of F132 and F223 nanocomposites.

It is important to note that modified clays with chain lengths of 16 and 18 affect the tensile modulus of the two different grades of PA-6 differently. In the case of the F132 grade, the modulus of OdPC decreases slightly by 5% compared to HdPC. In contrast, F223-D shows a decrease by 5% for HdPC before increasing to 40% for OdPC. As mentioned previously, the disappearance of the characteristic clay peak in sample DdPC (figure 1) is related to the sudden increase in tensile modulus (Figure 3). The sharp increase in modulus of the DdPC sample is due to dispersion and exfoliation of the clay particles occurring at a much higher level than in nanocomposites with a shorter chain length of modified clay. It is evident that the longer alkyl chains are allowing greater exfoliation of the clay particles within the polymer matrix to occur, increasing the mechanical properties of the resulting nanocomposite. Krishnamoorti et al. (*5*) reported that this reinforcing effect occurring in the PA-6 is much greater as the aspect ratio of individual clay particles is larger than that of the original clay particles.

The decreases in modulus observed at longer chain lengths resulted from the high level of clay exfoliation and ultimately the stiffness provided by multiple layer clay particles being lost. This is obvious in Figure 4, which shows the flexural modulus of the polymer nanocomposites. The flexural modulus of both nylon grades increases steadily by up to the HdPC sample by over 100% before decreasing again for the OdPC sample to 80-90%. It appears that alkyl chain

length (12-16) of modified clays provide additional stiffness and reinforcement to the nanocomposite due to the presence of some intercalated stacks and ability of the layers to align and be close together when the force is applied. Krishnamoorti et al. (*5*) described the mechanical behaviour of the clay platelets as more like sheets of paper rather than rigid plates, allowing more flexibility in the structure. In a more exfoliated and randomly (*7-10*) orientated sample the single layers only interact with the polymer matrix and hence do not provide as much reinforcement as a sample containing both intercalated and exfoliated layers.

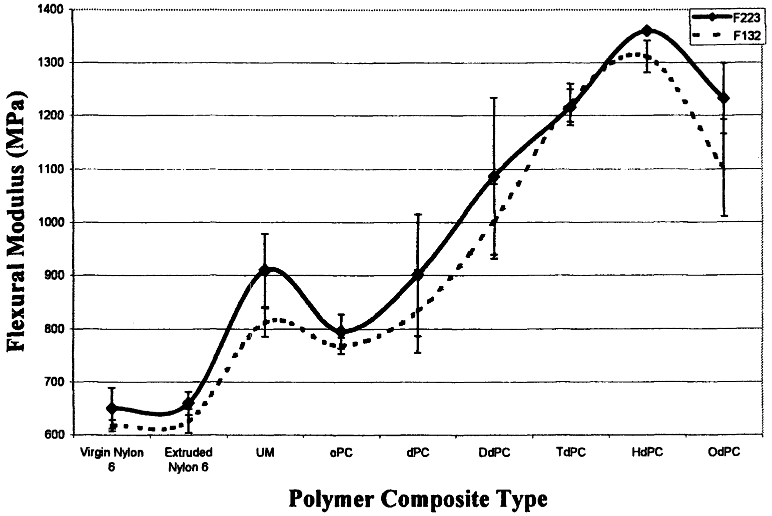

Figure 4. Flexural modulus of F132 and F223 nanocomposites.

Nanocomposite Crystal Structure

The crystal structure of the nanocomposites was studied with XRD and DSC. The XRD spectra in Figure 5 shows the effect of alkyl chain length on the different crystal structure formation in the skin (Figure 5a) and at the core (Figure 5b) of the nanocomposites. By observing the diffraction pattern of the injection moulded test bars core (Figure 5b) between 10 and 40°, the relative content of amorphous material and α and γ crystals in the polymer matrix can be determined. The peak at 24.6° corresponds to the γ crystal structure and the peaks at 23.7° and 27.3° to the α_1 and α_2 crystal in nylon 6 respectively. As reported in previous literature (*16-18*) the peak at 21.4° corresponds to the amorphous content in the matrix, but it is not prominent in Figure 5b Contrary to this literature however, the α and γ peaks are not located at the same 2θ values

due to the differences in polyamide 6 source, nature of the bond formation between polymer matrix and modified clay and its interaction with polyamide 6 chains and processing conditions.

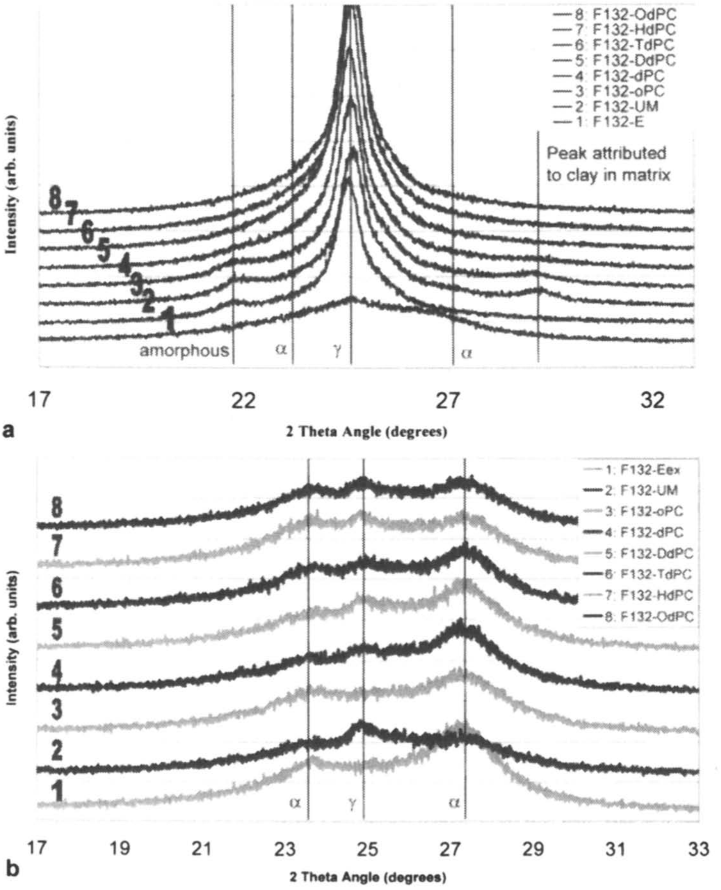

Figure 5. XRD spectra of nanocomposite from the a) skin and b) core of injection moulded test bars.

It is clear from Figure 5a that the sample containing unmodified clay has both crystalline and amorphous content present in the composite, as do the oPC and dPC samples. A small peak is noticed at 21.8° for the DdPC sample but this disappears completely for the remaining nanocomposites. This indicates that as the length of the alkyl chain increases, the amount of amorphous material forming in the composite decreases, producing a more uniform γ-type crystal

structure. The peak at 29.3° is determined to be due to the clay in the matrix and it can be seen that as more exfoliation occurs, this peak disappears.

It has been shown that clay can act as a nucleating agent in polymers (*19*) which accounts for the high level of crystallinity in the nanocomposites and it appears that this effect is increased as the average clay particle size decreases with higher levels of exfoliation. The larger clay tactoids present in the UM-dPC composites hinder crystallisation at the skin of the test bars and hence, the γ structure predominantly forms. With an increase in exfoliation, the decrease in particle size leads to a reduction of the nucleating effect, as the individual clay layers align with crystal growth.

In contrast to the crystal structure of the skin the formation of the more stable α structure occurs over the γ, in the core, with increasing exfoliation. With increasing chain length, the γ crystal increases slightly however most noticeable is the increases in the α_1 and α_2 crystal structures.

In order to mimic the formation of crystal structure in the core of injection moulded bars, DSC was carried out at low heating rates. The DSC scans presented in Figure 6 show the melting temperatures of crystals present in clay nanocomposites after slow heating and cooling from 255°C, to remove the thermal history and allowing time for the preferred crystal structure to form. From Figure 6, one broad melting peak consisting of two melting peaks is observed.

The DSC scans support findings from the XRD data, showing two distinct crystal structures arising in the polymer. Some contribution to this effect is expected from chain segmentation during the extrusion process (*19, 20*), however the effect on nylon 6 polymorphism due to the presence of clay is undeniable.

This structural information can also help explain changes observed in the mechanical properties of the nanocomposites. As the amorphous content of the samples decreases from UM to dPC and the material becomes more crystalline, the nanocomposites become stronger. Also in the core of the injection moulded test bars where slow cooling is prevalent, the more stable α structure appears to form readily. As the γ crystal structure is said to be more ductile than the α, it would be expected that the tensile strength of materials containing mostly α crystals, like DdPC-OdPC, to be much stronger than those with high levels of γ crystal in the core. So not only is the increase in modulus due to the reinforcement provided by the clay layers and increase in crystallinity, but also the reduction in γ crystal content.

Matrix/Clay Interaction

Chemical structures of the pristine and modified clays were analysed using FTIR . The assignments of various peaks are listed in Table 2 (*21*). Compared

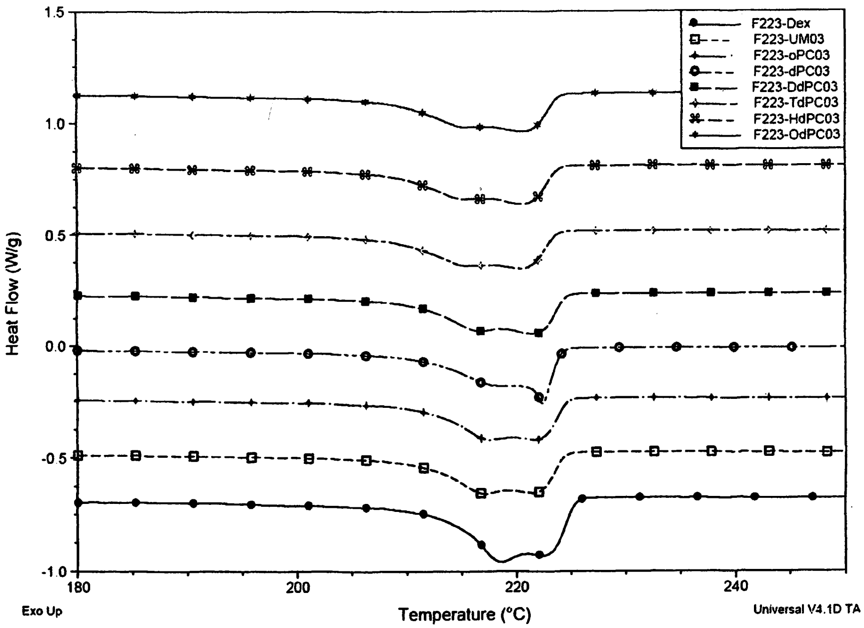

Figure 6. DSC scans of F223 nanocomposites.

with pristine clay, the modified clays with different alkyl chain lengths have new peaks corresponding to the organoclay modifier. From the spectrum of the clay before modification, two major peaks at ~3628cm^{-1} and ~1047cm^{-1} were observed, and have been assigned to the stretching mode of structural hydroxyl groups and Si-O bonds, respectively. In contrast, the modified clay with alkyl chain of 16 in particular, exhibits additional features, due to the characteristics of the modifier. From the spectra (not shown), the presence of the organic modifier is evident at the absorbance between 3200-2800 cm^{-1} and 1600-1400 cm^{-1}. The appearance of ionic bonded N-H stretching at 3094cm^{-1} and N-H bending at 1636cm^{-1} is an indication of the amide bond formation resulting from the ion exchange reaction between pristine clay and organic modifier. All spectra for the modified clays show the same peaks except for a slight change in the normalised intensity of the C-H peak at 2925 and 2853 cm^{-1} resulting from the increasing alkyl chain length of the modifying cation. The shift of 8 cm^{-1}(from 1039 to 1047) of the Si-O band upon modification with the organic cations was also observed, which has been attributed to the increase in gallery spacing (*22*).

The intercalation of clay particles into the clay matrix was evaluated from Figure 7. In the figure, spectra of neat nylon, modified clay (alkyl chain length 16) and related nanocomposites are presented and the additional peak in the region between 1200-800 cm^{-1}, corresponding to Si-O bonding, was detected. The Si-O band at 1047 cm^{-1} present in the modified clay spectra also appears in

Table 2. FTIR Band Assignments

Modified Clay	
461	Si-OSi Deformation
520	Al-OSi Deformation
681	Si-O Stretching of quartz and silica
729	Si-O Stretching of quartz and silica
798	Si-O Stretching of quartz and silica
886	Al-FeOH deformation
918	Al-AlOH deformation
1039	Si-O
1468	CO-H bending
1502	R-COO-
1636	Combination of OH deformation and N-H bending
2851	C-H Symmetric Stretching
2926	C-H Asymmetric Stretching
3094	Ionic bonded N-H stretching
3628	O-H Stretching of structural hydroxyl group

Unmodified Clay	
468	Si-OFe Vibration
526	Al-Osi
801	Si-O Stretching
919	Al-O/Al0OH stretching
1047	Si-O
1456	CH2
1635	O-H deformation of trapped water
3628	O-H Stretching of structural hydroxyl group

Nylon 6	
581.8	Amide VI vibration band
693.6	Amide V
975.7	Skeletal Vibration
1074.5	C-C stretching
1119	C-C stretching
1204.7	CH2 twisting or wagging
1262.7	Amide III and CH2 wagging
1436.8	CH2 scissoring
1540.8	Amide II
1651.2	Amide I
2861.1	CH2 Symmetric
2933.7	CH2 Asymmetric
3085.3	Fermi Resonance of N-H Stretching
3302.3	N-H bound Stretching

Polymer Nanocomposites	
588.4	Amide VI
692.8	Amide V
729.1	Si-O Stretching of quartz and silica
927.9	Al-AlOH deformation
975.4	Si-OH
1042.3	Si-O
1119.7	Si-O in Plane Stretching
1170.9	CH2 twist/wagging
1204	Amide III and CH2 wagging
1262.9	Amide III and CH2 wagging
1372.1	Amide III and CH2 wagging
1558.3	Amide II
1652.5	Amide I
2860	CH2 Symmetric
2933.2	CH2 Asymmetric
3085.3	Fermi Resonance of N-H Stretching
3301.9	N-H bound Stretching

the nanocomposite, shifted by 5 cm^{-1} (to 1042 cm^{-1}). The intensity of the C-H peaks at 2933 cm^{-1} and 2860 cm^{-1} increases with increasing chain length until OdPC, where it decreases slightly. These two features indicate the organic modifier is still present in the clay after processing via extrusion (*22*). This shows both that the organic modifier is thermally stable at the extrusion temperatures and that the organoclay structure is retained throughout the extrusion process, which is necessary for exfoliation to occur. There is no indication of actual bonding between either the matrix and clay or matrix and modifier from these results. An investigation of hydrogen bonding using Near IR is currently underway.

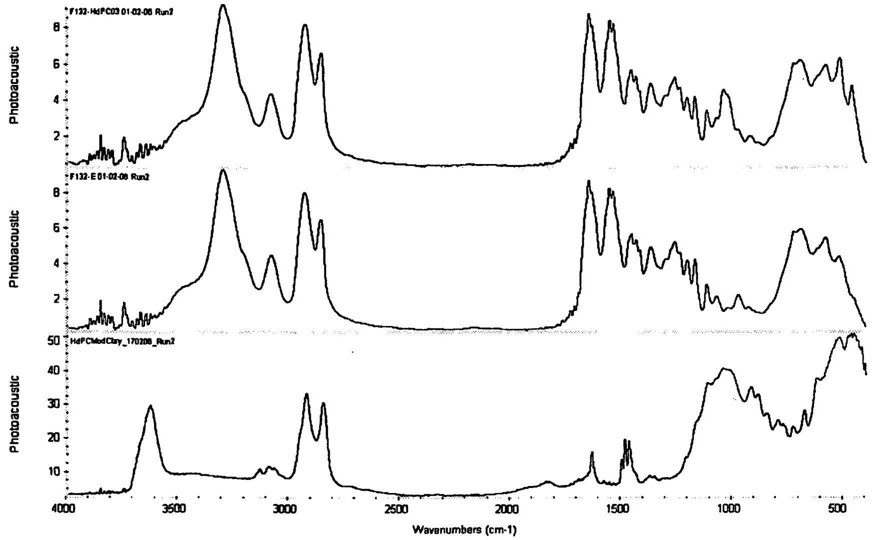

Figure 7: PA-FTIR spectra of (top to bottom) F132-HdPC Nanocomposite, VirginF132-E and hexadecylpyridinium modified clay.

Conclusion

A range of nylon 6 and modified clay nanocomposites formed by melt processing was successfully produced. Exfoliation only occurs readily when the alkyl chain length of clay modifier is greater than 12, which corresponds to a clay gallery spacing of 12-13Å. With an increase of alkyl chain length, the combination of clay structure and extrusion process forms highly exfoliated nanocomposites with mechanical properties superior to that of the original material. At the highest level of exfoliation achieved however, a decrease in mechanical performance was noted, due to the lack of reinforcement that clay

In Polymer Durability and Radiation Effects; Celina, M., et al.;
ACS Symposium Series; American Chemical Society: Washington, DC, 2007.

tactoids of 5-10 layers provide. Study of the crystalline structure of the nanocomposites revealed that increasing the chain length of the modifying cation leads to increased crystallinity and hence, greater mechanical strength. X-ray studies of the core and DSC showed a predominance of α crystals, further adding to the strength of the materials. The FTIR results show that the organic modifier is still present in the clay after processing, indicating the importance of the organoclay structure being retained during extrusion.

Acknowledgments

This work is supported by International Science Linkages program established under the Australian Government's innovation statement Backing Australia's Ability, CG060005. We thank Kerry Gascoigne from the Flinders Microscopy and Image Analysis facility for the high quality TEM images.

References

1. Kojima, Y.; Usuki, A.; Kawasumi, M.; Okada, A.; Kurauchi, T.; Kamigaito, O. *J. Pol. Sci. Part. A. Polymer Chem.* **1993**, *31*, 1755.
2. Vaia, R.; Jandt, K.; Kramer, E.; Giannelis, E. *Macromolecules* **1995**, *28*, 8080.
3. Yang, F.; Yngard, R.; Nelson, G. *J. Fire Sci.* **2005**, *23*, 209.
4. Alexandre, M.; Dubois, P. *Mat. Sci. Eng. R-Reports* **2000**, *28*, 1.
5. Krishnamoorti, R.; Vaia, A.; Giannelis, E. *Chem. Mater.* **1996**, *8*, 1728.
6. Kojima, Y.; Usuki, A.; Kawasumi, M.; Okada, A.; Fukushima, Y.; Kurauchi, T.; Kamigaito, O. *J. Mat. Res.* **1993**, *8*, 1993.
7. Dennis, H.; Hunter, D.; Chang, D.; Kim, S.; White, J.; Cho, J.; Paul, D. *Polymer* **2001**, *42*, 9513.
8. Fornes, T.; Hunter, D.; Paul, D. *Macromlecules* **2004**, *37*, 1793.
9. Fornes, T.; Paul, D. *Polymer* **2003**, *44*, 3945.
10. Fornes, T.; Yoon, P.; Hunter, D.; Keskkula, H.; Paul, D. *Polymer* **2002**, *43*, 5915.
11. Usuki, A.; Mizutani, T.; Fukushima, Y.; Fujimoto, M.; Fukumori, K.; Kojima, Y.; Sato, N.; Kurauchi, T.; Kamigaito, O. *Kabushiki Kaisha Toyota Chuo Kenkyusho (Aichi, Jp)*, United States, **1989**, p. 25.
12. Pozsgay, A.; Frater, T.; Szazdi, L.; Muller, P.; Sajo, I.; Pukanszky, B. *Eur. Pol. J.* **2004**, *40*, 27.
13. Ahmadi, S. J.; Huang, Y. D.; Li, W. *J. Mat. Sci.* **2004**, *39*, 1919.
14. Morgan, A.; Gilman, J. *J. App. Pol. Sci.* **2003**, *87*, 1329.
15. Huang, L.; Yuan, Q.; Jiang, W.; An, L.; Jiang, S.; Li, R. *J. App. Pol. Sci.* **2004**, *94*, 1885.

16. Varlot, K.; Reynaud, E.; Kloppfer, M.; Vigier, G.; Varlet, J. *J. Pol. Sci. Part B. Polymer Phys.* **2001**, *39*, 1360.
17. Maiti, P.; Okamoto, M. *Macromol. Mat. Eng.* **2003**, *288*, 440.
18. Liu, X. H.; Wu, Q. J. *Eur. Pol. J.* **2002**, *38*, 1383.
19. Homminga, D.; Goderis, B.; Mathot, V.; Groeninckx, G. *Polymer* **2006**, *47*, 1630.
20. Homminga, D.; Goderis, B.; Hoffman, S.; Reynaers, H.; Groeninckx, G. *Polymer* **2005**, *46*, 9941.
21. Skrovanek, D.; Howe, S.; Painter, P.; Coleman, M. Macromolecules. **1985**, *18*, 1676.
22. Katti, K.; Sikdar, D.; Katti, D.; Ghosh, P.; Verma, D. *Polymer* **2006**, *47*, 403.

Chapter 23

Non-Aromatic Polyimides Derived from Alicyclic Monomers

Toshihiko Matsumoto, Risa Takahashi, Motoaki Kaise, and Shuichi Kawabata

Center for Nano Science and Technology, Tokyo Polytechnic University, Atsugi, Kanagawa 243–0297, Japan

Nonaromatic polyimides were synthesized by the polycondensation of cyclopentane-1,2,3,4-tetracarboxylic 1,2;3,4-dianhydride (CpDA) and bicyclo[2.2.1]heptane-2,3,5,6-tetracarboxylic 2,3;5,6-dianhydride (BHDA) with alicyclic diamines. The poly(amic acid)s had inherent viscosities (η_{inh}) in the range from 0.1 to 0.4, and they formed free-standing and flexible films after being cast then cured. The nonaromatic polyimide prepared from polyalicyclic monomers PI(BHDA+ BBH) had good thermal stability with no significant weight loss up to 350 °C, and the T5 is around 430 °C. The high-temperature stability can be explained by the introduction of a bicyclic structure. The nonaromatic polyimide films had the temperatures with a maximum rate of the decomposition in N_2 in the range of 450-490 °C. Char yields at 545 °C of the nonaromatic polyimides were lower than those of semi-aromatic and aromatic polyimides. The nonaromatic polyimide films exhibited a cutoff around 230 nm, and they were transparent even in the near IR region. Optically estimated dielectric constant ε's of the polyimides were approximately 2.6 and the polyimides possessed negligibly small birefringence below 10^{-4}. All the polyimide films exhibited broad dispersive peaks of diffraction around 16 °(2θ) and they were insoluble in common organic solvents. The PI(BHDA+BBH) film had a tensile modulus of 2.1 GPa and a tensile strength of 52 MPa.

© 2008 American Chemical Society

Introduction

Nonaromatic polyimides are derived from aliphatic dianhydrides and aliphatic diamines, and only a few papers have been reported on these polyimides. Pioneer research was done in 1962 by Wu using bicycle[2.2.2]oct-7-ene-2,3,5,6-tetracarboxylic 2:3,5:6-dianhydride derivatives and aliphatic diamines having a straight chain.[1] Volksen et al. reported the synthesis of a nonaromatic polyimide from cyclobutane-1,2,3,4-tetracarboxylic dianhydride (CBDA) and 1,1-bis(4-aminocyclohexyl)methane and investigated the optical properties such as the light transmittance and the refractive index.[2] They also pointed out that nonaromatic diamines formed salts during the initial stages of the polymerization, involving pendant carboxylic acid groups from the amic acid moieties along with unreacted amino-functionalities and that in the case of insoluble quaternaized oligomers, only low molecular weights would predominate. Recently, Ueda et al. synthesized the nonaromatic polyimides by the polymerization of *N*-trimethylsilylated alicyclic diamines with CBDA.[3,4] In the present article, the synthesis and the properties of nonaromatic polyimides derived from alicyclic monomers will be described.

Experimental

Materials

Cyclopentane-1,2,3,4-tetracarboxylic 1,2;3,4-dianhydride (CpDA) was prepared from *cis,cis,cis,cis*-1,2,3,4-cyclopentanetetracarboxylic acid by thermal dehydration reaction then sublimation at 170-190 °C. Bicyclo[2.2.1]heptane-2,3,5,6-tetracarboxylic 2,3;5,6-dianhydride (BHDA) was synthesized according to the previous paper.[5] Bis(aminomethyl)bicyclo[2.2.1]heptane (BBH) was donated by Mitsui Chemical Co. Ltd, and used without further purification. BBH consists of four isomers; 2-*exo*,5-*exo*- (30 wt %), 2-*endo*,5-*exo*- (35 wt %), 2-*exo*,6-*exo*- (20 wt %), 2-*endo*,6-*exo*- (15 wt %). 4,4'-Methylenebis(2-methylcyclohexylamine) (MCHM) and hexamethylphosphoramide (HMPA) were purchased from Aldrich Chemical Co Inc and Tokyo Kasei Kogyo Co. Ltd, respectively, and used as received.

General Procedure for Polymerization and Film Preparation

Poly(amic acid)s were prepared by the polycondensations of dianhydrides (4 mmol) with alicyclic diamines (4 mmol) in HMPA (20 wt-% solid content) at room temperature for two days. An aliquot of the polymerization solution was

cast on a glass plate and the plate was heated in vacuum. The temperature was elevated from room temperature to 250 °C at a heating rate of 2 K min^{-1}, and then kept for 1 hour. After curing, the glass plate was immersed into boiling water to facilitate removal of the free-standing polyimide film.

Measurements

Thermal analyses were carried out using a Seiko SSC 5200-TG/DTA 220 instrument at a heating rate of 10 K min^{-1} in a nitrogen atmosphere for the thermogravimetric analysis (TGA). Thermomechanical analyses (TMA) were made using a Seiko Instruments TMA/SS equipped with a penetration probe of 1.0 mm diameter and using an applied constant load of 10 g (stress, 0.125 MPa) at a heating rate of 10 K min^{-1} in air. Infrared spectra were recorded using a JASCO FT/IR-460 plus Fourier transform infrared spectrometer. Transmission and reflection UV-Vis-NIR spectra were measured using a JASCO V-570 UV/Vis/NIR spectrophotometer with a SLM-468 reflection unit. Refractive index of a polyimide film at 589 nm was recorded on an ATAGO Abbe refractometer at room temperature. The birefringence of sample films was evaluated by means of ellipsometry. The mechanical properties were examined at room temperature in air using a specially made machine at a drawing rate of 1 mm/min; the sample size (film) was 10-mm length, 10-mm width, and about 20-μm thick. The wide-angle X-ray diffraction measurements (WAXD) were performed on a Rigaku Rint 2500 X-ray diffractometer with graphite monochromated Cu Kα radiation and a 12 kW (40 kV, 300 mA) rotating anode generator. The film thickness was measured using a G-6 dial gauge (Ozaki Mfg. Co. Ltd). Inherent viscosities (η_{inh}) were measured with an Ostwald viscometer in a 0.5 g dl^{-1} HMPA solution of poly(amic acid) at 30 °C.

Results and Discussions

Monomer and Polymer Synthesis

The cyclopentane-type dianhydride CpDA was synthesized by thermal dehydration of *cis,cis,cis,cis*-1,2,3,4-cyclopentanetetracarboxylic acid at 170-190 °C. The norbornane-type dianhydride BHDA was prepared from *endo*-nadic acid *via* three steps.[5] The ^{1}H-NMR spectrum revealed that BHDA consisted of the two isomers, bicyclo[2.2.1]heptane-2-*endo*,3-*endo*,5-*exo*,6-*exo*-tetracarboxylic dianhydride and the all-*exo* derivative. The ratio was estimated to be 1:1 from the spectrum. The structures and abbreviations of alicyclic monomers are illustrated in Figure 1.

The polyimides were prepared according to the previous report.[6] Poly(amic acid)s were obtained by reacting BHDA or CpDA with MCHM and BBH in HMPA at room temperature for 2 days under a nitrogen atmosphere. Although in the initial stage of the polymerization a solid appeared, the solid was gradually dissolved and the mixture yielded a clear solution. The resultant viscous poly(amic acid) solutions were cast on glass plates, and the poly(amic acid)s were transformed into the corresponding polyimides by curing the plates.

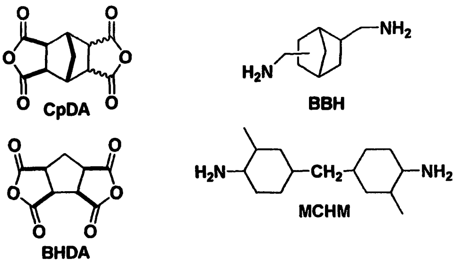

Figure 1. The structures and abbreviations of alicyclic monomers.

Inherent viscosities (η_{inh}) of the poly(amic acid)s were as low as 0.08-0.23, however, they formed flexible and tough films. In the IR spectra of nonaromatic polyimides, characteristic imide absorptions at 1767 cm^{-1} (asym C=O str.) and 1699-1703 cm^{-1} (sym C=O str.) were observed, and the absorptions of amic acid groups have practically disappeared.

Properties of Polymers

The transmission and reflection UV-Vis-NIR spectra of the free-standing films are shown in Figure 2 together with that of a Kapton®-type polyimide PI(PMDA+DDE) which was prepared from pyromellitic dianhydride and 4,4'-diaminodiphenyl ether in our laboratory. The nonaromatic polyimide films exhibit cutoff's in the range of 226-238 nm, and are transparent even in the near IR region. A cutoff wavelength is defined here as a point where the transmittance becomes below 1 % in the spectrum. The aromatic polyimide PI(PMDA+DDE) absorbs visible light due to the charge transfer, and the cutoff wavelength is 412 nm. In the reflection UV-Vis-NIR spectra of polyimide films, the reflectance of nonaromatic polyimides is smaller than that of an aromatic one.

Film refractive index n was determined using an Abbe refractometer at room temperature. The dielectric constant ε of the material at a frequency near 1 MHz is evaluated roughly from the refractive index to be $\varepsilon = 1.1n^2$.[7] These results are listed in Table 1. Optically estimated ε's of the nonaromatic polyimides were approximately 2.6, whereas those of semi-aromatic and aromatic polyimides were around 2.8 and 3.1, respectively.[6] The birefringence Δn (optical anisotropy) of sample films was evaluated by means of ellipsometry. All the nonaromatic polyimides examined in this study possessed small birefringence below 10^{-4}.

The thermal properties of the polyimide film were evaluated by the 5 % weight loss (T5), 10 % weight loss (T10), the decomposition temperatures

In Polymer Durability and Radiation Effects; Celina, M., et al.;
ACS Symposium Series; American Chemical Society: Washington, DC, 2007.

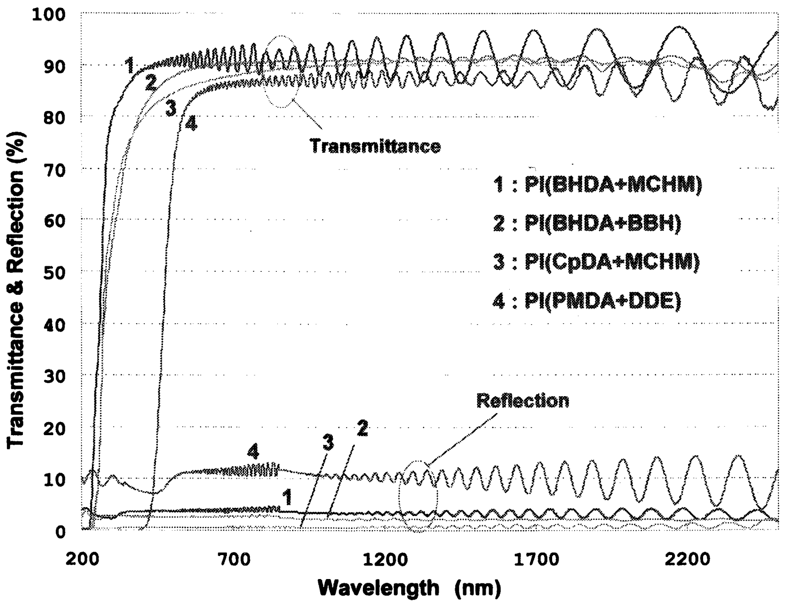

Figure 2. Transmission and reflection UV-Vis-NIR spectra of the free-standing polyimide films.

(Tdec), the temperatures for maximum degradation rate (Tmax), and char yield at 545 °C (CY) measured using the thermogravimetric analyses (TGA), and by the Tg measured using a thermomechanical analyzer (TMA) with a penetration probe. Tdec is noted as the point where the extrapolations of the two slopes in the TGA curve intersect. The Tg was measured using a thermomechanical analyzer (TMA) with a penetration probe.

The TGA profiles of the polyimide films measured in nitrogen atmosphere with a heating rate of 10 K min^{-1} are shown in Figure 3. The nonaromatic polyimide prepared from polyalicyclic monomers PI(BHDA+BBH) has good thermal stability with no significant weight loss up to 350 °C, and the T5 is around 430 °C. The high-temperature stability can be explained by the introduction of a bicyclic structure, which would foster less probability of main chain scission because of the presence of multiple main-chain bonds in the cyclic units. The degradation of polymers in an inert atmosphere is caused by homolytic C-C bond scission. If the polymer backbone consists of a single-chain like that of poly(ethylene), the scission results in direct decreasing of the molecular weight. In most cases, volatile compounds are produced and released as a decomposed gas. On the other hand, in the case of step-ladder type polymers bearing double strands like the alicyclic polyimides, even if the C-C bond scission occurs, it does not lead to a significant decrease in the molecular

Table 1. Synthesis and the properties of nonaromatic polyimide films.[a]

polyimide	η_{inh} [b] (dl g^{-1})	film quality	film thickness (μm)	λcut-off [c] (nm)	ε [d]	Δn [e]
PI(BHDA+MCHM)	0.23	flexible	20	226	2.55	$<10^{-4}$
PI(BHDA+BBH)	0.13	flexible	13	234	2.61	$<10^{-4}$
PI(CpDA+MCHM)	0.08	flexible	15	238	2.55	$<10^{-4}$

[a] polymerization: in HMPA at r.t. for 2 days. imidization: r.t.-250 °C at 2 K min^{-1}, 250 °C for 1 h *in vacuo*.

[b] inherent viscosity, poly(amic acid) in HMPA, 0.5 g dl^{-1} at 30 °C.

[c] wavelength at 1 % transmittance point in the UV-Vis-NIR spectrum.

[d] optically estimated from refractive index, $\varepsilon = 1.1n^2$.

[e] birefringence, measured by ellipsometry.

weight or to the production of volatile compounds. In other words, the introduction of the multibonds facilitates less probability of main chain scission. The thermal properties of the nonaromatic polyimide films are summarized in Table 5. The temperatures with a maximum rate of the decomposition in N_2 appear in the range of 450-490 °C, although decomposition of PI(CpDA+MCHM) seems to proceed through two steps. The first decomposition occurs around 380 °C, and the second at 450 °C. Char yields at 545 °C (CY) of the nonaromatic polyimides are lower than those of semi-aromatic and aromatic polyimides, and especially that of PI(CpDA+MCHM) is nearly zero.

The crystallinity of the polyimide films was examined by wide angle X-ray diffractions (WAXD). All polyimides exhibited amorphous patterns and broad dispersive peaks of diffraction around at 16 °(2θ), as shown in Figure 3. This observation is quite reasonable because the presence of polyalicyclic (bicyclic) structure decrease the intermolecular force between the polymer chains with a consequent decrease in crystallinity.

The mechanical properties of the polyimide films (the sample size: 10-mm length, 10-mm width) were examined at room temperature using a specially made machine with a constant drawing rate of 1 mm min^{-1}. A profile of elongation *vs.* load for PI(BHDA+BBH) film is shown in Figure 4. The polyimide film possessed a tensile modulus of 2.1 GPa and a tensile strength of 52 MPa, and these values can compete in terms of strength with those of a commercial polycarbonate (PC).[8] The authors believe that this is the first example of a fully alicyclic polyimide for which the mechanical property was evaluated.

The solubility of the polyimide films was qualitatively studied and the results are listed in Table 3. All the polyimide films were insoluble in common organic solvents except sulfuric acid. The BBH-based polyimides swelled in some solvents. BBH is bulky and consists of four isomers, and it would make the polymer chains somewhat loosely packed.

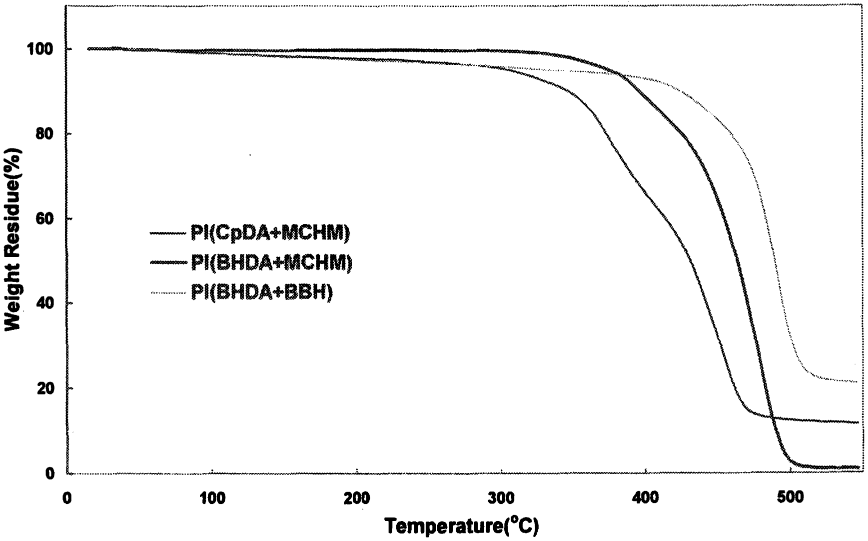

Figure 3. TGA profiles of nonaromatic polyimide films under nitrogen.

Table 2. Thermal properties of nonaromatic polyimide films.

polyimide	T5 [a] (°C)	T10 [b] (°C)	Td [c] (°C)	Tmax [d] (°C)	CY [e] (%)	Tg [f] (°C)
PI(BHDA+MCHM)	395	398	431	472	11.1	219
PI(BHDA+BBH)	426	426	466	487	21.5	212
PI(CpDA+MCHM)	295	343	381	381, 447	0.6	191

[a] 5 %-weight loss, [b] 10 %-weight loss, [c] decomposition temperatures measured by TGA at heating rate of 10 K m

[d] temperatures for the maximum degradation rate measured by TGA at heating rate of 10 K min^{-1} in N_2.

[e] char yield at 545°C measured by TGA at heating rate of 10 K min^{-1} in N_2.

[f] measured by TMA at heating rate of 10 K min^{-1} in N_2.

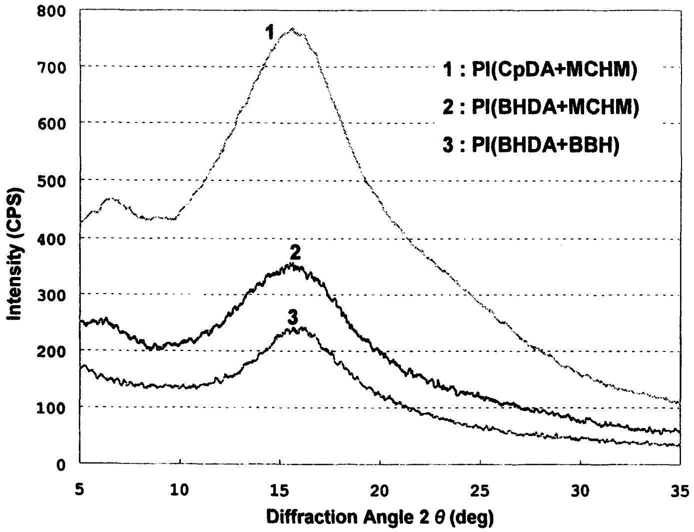

Figure 4. WAXD patterns of the nonaromatic polyimide films.

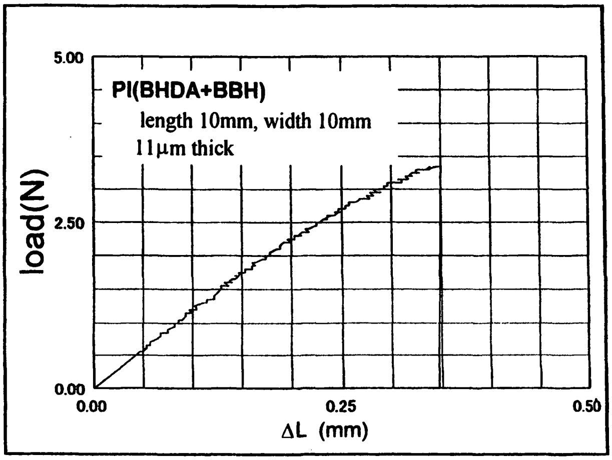

Figure 5. Elongation vs. *load curve of the nonaromatic PI(BHDA+BBH) film.*

Table 3. Solubility of nonaromatic polyimide films.

solvent	PI(BHDA+MCHM)	PI(BHDA+BBH)	PI(CpDA+MCHM)
N-methyl-2-pyrrolidone	I	SW	I
N,*N*-dimethylacetamide	I	SW	I
1,3-dimethyl-2-imidazolinc	SW	SW	I
dimethyl sulfoxide	SW	SW	I
pyridine	I	SW	I
m-cresol	I	SW	I
chloroform	I	I	I
dioxane	I	I	I
benzene	I	I	I
hexane	I	I	I
sulfuric acid	S	S	S

[a] S: soluble, SW: swelling, I: insoluble.

Conclusion

Nonaromatic polyimides were synthesized by a two-step polycondensation of bicyclo[2.2.1]heptane-2,3,5,6-tetracarboxylic 2,3;5,6-dianhydride (BHDA) and cyclopentane-1,2,3,4-tetracarboxylic dianhydride (CpDA) with aliphatic diamines in HPMA. Inherent viscosities of the poly(amic acid)s were rather low, but they formed free-standing and flexible films after being cast then cured. The nonaromatic polyimide prepared from polyalicyclic monomers PI(BHDA+BBH) has good thermal stability with no significant weight loss up to 350 °C, and the T5 is around 430 °C. The high-temperature stability can be explained by the introduction of a bicyclic structure. The temperatures with a maximum rate of the decomposition in N_2 appear in the range of 450-490 °C. Char yields at 545 °C of the nonaromatic polyimides are lower than those of semi-aromatic and aromatic polyimides. These polyimide films were colorless and transparent in the near IR region. They exhibited a cutoff around 230 nm. All the alicyclic polyimide possessed negligibly small birefringence below 10^{-4} and exhibited amorphous nature. The PI(BHDA+BBH) film had a tensile modulus of 2.05 GPa and a tensile strength of 52 MPa. It may be the first example of nonaromatic polyimides for which the mechanical property was evaluated. All the polyimide films were insoluble in common organic solvents.

Acknowledgement

The authors thank Ms Chiharu Sekiya and Mr. Michiaki Yoshida of Tokyo Polytechnic University for the X-ray measurement and their technical assistance. This work was supported financially by Academic Frontier Project for Private Universities: matching fund subsidy from MEXT (Ministry of Education, Culture, Sports, Science and Technology, Japan), 2001-2005.

References

1. Wu, S.; Whelan, J. M. Jr. U. S. Patent 3,037,966, 1962.
2. Volksen, W.; Cha, H. J.; Sanchez, M. I.; Yoon, D. Y. *React. Funct. Polym.* **1996**, *30*, 61-69.
3. Watanabe, Y.; Sakai, Y.; Ueda, M.; Oishi, Y.; Mori, K. *Chem. Lett.* **2000**, *5*, 450-451.
4. Watanabe, Y.; Sakai, Y.; Shibasaki, Y.; Ando, S.; Ueda, M. *Macromolecules* **2002**, *35*, 2277-2281.
5. Yamada, M.; Kusama, M.; Matsumoto, T.; Kurosaki, T. *J. Org. Chem.* **1992**, *57*, 6075-6077.
6. Matsumoto, T. *Macromolecules* **1999**, *32*, 4933-4939.
7. Boese, D.; Lee, H.; Yoon, D. Y.; Swalen, J. D.; Rabolt, J. F. *J. Polym. Sci., Part B: Polym. Phys.* **1992**, *30*, 1321-1327.
8. Honma, S. In *Handbook of plastics and functional polymers*; Ide F, Ed.; Sangyo Chosakai: Tokyo, 2004; pp 356-371.

Chapter 24

A Review of Biodegradable Thermoplastic Starch Polymers

Peter J. Halley, Rowan W. Truss, Martin G. Markotsis, Celine Chaleat, Melissa Russo, Anna Lisa Sargent, Ihwa Tan, and Peter A. Sopade

Centre for High Performance Polymers, School of Engineering, The University of Queensland, Brisbane, Queensland 4072, Australia

This article provides a review of thermoplastic starch polymers [unlike polymers with added granular starch] including an introduction to biodegradable polymers and thermoplastic starch polymers; a review of thermoplastic starch polymer development; a review of reactive modification of thermoplastic starch, examining the structure-property relationships of thermoplastic starch and a review of commercial thermoplastic starch polymer applications.

© 2008 American Chemical Society

Introduction

Both natural and synthetic biodegradable polymers are an exciting novel class of polymer materials. Biodegradable polymers are polymers that by a biological action breakdown to biomass, CO_2 and water in a given time period (defined by a specific biodegradation standard) and in a given environment (i.e. marine, compost, anaerobic sludge). Biodegradable polymers can be further subdivided into Renewable and Non-renewable biodegradable polymers. Renewable biodegradable polymers utilise a renewable resource (ie a plant by-product) in the development of the polymer, rather than a non-renewable (ie petroleum-based) resource. The long term research and development focus of many laboratories is on renewable/biodegradable polymers, but initial R&D work on petroleum-based biodegradable polymers has been very useful for many of the initial biodegradable products. Biodegradable polymers traditionally have also been categorised by base polymers [refer to Table 1 in [1] which summarises various biodegradable polymers, along with their generic advantages, disadvantages, potential applications and some current suppliers].

Starch is the major polysaccharide reserve material of photosynthetic tissues and of many types of plant storage organs such as seeds and swollen stems. Starch occurs in nature as water insoluble granules. The starch granule is essentially composed of two main polysaccharides, amylose and amylopectin with some minor components such as lipids and proteins. Starches from different botanical origin have different biosynthesis mechanisms and hence may exhibit distinct molecular structure and characteristics as well as diversity in shape, size, composition and other macroscale constituents of the starch granules. Thus the ultimate processing and properties of the starch are linked to starch genetics as well as various structure levels from granule structure, macromolecular structure and crystalline macrostructures.

Thermoplastic Starch

Plasticized starch is essentially starch that has been modified by addition of plasticizers (or other plasticising additives) to enable processing. Thermoplastic starch is plasticized starch that has been processed [typically using heat and pressure] to completely destroy the crystalline structure of starch to form an amorphous thermoplastic starch. Thermoplastic starch processing typically involves an irreversible order-disorder transition termed gelatinisation. Starch gelatinisation is the disruption of molecular organization within the starch granules and this process is affected by starch-water interactions. Due to its relevance in starch processing both in food and non-food industry, starch gelatinisation has been extensively studied in the past decades. Most starch

processing involves heating in the presence of water and some other additives [for instance, sugar and salt to control gelatinization in the food industry, or glycerol as a plasticiser for biodegradable plastics applications]. Understanding the mechanism of starch gelatinization and how the starch characteristics dictate the gelatinisation behaviour is thus necessary for better and more effective control of the structure development during processing and to allow design of optimum processing conditions of starch based polymer blends. From many studies, it is clear that starch gelatinisation involves: 1) the loss of crystallinity of the granule as measured by the loss of birefriengence and its x-ray diffraction pattern, 2) an uptake of heat as the conformation of the starch is altered, 3) hydration of the starch as accompanied by swelling of the granules, 4) a decrease in the relaxation time of the water molecules, 5) loss of molecular (double helical) order and 6) leaching of the linear molecules (amylose) from ruptured granules [2]. Lai [3] shows raw starch granules made up of amylose (linear) and amylopectin (branched) molecules. Then the addition of water breaks up crystallinity and disrupts helices. Addition of heat and more water causes granules to swell and amylose diffuses out of the granule. Granules, mostly containing amylopectin are collapsed and held in a matrix of amylose.

More complex models of gelatinisation have been described but they are usually along the following three themes: (a) Water mediated melting of starch crystallites [2, 4, 5] (b) Melting process in semi crystalline polymers [6-9] (c) The breakdown of starch structure as side chain liquid crystalline polymer (SCLCP) [10-14]. Recent work in our laboratories [15] using modulated DSC to separate glass transition and gelatinization events has further supported an extension of the SCLCP model and hypothesized gelatinization occurs via (i) breakage of starch-starch–OH bonds, (ii) formation of starch-solvent –OH bonds and (iii) an unwinding helix-coil transition. These insights into gelatinization will help us understand and control the final structure and properties of the thermoplastic starch polymer.

Thermoplastic Starch Polymers

Thermoplastic starch polymers have been widely investigated since the 1970s and are attractive in that they start from a low cost base (are therefore on par with competing synthetic non-biodegradable polymers) and are able to be modified or blended with other polymers in order to 'engineer-up' their processing and properties. [This is opposite to the development of high performance biodegradable polymers where the objective is to lower the cost base of the material].

A review of initial research on processing, rheology and properties of thermoplastic starch is provided by Lai [3] and concentrates on effects of starch

constituents and moisture on gelatinization, rheological properties and fragmentation during extrusion of thermoplasticized starch. Effects of temperature, moisture content and additives on the rheological properties of thermoplastic starch has also been examined [16,17]. These studies generally find a power-law behaviour of the viscosity-shear rate profile and a reduction in viscosity with increasing moisture, temperature and plasticizers, with the exception of glycerol monostearate (GMS) which increases viscosity (theoretically due to unmelted helical complexes of starch-GMS). More detailed studies of effects of structural changes and rheological properties [18,19] highlighted the importance of the semi-crystalline gel-like structure of starch on the rheological properties and the ability of strong shear conditions to disrupt this structure.

Jane [20] examined the effects of addition of various salts on the breakdown of starch structure where the salts interact with free water to affect plasticization. It was found that there are both water structure effects (which depends on salt charge density as to whether salt increases [high charge density; structure maker with water, ex NaCl] or decreases [low charge density; structure breaker with water, ex NaCl] gelatinisation temperature) and electrostatic effects (where since starch is electronegative [OH-ion abundance]) so cations destabilize starch granules and anions stabilise starch granules. Onteniente [21] examined the extrusion blending of starch plastics with epoxidised linseed oil and found some improvements in water resistance afforded by the oils. It is known that lipids [where lipids content varies between various starch types from potato (0.05%), corn (0.6%), wheat (0.8%), tapioca (0.1%) to waxy maize starch (0.15%)] reduce solubilisation, decrease thickening power and increase cloudiness by forming amylose-lipid complexes [22].

However in these studies above, although they are instructive to understanding thermoplastic starch processing it should be noted that thermoplastic starch polymers based solely on starch are extremely water sensitive, can suffer from significant molecular weight change in extrusion [23-25] and are thus of limited practical value. Therefore most of the commercial research on thermoplastic starches has involved modified starches and/or blends with additives and other polymers. Early work on thermoplastic starch blends includes the study by Otey [26] who investigated castable degradable mulch film derived from starch-polyvinylacetate (PVAc) blends with Polyvinyl chloride (PVC) coatings. Additionally Otey [27, 28] investigated the development of blown starch based agricultural mulch films based on gelatinized corn starch, polyethylene (PE) and poly ethylene-acrylic-acid (PEAA) polymers and various additives. Good film blowing performance was achieved with increased ammonia and urea [to improve starch-EAA interactions]. Bastioli and coworkers [29, 30] and Shogren and colleagues [31] also investigated starch-ethylene-vinyl alcohol (EVOH) blends and Novamont MaterBi (starch-EVA) materials looking at the ratio of amylose and amylopectin and moisture content in the starch. However, these studies are symptomatic of early biodegradable plastics work,

where the material was not entirely biodegradable and did not meet biodegradability standards [32, 33]. But of course it should be noted that much of this earlier work has led to the science behind modern biodegradable blends.

Mao [34] examined the extrusion of thermoplastic cornstarch-glycerol-polyvinyl alcohol (PVOH) blends and noted the effect of PVOH to improve mechanical properties and slow biodegradation. Much debate on PVOH degradability has been well reviewed by Chiellini [35] who summarises that molecular weight and type of PVOH may affect its biodegradability, which although much slower than starch, appears to show degradability with specific enzymes. Doane [36] has reviewed thermoplastic starch/biodegradable polymer blends research and highlighted work at USDA focussing on developing either (1) starch/biodegradable polymer blends (starch/polylactic acid(PLA), starch/polyhydroxybutrate(PHB), starch/polycaprolactam(PCL), and starch/polysaccharide/protein blends) and (2) starch with grafted thermoplastic sidechains (free radical initiated starch-g-polymethacrylate (PMA), starch-g-polystyrene (PSty)) for blending with thermoplastics. All systems were generally plasticized with urea and other polyols. Doane and co-workers [37, 38] highlighted development of fully degradable systems including starch/polylactic acid (PLA), starch-polycaprolactam(PCL) and reactively modified starch copolymers. However as described by Jopski [39] prices for some synthetic biodegradable polymers were still cost prohibitive. Recent research work has shown promise for reducing base costs of synthetic biodegradable polymers, by examining the development of polylactic acid (PLA) polymers via various novel conversion methods from starch [40, 41]. Obviously the low cost conversion methods of Cargill-Dow's PLA production process established in 2003 (Natureworks^{TM}) where PLA is developed from corn starch fermentation and polymerization during extrusion is based on this earlier work. Ratto [42] examined poly butylene succinate adipate (PBSA) terpolymer/ granular starch composites for blown films and which showed good film tensile properties and control biodegradation with granular starch addition. Thermoplastic starch/cellulose fibre extrudates and injection molded products were examined [43] and showed a reduction in water adsorption with increasing fibre content. Work [44] examined the use of thermoplastic starch-polyester blends for use in mulch film applications noting excellent field performance and biodegradability for these materials.

Modified processing techniques have been useful for thermoplastic starch polymers. Recent work [45, 46] has examined the use of coextruded sheet processing to produce polyester / thermoplastic wheat starch / polyester multilayer films. They found that adhesion strength between the layers and stability of the interface were crucial properties in controlling the final performance properties of the films. Work by Sousa [47] has examined use of the novel shear controlled orientation injection molding (SCORIM) process to control morpholoiges and provide tensile property increases of thermoplastic starch/synthetic blends.

Reactively Modified Thermoplastic Starch Polymers

In terms of modification of starch, many laboratory approaches have been taken from acetylation/esterification of starch to starch acetates, carbanilation of starch with phenyl isocyanates, addition of inorganic esters to starch to produce phosphate or nitrate starch esters, production of starch ethers, and hydroxypropylation of starches via propylene oxide modification [48]. Generally all these modifications involve hydroxyl group substitution on the starch (increasing the degree of substitution (DOS) of OH groups) that will lower gelatinization temperatures, reduce retrogradation (recrystallisation over time) and improve flexibility of final products.

Takagi [49] examined corn starch acetate/polycaprolactone (PCL) blends and showed that the blends are able to maintain biodegradability (after acetylation) and have stable viscosities with increasing acetylation. This is due to the increasing stability and thermoplasticity afforded by the acetylation. Increasing acetylation also reduces retrogradation. Tomasik [50] examined the acetylation of starch via extrusion with succinic, maleic and phthalic anhydrides and found a decrease in water binding capacity of the extrudates. However they also noted the reactive extrusion process was difficult to control. Fringant [51] examined the acetylation of starch via the pyridine-acetic anhydride procedure and produced modified starches with DOS of 1.7 that were easily processible but had deterioration in some mechanical properties. Of course acetylation levels can reduce biodegradation of the starch polymer [52], so a balance between property water resistance and biodegradation must always be maintained. Fatty acid ester modification of starches was also examined [53] and although thermoplastic processible starch-ester polymers could be produced, it was stated that the additional costs of these modifications probably would limit industrial use of these materials. Hydroxypropylation of normal and high amylose starch was conducted [54] and showed an increase in ease of extrusion, decrease in water absorption and increase in flexibility and strength.

Crosslinked starch may be induced by addition of organic esters (ie succinic anhydride), inorganic esters (ie trisodium trimetaphosphate (TSTMP)), hydroxydiethers (ie epichlorohydrin) and irradiation. Kulicke [55, 56] examined solution phase crosslinking of starch with epichlorohydrin and TSTMP, and although some of this work was extended to cast starch/PVOH films [57], no reported work has examined crosslinking thermoplastic starch in the melt during extrusion processing. Jane [20] examined the crosslinking of starch/zein cast films for improving water resistance.

Reactive blending of thermoplastic starch/polymer blends has been examined recently and aims to increase properties and performance via control of blend morphologies. Mani [58, 59] examined different techniques for compatibilising starch-polyester blends. They examined development of maleic anhydride grafted polyester/starch blends and starch-g-polycaprolactone

compatibilised starch/polycaprolactone blends, and found significant increases in tensile properties of the compatibilised blends, over the uncompatibilised blends. Recent work extending this original work [60] has shown improved properties for injection molded starch/biodegradable polyester materials via addition of anhydride-modifed polyester compatibilisers. Dubois [61] also examines the reactive compatibilisation of starch/PLA and starch/PCL polymers via MA-g-PLA and PCL-g-dextran compatibilisers. Interestingly they find no difference between compatibilisation when using starch granules or thermoplastic starch, which may indicate the granules are quickly gelatinized during processing.

In terms of nanocomposite reinforcement of thermoplastic starch polymers there has been many exciting new developments. Dufresne [62] and Angles [63] highlight work on the use of microcrystalline whiskers of starch and cellulose as reinforcement in thermoplastic starch polymer and synthetic polymer nanocomposites. They find excellent enhancement of properties, probably due to transcrystallisation processes at the matrix/fibre interface. McGlashan [64] examine the use of nanoscale montmorillonite into thermoplastic starch/polyester blends and find excellent improvements in film blowability and tensile properties. Perhaps surprisingly McGlashan [64] also found an improvement in the clarity of the thermoplastic starch based blown films with nanocomposite addition which was attributed to disruption of large crystals.

It is clear that research into modifications to thermoplastic starch based polymers is burgeoning and that property and processing improvements derived from this research will help thermoplastic starch polymers widen their application products and markets.

Understanding Thermoplastic Starch Structure-Property-Processing-Performance-Biodegradation Relationships

Many studies interested in formulation of thermoplastic starch polymers or reactively modified thermoplastic starch polymers are based around development of formulations using conventional polymer processing equipment such as single screw extrusion or twin screw extrusion. This melt processing provides mixing, melting and gelatinization of formulations and blends, and produces new materials in [typically] polymer pelletised form. These pellets can then be reprocessed on polymer conversion equipment such as film blowers, injection molders, blow molders, thermoformers, sheet extruders and other conventional equipment. Many studies that are focused on the structure-property relationships of thermoplastic starch, focus on the initial formulations and omit the effects of this reprocessing on polymer conversion equipment. To fully understand thermoplastic starch polymer system one must understand the structure-property-processing-performance-biodegradation relationships. Currently studies [65, 66] in our laboratory have focused on understanding structure-processing-property

relationships (effects of relative humidity and temperature on ultimate mechanical properties) and structure-processing-biodegradation relationships (diffusion of water in thermoplastic starch blends) for compression molded products. Initial work has shown that modulus, yield stress and crack energy is highly affected by relative humidity. Figure 1 shows tensile data from compression molded samples that have been stored at various relative humidities. The work to date has shown a transition from ductile elastic material at higher humidities through to hard brtille material at lower humidities. Further studies are continuing to examine the ductile to brittle transition with changes in moisture content.

Additionally the water uptake [as determined by MRI imaging after storage of compression molded sheets at selected relative humidites] is also a function of relative humidity as can be seen by the effects of relative humidity (RH) and temperature (T) on water diffusivity (D_0) in Table 1. This has obvious implications for product performance and initial biodegradation rates [aided by water].

Clearly, understanding these relationships will provide the ability to understand these systems and aid in the smart design of new thermoplastic starch products. Our future work is focussing on effects of subsequent conversion processing conditions on structure-property-biodegradation relationships.

Commercial Applications and Products for Thermoplastic Starch Polymers

Table 2 highlights companies producing thermoplastic starch, the types of polymers used, the types of applications and the contact details for more information.

The above is focused on thermoplastic starch polymers for traditional polymer markets, and thus much research and development for these materials has focused on improved water resistance and better mechanical properties for engineering and packaging applications.

Additionally, thermoplastic starch polymers are also been designed for newer application areas such as controlled drug delivery matrices. For example polyacrylate modifed starch microparticles have been used as protein and drug carriers, and starch/albumin microparticles have been designed for controlled protein release [67]. Research into starch based controlled release tissue scaffolds for growth factor release is also noted [67]. In tissue engineering applications obviously control of the breakdown of the starch matrix is crucial to maintain control over drug or macromolecule release. Also Alpeter [68] examined the use of novel shear controlled orientation injection moulding (SCORIM) to develop starch-polylactide and starch-poly(ethylene-co-vinyl

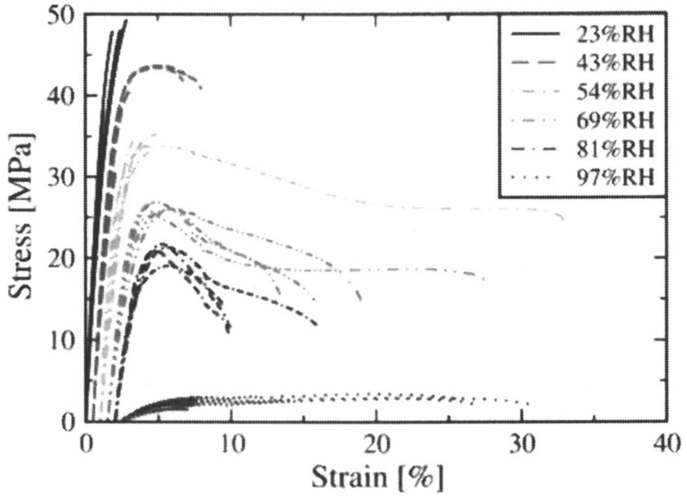

Figure 1. The effect of relative humidity (RH) on mechanical properties [stress-strain curves] of at thermoplastic starch polymer. (See page 5 of color inserts.)

Table 1. Diffusivity of Water at different Temperatures in Thermoplastic Starch Polymers pre-stored at various relative Humidities

	D_0 x 10^{-7} (cm^2/s)		
Pre-Storage Condition	T=25C	T=37C	T=45C
vac dried	0.53	1.00	2.56
23% RH	1.56	2.00	2.85
43% RH	1.57	2.00	3.63
54% RH	2.13	2.66	3.00
81% RH	3.80	4.07	4.20

In Polymer Durability and Radiation Effects; Celina, M., et al.;
ACS Symposium Series; American Chemical Society: Washington, DC, 2007.

Table 2. Commercial Thermoplastic Starch Polymers

Company	*Product name*	*Material*	*Application areas*
National Starch www.eco-foam.com/loosefill.asp	ECOFOAM	Modified maize/tapioca starch	Expanded foams, injection molded toys, extruded sheet and blown film applications
Novamont www.novamont.com/	Materbi	Thermoplastic starch polymer blends	biodegradable mulch films and bags, thermoformed products, injection molded items, and packaging foam
Rodenberg Biopolymers www.biopolymers.nl	Solanyl™	Modified potato starch	Injection molded products
Biotec GmbH www.biotec.de/engl/index_engl.htm	Bioplast™	Thermoplastic starch	bags, boxes, cups, cutlery, horticultural films, packaging films, planting pots, tableware, trays and wrap film
Earthshell www.earthshell.com/foam.html	EarthShell Packaging®	starch [from sources such as potatoes, corn, wheat, rice and tapioca] along with fiber, other processing agents, air, water and micro-thin biodegradable coatings	foamed trays, plates and packaging films and laminate
Plantic Technologies Ltd. http://www.plantic.com.au	Plantic™	Thermoplastic corn starch polymer	Thermoformed trays

alcohol) blends for replacing biomedical implants for temporary applications. However, although initial properties were improved by the novel processing, they found degradation rates too high for their applications. However this work and earlier work [69] showed that starch-based polymers exhibit a cytocompatibility that was promising for their use as biomaterials.

Future Developments

Clearly thermoplastic starch based polymers offer a very attractive base for new biodegradable polymers due to their low material cost and ability to be processed on conventional plastic processing equipment. The engineering of more advanced properties into these low cost base materials will continue to be

the main technological drive into the future. This development will most probably be in the form of integrating research already being developed in parallel from (a) thermoplastic starch polymers (like blending, nanocomposites and reactive modification) and (b) novel research from conventional thermoplastic polymer (such as nano- and microstructure control using novel additives and novel polymer processing to control morphology and properties). Additionally, the development of new biodegradable polymers with lower base costs (such as PLA from corn starch (Cargill Dow) and PHB from wheatgrass (Metabolix)) will also widen the types and applications of biodegradable polymers from niche applications to wider markets in the future.

Acknowledgements

PJH would like to acknowledge my colleagues and students over the past 12 years (the 35 researchers who know who you are) in biodegradable polymers. Thanks to the CRC for International Food Manufacture and Packaging Science, the Australian Research Council, The University of Queensland and Plantic Technologies for research funding.

References

1. Halley P. J. Thermoplastic starch polymers, *in Biodegradable polymers for industrial applications* R.Smith (ed), Woodhead Pub. , London, UK **2005**.
2. Donovan, J. W. *Biopolymers* **1979**, *18*, 263-275.
3. Lai L. S.; Kokini J. L. *Biotechnol. Prog.* **1991**, *7*, 251-266.
4. Liu, Q.; Charlet, G.; Yelle, S.; Arul, J. *Food Res. Int.* **2002**, *35*, 397-407.
5. Maaruf, A. G.; Man, Y. B. C.; Asbi, B. A.; Junainah, A. H.; Kennedy, J. F. *Carbohydrate Polymers* **2001**, *46*, 331-337.
6. Slade, L.; & Levine, H. *Carbohydrate Polymers*, **1988**, *8*, 183-208.
7. Billiaderis, C. G. *Food Technol.* **1992**, *46*, 98-109.
8. Blanshard, J. M. V. in T. Galliard, *Starch: Properties and potential* (pp. 16-54). Great Britain: John Wiley & Sons **1987**.
9. Roos, Y. H. *Phase Transitions in Foods*. San Diego, Academic Press **1995**.
10. Donald, A. M.; Kato, K. L.; Perry, A. P.; & Waigh, T. A. *Starch* **2001**, *53*, 504-512.
11. Jenkins, P. J.; Cameron, R. E.; Donald, A. M. *Starch* **1993**, *45*, 417-420.
12. Waigh, T. A.; Kato, K. L.; Donald, A. M.; Gidley, M. J.; Clarke, C. J.; Riekel, C. *Starch*, **2000**, *52*, 450-460.
13. Waigh, T. A.; Perry, A. P.; Riekel, C.; Gidley, M. J.; Donald, A. M.; *Macromolecules* **1998**, *22*, 7980-7984.

14. Jenkins P. J.; Donald, A. M. *Int. J. Biol. Macromolecules* **1995**, 315-321.
15. Tan I.; Wee C. C.; Sopade P. A.; Halley P. J. *Carbohydrate Polymers* **2004**, *58*, 191-204.
16. Willett J. L.; Jasberg B. K.; Swanson C. L. *Polym. Eng. Sci.* **1995**, *35*, 202-210.
17. Willett, J.; Jasberg B. K.; Swanson C. L. *Polym. Eng. Sci.* **1995**, *35*, 202.
18. Della Valle G.; Buleon A.; Carreau P. J.; Lavioie P. A. Vergnes B. *J. Rheol.* **1998**, *42*, 507-525.
19. Dintzis F. R.; Bagley E. B.; Felker F. C. *J. Rheol.* **1995**, *39*, 1399-1409.
20. Jane J. L.; Lim S.; Paetau I.; Spence K.; Wang S. in Polymers from Agricultural Co-products, Eds. M.Fishman, R.Friedman, Huang SJ, *ACS Symp. Ser.* **1993**.
21. Onteniente J. P.; Entienne F.; Bureau G.; Prudhomme J. C. *Starch* **1998**, *48*, 10.
22. Swinkels J. J. M. *Starch* **1985**, *37*, 1.
23. Davidson V. J.; Paton D.; Iosady L. L.; Laroque G. *J. Food Sci.* **1984**, *49*, 453-458.
24. Sagar A. D.; Merrill E. W. *J. Appl. Polym. Sci.* **1995**, *58*, 1647-1656.
25. Gomez M. H.; Aguilera J. M. *J.Food Sci.* **1983**, *48*, 378-381.
26. Otey F. H.; Mark A. M.; Mehlretter C. L.; Russel C. R. *Ind. Eng. Chem. Prod. Res. Dev.* **1974**, *13*, 90-92.
27. Otey F.; Westoff R. P.; Doane W. M. *Ind. Eng. Chem. Prod. Res. Dev.* **1980**, *19*, 592-598.
28. Otey F.; Westoff R. P.; Doane W. M. *Ind. Eng. Chem. Prod. Res. Dev.* **1980**, *19*, 1659-1666.
29. Bastioli C.; Bellotti V.; Rallis A. *Rheol. Acta* **1994**, *33*, 307-313.
30. Bastioli C.; Bellotti V.; Camia M.; Del Giudice L.; Rallis A. in *Biodegradable Plastics and Polymers*, (eds) Y.Doi and K.Fukuda, Elsevier Sci., Amsterdam, p200-213, **1994**.
31. Shogren R.; Fanta G.; Doane W. M. *Starch*, **1993**, *45*, 276-284.
32. De Kesel C.; vander Wauven C.; David C. *Polym. Degrad. Stab.* **1997**, *55*, 107-115.
33. Breslin V. *J. Env. Polym. Degrad.* **1993**, *1*, 127-135.
34. Mao L. J.; Imam S.; Gordon S.; Cinelli P.; Chiellini E. *J. Polym. Environ.* **2000**, *8*, 205-211.
35. Chiellini E.; Corti A.; D'Antone S.; Solaro R. *Prog. Polym. Sci.* **2003**, *28*, 963-1014.
36. Doane W. M. *Starch* **1992**, *44*, 293-303.
37. Doane W. M.; Swanson C. L.; Fanta G. F. in *Emerging Technologies for materials and chemicals from biomass*, (eds) R.M.Rowell, Schultz TP, R.Narayan, **1992** Elsevier, Amsterdam, 1-20.
38. Shogren R. L.; Fanta G. F.; Doane W. M. *Starch* **1993**, *45*, 276

39. Jopski T. *Kunststoffe German Plastics*, **1993**, *83*, 17-24.
40. Warth H.; Muelhaupt R.; Schaetzle J. *PPS-13 Int. Meet. Polym. Proc. Soc.* **1997** NJ, USA.
41. Gruber P.; Kolstad J.; Ryan C.; Hall E.; Eichen R. *US Patent 5484881* Melt stable amorphous lactide polymer film, **1996**.
42. Ratto J. A.; Stenhouse P. J.; Auerbach M.; Mitchell J.; Farrell R. *Polymer* **1999**, *40*, 6777-6788.
43. Funke U.; Bergthaller W.; Lindhauer M. G. *Polym. Degrad. Stab.* **1998**, *59*, 293-296.
44. Halley P.; Rutgers R. Coombs S.; Christie G.; Lonergan G. *Starch* **2001**, *53*, 362-367.
45. Martin O.; Schwach E. *Starch* **2001**, *53*, 372-380.
46. Martin O.; Avernous L. *J. Appl. Poly. Sci.*, **2002**, *86*, 2586-2600.
47. Sousa R. A.; Kalay G.; Reis R. L.; Cunha A. M.; Bevis M. J. *J. Appl. Polym. Sci.* **2000**, *77*, 1303-1315.
48. Gilliard T. *Critical Reports on Applied Chemistry* **1984**, 13.
49. Takagi S.; Koyama M.; Kameyama H.; Tokiwa Y. in *Biodegradable plastics and polymers*, Y.Doi and K.Fukuda (eds), pp437 **1994**.
50. Tomasik P.; Wang Y. J.; Jane J. L. *Starch* **1995**, *47*, 96-99.
51. Fringant C.; Desbrieres J.; Rinaudo M. *Polymer* **1996**, *37*, 2663-2673.
52. Rivard C.; Moens L.; Roberts K.; Brigham J.; Kelley S. *Enzyme Microb. Technol.* **1995**, *17*, 1848-852.
53. Sagar A. D.; Merrill E. W. *Polymer* **1995**, *36*, 1883-1886.
54. Bae S. O.; Lim S. T.; *Cereal Chem.* **1998**, *75*, 449-454.
55. Kulicke W. M.; .Aggour Y. A.; Nottelmann H.; Elsabee M. Z. *Starch*, **1989**, *41*, pp 140.
56. Kulicke W. M.; Aggour Y. A.; Elsabee M. Z. *Starch* **1990**, *42*, 134.
57. Chen L.; Imam S. H.; Gordon S. H.; Greene R. V. *J. Environ. Polym. Degrad.* **1997**, *5*, 111-117.
58. Mani R.; Tang J.; Bhattacharya M. *Macromol. Rapid Comm.* **1998**, *19*, 283-286.
59. Mani R.; Bhattacharya M.; Tang J. *J. Polym. Sci. A*, **1999**, *37*, 1693-1702.
60. Mani R.; Bhattacharya M. *Eur. Polym. J.* **2001**, *37*, 515-526.
61. Dubios P.; Narayan R. *Macromol.Symp.* **2003**, *198*, 233-243
62. Dufresne A.; Cavaille J. Y.; *J. Polym. Sci. B*, **1998**, *36*, 2211-2224.
63. Angles M. N.; Dufresne A. *Macromolecules* **2000**, *33*, 8344-8353.
64. McGlashan S. A.; Halley P. J.; *Polym. Int.* **2003**, *52*, 1767-1773.
65. Chaléat, C.; Markotsis, M.; Frances, F.; Pei, H. S.; Truss R. W.; Halley P. J. *RACI APS27 proc.* **2004**, P3-5.
66. Russo, M. A. L.; Strounina, K.; Waret M.; Nicholson, T. M.; Truss, R. W.; Halley P. J. *RACI APS28 proc.* **2006**, P4-2.

67. Piskin E., 'Chapter 9- Biodegradable polymers in medicine', in G. Scott (ed) *Degradable Polymers*, 2nd Ed., p379-412 Kluwer Acad. Pub., The Netherlands, **2002**.
68. Altpeter H.; Bevis M. J.; Gomes M. E.; Cunha A. M.; Reis R. L.; *Plast. Rubber Comp.* **2003,** *32*, 173-181.
69. Marques A. P.; Reis R. L.; Hunt J. A. *Biomaterials* **2002,** *23*, 1471-1478.

Chapter 25

The Role of Citrate Anions in Prevention of Calcification of Poly(2-hydroxyethyl methacrylate) Hydrogels

Zainuddin[1,4], David J. T. Hill[1], Andrew K. Whittaker[2], Anne Kemp[3], and Traian V. Chirila[4]

[1]Department of Chemistry, [2]Center for Magnetic Resonance, and [3]Centre for Microscopy and Microanalysis, The University of Queensland, St. Lucia, Brisbane, Queensland 4072, Australia
[4]Queensland Eye Institute, 41 Annerley Road, South Brisbane, Queensland 4101, Australia

The deposition of sparingly soluble calcium phosphates on PHEMA hydrogels, both *in vitro* and *in vivo,* can be modified by the incorporation of citric acid into the PHEMA hydrogels. In the presence of citrate anions the formation of hydroxyapatites was prevented. The calcium phosphate deposits which formed *in vitro* on PHEMA were mainly monocalcium phosphate monohydrate and dicalcium phosphate dihydrate. The types of deposits formed *in vivo* were quite different from those formed *in vitro*. The *in vivo* deposits formed on PHEMA were mostly hydroxyapatites deficient in calcium and hydroxyl ions. Citrate anions were also observed to prevent significantly the deposition *in vivo* of protein onto PHEMA hydrogels.

© 2008 American Chemical Society

Poly(2-hydroxyethyl methacrylate) (PHEMA) hydrogels are one of the most widely used hydrogels for soft lenses and soft tissue replacement devices. However, due to the susceptibility of PHEMA towards calcification, its application in implanted devices may be limited. Experimental evidence has shown that the spoliation of hydrogel contact lenses is caused by a large variety of deposits (white spots, surface films and plaque, brown discoloration) of which components originate mostly in the tear film (1-9). The lipids, proteins and inorganic salts in the tears appear to play a major role in spoliation, however the composition and appearance of deposits is of great diversity and influenced by many variables. Recently, several instances of spoliation of implanted HEMA-based hydrogel lenses have become available (*10-19*). An intraocular lens (IOL) made from PHEMA, distributed by Alcon (USA) as IOGEL 1103, was the first hydrogel IOL reported to calcify after implantation (*10*). Opacification of IOLs manufactured from a copolymer of HEMA and methyl methacrylate (MMA) (Vista Optics, UK) and distributed by MDR Inc. (USA) was reported in patients (*11*), occurring both superficially and in the bulk of the hydrogel. Calcium phosphate was identified in the superficial deposits, but not in the opacified zones inside the IOL. In another study (*12*), the destrophic calcification of five different IOL materials was assessed in rabbits (as intramuscular, subcutaneous and intracapsular implants). Calcification was noted only in PHEMA and a hydrogel made from 1-vinyl-2-pyrrolidinone, phenylethyl acrylate and n-hexyl acrylate. Many more examples of IOL failure due to calcification refer to the implantation of Hydroview™ IOL (Bausch & Lomb, USA) manufactured from a copolymer of HEMA and 6-hydroxyhexyl methacrylate. About half a million of these IOLs have been implanted to date (*13-19*), and opacification due to calcium phosphate deposits has been noted over 4 years in hundreds of cases. These involve both surface and sometimes the sub-surface areas of the IOL optic and generally require explantation. Similar deposits were also noted in implanted artificial corneas which caused cloudiness of the central zone (optic part) of the Alphacor™ (*20*).

To the best of our knowledge, only a few studies have attempted to prevent the calcification of HEMA-based hydrogels. It has been reported that introduction of carboxylate anions can either prevent or enhance calcification. Cerny et al. (*21*) found that copolymers of HEMA with 4 wt% methacrylic acid (MAAc) did not calcify under subcutaneous implantation in a rat for 14 months. A similar result was also observed after the implantation of HEMA/MAAc copolymers in the animal urinary tract (*22*). Other studies carried out *in vitro* showed that the presence of carboxylate anions significantly reduced the deposition of calcium phosphate (*23*) and calcium oxalate (*24*) on acrylic polymers and certain biopolymers. These findings obviously suggest an inhibitory effect of carboxylate anions on calcification. However, by contrast,

Filmon et al. (*25*) observed that modification of PHEMA through carboxymethylation with bromoacetic acid in alkaline medium induced considerable calcium deposition. For immersion in simulated body fluid (SBF), Miyazaki et al. (*26*) found that calcification was favorable in some circumstances when the polymer contained 20 and 50 mole% carboxyl groups.

Other reports (*27-29*) have focused on the role of citric acid, as a source of carboxylate anions, during precipitation of calcium phosphates from electrolyte solutions. It has been found that citrate anions inhibit the crystal growth of calcium phosphates and hinder their transformation into hydroxyapatites. This was attributed to the adsorption of citrate anions into the crystals and the displacement of an equivalent amount of phosphate anions. Interestingly, Rhee and Tanaka (*30*) found that the presence of a collagen membrane in the medium changed the behavior of citrate anions from being an inhibitor to becoming a promoter of calcification, provided that the molar ratios of calcium to citric acid were between 2 and 12.

Citric acid (H_3Cit) is a naturally occurring triprotic acid with acid dissociation constants (pKa) between 3 and 6.5. The carboxylic groups of citric acid can dissociate to form three different species, namely H_2Cit^-, $HCit^{2-}$ and Cit^{3-}, with different concentrations as a function of pH (*31*). As the pH of SBF (7.4) is higher than the pKa of $Hcit^{2-}$, most of the carboxylic groups will dissociate in SBF to form the citrate anion Cit^{3-}, as demonstrated in the following reaction.

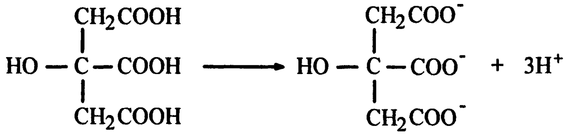

Citrate anions are present in fresh wet bone to about 1 wt%, and they play an important role in the formation and/or dissolution of bone apatite through their adsorption onto both the reactant and the product phases (*27-30,32*). Thus, citric acid and its salts play important roles in calcium phosphate deposition in biological systems.

The inhibitory effect of citrate anions on the calcification of PHEMA hydrogels has been evaluated in this study. Here the release of citric acid from the hydrogels was designed such that the molar ratios of calcium to citric acid were unfavorable for nucleation of calcium phosphates (*30*). The study constitutes the first model investigation of the role of citrate anions in prevention of calcification of PHEMA hydrogels.

Experimental

Preparation of PHEMA Hydrogels

The method used for preparation of the PHEMA hydrogels was described in an earlier report (*33*). Fully hydrated samples equilibrated at room temperature were immersed in Millipore water at 37 ± 0.5 °C for at least 2 weeks before calcification experiments commenced. The incorporation of citric acid into PHEMA was performed by the swelling equilibrium partition method using a 2.5 M citric acid solution. Prior to incubation in SBF or subcutaneous implantation of the hydrogels in rats, the citric acid-equilibrated gels were kept in Millipore water at 37 ± 0.5 °C for one week. The hydrogels were sterilized by autoclaving for 20 min before implantation in the rats.

UV Analysis for Citric Acid

To obtain an estimate of the extent of release of citric acid from the PHEMA hydrogels during calcification in SBF, the concentration of citric acid released from PHEMA hydrogels into water was monitored using a Perkin-Elmer UV spectrometer. The measured UV absorbances at 205 nm were corrected for the absorbances of solutions equilibrated for the corresponding time with PHEMA samples containing no citric acid (*34*). A calibration curve for measuring citrate concentration was produced from the absorbance at 205 nm of solutions with different concentrations of citric acid ranging from 0.1 to 10 mM.

In the study of the extent of citrate release over time, measurements of the citrate concentration were made every week and the surrounding solution was changed. This followed the procedure adopted for the calcification studies in SBF. Figure 1 shows the citrate concentration in the solution at the end of each week.

Based on this release profile, it is obvious that the concentration of citric acid at the end of one week is ≈ 45 mM. The concentration dropped significantly at the end of week 2 to ≈ 0.6 mM. Thereafter it changed more slowly, dropping from 0.15 to 0.05 mM through weeks 3 to 14, and then approached zero at the end of week 17.

In Vitro Calcification

Cylindrical PHEMA samples were each immersed in glass vials containing 20 mL of SBF and incubated in an oven at 37 ± 0.5 °C for one to nine weeks. The SBF was prepared according to the procedure described by Tas (*35*) and Saiz et al. (*36*), and the solutions were changed every week. After completion of

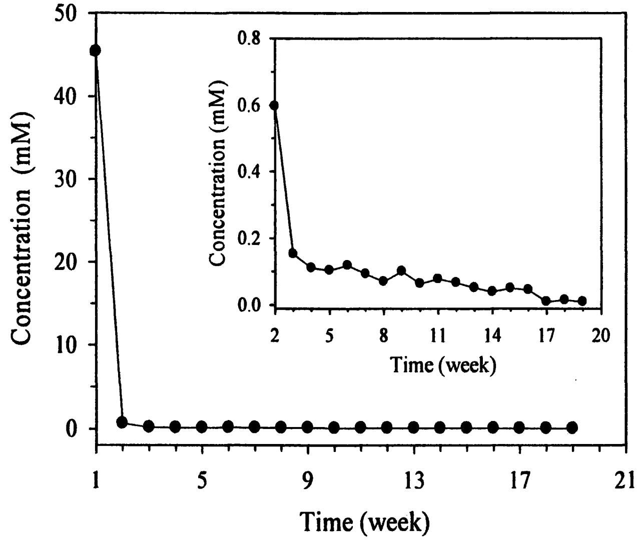

Figure 1. Plot of citric acid released from a PHEMA+citric acid hydrogel into 20 mL Millipore water at 37 ± 0.5 °C.

the experiments, the samples were thoroughly rinsed with Millipore water, dried at ambient temperature and pressure, further vacuum dried at room temperature, and then stored in a desiccator prior to XPS, SEM and EDS analyses.

In Vivo Calcification

Five 11-week old female Wistars (weight = 230 - 260 g) supplied by the Centre for Breeding Animal House, University of Queensland were used in this study. All surgical procedures were performed in accordance with the Australian Code of Practice for the Care and Use of Animals for Scientific Purposes (2003).

The hairs at the surgical areas of the rats were shaved under anaesthetic (halothane) using electrical clippers, and the skin cleaned by scrubbing with an antiseptic agent (betadine) and finally with 70% alcohol/water using clean and sterile gauze swabs. An approximately 0.5 cm subcutaneous incision was made for each hydrogel implant using sterile (new), sharp scalpel blades. Dissection of deeper tissues (connective tissues) was performed using blunt scissors. After implantation of the hydrogel sample, the wound was sutured.

On day 61 after surgery, the rats were sacrificed by anaesthetizing them with carbon dioxide (CO_2) gas, followed by cervical dislocation. Immediately after the animal was dead, an incision of about 1 cm at the sample location was made using a scalpel blade and the hydrogel implants were removed with forceps. The

hydrogels were first immersed in 10% formalin solution and then washed thoroughly with Millipore water and kept in water before staining with alizarin red.

For SEM, XPS and EDS analyses, the samples were treated with a 10% formalin solution, then washed thoroughly with Millipore water, and finally dehydrated in a graded series of water-ethanol mixtures and subjected to vacuum drying at room temperature.

Characterization of Calcium Deposits

Scanning Electron Microscope (SEM) Analysis

After coating the samples with platinum, SEM images were taken using a JEOL 6400F instrument with an accelerated electron energy of 5 keV.

Staining with Alizarin Red

To confirm the presence of calcium deposits in the *in vivo* explants, the samples were stained with alizarin red, a common specific stain for calcium, and were examined using a conventional light microscope (LM) (OLYMPUS SZH10). The staining of the samples was performed by immersing them in a 1% solution of alizarin red in alkaline solution (0.5% KOH) at room temperature for one day, followed by washing with water and then storage in 0.5% KOH solution until there were no further changes in color. The samples were kept in water for at least 2 weeks prior to observation under the microscope.

X-Ray Photoelectron Spectroscopic (XPS) Analysis

Semi quantitative analyses of the calcium phosphate deposits were acquired using a Kratos Axis ULTRA XPS spectrometer incorporating a 165-mm hemispherical electron energy analyzer. The source of X-ray incident radiation was a monochromatic Al Kα (1486.6 eV) at 150 W (15 kV, 10 mA). Survey (wide) scans were taken at an analyzer pass energy of 160 eV.

Energy Dispersive X-Ray Spectroscopic (EDS) Analysis

For complementary quantification of the elements present in the calcium phosphate deposits, EDS analyses were performed on carbon-coated samples using an electron energy of 15 keV and a JEOL 6460LA EDS instrument.

Results and Discussion

In Vitro Analysis

We demonstrated in a previous paper (*33*) that the inhibition of calcification in SBF through copolymerization of HEMA with other monomers was only effective for a short time - about one week. So, in an attempt to extend the inhibition time, another approach was adopted in this study.

It is well known that carboxylate anions have the ability to form a strong complex with divalent cations, particularly with calcium ions (*37,38*). Therefore, citric acid which carries three carboxyl groups may be effective in preventing the formation of calcium phosphate deposits on PHEMA. Figure 2 shows the morphology of the calcium citrate crystals which were precipitated during the first week of immersion of the PHEMA hydrogels in the SBF solution. It can be seen that the precipitates were fibre-like crystals (Figure 3A). According to a previous study on the dissolution of hydroxyapatite and formation of calcium citrate, Mirsa (*29*) identified similar precipitates as $Ca_3(citrate)_2.4H_2O$. Interestingly, for the SBF solution which contained 0.6 mM citrate anions at the end of week 1 in the SBF solution, calcium phosphate deposits were observed on the growing calcium citrate crystals (Figure 3B). However, the deposition of calcium phosphates onto the surface of the PHEMA was significantly diminished in the presence of the citrate anions. This finding was consistent with the XPS analysis which showed an insignificant amount of calcium phosphate on the sample surface after two weeks.

Further monitoring of the precipitation process showed no crystallization of calcium citrate during weeks 2 to week 9 of immersion in SBF, although citric acid was still being released slowly from the PHEMA matrix over this period. However, deposition of calcium phosphate on the PHEMA surface did occur over this period, albeit very slowly.

The above observations may be explained on the basis of supersaturation of the solutions with respect to calcium citrate and calcium phosphate. Calcium citrate and calcium phosphate can be precipitated from a supersaturated solution. Ciavatta et al. (*39*) have reported that the solubility of calcium citrate in water at 25 °C is ≈ 1.5 mM, which corresponds to an overall calcium concentration of 4.5 mM and a citrate concentration of 3.0 mM. Since the concentration of calcium ion in a fresh SBF solution is 2.5 mM, and the total citrate ion concentration varies between 0.15 mM and 0.05 mM during weeks 2 through 9 for immersion in SBF, it is not surprising that calcium citrate does not precipitate during this period.

Citrate ions form strong ion pairs with a variety of the ions present in an SBF solution (*39,40*), including with magnesium and calcium ions. Weaker ion pairs are formed with sodium ions. So very complex citrate equilibria, which are still not fully understood, become involved when citric acid diffuses out of

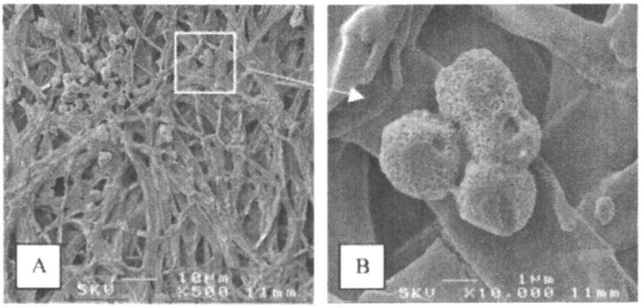

Figure 2. (A) an SEM micrographs of the calcium citrate crystals formed in SBF during the first week of calcification; (B) enlarged micrograph, showing the presence of calcium phosphate deposits on the citrate crystals. The concentration of citric acid released into the SBF was 0.6 mM.

PHEMA into an SBF solution. At the higher released citric acid concentrations, the formation of calcium citrate crystals can bring about a depletion of the calcium ion concentration in the SBF solution, so less calcium phosphate will precipitate onto the polymer. At lower citric acid concentrations, the inhibition effect of citrate anions on formation of calcium phosphates has been attributed to the complex equilibria between calcium, citrate and phosphate ions (*27-29*). Precipitated calcium phosphates may undergo dissolution via surface exchange between phosphate and citrate ions (calcium citrate is much more soluble than calcium phosphate).

The SEM micrographs shown in Figure 3 provide evidence for the proposed prevention of calcification by citrate anions. It can be seen that the calcium phosphate deposits formed on PHEMA in the presence of citric acid are much lower in amount and smaller in size (Figure 3C). In other words, under the action of citrate anions, the extent of the deposition of calcium phosphates was significantly reduced and the nature of the deposits modified. This is confirmed by the very low calcium contents of the calcium phosphate deposits over the whole range of calcification times (see Figure 4), as determined by XPS. It should be mentioned here that after 5 weeks of calcification time, at least one layer of calcium phosphate (with a thickness of $\approx$ 0.4 μm (*33*)) was deposited on the surface of PHEMA containing no citric acid. Thus, it is anticipated that the calcium content of the calcium phosphate deposits tends to plateau after 5 weeks in SBF solution.

Semi-quantitative XPS analyses on the calcium phosphate deposits revealed that due to the inhibition and dissolution effects of citric acid, the calcium phosphates have Ca/P molar ratios between 0.5 and 1.2. These values are lower than the Ca/P molar ratios for the deposits formed on PHEMA containing no

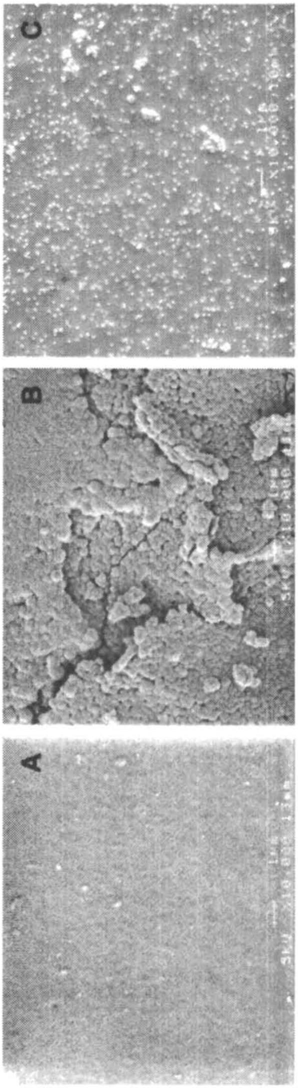

Figure 3. SEM micrographs after calcification in SBF for 7 weeks. (A) PHEMA control; (B) PHEMA without added citrate and (C) PHEMA with added citrate.

citric acid, for which the Ca/P ratios ranged from 1.0 to 7.5 (*33*). This suggests that in the presence of citric acid, the types of calcium phosphate phases formed on the polymer probably consist mainly of monocalcium phosphate monohydrate (MCPM) and dicalcium phosphate dihydrate (DCPD). These two calcium phosphate phases have higher solubility products compared to the other types of calcium phosphates (*41,42*).

Another interesting role of citic acid observed during *in vitro* calcification was to prevent the involvement of magnesium in the formation of calcium phosphate deposits. Magnesium has been known to stabilize the calcium phosphates, e.g. in the form of *whitlockite* phase. Thus magnesium inhibits the transformation of these calcium phosphate deposits into hydroxyapatites (33, *43,44*).

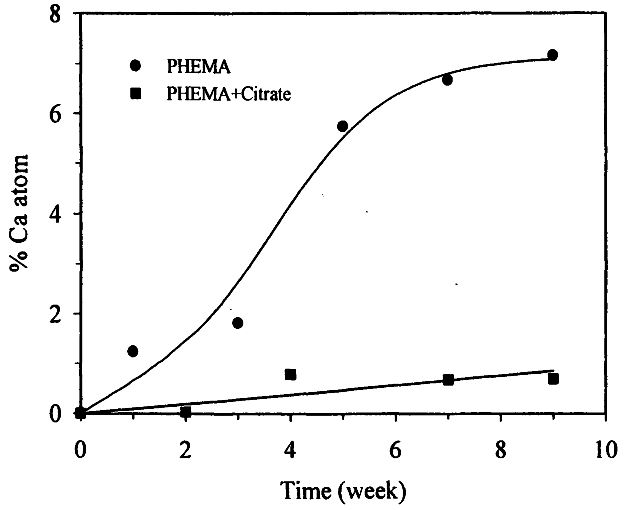

Figure 4. Changes in calcium content of calcium phosphates formed on the surface of PHEMA and PHEMA+Citrate as a function of immersion time in SBF, measured by XPS technique.

In Vivo Analysis

The images shown in Figure 5 demonstrate that the PHEMA hydrogels releasing citric acid during *in vivo* experiments did not show evidence of calcium phosphate deposits (Figure 5D), although they became slightly opaque (Figure

5E). On the other hand, the PHEMA hydrogels containing no citrate were covered by thick, white deposits (Figure 5A and 5B), with the interior parts of these gels being much less opaque, as demonstrated in the Figure 5B.

The opacity was attributed to the formation of stable complexes between calcium ions and low molecular weight biomolecules, possibly lysozymes, rather than being caused by calcium phosphate deposits. Lysozyme has been reported to be able to penetrate the intertices of PHEMA hydrogel networks (*45,46*). It has molecular dimensions of approximately 4.0 nm x 4.0 nm x 1.9 nm (*47*), which are smaller than the PHEMA hydrogel mesh size of 10 – 100 nm which was estimated from SEM micrographs (*48*).

The orange-red staining color in the light microscope image presented in Figure 5F confirms the presence of calcium. However, the lack of a phosphorous peak in the EDS spectrum (Figure 6B) indicates the absence of phosphates, while the presence of nitrogen peaks in the EDS (Figure 6B) and XPS (Figure 7B) spectra confirm the presence of proteins or peptides.

XPS analyses of the thick, white deposits found on the surface of the PHEMA hydrogels without citrate showed that the outer surfaces of these deposits were coated in protein/peptide, as the calcium and phosphorous peaks were much smaller in intensity than the peak for nitrogen (Figure 7A).

In order to verify the above conclusions, the thick, white deposits were subjected to EDS analysis. Unlike XPS analysis, which provides the composition of just the surface layers, EDS is capable of providing an analysis of the elemental composition to a depth of $\approx$ 10 μm beneath the surface. As expected, the EDS analyses showed that the white deposits were not made up only of protein/peptide, but indeed did contain significant amounts of both calcium and phosphorous (Figure 6A). However, the presence of proteins or peptides were also indicated in the EDS spectra, although in the spectra the nitrogen peaks were partly masked by oxygen peaks. Moreover, the presence of a significant amount of carbon was also observed to be present in both the XPS and EDS spectra. This strongly suggested the possible formation of carbonated deposits. Traces of sodium and magnesium were also frequently observed in the EDS, but not in XPS spectra, which suggested that these elements were possibly present as impurities and were not incorporated within the calcium phosphate lattices.

Semi-quantitative X-ray analyses on the calcium phosphate deposits based on Figure 6A (EDS data) and Figure 7A (XPS data) provided Ca/P molar ratios of 1.52 and 1.55, respectively. A Ca/P molar ratio of $\approx$ 1.50 suggests that the white deposits found on the PHEMA samples may be mainly Ca^{2+} and OH^- deficient hydroxyapatite (PHAp), with carbonate and *brushite* (DCPD) as the major impurities.

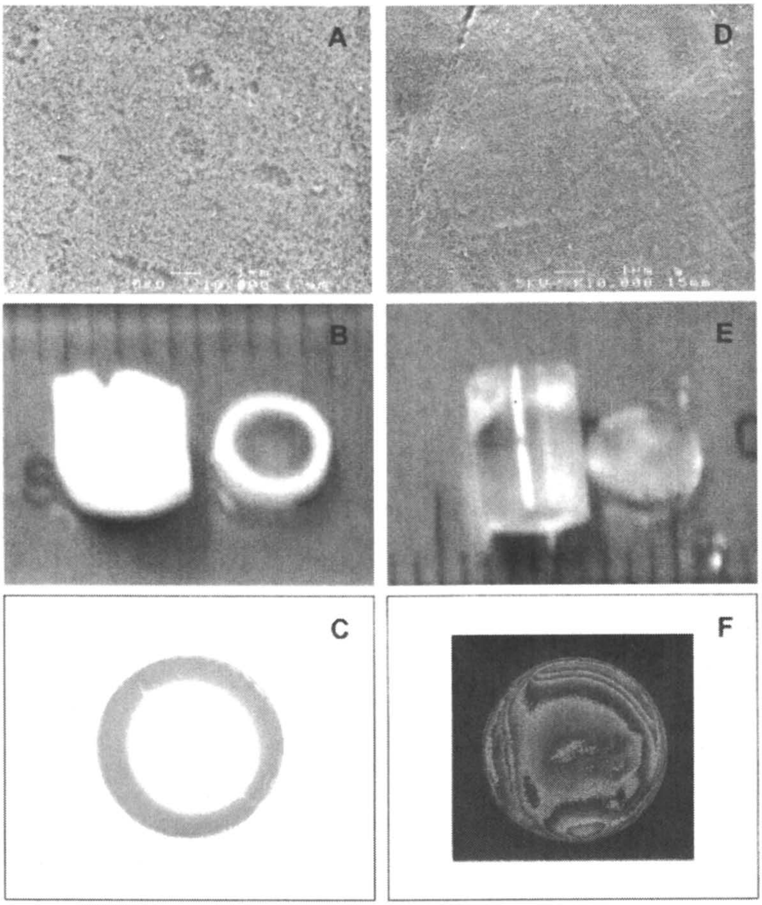

Figure 5. SEM, photographs, and LM images of PHEMA without citrate (A-C) and PHEMA plus citrate (D-F) after subcutaneous implantation in rats for 2 months. (See page 6 of color inserts.)

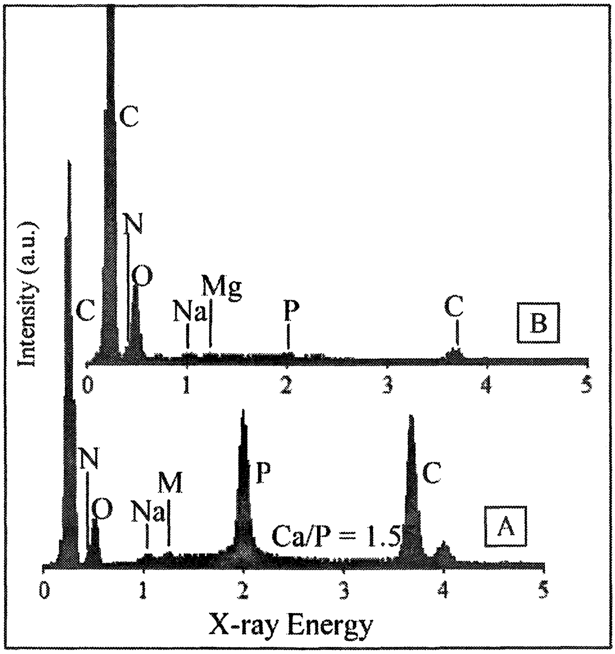

Figure 6. EDS spectra of PHEMA (A) and PHEMA+Citrate (B) after subcutaneous implantation in rats for 2 months.

Conclusions

It has been demonstrated that the release of citric acid from PHEMA hydrogels hinders the formation of calcium phosphates, especially hydroxyapatites. Because of this inhibitory effect, the calcium phosphate phases formed during *in vitro* calcification were mainly present as non-apatite phases, possibly MCPM and DCPD. The porous morphology of the outer surface of the spherical calcium phosphate deposits could be due to the dissolution of precipitates in the presence of citric acid. The results obtained after subcutaneous implantation of PHEMA and PHEMA containing citric acid in rats confirmed the resistance of PHEMA-citric acid to calcification. The calcium phosphate deposits which formed *in vivo* consisted mainly of Ca^{2+} and OH^- deficient hydroxyapatites. However, it is not yet known whether or not the differences between the calcium phosphate phases found *in vivo* and *in vitro* arise from the presence of proteins/peptides in the *in vivo* calcifying medium.

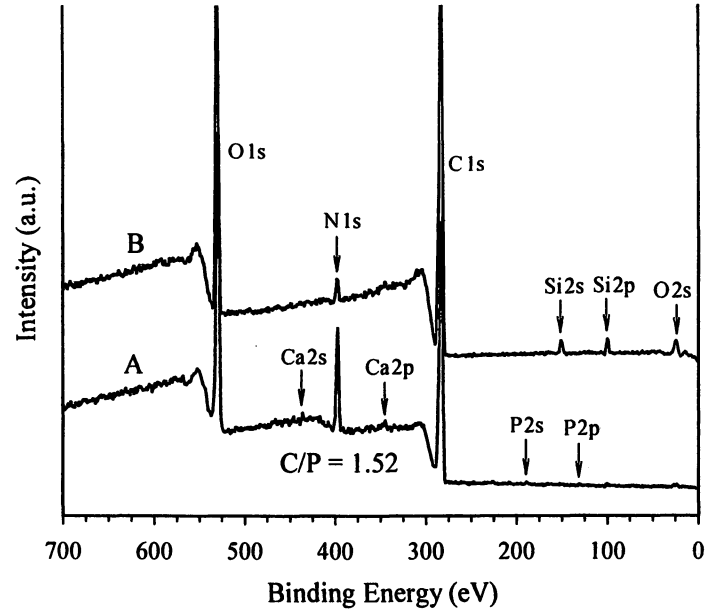

Figure 7. XPS spectra of PHEMA (A) and PHEMA+Citrate (B) hydrogels after subcutaneous implantation in rats for 2 months.

Acknowledgements

The authors would like to acknowledge the Australian Research Council for the financial support through a grant DP0208223. They also acknowledge support from The University of Queensland for postgraduate scholarships for Z. The authors would also like to thank Dr. Barry Wood, Mr. John Nailon and Mr. Kim Sewel for their assistance in using XPS, SEM, LM and EDS instruments.

References

1. Ruben, M.; Tripathi, R.C. *Br. J. Ophthalmol.* **1975**, *59*, 141-148.
2. Hilbert, J.; Lowther, G.; King, J. *J. Optom. Physiol. Optics.* **1976**, *53*, 51-54.
3. Dreyer, V.; Jensen, O.A.; Prause, J.U. *Acta Ophthalmol.* **1979**, *57*, 847-859.
4. Bowers, R.W.J.; Tighe, B.J. *Biomaterials.* **1987**, *8*, 83-88.
5. Bowers, R.W.J.; Tighe, B.J. *Biomaterials.* **1987**, *8*, 89-93.
6. Bowers, R.W.J.; Tighe, B.J. *Biomaterials.* **1987**, *8*, 172-176.
7. Abbott, J.M.; et al. *J. Br. Contact Lens Assoc.* **1991**, *14*, 21-28.

8. Tripathi, R.C.; Tripathi, B.J.; Silverman, R.A.; Rao, G.N. *Int. Ophthalmol. Clin.* **1991**, *31*, 91-120.
9. Tighe, B.; Franklin, V. In *The Eye in Contact Lens Wear;* Larke, J.R. Ed; 2nd Edition, Butterworth-Heinemann, Boston, 1997; pp 49-100.
10. Bucher, P.J.M.; Buchi, E.R.; Daicker, B.C. *Arch. Ophthalmol.* **1995**, *113*, 1431-1435.
11. Werner, L.; Apple, D.J.; Kaskaloglu, M.; Pandey, S.K. *J. Cataract Refract. Surg.* **2001**, *27*, 1485-1492.
12. Buchen, S.Y.; Cunanan, C.M.; Gwon, A.; Weinschenk, J.I.; Gruber, L.; Knight, P.M. *J. Cataract Refract. Surg.* **2001**, *27*, 1473-1484.
13. Apple, D.J.; Werner, L.; Pandey, S.K. *Arch. Ophthalmol.* **2001**, *119*, 581-582.
14. Fernando, G.T.; Crayford, B.B. *Clin. Exper. Ophthalmol.* **2000**, *28*, 280-286.
15. Yu, A.K.F.; Shek, T.W.H. *Arch. Ophthalmol.* **2001**, *119*, 611-614.
16. Yu, A.K.F.; Kwan, K.Y.W.; Chan, D.H.Y. *J. Cataract Refract. Surg.* **2001**, *27*, 1596-1606.
17. Yu, A.K.F.; Ng, A.S.Y. *J. Cataract Refract. Surg.* **2002**, *28*, 1217-1222.
18. Habib, N.E.; Freegard, T.J.; Gock, G.; Newman, P.L. *Eye.* **2002**, *16*, 69-74.
19. Dorey, M.W.; et al. *Am. J. Ophthalmol.* **2003**, *135*, 591-598.
20. Hicks, C.R.; Chirila, T.V.; Werner, L. *Clin. Exp. Ophthalmol.* **2004**, *32*, 185-191.
21. Cerny, E.; Chromecek, R.; Opletal, A.; Papousek, F.; Otoupalova, J. *Scripta Med.* **1970**, *43*, 63-75.
22. Eckstein, E.C.; Pinchuk, L.; Van De Mark, M.R. *Polym. Prepr.* **1983**, *24*, 58-60
23. Smetana, K.; Stol, M.; Novak, M.; Danes, J. *Biomaterials.* **1996**, *17*, 1563-1566.
24. Burdon, J.; Oner, M.; Calvert, P. *Mater. Sci. Eng. C.* **1966**, *4*, 133-137.
25. Filmon, R.; Grison, F.; Basle, M.F.; Chappard, D. *Biomaterials.* **2002**, *23*, 3053-3059.
26. Miyazaki, T.; et al. *J. Mater. Sci. Mater. Med.* **2003**, *14*, 569-574.
27. Brecevic, L.; Furedi-Milhofer, H. *Calcif. Tiss. Int.* **1979**, *28*, 131-136.
28. Tenhuisen, K. S.; Brown, P. W. *J. Mater. Sci. Mater. Med.* **1994**, *5*, 291-298.
29. Misra, D. N. *J. Dent. Res.* **1996**, *75*, 1418-1425.
30. Rhee, S.-H.; Tanaka, J. *Biomaterials.* **1999**, *20*, 2155-2160.
31. Hidber, P.C.; Graule, T.J.; Gauckler, L.J. *J. Am. Ceram. Soc.* **1996**, *79*, 1857-1867.
32. Sarda, S.; et al. *J. Biomed. Mater. Res.* **2002**, *61*, 653-659.
33. Zainuddin.; Hill, D.J.T.; Whittaker, A.K.; Chirila, T.V. *J. Mater. Sci. Mater. Med.* **2006**, in press.
34. Brynda, E.; Stol, M.; Chytry, V.; Cifkova, I. *J. Biomed. Mater. Res.* **1985**, *19*, 1169-1179.

35. Tas, A.C. *Biomaterials.* **2000,** *21,* 1429-1438.
36. Saiz, E.; Goldman, M.; Gomes-Vega, J.M.; Tomsia, A.P.; Marshall, G.W.; Marshall, S.J. *Biomaterials.* **2002,** *23,* 3749-3756.
37. Elvira, C.; Roman, J.S. *J. Mater. Sci. Mater. Med.* **1997,** *8,* 743-746.
38. Tanahashi, M.; Matsuda, T. *J. Biomed. Mater. Res.* **1997,** *34,* 305-315.
39. Ciavatta, L.; Tommaso, G.D.; Iuliano, M. *Anal. Let.* **2001,** *34,* 1053-1062.
40. Singh, R.P.; et al. *J. Chem. Eng. Data.* **1991,** *36,* 52-54.
41. Bohner, M. *J. Care Injured.* **2000,** *31,* S-D37-47.
42. Nancollas, G.H.; Zhang, J. In *Hydroxyapatite and Related Materials;* Brown, P.W.; Constantz, B. Eds; CRC Press Inc., Boca Raton, 1994; pp 73-81.
43. Abbona, F.; Franchini-Angela, M. *J. Cryst. Growth.* **1990,** *104,* 661-671.
44. Tenhuisen, K. S.; Brown, P. W. *J. Biomed. Mater. Res.* **1997,** *36,* 306-314.
45. Refojo, M.F.; Leong, F.L. *J. Polym. Sci., Polym. Symp.* **1979,** *66,* 227-237.
46. McArthur, S.L.; McLean, K.M.; St. John, H.A.W.; Griesser, H.J. *Biomaterials.* **2001,** *22,* 3295-3304.
47. Odabasi, M.; Denizli, A. *J. Appl. Polym. Sci.* **2004,** *93,* 719-725.
48. Zainuddin. PhD thesis, The University of Queensland, Brisbane, Australia, 2005.

Chapter 26

Photocross-Linkable Epoxy Polymers Bearing Sulfonate Ester Units and Their Redissolution in Water by Thermal Decross-Linking

Haruyuki Okamura, Akiya Kawaue, and Masamitsu Shirai

Department of Applied Chemistry, Osaka Prefecture University, Sakai 599–8531, Japan

p-Styrenesulfonate derivatives having cycloaliphatic epoxide or oxetane in a molecule were oligomerized and copolymerized. From TGA analysis degradation temperatures (Td, 5 wt% degradation) of the polylmers were ranged from 133 to 238 °C. When the polymer films containing a photoacid generator (PAG) were irradiated, they became insoluble in solvents. The insoluble films became soluble in water on baking at 120–260 °C. The insolubilization and redissolution profiles were strongly affected by the structure of the monomer, irradiation and baking conditions, and a type of PAG used. The reaction mechanism was studied by FT-IR spectroscopy.

© 2008 American Chemical Society

Photo-initiated crosslinkable resins were widely used as adhesives, printing plates, coatings, and so on, due to its toughness and high reactivity (*1*). However, it is very difficult or impossible to remove crosslinked resins from underlying materials completely without damage. Scratching or chemical treatments with strong acid or base must be applied to remove the insoluble and infusible networks from substrates. Recently, some thermosets that can be degradable thermally or chemically under a given condition, have been reported. Reserach of reworkable resins have been mainly focused on epoxy resins, one of the representative thermosets. Epoxy resins having disulfide linkages (*2, 3*), acetal linkages (*4*), tertiary ester linkages (*5, 6*), and carbamate ester linkages (*7*) have been studied. These linkages can be cleaved by thermolysis or chemical treatments under desired conditions. This system is useful as a photocrosslinkable material which can be removed from substrates after use. The thermally decomposed resins were soluble in methanol, aqueous alkaline solution, or water. Water is the most environmentally friendly solvent compared with methanol or aqueous alkaline solution. If the decomposed resins were washed away by water, the resins have a great advantage for practical use.

Sulfonate esters is known as a precursor of alkenes in addition to sulfonic acids by thermolysis *(8-10)*. Corey et al reported that sulfonate esters of secondary alcohols decomposed at moderate temperatures to give olefins in high yield *(8)*. Endo et al also reported that cyclohexyl arenesulfonate works as an excellent initiator of isobutyl vinyl ether due to the formation of arenesulfonic acid by thermolysis *(9)*. We have reported that poly(neopentyl styrenesulfonate) (PNPSS) can be convered to poly(styrenesulfonic acid) by heating at 150 °C *(10)*. Poly(styrenesulfonic acid) is highly soluble in water. Sulfonate ester linkages can be used not only as thermocleavable units but also as a group for the enhancement of solublitiy in water after thermolysis.

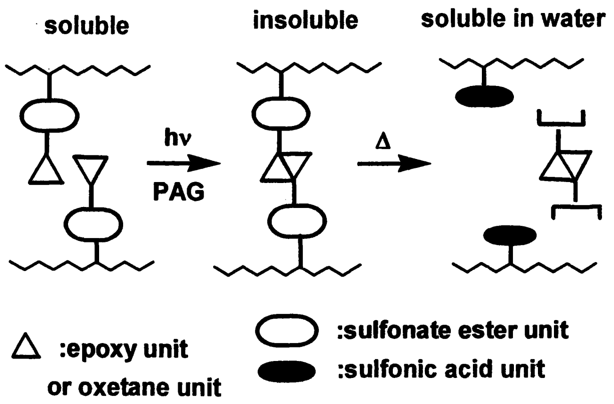

Figure 1. Concept of thermally degradable photocrosslinking polymer.

In this paper, polymers of styrenesulfonate esters having an epoxy or oxetane moiety were synthesized and characterized. Polymers bearing epoxy moieties or oxetane moieties in the side chain are photocrosslinkabe in the presence of a photoacid generator *(11, 12)*. Oxetanes have attracted much attentions due to interesting applications in cationic UV curing *(13, 14)*. The concept of the present system is shown in Figure 1. On irradiation network formation takes place by the photoinduced-acid catalyzed reactions of the crosslinkable moieties. A thermal treatment of the crosslinked polymers induces the cleavage of the network linkages. Sulfonic acid groups produced enhance the dissolusion of the polymers in water. These polymers are important as a photocrosslinkable material which can be removed by baking after use.

Experimental

Materials

Pyridine and *tert*-butyl methacrylate (TBMA) were distilled over CaH_2 before use. 2,2'-Azobis(isobutyronitrile) (AIBN) was purified by recrystallization from ethanol. Benzyltriethylammonium chloride was purchased from Wako Pure Chemical and used as received. 3-Ethyl-3-oxetanemethanol, sodium *p*-styrenesulfonate (SSNa), thionyl chloride, and solvents were purchased from Tokyo Kasei (Japan) and used as received. 1-Dodecanethiol and Oxone (potassium peroxymonosulfate) were purchased from Aldrich and used as received. Triphenylsulfonium triflate (TPST) was obtained from Midori Kagaku. *p*-Styrenesulfonyl chloride was prepared by the reaction of thionyl chloride with SSNa as described elsewere *(10)*. 9-Fluorenilideneimino *p*-toluenesulfonate (FITS) (*15*), 1-methyl-1-(6-methyl-7-oxabicyclo[4.1.0]hept-3-yl)ethyl methacrylate (MOBH) (*16*), 7-oxabicyclo[4.1.0]hept-3-yl)methyl *p*-styrenesulfonate (OHMSS) (*11*), and 2-(6-methyl-7-oxabicyclo[4.1.0]hept-3-yl)propyl *p*-styrenesulfonate (MOPSS) (*11*) were prepared according to the method described elsewhere. Synthetic routes of OHMSS, MOPSS, and EOMSS are shown in Figure 2.

3-Ethyl-3-oxetanylmethyl p-styrenesulfonate (EOMSS) (12)

p-Styrenesulfonyl chloride (11.6 g, 5.16×10^{-2} mol) was mixed with toluene (20.0 mL) and benzyltriethylammonium chloride (0.74 g, 3.99×10^{-3} mol) and cooled to 0 °C. A 5.5 mL aliquot of 35 wt% NaOH was added, and 3-ethyl-3-oxetanemethanol (5.0 g, 4.30×10^{-2} mol) was added dropwise to the solution and kept at 0 °C for 24 h. The organic phase was separated and washed with saturated sodium bicarbonate solution and then with water. The organic layer was dried over anhydrous $MgSO_4$. The product was purified by column

chromatography (silica gel; 1:3 ethyl acetate:hexane); colorless liquid; yield 7.31 g (60 %). ^{1}H NMR (270 MHz, $CDCl_3$) δ 7.86 (d, 2H, phenyl), 7.57 (d, 2H, phenyl), 6.76 (dd, 1H, CH_2=C*H*-), 5.92 (s, 1H, CH_2=CH-), 5.46 (s, 1H, CH_2=CH-), 4.33 (m, 4H, -O-CH_2-), 4.17 (m, 2H, -O-CH_2-), 1.73 (q, 2H, CH_2) 0.78 (t, 3H, CH_3).

Preparation of Polymers

Poly(MOPSS-*co*-TBMA) (MOPSS(20)-TBMA) and poly(EOMSS) (PEOMSS) were prepared by radical polymerization in degassed THF solution at 30 °C using AIBN (0.12 mol/L) as an initiator with irradiation using a medium-pressure mercury lamp (Toshiba SHL-100UV) with a cutoff filter (Toshiba UV-35). Oligo(MOPSS), oligo(OHMSS-*co*-TBMA) (OHMSS(20)-TBMA and OHMSS(43)-TBMA), oligo(OHMSS), oligo(EOMSS), and oligo(EOMSS-*co*-MOBH) (EOMSS(69)-MOBH) were prepared by conventional radical polymerization of corresponding monomers in degassed THF or chloroform solution at 50 °C using AIBN as an initiator and 1-dodecanethiol as a chain transfer reagent. Monomer concentrations were 1.8 – 3.2 mol/L. The resulting polymers were purified by reprecipitation from chloroform / methanol. Yields of polymers were 19 – 63%. The fraction of the TBMA or MOBH incorporated into the polymers was determined from the peak intensity of the ^{1}H NMR spectra. Number-average molecular weights of the polymers were 1.8 – 44 x 10^3. Onset temperatures for thermal decomposition (T_ds) of the polymers were 133 – 238 °C. Structures and properties of the polymers are shown in Figure 3.

Measurements

All sample films were prepared on silicon wafers by spin-casting from solutions of cyclohexanone containing sample polymer and photoacid generators. The sample films were dried on a hot plate at 120 °C for 2 min. The thickness of films was about 0.5 μm except for the sample films for the FT-IR measurements (1.9 μm). Irradiation was performed at 254 nm in air using a low-pressure mercury lamp (Ushio ULO-6DQ, 6 W) without a filter. The intensity of the light was measured with an Orc Light Measure UV-M02. Insoluble fraction was determined by comparing the film thickness before and after dipping the samples into a solvent. Thickness of films was measured by interferometry (Nanometrics Nanospec M3000).

^{1}H NMR spectra were observed at 400 MHz using a JEOL LA-400 or at 270 MHz using a JEOL GX-270 spectrometer. UV-vis spectra were taken on a

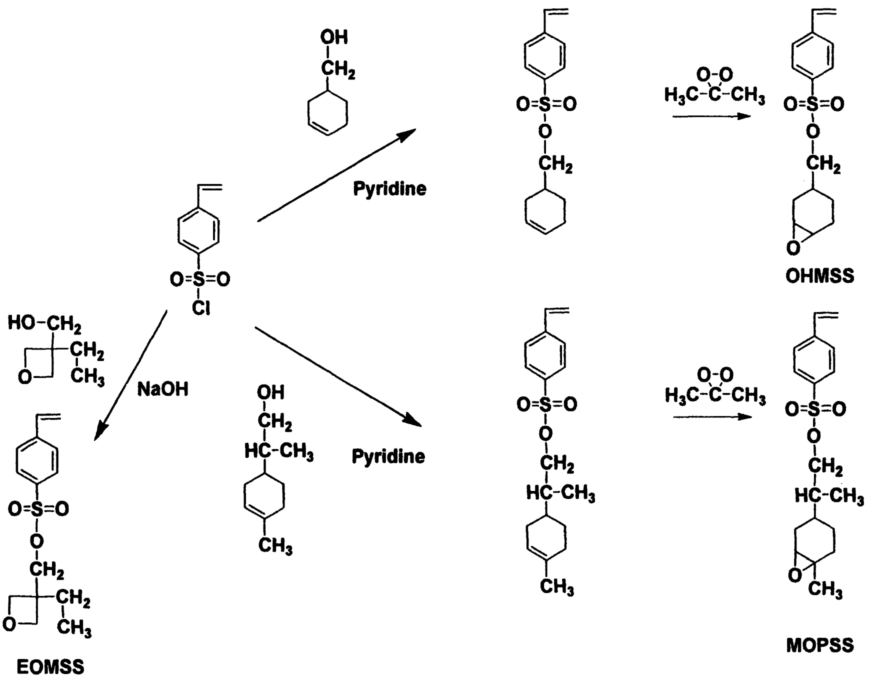

Figure 2. Synthesis of the monomers OHMSS, MOPSS, and EOMSS.

Shimadzu UV-2400 PC. FT-IR measurements were carried out using a JASCO IR-410. Thermal decomposition behavior was investigated with a Rigaku TAS 100 thermogravimetric analyzer (TGA) and differential scanning calorimeter (DSC) under nitrogen flow. Heating rate was 10°C/min for both measurements. Size exclusion chromatography (SEC) was carried out in THF on a JASCO PU-980 chromatograph equipped with polystyrene gel columns (Shodex GMNHR-$_H$ + GMNHR-$_N$; 8.0 mm i.d. x 30 cm each) and a differential refractometer JASCO RI1530. Number-average molecular weight (M_n) and molecular weight distribution (M_w/M_n) were estimated on the basis of a polystyrene calibration.

Results and Discussion

Photocrosslinking

Polymer films containing the photoacid generators FITS and TPST were irradiated at 254 nm and insoluble fraction in THF was studied. FITS and TPST

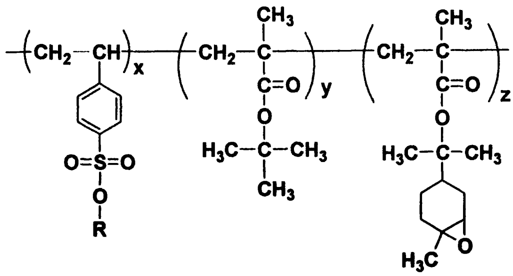

polymer or oligomer	R	composition (mol%) x	y	z	M_n x 10^{-3}	T_d (°C)
MOPSS(20)-TBMA	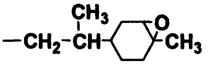	20	80	0	44	158
oligo(MOPSS)	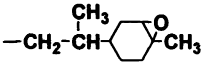	100	0	0	5.4	133
OHMSS(21)-TBMA	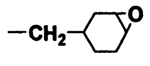	21	79	0	4.8	207
OHMSS(43)-TBMA	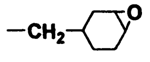	43	57	0	2.9	199
oligo(OHMSS)	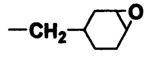	100	0	0	2.7	192
oligo(EOMSS)	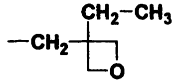	100	0	0	1.8	238
PEOMSS	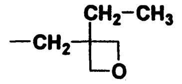	100	0	0	7.3	232
EOMSS(69)-MOBH	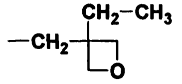	69	0	31	3.1	228

Figure 3. Structures and properties of polymers used.

were photolyzed to generate *p*-toluenesulfonic acid and triflic acid, respectively. The photoinduced-acid initiated cationic polymerization of epoxy or oxetane units in the side chain to generate networks.

Using FITS as a PAG, photo-induced insolubilization of MOPSS(20)-TBMA and oligo(MOPSS) was observed. The insoluble fraction increased with irradiation dose. On the other hand, insolubilization of the other polymers or oligomers did not observed with irradiation at 300 mJ/cm^2. The molecular weight of the polymer and oligomers strongly affected the insolubilization

profiles. The high insolubilization efficiency of MOPSS(20)-TBMA was due to the higher molecular weight compared to other oligomers. TPST generates stronger acid than FITS on irradiation. In using TPST as a PAG, effective insolubilization was observed for all the polymer and oligomers. Ring-opening reaction of the epoxy moiety is known to easily occur by strong acids. Figure 4 shows the insolubilization profiles of oligo(OHMSS), oligo(MOPSS), and oligo(EOMSS) containing 3.5 mol% TPST after irradiation at ambient temperature. Reactivity for insolubilization of the oligomers was observed to be in the order oligo(OHMSS) > oligo(MOPSS) > oligo(EOMSS). The lowest reactivity of oligo(EOMSS) was due to slower propagating rate of oxetane moieties than that of epoxy units in cationic polymerization. The lower insoluble fractions of oligo(MOPSS) than that of oligo(OHMSS) may be caused from the lower reactivity of epoxy units due to the steric hindrance of methyl group adjacent to epoxy units. The insoluble fraction of the present polymers increased and reached 80% by the post-exposure-baking (PEB) treatment at relatively lower temperatures (60-140 °C).

Thermal Degradation

It is known that sulfonate esters thermally decompose to form sulfonic acids and alkene (*8, 9*). Figure 5 shows FT-IR spectral changes of oligo(OHMSS) film containing 3.5 mol% TPST on irradiation. After irradiation of the film with a dose of 60 mJ/cm^2 at room temperature, no significant changes in the FT-IR spectrum were observed though the film became insoluble in THF. When the irradiated film was baked at 120 °C for 10 min, the FT-IR spectrum showed no significant changes except the slight decrease of the peak at 832 cm^{-1} due to epoxy moieties. When the irradiated film was baked at 200 °C for 10 min, the peaks at 1180 and 1385 cm^{-1} due to sulfonate ester decreased and the peak at 1018 cm^{-1} ascribed to sulfonic acid increased. Furthermore, a broad peak appeared at 3000 ~ 3500 cm^{-1} due to OH of sulfonic acid units. This observation was consistent with the result of thermolysis for PNPSS previously reported *(10)*. This finding suggests that the cleavage of the sulfonate ester moiety in oligo(OHMSS) occurred to generate poly(styrenesufonic acid). As for copolymers of OHMSS or MOPSS and TBMA, decomposition of carboxylate esters was also observed. It is known that *tert*-butyl esters of carboxylic acids thermally decompose to form carboxylic acids and isobutene (*17*). The thermal decomposition temperature is lowered if strong acids are present (*17*). The decomposition of carboxylate esters in the copolymers of OHMSS and TBMA was observed at slightly lower PEB temperature (170 °C) than that of sulfonate esters (200 °C). This observation was consistent with the result of thermolysis for poly(MOBH-*co*-(neopentyl *p*-styrenesulfonate)) previously reported *(18)*.

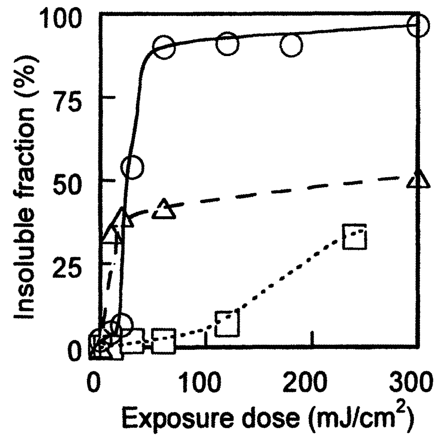

Figure 4. Photo-induced insolubilization of oligo(OHMSS) (○), oligo(MOPSS) (△), and oligo(EOMSS) (□) films containing 3.5 mol% TPST.

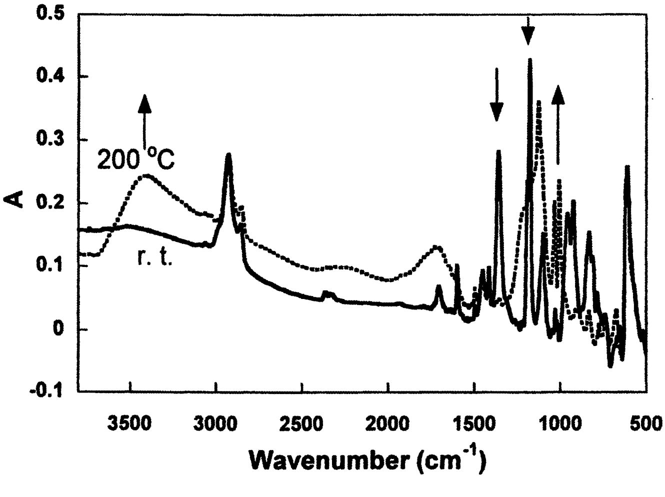

Figure 5. FT-IR spectral changes of the photocrosslinked oligo(OHMSS) film containing 3.5 mol% TPST on baking. Baking time: 10 min. Film thickness: 1.9 μm. Irradiation dose to cross-link the polymer: 60 mJ/cm^2.

Dissolution properties of the photochemically crosslinked oligo(OHMSS), oligo(MOPSS), and oligo(EOMSS) are shown in Figure 6. Oligo(OHMSS) film containing 3.5 mol% of TPST was irradiated and followed by baking at 80 – 200 °C for 10 min. The film baked at 170 °C was not soluble in water. When baked at 180 or 200 °C, the crosslinked film became soluble in water. Baking tempertures for complete dissolution in water were 180, 140, and 220 °C for oligo(OHMSS), oligo(MOPSS), and oligo(EOMSS), respectively. The results agreed with the TGA measurements shown in Figure 3. The dissolved products were recovered and characterized by ^{1}H NMR and FT-IR. It was confirmed that the separated polymer was poly(*p*-styrenesulfonic acid) by reference to the FT-IR and ^{1}H-NMR spectra of the authentic poly(*p*-styrenesulfonic acid). Photocrosslinking and thermal degradation mechanism of OHMSS or MOPSS-containing polymers are shown in Figure 7. "Others" in Figure 7 include isobutene and other olefinic species produced by thermolysis of sulfonate esters.

Conclusion

We have designed and synthesized novel photocrosslinkable polymer and oligomers having redissolution properties in water after thermolysis. Copolymers containing OHMSS, MOPSS, or EOMSS which have epoxy or oxetane moieties and sulfonate ester linkages were photocrosslinkable when irradiated in the presence of photoacid generators. The photochemically crosslinked polymers became soluble in water if baked at a given temperature. Thermal decomposition of the sulfonate ester linkage of the network generated linear polymers. The crosslinked polymers were removable from substrates after use by baking and soaking in water. Oligo(OHMSS) films with TPST is the most useful in this application because of high sensitivity for crosslinking and wide temperature range of the bake treatment for redissolution. The present polymers are environmentally friendly materials.

Acknowledgment

This work was supported by the Ministry of Education, Science, Sports, and Culture, Grant-in-Aid for Scientific Research (B)(2) No. 13450382 and for Young Scientists (B) No. 16750166. We are also grateful to the Ministry of Education, Science, Sports, Culture and Technology for financial support through 21st Century COE Program 24403 E-1.

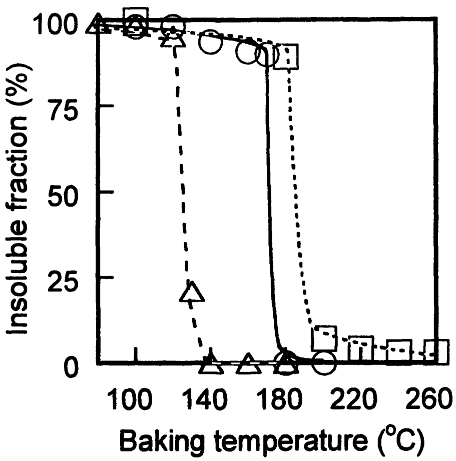

Figure 6. Dissolution properties of the crosslinked oligo(OHMSS) (○), oligo(MOPSS) (△), and oligo(EOMSS) (□) films containing 3.6 mol% TPST.

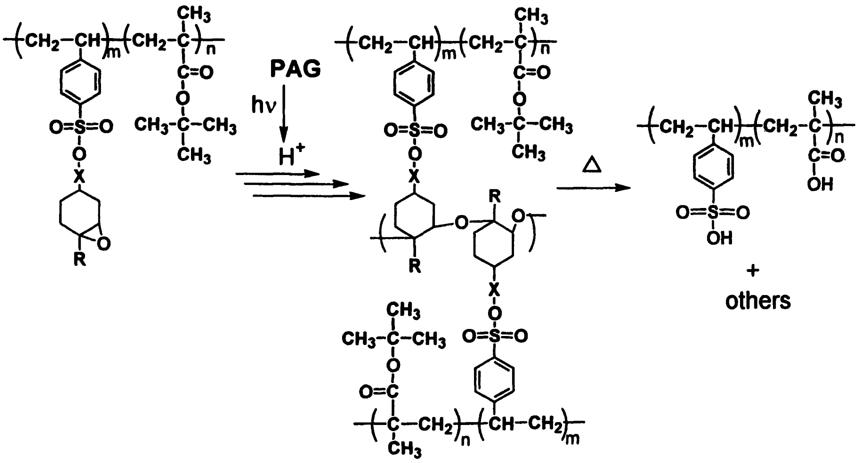

Figure 7. Photocrosslinking and thermal degradation mechanism of OHMSS or MOPSS-containing polymers.

References

1. Fouassier, J. P.; Rabek, J. F. *Radiation Curing in Polymer Science and Technology*, Elsevier Applied Science, New York, 1993.
2. esero, G. C.; Sastri, V. *J. Appl. Polym. Sci.* **1990,** *39*, 1425.
3. astri, V. J.; Tesero, G. C. *J. Appl. Polym. Sci.* **1990,** *39*, 1439.
4. uchwalter, S. L.; Kosber, L. L. *J. Polym. Sci. Part A: Polym. Chem.* **1996,** *34*, 249.
5. Yang, S.; Chen, J.- S.; Korner, H.; Breiner, T.; Ober, C. K. *Chem. Mater.* **1998,** *10*, 1475.
6. Okamura, H.; Toda, S.; Tsunooka, M.; Shirai, M. *J. Polym. Sci. Part A: Polym. Chem.* **2002,** *40*, 3055.
7. Wang, L.; Wong, C. P. *J. Polym. Sci. Part A: Polym. Chem.* **1999,** *37*, 2991.
8. Corey, E. J.; Posner, G. H.; Atkinson, R. F.; Wignard, A. K.; Halloran, D. J.; Radzic, D. M.; Nash, J. J. *J. Org. Chem.* **1989,** *54*, 389.
9. Lee, S. D.; Takata, T.; Endo, T. *Macromolecules* **1996,** *29*, 3317.
10. Okamura, H.; Takatori, Y.; Tsunooka, M.; Shirai, M. *Polymer* **2002,** *43*, 3155.
11. Shirai, M; Kawaue, A.; Okamura, H.; Tsunooka, M. *Polymer* **2004,** *45*, 7519.
12. Okamura, H.; Tajima, Y.; Shirai, M. *Photopolym. Sci. Technol.* **2005,** *18*, 715.
13. Sasaki, H.; Crivello, J. *Macromol. Sci., Pure Appl. Chem.* **1995,** *A29*, 915.
14. Kameyama, A.; Nishikubo, T. *J. Photopolym. Sci. Technol.* **2004,** *17*, 53.
15. Shirai, M.; Kinoshita, H.; Tsunooka, M. *Eur. Polym. J.* **1992,** *28*, 379.
16. Shirai, M; Morishita, S.; Okamura, H.; Tsunooka, M. *Chem. Mater.* **2002,** *14*, 334.
17. Ito, H.; Ueda, M. *Macromolecules* **1988,** *21*, 1475.
18. Shirai, M; Kawaue, A.; Okamura, H.; Tsunooka, M. *Chem. Mater.* **2003,** *15*, 4075.

Chapter 27

Fracture Toughness and Rheology of Alumina-Filled Epoxy Composites

Laura M. McGrath[1,2], Joseph L. Lenhart[2], Richard S. Parnas[1], and Saskia H. King[3]

[1]Institute of Materials Science: Polymer Program, University of Connecticut, Storrs, CT 06269–3136
[2]Organic Materials Department, Sandia National Laboratory, Albuquerque, NM 87185
[3]Manufacturing Systems: Science and Technology Division, Sandia National Laboratory, Albuquerque, NM 87185–0855

The structure-property relationship in alumina (α-Al_2O_3) filled epoxy composites was determined via dynamic shear rheology, scanning electron microscopy (SEM), and K_{Ic} fracture toughness. The shear storage modulus (G′) increased with increasing Al_2O_3 vol. % while the glass transition temperature, T_g, remained unchanged. K_{Ic} increased ~2MPa*m$^{1/2}$ with increasing Al_2O_3 loading (0-50 v/v). The particle size and size distribution did not affect G′ or fracture toughness. An increase in fracture toughness was observed with decreasing epoxy crosslink density. These results, in conjunction with SEM investigation, support poor adhesion between the Al_2O_3 and the epoxy matrix.

 © 2008 American Chemical Society

Introduction

With the first commercial production of epoxide-based ("epoxy") materials (*1*), there has been a interest in tailoring its properties with fillers/reinforcement. Inorganic fillers provide rigidity and toughness while maintaining the mechanical properties, good chemical resistance, and modification versatility of the epoxy. The inorganic filled composites are utilitarian because they provide enhanced properties while reducing cost and have been used to improve the fracture toughness (*2*), lower the coefficient of thermal expansion (CTE) (*3*) and increasing wear resistance (*4*). The resulting composite specimens have a wide range of uses from automobile parts, dental restoratives (*5*), and electronic packaging/underfill for circuit cards (*6*).

To design and synthesize the next generation of high performance epoxy composites, a proper understanding of the structure/property relationship between composite variables is needed. Variables that define the stress state and mechanical response of the sample to deformation are epoxy crosslink density, particle shape, size, size distribution, and vol. % loading. These variables control the manner in which the matrix deforms and defines the stress field in the sample which in turn determines the mechanical properties and fracture toughness. Fracture occurs when stored elastic and potential energy is released by the growth of a new crack which supports the energy requirements of the new fracture surfaces (*7*). Inorganic fillers, with good interfacial adhesion, do not decrease modulus but do not provide the increase in toughness shown by their organic counterparts (*8*).

The interfacial area, determined by particle size, is critical to the composite properties. The stronger the interface, the more energy required to propagate a crack and the greater load the composite can carry (*9*). The key to interface design is in the ability to transfer stress between the two faces but not necessarily to generate the best adhesion, as strong adhesion may lead to interface brittleness, premature failure, and induced stresses (*10*). Using dynamic testing, it is possible to characterize the microstructure of the composite and examine the mechanical changes due to particle and matrix variables (*2,11*).

In this study the thermal, mechanical, and fracture properties of epoxy-alumina composites is explored as a function of the resin crosslink density, as well as alumina shape, size, size distribution, and vol. % loading. Al_2O_3 was chosen because of its high dielectric constant with low dielectric loss especially at high frequencies which is critical in many electronic and encapsulant industries. Rigid inorganic particles are widely used to toughen epoxy or other polymer matrices, but the micro-level fracture toughening mechanisms have not been firmly established (*2*). Practically, there is a need to understand what are the crucial variables and material specifications as well as the sensitivity of the finished product to these variables.

Experimental

Materials

2,2-Bis[4-(glycidyloxy)phenyl]propane (DGEBA, 97%) and polypropyl eneoxide diamines (Mn = 230, 400, and 2000, i.e. D230, D400 and D200(purity) both from Aldrich Chemical Company) were used as-received. α alumina (Al_2O_3) corundum (AA2, AA5, AA10, AA18 from Sumitomo Chemica Co. Japan and T60 from Alcoa Co.) was dried in an oven at 110°C unde vacuum for at least 12 hours prior to use. A Beckman Coulter Light Scatterin; particle size analyzer was used to determine the Al_2O_3 particle size and siz distribution (Table 1). The AA- system was chosen because of its narrov distribution compared to T60 Al_2O_3.

Table 1. Al_2O_3 Particle Size and Size Distribution

Particle Size (μm)	*AA2*	*AA5*	*AA10*	*AA18*	*T60*
Mean	3.683	5.064	8.083	16.700	18.81
Mode	3.359	5.064	8.536	18.000	26.14
Standard Dev.	1.589	4.878	2.614	4.713	14.45

Composite Preparation

DGEBA and the respective diamine were weighed and mixed in 1:1 stoichiometry and preheated to 50°C, lowering the viscosity and eliminatin; crystallinity. The epoxide ring-opening reaction was started by placing th mixture in an oven at 75°C for 15 to 45 minutes, depending on gel time, and wa: periodically stirred. The Al_2O_3 was weighed to the appropriate amount (0-5(v/v) and placed in a 75°C oven. After an initial viscosity increase that prevent: the settling of powders, Al_2O_3 was added and mixed vigorously by hand t ensuring proper particle wetting and homogeneity. The composite mixture wa: degassed at 55°C. The viscous mixture was subsequently poured into preheated release agent coated, Al molds (63.5mm x 63.5mm x 12.7mm). The resin in th molds was degassed and cured as follows: 25°C, 2.5h; 25°C to 93°C over 8h 93°C, 3h; 93°C to 120°C over 2h; 120°C, 2h and finally 120°C to 25°C over 2 h

Characterization

Single-edge-notch (SEN) fracture toughness samples were prepared b; cutting samples into 63.5 mm, 12.7 mm (W = width), 6.35 mm (thicknes:

defined as B) sections by diamond blade saw. 5-10 samples were prepared from 1-3 sample sets. A razor blade was tapped into the center of the sample and a crack was propagated, to a crack length equal to 20-80% of sample width W. The crack length, a, should ideally be twice as long as the razor blade insertion. The ratio a/W should lie in the range $0.45 < a/W < 0.55$. The SEN test was conducted in the 3-pt bend compression geometry (ASTM D1621) in an Instron-5589. A 1 kPa load cell with a 50.8 mm span (S = 4W) was used at a crosshead speed of 6.35mm/min. Samples were tested in the brittle regime (40 °C below T_g). T_g was determined from the peak of the shear loss modulus.

K_{Ic}, plane-strain fracture toughness (eqs 1, 2) was used to calculate the fracture toughness, where Y is the shape factor, P is the load to failure, S is span of the Instron supports.

$$K_{Ic} = Y\frac{3PS\sqrt{a}}{2BW^2} \quad (1)$$

where:

$$Y = 1.93 - 3.07\left(\frac{a}{W}\right) + 14.53\left(\frac{a}{W}\right)^2 - 25.11\left(\frac{a}{W}\right)^3 + 25.80\left(\frac{a}{W}\right)^4 \quad (2)$$

Dynamic torsional shear experiments were conducted on a Rheometric Scientific ARES rheometer. The samples were cut 6.35 cm in length strips, 0.30 cm thick. The single frequency temperature ramp test was taken at 1 Hz from -100°C to 150°C at 2°C/min in the linear strain regime (0.01 to 2.00%).

Environmental scanning electron microscopy (ESEM) studies of the fracture surface were conducted in a Philips ESEM 2020, at 10-12 mm and 20.0 kV.

Results and Discussion

With the exception of changes in crosslink density of the epoxy and the vol. % loading of Al_2O_3 filler, the thermal/mechanical properties and fracture toughness of the composite are not dramatically altered by varying the particle size, size distribution, or particle shape. It was found that with increasing vol. % of Al_2O_3, there is an increase in G′ and an increase in K_{Ic}. When the crosslink density of the epoxy matrix is decreased, there is a broadening of the rubbery plateau above the T_g and an increase in K_{Ic}. There is also an interesting inversion of G′ in the D400 and D230 systems between the rubbery and brittle regimes. These results coupled with SEM micrographs and the lack of T_g change with filler inclusion, lead to the conclusion that there is poor interfacial adhesion between the Al_2O_3 surface the epoxy.

In Polymer Durability and Radiation Effects; Celina, M., et al.;
ACS Symposium Series; American Chemical Society: Washington, DC, 2007.

Dynamic Shear Rheology of Al_2O_3 Filled Composites

The G′ in the brittle regime (40°C below T_g) and the rubbery regime (40°C above T_g) for DGEBA composites cured with either D230 or D400, as a function of the Al_2O_3 type and vol. % loading, is presented in Figure 1. The G′, in both the rubbery and brittle regime, increases with increasing vol. % of Al_2O_3. These results are consistent with other epoxy systems where inorganic particles [silica (*12*) and glass (*13*)] were used. With increasing particle size, there is no trend in either the rubbery or brittle region or with crosslink density, signifying that particle size/shape has no effect on the G′ on this length scale. In addition, no difference exist between the AA-system and the T60 data, thus particle size distribution has no effect. G′ of DGEBA/D230 in the rubbery region is higher that than the G′ of DGEBA/D400 because of the higher crosslink density, consistent with the kinetic theory of rubber elasticity. Although in the brittle region, the G′ of the D400 system is greater than that of the D230 system.

The dependence of G′ on temperature and vol. % Al_2O_3 is shown in Figure 2 for DGEBA/D400 composites with AA18. G′ increases with Al_2O_3 vol. %, exceeding the modulus of the unfilled polymer. The characteristic drop of three orders of magnitude in G′ represents the glass transition temperature, T_g. There is no appreciable shift in T_g with increasing vol. % of Al_2O_3 but there is a broadening of the transition region associated with an increase in the rubbery plateau close to the Tg. Broadening is the consequence of particle-particle and particle-polymer interactions during the relaxation transition, but not necessarily agglomeration, as has been supposed in other work (*14*).

The broadening in the α-transition region is also a result of the changing relaxation mechanisms in the composite and can be partially attributed to the larger modulus difference between the filler and the matrix, a larger Poisson's ratio above T_g, and induced thermal stresses affecting the particle-particle interactions (*14*). Below T_g, forces associated with sample deformation are large and frictional forces associated with particle-particle contact may not contribute substantially to the modulus. Above T_g, the deforming forces are weaker and frictional forces between particles can contribute to the material stiffness resulting in broadening of the modulus-temperature profile at higher temperatures. A clear epoxy crosslink density dependence on the degree of broadening is exhibited. The lower the epoxy crosslink density the greater the broadening. The lower crosslink density epoxy allows more energy to be dissipated through the deformation of the molecular network resulting in Al_2O_3 particles which may exert forces on each other during deformation. This is especially true in the region of changing modes of relaxation. There is no change in broadening response to particle size. The epoxy matrix itself, is the variable that results in the greatest changes in the filled composites.

In Polymer Durability and Radiation Effects; Celina, M., et al.;
ACS Symposium Series; American Chemical Society: Washington, DC, 2007.

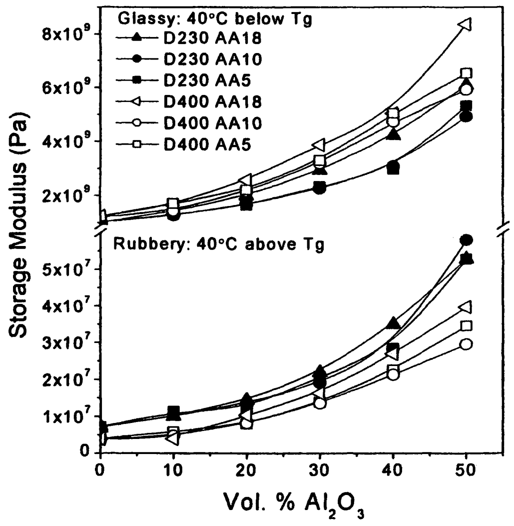

Figure 1. Dependence of G′ on Al_2O_3 vol. %.

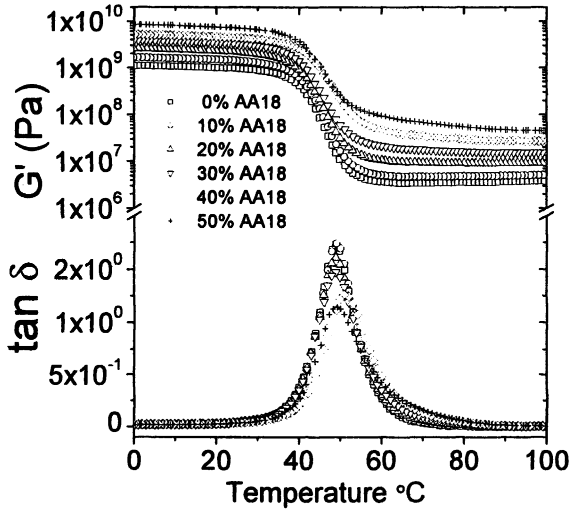

Figure 2. G′ and tan δ temperature dependence of DGEBA/D400 with AA18.

Effect of Storage Modulus and T_g on Adhesion

While the Al_2O_3 did increase the G′ with increasing vol. %, it was not dependent on the particle size. Work by Heikens (*15*) found that when there is excellent adhesion between the particle surface and the polymer matrix, the particle size altered the modulus values. This resulted from varying the particle surface area with strong interfacial adhesion. Although the interfacial adhesion must be substantial to change the modulus and it has to be optimized with the change in particle surface area. In many cases, a change in the modulus of the composite is not observed because a large force is exerted on the particle as the polymer shrinks during post cure (*2*).

Further support for the lack of adhesion between the Al_2O_3 surface and the epoxy matrix comes from the T_g results. With good interfacial adhesion a shift in the T_g to higher temperatures is often observed (*2,16*). As the matrix molecular motion is altered in the interphase region, the T_g can increase. Since the porosity of the Al_2O_3 is low, the interfacial region is likely comprised of a thin shell around the particle surface. Depending on the length scale of the interphase region only subtle changes in the T_g of the bulk composite may be observed. In a similar composite involving quartz powder in epoxy resin (*14*) the tan δ associated with the T_g, decreased in amplitude and shifted about 7 °C towards higher temperatures as the quartz loading increased from 0 to 25 vol. %.

Particle Size and Size Distribution Effects on Fracture Toughness

The K_{Ic} of all combinations of epoxy and Al_2O_3 increased with vol. % of filler loading (Figure 3). The particle size did not have an effect on the fracture toughness, perhaps because the range of particle sizes is only one order of magnitude. The largest particle diameters used were in the T60 Al_2O_3 distribution, with an average particle diameter of 26 μm, and the smallest, AA2 had an average particle size of 2 μm. When the different particle sizes are compared in the epoxy, there is no significant difference in the K_{Ic} value. Though the T60 has the highest K_{Ic} value at 50% loading, it is not consistently higher than other sized Al_2O_3 particles when compared at several other loadings. The AA2 at 50% volume loading is slightly greater than the AA5 and AA18 particle sizes but nearly within the standard deviation. Since no consistent trend was observed with changing particle size at each vol. %, the conclusion is that the fracture toughness is independent of the Al_2O_3 particle size. When comparing the T60 and AA- systems, there were no changes in K_{Ic}, that could be attributed to particle size distribution effects.

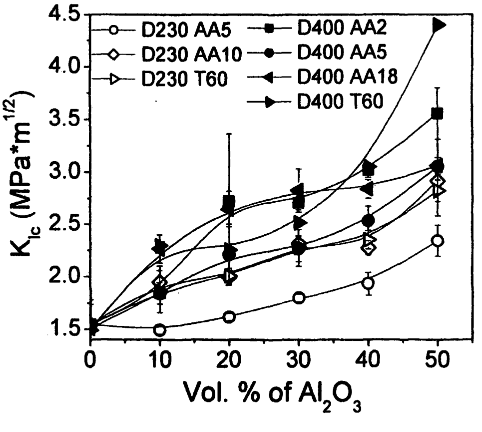

Figure 3. Dependence of fracture toughness on vol. % Al_2O_3.

Effect of Diamine Spacer Length on Composite Fracture Toughness

A decrease in crosslink density of the epoxy via the use of D400 diamine rather than D230 diamine increases the K_{Ic}, relative to their respective T_g. The MW of the diamine spacer was changed in order to study the effect of the inherent properties of the epoxy matrix on the toughening ability of Al_2O_3. However, the mechanism responsible for fracture in un-filled epoxy resins is plastic deformation at the crack tip (*10,17*). Thus, when increasing the K_{Ic} of the overall composite, it is crucial to understand the energy dissipation and plasticity, as well as the molecular weight control on toughness in the un-filled matrix (*11*). Nonetheless, variations in the molecular weight of the diamine hardener alter the percent of PPO groups in the resin and subsequently may change the likelihood of interactions with the Al_2O_3 surface hydroxyl groups. Lee and Yee, working with glass bead filled epoxies, found that when the crosslink density was decreased, (via increasing the epoxide molecular weight), the matrix toughness was increased i.e. higher MW composites were tougher than the lower molecular weight composites of the same vol. % of filler (*8*).

Effect of Adhesion on Fracture Toughness

Fracture mechanisms in most inorganic particle filled composites can be described by the crack-front bowing theory (*1,18,19*). Originally proposed by Lange in 1970 (*18*), it describes the relationship between a mobile crack front

and a dispersive second phase. Energy dissipation is increased by the rigid-inorganic particles because the crack front needs to bow or move around the particle, yet when it encounters a particle it remains pinned to it. When the crack is initially forming, the length of the crack front increases as it moves around the particles which pin it, creating a new fracture surface. Energy is required to generate the increased crack length; thus, changing the particle size and shape will alter the energy required to propagate the crack front (*19*).

Our results show only an increase in K_{Ic} with increasing vol. % of Al_2O_3, not with particle size or shape. The smaller particle sizes were just as tough at their respective vol. % loadings. Thus, the amount of interface area did not affect the ability of the material to resist crack propagation. As a crack arrives at an Al_2O_3 particle, the lowest energy pathway is for the crack to pass around the particle and cleave any bonds located at the interface of the filler and the epoxy. If the interface is poor, the Al_2O_3 simple diverts the crack resulting in only marginal composite toughening without the crack breaking high energy covalent bonds in the bulk matrix. This is corroborated with Green al. (*20*) which found that with low interfacial adhesion that the particles cannot pin the crack front and offer little resistance.

SEM Characterization of the Interface

SEM micrographs of the SEN composite fracture surface shown in Figure 4 (a) and (b) clearly illustrate that there is no agglomeration of the Al_2O_3. The Al_2O_3 particles are raised and debonded cleanly from the epoxy. As the crack is propagating, the least energy environment is to embrace the surface of the Al_2O_3 even though this requires additional energy in perpetuating a longer crack. Less energy is required to break this interfacial bond if the adhesion is poor.

In the case of no adhesion or extremely poor particle-polymer adhesion, the particle cannot effectively pin a crack. However, evidence for crack pinning in these composites was observed at the lower volume percent Al_2O_3 loadings Figure 4 (b) shows the DGEBA/D230 composite with 10% AA10. Tails (*8,13,18,21*) or ridges in the epoxy, are shown in the fracture surface below an Al_2O_3 particle in the crack front. This is direct conformation that crack front bowing is occurring in these composites. The crack approaches the particle and is pinned by the Al_2O_3. It subsequently moves around the particle, but when the crack front meets again on the opposite side of the particle the two cracks are not on the same plane, leading to small variations in the epoxy height and tail observation. Since the crack breaks cleanly at the Al_2O_3-epoxy interface adhesion is not strong enough to promote cohesive failure in the matrix

However, the presence of crack-front bowing indicates that some interfacial adhesion in these composites does exist. The extent of bowing will be dependent on the strength of adhesion, with more extensive crack bowing occurring with strong adhesion.

The Al_2O_3 in the fast facture region where the crack is accelerating, is clean and is evident that the crack propagates at the interface between the Al_2O_3 and the epoxy. This area does not have the elevation change that is prevalent in the process zone. Crack propagation occurs between particles which act as bridges. The epoxy is not cut cleanly but rather is removed from around the outside of the Al_2O_3, supporting our hypothesis that the Al_2O_3 is poorly adhered to the epoxy.

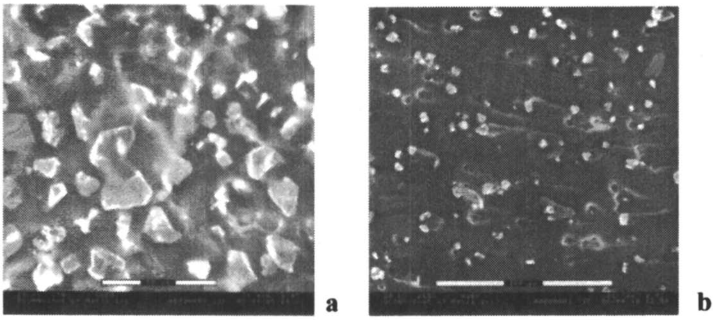

Figure 4. SEM micrographs of epoxy/Al_2O_3 composite fracture surface (a) D230 AA18 50% and (b) crack pinning tails in DGEBA/D230 with 10% AA10 Al_2O_3.

Conclusions

To further understand the structure-property relationship between inorganic particle fillers and a thermoset matrix, Al_2O_3 is included in epoxy to improve the K_{Ic} while studying the resulting mechanical properties. The modulus in both the glassy and rubbery regime increased with increasing particle loading, as did the K_{Ic} fracture toughness. The glass transition temperature did not change with particle loading. The modulus, glass transition temperature, and K_{Ic} results were not a function of particle size, size distribution or shape. However, crosslink density of the epoxy matrix did impact the modulus, T_g, and fracture toughness. The lack of dependence of composite properties on the size, size distribution, and particle shape was attributed to a relatively weak epoxy- Al_2O_3 interface.

Acknowledgements

Sandia National Laboratories (Albuquerque, NM) is gratefull acknowledged for financial support. Sandia is a multiprogram laborator operated by Sandia Corporation, a Lockheed Martin Company, for the Unitec States Department of Energy under Contract No. DE-AC04-94AL85000.

References

1. Lee, H.; Neville, K. *Handbook of epoxy resins;* McGraw-Hill; NY, 1967.
2. (a) Nielsen, L. E., Landel, R. F. *Mechanical properties of polymers anc composites*; 2nd ed.; Marcel Dekker; NY, 1994. (b) *Particulate-fillec polymer composites;* Rothon, R., Ed.; Longman Scientific &Technical London, 1995.
3. Zhang, Z.; Wong, C. P.; *IEEE T. Adv. Packaging* **2003**, *26*, 199.
4. Wetzel, B.; Haupert, F.; Zhang, M.; *Compos. Sci. Technol.* **2003**, *63*, 2055.
5. (a) *Restorative dental materials;* Craig, R. G., Ed.; 10th ed.; Mosby-Yea Book, Inc; St. Louis, 1997. (b) Stannard, J. G. *Materials in dentistry*; 2nc ed.; Denali Pub; Hanover, 1988.
6. Voa, H. T.; Todd, M.; Shia, F. G.; Shapiroa, A. A.; Edwards, M. *Microelectron. J.* **2001**, *32*, 331.
7. Griffith, A. A.; *Phil. Trans. Roy. Soc.* **1920**, *A221*, 163.
8. (a) Yee, A. F.; Pearson, R. A.; *J. Mater. Sci.* **1986**, *21*, 2462. (b) Lee, J. Yee, A. F.; *Polymer* **2000**, *41*, 8363.
9. Nakamae, K.; Nishino, T.; Airu, X.; *Int. J. Adhes. Adhes.* **1995**, *15*, 15-20.
10. Kinloch, A. J.; Young, R. J.; *Fracture Behavior of Polymers*; Chapman anc Hall: London, 1983.
11. Ferry, J. D. *Viscoelastic properties of polymers*, 3rd ed. NY: Wiley; 1980.
12. Ishai, O.; Cohen, L. J.; *Int. J. Mech. Sci.* **1967**, *9*, 539.
13. (a) Young, R. J.; Beaumont, P. W. R.; *J. Mater. Sci.* **1977**, *12*, 684. (b Spanoudakis, J.; Young, R. J.; *J. Mater. Sci.* **1984**, *19*, 473.
14. Goyanes, S.; König, P.; Marconi, J. D.; *J. Appl. Polym. Sci.* **2003**, *88*, 883.
15. Vollenberg, P. H. T.; Heikens, D.; *Polymer* **1989**, *30*, 1656.
16. Cousin, P.; Smith, P.; *J. Polym. Sci.: Polym. Phys. Ed.* **1994**, *32*, 459.
17. Lee, J.; Yee, A. F.; *Polymer* **2000**, *41*, 8375.
18. Lange, F. F.; *Phil. Mag.* **1970**, *22*, 983.
19. Lange, F.; Radford, K.; *J. Mater. Sci.* **1971**, *6*, 1197.
20. Green, D.; Nicholson, P.; Embury, J.; *J. Mater. Sci.* **1979**, *14*, 1413.
21. Spanoudakis, J.; Young, R. J.; *J. Mater. Sci.* **1984**, *19*, 487.

Author Index

Allred, Ronald E., 180
Anchordoquy, T. J., 195
Assink, Roger A., 26
Balazs, Bryan, 2
Black, Steve, 16
Blinco, James, 59
Bottle, Steven, 59
Brunsvold, Amy L., 140
Celina, Mathew C., 26, 37, 153
Chaleat, Celine, 287
Chinn, Sarah, 2
Chirila, Traian V., 301
Clarke, Stephen, 261
Clough, Roger L., 37, 153
Dargaville, Tim R., 153
Dhevi, D. Manjula, 103
Elliott, Julie M. , 26
Gee, Rid, 2
George, Graeme, 59
Gijsman, Pieter, 48
Ginic-Markovic, Milena, 261
Gjersing, Erica, 2
Guenthner, Andrew J., 140
Halley, Peter J., 287
Hama, Yoshimasa, 131
Hamskog, Mikael, 48
Han, Song-Hee, 232
Harrah, Larry A., 180
Herberg, Julie, 2
Hill, David J. T., 116, 301
Hong, John Hee, 103
Hoyt Haight, Andrea E., 180
Itani, Toshiro, 253
Ito, Kenji, 131
Ito, Masayuki, 70
Iwata, Minoru, 131
Jones, Gary D., 37
Kaise, Motoaki, 277
Katsumura, Yosuke, 131, 166
Kawabata, Shuichi, 277
Kawaue, Akiya, 317
Kemp, Anne, 301
Kempner, E. S., 195
Kim, Jae Yong, 232
Kim, Kap Jin, 103
King, Saskia H., 328
Kobayashi, Yoshinori, 131
Kondo, Mitsuaki, 131
Kudo, Hisaaki, 131, 166
Kuzviwanza, Pfumai, 92
Lacevic, Naida, 2
Lee, Chong Oh, 232
Lee, Jong Soon, 103
Lee, Takhee, 232
Lenhart, Joseph L., 328
Lou, Jianzhong, 92
Mabry, Joseph M., 140
MacDonald, Ian, 261
Marchant, Darrell, 140
Markotsis, Martin G., 287
Matisons, Janis, 261
Matsui, Yoshinori, 253
Matsumoto, Toshihiko, 277
Maxwell, Robert, 2
McGrath, Laura M., 328
Micallef, Aaron, 59
Minton, Timothy K., 140
Molina, M. D. C., 195

Murakami, Takeshi, 131
Muroya, Yusa, 166
Murphy, Julian, 16
Nagasawa, Naotsugu, 166
Najafi, Ebrahim, 232
Oka, Toshitaka, 131
Okamura, Haruyuki, 317
Oshima, Akihiro, 131, 204
Parnas, Richard S., 328
Patel, Mogon, 2, 16
Petteys, Brian J., 140
Russo, Melissa, 287
Saiki, Seiichi, 166
Sargent, Anna Lisa, 287
Schimmel, Keith, 92
Seki, Shu, 220, 253
Shin, Kwanwoo, 232
Shirai, Masamitsu, 317
Sopade, Peter A., 287
Sugimoto, Masaki, 220
Tagawa, Seiichi, 220, 253
Takahashi, Risa, 277
Tan, Ihwa, 287
Tomczak, Sandra J., 140
Truss, Rowan W., 287
Tsuji, Shou, 253
Tsukuda, Satoshi, 220
Vij, Vandana, 140
Warren, Dana, 92
Washio, Masakazu, 131, 204
Wheeler, Hilary, 2
Whittaker, Andrew K., 301
Wilson, Thomas W., III, 83
Wilson, Mark, 2
Wright, Michael E., 140
Wu, Dong Yang, 261
Yan, Jizhong, 92
Yandek, Gregory R., 140
Yoshii, Fumio, 166
Zainuddin, 301

Subject Index

A

Abrasion, rubber aging study, 86, 88
Accelerated aging
  single or multiple mechanisms, 7–10
  time accelerated aging method, 71
  See also Elastomer lifetime prediction; Oxidative aging
Adhesion
  fracture toughness of particle filled composites, 335–336
  See also Alumina-filled epoxy composites
Aging. *See* Oxidative aging; Rubber aging study
Aging mechanisms
  molecular dynamics studies of, 10–12
  See also Polymer lifetime prediction
Aging tests, accelerated, 7–10
Alcohol groups
  chemical derivatization, 29–31
  concentration in hydroxyl-terminated polybutadiene (HTPB) vs. aging time, 30*f*
  ^{19}F derivatization reaction for, 29
  functionalization with trifluoroacetic anhydride (TFAA), 27
Alicyclic monomers. *See* Polyimides, nonaromatic
Alumina-filled epoxy composites
  adhesion and fracture toughness, 335–336
  Al_2O_3 particle size and size distribution, 330*t*
  characterization methods, 330–331
  composite preparation, 330
  diamine spacer length and fracture toughness, 335
  dynamic shear rheology, 332, 333*f*
  experimental, 330–331
  glass transition temperature and adhesion, 334
  interfacial area as critical property, 329
  materials, 330
  particle size and size distribution effects on fracture toughness, 334, 335*f*
  plane-strain fracture toughness, 331
  scanning electron microscopy (SEM) characterization of interface, 336–337
  storage modulus and adhesion, 334
  tailoring properties, 329
  varying particle size, size distribution, or particle size, 331
Amines. *See* Hindered amine stabilizers (HAS)
Atomic force microscopy (AFM)
  radii of polystyrene nanowires, 222–223
  sizes of poly(methylphenylsilane) (PMPS)-based nanowires, 226–227
Atomic oxygen (AO)
  combined effects of, and vacuum UV radiation on polyvinylidene fluoride (PVDF) polymers, 160, 162
  polyhedral oligomeric silsesquioxane-polyimides (POSS-PI), 143
  PVDF polymers, 158
  Si_8O_{11}-main chain (MC)-POSS-PI films, 145

See also Polyvinylidene fluoride (PVDF) polymers
Attack, biodegradation kinetics, 94
Attenuated total reflectance–infrared (ATR–IR), nylon 6,6 studies, 107, 108*f*

B

Benzoyl peroxide (BPO)
degradation studies, 39
PP degradation and initiation by, 42, 43*f*
remote action of peroxides, 40, 42
Biochemical oxygen demand (BOD). *See* Biodegradable polymers
Biodegradable polymers
American Society of Testing and Materials (ASTM) method D5271, 94–95
biochemical oxygen demand (BOD) curves, 97, 98*f*, 99*f*
classification, 94, 288
cumulative oxygen uptake for poly(vinyl alcohol) (PVOH) samples, 97*f*, 98*f*
degrees of PVOH biodegradation, 100, 101*f*
effects of temperature and substrate concentration on BOD and degradation, 99
experimental, 95–96
four-stage kinetics, 94
future thermoplastic starch polymer development, 296–297
nutrient-mineral-buffer (NMB) stock solution, 96*t*
oxygen uptake data, 96–97
polysaccharide, 167
potential solutions to environmental problems, 93–94
respirometric characterization, 94–95
ultimate BOD and polymer concentration, 99–100
See also Thermoplastic starch polymers
Biodegradation relationships, understanding thermoplastic starch, 293–294
Biotec GmbH, thermoplastic starch polymers, 296*t*
Blends, thermoplastic starch polymers, 291
Braking energy (BE). *See* Elastomer lifetime prediction

C

Calcification of hydrogels
characterization of deposits, 306
See also Poly(2-hydroxyethyl methacrylate) (PHEMA) hydrogels
Calcium chloride. *See* Nylon 6,6 (NY66)
Calcium phosphates. *See* Poly(2-hydroxyethyl methacrylate) (PHEMA) hydrogels
Carbon nanotubes (CNTs)
addition of fillers for durability, 233
advantages, 234
atomic oxygen generation, 244*f*
charged particle energy, 235*f*
chemical changes, 240–244
conditions for proton, electron, and UV radiation, 237*t*
electron beam accelerator for electron radiation, 239*f*
experimental, 235–236
Fourier transform infrared spectroscopy (FT-IR) on multi-walled NT (MWNTs), 242, 244, 245*f*
materials, 236
modification by radiation, 234

nonlinear optical properties of exposed, to electron beam, 247, 250*f*
proton radiation, 235*f*
radial breathing mode (RBM), 245–246, 248*f*, 249*f*
radiation on CNT-containing devices, 234–235
radiation sources, 235–236
Raman spectra for SWNT powders, 246, 249*f*
Raman spectroscopy of SWNT, 245–246, 248*f*, 249*f*
scanning electron microscopy (SEM) image of single-walled nanotube (SWNT) sheets for proton and electron radiation, 240*f*
setup for proton radiation, 238*f*
space radiation, 235*f*
structural changes, 244–247
transmission electron microscopy (TEM) image of MWNT exposed to Bragg peak regions, 246, 249*f*
ultraviolet (UV) treatment, 242, 244*f*
unique properties, 233–234
X-ray photoelectron spectroscopy (XPS) of electron beam irradiated SWNTs, 241–242, 243*f*

Carboxylate anions
citric acid as source, 303
See also Poly(2-hydroxyethyl methacrylate) (PHEMA) hydrogels

Catalysis
tin (II) and tin (IV) condensation catalysts, 17
See also Foamed polysiloxane elastomers

Chain branching, free radical reactions, 61*f*

Chain confinement, tin species on polymer transition behavior, 20–21

Chemical crosslinking. *See* Polytetrafluoroethylene (PTFE)

Chemiluminescence (CL)
analysis of polymer oxidation, 62–65
dual-stage instrument, 38, 44
early stage of CL curves during PP oxidation, 63*f*
individual and combined degradation of polypropylene (PP) and hydroxyl-terminated polybutadiene (HTPB) by, 41*f*
kinetic analysis of CL - time curves, 64–65
retardation region of CL curve vs. nitroxide concentration, 65*f*
schematic of setup, 39*f*
See also Polymer degradation

Chitin, polysaccharide, 167

Chitosan, polysaccharide, 167

Citric acid
source of carboxylate anions, 303
See also Poly(2-hydroxyethyl methacrylate) (PHEMA) hydrogels

Clay
modifying surface, 262
See also Polymer clay nanocomposites

Coatings on polymers. *See* Silicon oxide coatings

Coefficient of thermal expansion, polyhedral oligomeric silsesquioxane (POSS) polyimides, 149*t*

Composites. *See* Alumina-filled epoxy composites; Polymer clay nanocomposites

Compounding formulations. *See* Elastomer lifetime prediction

Compression, thermal degradation and, 8, 9*f*

Crosslink density, polymer network, 7*f*, 8
Crystallinity, nonaromatic polyimide films, 282, 284*f*
Crystal structure
  polyamide-6/montmorillonite nanocomposites, 262
  polymer clay nanocomposites, 269–271
Cure conditions, rubber study, 84

D

Decalin
  influence of lauryl aldehyde addition on oxidation, 53, 54*f*
  oxidation, 52, 53*f*
Degradation
  oxidative, of SiO_2-coated high density polyethylene, 137–138
  See also Nylon 6,6 (NY66); Polymer degradation; Silicon oxide coatings
Deoxyribonucleic acid (DNA)
  assays, 197
  circular form of, (plasmid), 196
  circularized and twisted into supercoiled form, 196*f*
  classical DNA double helix, 196*f*
  effects of ionizing radiation, 195
  gamma rays and high-energy electrons, 195–196
  green fluorescent protein (GFP) plasmid, 196
  linear form, 199–200
  map of GFP plasmid, 202*f*
  materials and methods, 197
  properties as function of radiation dose, 201
  radiation exposure to open circle and linear forms, 201
  radiation target theory, 198–199
  rise and fall of open circle form, 199
  supercoiled forms, 198, 199
  surviving forms of GFP-plasmid after ionizing radiation, 198*f*
  target sizes in irradiated GFP plasmid, 199*t*
  transfection and expression of GFP protein, 200, 202
  unwinding of supercoiled DNA, 201–202
Differential respirometer
  acceleration factors for oxidation and compressive force of polyurethane foam, 34–35
  comparing oxidation rates by, and ultrasensitive oxygen consumption (UOC) method, 33, 34*f*
  outline, 31
  oxygen deficit trace for aged carbon-filled natural rubber, 32
  oxygen deficit trace for aged polyurethane foam, 32–33
Differential scanning calorimetry (DSC)
  crystalline structure of polymer clay nanocomposites, 271, 272*f*
  method, 264
  polymer transition behavior containing tin species, 20–21, 22*f*
Disintegration, biodegradation kinetics, 94
DNA. *See* Deoxyribonucleic acid (DNA)
Dynamic shear rheology, alumina-filled composites, 332, 333*f*

E

Earthshell, thermoplastic starch polymers, 296*t*
Elastomer lifetime prediction
  "braking energy" (BE) equation, 78

changes of tensile strength of EPDMs, 76*f*, 77*f*
compounding formulation of EPDM formulations, 72*t*, 73*t*
compounding receipt of EPDM-8 and EPDM-10, 73*t*, 74*t*
decrease in tensile energy (TE) of EPDMs by irradiation, 81*f*
decrease in ultimate elongations of EPDMs, 76*f*
experimental, 71–74
irradiation conditions, 74
map of lifetime based on TE and ultimate elongation, 81*f*
materials, 71
modulus-ultimate elongation correlation of EPDMs, 77*f*, 79*f*
relationship between BE and TE, 80*f*
relationship between modulus and ultimate elongation, 75, 78
tensile energy, 78–79
tensile strength, 75
tensile testing method, 74
time accelerated aging method, 71
ultimate elongation, 74–75
See also Polymer lifetime prediction
Elastomers. *See* Foamed polysiloxane elastomers
Electron beam radiation
accelerator for electron radiation, 239*f*
experimental conditions for carbon nanotubes, 237*t*
γ- and e-beam, of polyimides, 125–126, 128
G-values for radical formation, 126, 128
method for polyimides, 121
nonlinear optical properties of exposed carbon nanotubes, 247, 250*f*
radical formation in polyimides, 126, 128
Raman spectroscopy for changes in polyimides, 128, 129*f*
See also Carbon nanotubes (CNTs); Transparent polyimides
Elongation
rubber aging study, 85, 86
See also Elastomer lifetime prediction; Ultimate elongation
Energy dispersive X-ray spectroscopy (EDS)
characterization of calcium deposits, 306
poly(2-hydroxyethyl methacrylate) (PHEMA) and PHEMA + citrate, 311, 313*f*
Environmental issues
biodegradation as potential solution, 93–94
polymers, 93
See also Biodegradable polymers
Epoxy composites
design of high performance, 329
See also Alumina-filled epoxy composites
Epoxy polymers. *See* Photocrosslinkable epoxy polymers
Erosion
polyhedral oligomeric silsesquioxane (POSS)-polyimides to low earth orbit (LEO), 143
temperature effects, 146–147
Ethylene glycol (EG)
nylon degradation, 104–105
See also Nylon 6,6 (NY66)
Ethylene-propylene-diene elastomer (EPDM). *See* Elastomer lifetime prediction

F

Fabrication, fluoropolymers, 254
Failure criteria, understanding, for polymer lifetimes, 13

Film refractive index, nonaromatic polyimides, 280, 282*t*
Films. *See* Polyimides, nonaromatic
Flexural modulus, polymer clay nanocomposites, 268–269
Fluorescence
  growth with time of oxidation of polypropylene (PP) at different nitroxide concentrations, 67*f*
  intensity measuring alkoxyamine reaction, 65, 67
  kinetic analysis of, intensity - time curves, 68–69
  nitroxide retardation of oxidation, 65–69
  See also Free radical reactions; Profluorescent nitroxide
Fluorinated compounds. *See* Polytetrafluoroethylene (PTFE)
Fluorinated-pitch
  chemical crosslinking of polytetrafluoroethylene, 207–212
  See also Polytetrafluoroethylene (PTFE)
Fluoropolymers
  applications and properties, 254
  experimental set-up for measuring outgassed species, 255*f*
  fabrication, 254
  mass spectra of outgassed species from, 258*f*
  outgassed species from, for F_2 lithography, 256
  outgassing, 254
  semiconductor industry, 257, 259
  structures, 257*f*
  See also Polytetrafluoroethylene (PTFE)
Foamed polysiloxane elastomers
  chain confinement effects, 20–21
  isomer shift (IS), 17
  long T_2 as function of tin catalyst concentration, 24*f*
  materials, 18
  Mössbauer active ^{119}Sn, 17
  Mössbauer experiments, 18, 19*f*
  Mössbauer tin intensities as function of age, 19, 20*f*
  nuclear magnetic resonance Mobile Unit for Surface Exploration (NMR MOUSE), 23, 24*f*
  organotin hydroxide, 17
  oxidation of tin(II) with conversion of 2-ethylhexanoate ligands, 18
  quadrupole splitting (QS), 17
  segmented chain dynamics, 23, 24*f*
  short T_2 as function of tin catalyst concentration, 23*f*
  solvent extraction and tin(IV) species, 19
  thermal aging effects, 18–20
  tin(II) and tin(IV) catalysts, 17
  tin distribution by X-ray fluorescence, 20, 21*f*
  typical differential scanning calorimetry (DSC) trace, 22*f*
Focused ion beam (FIB)
  experimental set-up for measuring outgassed species from polytetrafluoroethylene (PTFE), 255*f*
  outgassed species from exposure of PTFE to, 257, 259*f*
  outgassing characteristics of PTFE on exposure, 254
Fourier transform infrared (FTIR) spectroscopy
  analysis of carbon nanotubes, 242, 244, 245*f*
  chemical structures of pristine and modified clays, 271–272, 273*t*
Fracture toughness
  adhesion in particle filled composites, 335–336
  diamine spacer length in epoxy composites, 335

equation for plane-strain, 331
particle size and size distribution of alumina-filled composites, 334, 335*f*
See also Alumina-filled epoxy composites
Fragmentation, biodegradation kinetics, 94
Free radical reactions
chemical changes to polymer during oxidation, 61*f*
chemiluminescence (CL) analysis of polymer oxidation, 62–65
comparing flash illumination and continuous illumination, 187, 189*f*, 190
competing stabilizer reactions, 61*f*
curing mechanisms, 185, 187, 190, 192
elementary reactions and rates for propagations for polymer oxidation, 61*f*
fluorescence analysis of nitroxide retardation of oxidation, 65–69
fluorescence intensity measuring alkoxyamine reaction, 65, 67
hindered phenol inhibitor, 61*f*
kinetic analysis of CL - time curves, 64–65
kinetic analysis of fluorescence intensity - time curves, 68–69
nitroxide retarder, 61*f*
oxidation of PP by varying nitroxide concentrations, 67*f*
oxidations in polyolefins, 60, 62
photo-initiated aliphatic urethane triacrylate, 187, 188*f*
polypropylene (PP) before and after oxidation, 65, 66*f*
propagation in absence of stabilizers, 61*f*
retarding effect of nitroxide, 64, 65*f*

G

Geosynchronous earth orbits (GEO)
exposure to UV and VUV radiation, 118, 120
See also Transparent polyimides
Glass fiber reinforced nylon (GFNY66). *See* Nylon 6,6 (NY66)
Glass transition temperature, adhesion of alumina-filled composites, 334
Global orientational order parameter, molecular dynamics (MD), 11–12
Green fluorescent protein (GFP)
map of GFP plasmid, 202*f*
plasmid encoding GFP, 197
radiation target theory, 198–199
target sized of irradiated, 199*t*
See also Deoxyribonucleic acid (DNA)

H

Hardness, rubber aging study, 88, 89*f*
Heat stabilizers. *See* Hindered amine stabilizers (HAS)
High density polyethylene (HDPE)
absorbance in shallow region, 137*t*
absorbance of carbonyl groups, 133, 136
deposition of SiO_2 on sample, 132
depth profile of *trans*-vinylene absorbance, 133, 134*f*
depth profiles of carbonyl absorbance, 134*f*, 135*f*
depth profiles of end-vinyl absorbance, 136*f*
effect of ion-beam irradiation, 137
end-vinyl absorbance, 136–137
experimental, 132–133
irradiation method, 132, 133*t*
long-term oxidative degradation, 137–138
measurements, 133

oxidation during long-term storage, 138
Hindered amine stabilizers (HAS)
addition of lauryl aldehyde to decalin oxidation, 52, 54*f*
chemical formulas and trade names, 50*f*
chemiluminescence (CL) of preoxidized stabilized polypropylene (PP), 51, 52*f*
images of PP films with HAS-1 after oven aging, 51*f*
images of PP films with phenolic antioxidant (PAO-1) after oven aging, 51*f*
influence of amines on oxidation of PP, 57, 58*f*
influence of HAS-1 and PAO-1 on oxidation rate of decalin/lauryl aldehyde, 52, 54*f*
influence of HAS-1 and PAO-2 on oxidation rate of decalin, 53*f*
influence of peroxides on oxidation rate, 55, 56*f*
luminescence intensity for PP with HAS-1, 53*f*
mechanisms underlying action, 57
oxidation of decalin, squalane, and mixture of lauryl aldehyde and decalin, 52, 54–55
oxidation of squalane, 53, 54*f*
oxidation of unstabilized PP, 55, 57
peroxide concentrations by equations and iodometric method, 56*f*
thermo-oxidation of stabilized PP films, 49–51
See also Polypropylene (PP)
Humidity, thermoplastic starch polymers, 294, 295*f*
Hydrogel contact lenses
spoliation by deposits, 302
See also Poly(2-hydroxyethyl methacrylate) (PHEMA) hydrogels
2-Hydroxyethyl methacrylate (HEMA). *See* Poly(2-hydroxyethyl methacrylate) (PHEMA) hydrogels
Hydroxy-terminated polybutadiene (HTPB)
chemiluminescence monitoring individual and combined degradation of polypropylene (PP) and, 40, 41*f*
combination experiment with PP, 43–44, 45*f*
infectious cross-talk between polymers, 39–40, 41*f*
simulated degradation, 45*f*
See also Oxidative aging; Polymer degradation

I

Infectious cross-talk
intermediate volatiles, 44
polymers, 39–40, 41*f*
See also Polymer degradation
Initiation, free radical reactions, 61*f*
Interactive behavior. *See* Polymer degradation
Interfacial area
critical to composite properties, 329
scanning electron microscopy (SEM) characterization of composites, 336–337
See also Alumina-filled epoxy composites
Ionizing radiation. *See* Deoxyribonucleic acid (DNA)
Ion track
energy distribution in, 222–225
formula for coaxial energy in, 224
model, 225
nanowire thickness and linear energy transfer (LET) of ion beam, 222

radius for crosslinking reactions, 221
See also Polymer nanostructures
Irradiation
aqueous polysaccharide, 167–168
degradation to electrical wires and cables, 71
high density polyethylene (HDPE), 132
ion-beam, of SiO_2-coated HDPE, 137
See also Elastomer lifetime prediction; High density polyethylene (HDPE); Polysaccharides
Isomer shift (IS), Mössbauer active ^{119}Sn, 17
Izod impact strength, nylon and glass fiber reinforced nylon by treatment, 111*f*, 112*f*

K

Kapton polyimides
chemical structure, 117*f*
Du Pont, 116
visible spectrum, 118*f*
See also Polyhedral oligomeric silsesquioxane (POSS) polyimides; Transparent polyimides
Kinetic experiments
cationic epoxy resin systems, 181
free radical resin systems, 182
See also Light curing resin systems
Kinetics
chemiluminescence - time curves, 64–65
fluorescence intensity - time curves, 68–69
four-stage, of biodegradation, 94

L

Lifetime prediction. *See* Elastomer lifetime prediction; Polymer lifetime prediction
Light curing resin systems
aromatic urethane hexaacrylate cure exotherm, 192, 193*f*
aromatic urethane hexaacrylate photocures, 190, 191*f*
calculated differential scanning calorimetry (DSC) curves for simple living polymer model, 185*f*
cationic curing mechanisms and modeling, 183–185
cationic epoxy resin systems, 181
comparing flash illumination and continuous illumination, 187, 189*f*, 190
curing of acrylate resins, 185, 187
DSC sample head, 182*f*
experimental, 181–182
free radical curing mechanisms, 185, 187, 190, 192
free radical systems, 182
inflatable wing application, 187
kinetics experiments, 181–182
light intensity effects on reaction exotherm, 185, 186*f*
modification of DSC for photocure analysis, 182*f*
urethane based polyacrylates, 187, 188*f*, 189*f*
Linear energy transfer (LET), ion beams, 221
Low Earth orbits (LEO)
dose rates for high-energy radiation, 118, 120
exposure of POSS-polyimides, 143, 149–150
sudden temperature changes, 149
thin film piezoelectric polymers, 154

See also Polyhedral oligomeric silsesquioxane (POSS) polyimides; Transparent polyimides

M

Magnetic resonance imaging (MRI). See Polymer lifetime prediction
Matrix and clay interaction, polymer nanocomposites, 271, 272, 274
Mechanical properties, polyimide films, 282, 284f
Mechanical strain, combining with radiation exposure or thermal degradation, 8, 9f
Mechanical studies
  nylon with calcium chloride solution, 110–112
  nylon with ethylene glycol (EG) solution, 109–110
Micro-fabrication. See Fluoropolymers
Mössbauer experiments
  active ^{119}Sn, 17
  spectrum from cured rubber showing tin (IV) oxidation, 19f
  tin (II) and tin (IV) oxidation states, 18
Models
  global configuration of polymer molecules, 226–229
  ion track, 225
Molecular dynamics (MD)
  aging mechanisms, 10–12
  global orientational order parameter, 11–12
  simulations of poly(dimethylsiloxane) (PDMS), 5
  See also Polymer lifetime prediction
Molecular weight
  gel permeation chromatography (GPC) studies of nylon samples, 107, 109
  pretreatment for GPC measurement of nylon, 105–106
Morphology, polymer clay nanocomposites, 265–267
Multiple quantum nuclear magnetic resonance (MQ–NMR)
  silica-filled silicone polymers, 4
  thermally aged samples, 7f, 8
  See also Polymer lifetime prediction
Multi-walled nanotubes (MWNTs). See Carbon nanotubes (CNTs)
Municipal solid waste, polymers, 93

N

Nanocomposites
  reinforcement of thermoplastic starch polymers, 293
  See also Polymer clay nanocomposites
Nano-fabrication. See Fluoropolymers
Nanostructures. See Polymer nanostructures
Nanotubes. See Carbon nanotubes (CNTs)
Nanowires
  precise size control, 226–229
  See also Polymer nanostructures
National Starch, thermoplastic starch polymers, 296t
Natural biodegradable polymers, classification, 94
Natural rubber, oxygen deficit trace for aged carbon–filled, 32
Nitroxide
  fluorescence analysis of, retardation of oxidation, 65–69
  See also Profluorescent nitroxide

Nonaromatic polyimides. *See* Polyimides, nonaromatic
Nonlinear optical properties, electron-beam exposed carbon nanotubes, 247, 250*f*
Novamont, thermoplastic starch polymers, 296*t*
Nuclear activation, oxygen-18, 27–28
Nuclear magnetic resonance (NMR)
  Mobile Universal Surface Explorer (MOUSE), 4, 23
  silica-filled silicone polymers, 4
  uniaxial relaxometry using NMR MOUSE of damaged and undamaged parts, 6*f*
  uniaxial relaxometry via NMR MOUSE on pristine DC745 ribbed pad, 7*f*
Nylon 6,6 (NY66)
  attenuated total reflectance (ATR)-infrared studies, 107, 108*f*
  changes in average molecular weight vs. treating time, 109*f*
  characterization methods, 106–107
  complexation of amide portion of, with aqueous $CaCl_2$, 108*f*
  degradation by ethylene glycol (EG), 104–105
  experimental, 105–107
  gel permeation chromatography (GPC) studies, 107, 109
  glass fiber reinforced, (GFNY66), 104
  immersion of specimens in aq. EG/$CaCl_2$ solution, 105
  materials, 105
  mechanical studies with $CaCl_2$ at 20°C/70°C, 110–112
  mechanical studies with EG solution at 108°C, 109–110
  modification via trifluoroacetylation, 106*f*
  pretreatment for GPC measurement, 105–106
  stress at break and izod impact strength vs. treating time, 111*f*, 112*f*

O

Olefins. *See* Free radical reactions
Organic esters, inducing crosslinking in starch, 292
Organotin hydroxide, catalyst, 17
Organotin ingredient. *See* Foamed polysiloxane elastomers
Oxidation
  chemical changes to polymer during, 61*f*
  chemiluminescence analysis of polymer, 62–65
  decalin, 52, 53*f*
  decalin with lauryl aldehyde, 52, 54*f*
  fluorescence analysis of nitroxide retardation of, 65–69
  influence of amines on, of polypropylene (PP), 57
  SiO_2-coated high density polyethylene, 137–138
  squalane, 53, 54*f*
  thermo-oxidation of stabilized PP films, 49–51
  unstabilized PP, 55, 57
Oxidative aging
  acceleration factors for, of polyurethane foam, 34
  accelerator factors for oxidation rate and compressive force of polyurethane foam, 35*f*
  alcohol concentration in hydroxyl-terminated polybutadiene (HTPB) vs. aging time, 29, 30*f*
  chemical changes during, of polymers, 27
  chemical derivatization of alcohol groups, 29–31

comparing oxidation rates by respirometer and ultrasensitive oxygen consumption (UOC) method, 33, 34*f*
differential respirometer, 31–35
^{19}F derivatization reaction for alcohol group, 29
^{19}F NMR of derivatization product of HTPB elastomer, 30*f*
HTPB elastomer, 27
neutron counts vs. ^{18}O content of HTPB, 28*f*
nonlinear function of time, 27
nuclear activation of ^{18}O, 27–28
outline of respirometer, 31
oxygen deficit trace of aged carbon filled natural rubber, 32*f*
oxygen deficit trace of aged polyurethane foam, 32–33
purpose of measuring acceleration factors, 34
time-temperature superposition vs. inverse temperature, 34, 35*f*
Oxygen-18, nuclear activation, 27–28
Oxygen demand. *See* Biodegradable polymers

P

Particle beams. *See* Polymer nanostructures
Particle size
fracture toughness of alumina-filled composites, 334, 335*f*
See also Alumina-filled epoxy composites
Performance relationships, understanding thermoplastic starch, 293–294
Peroxides. *See* Benzoyl peroxide (BPO)
Phenolic antioxidants (PAO)
chemical formula and trade name of PAO-1, 50*f*
comparison to hindered amine stabilizer (HAS), 49
images of polypropylene films with, after oven aging, 51*f*
influence on oxidation of decalin, 52, 53*f*
influence on oxidation of decalin/lauryl aldehyde, 52, 54*f*
mechanism underlying action of, 57
oxidation of squalane, 53, 54*f*
See also Hindered amine stabilizers (HAS)
Photoacoustic infrared spectroscopy (PAIR)
method, 265
polymer nanocomposites, 272, 274*f*
Photocrosslinkable epoxy polymers
2-(6-methyl-7-oxabicyclo[4.1.0]hept-3-yl)propyl p-styrenesulfonate (MOPSS), 319
3-ethyl-3-oxetanylmethyl p-styrenesulfonate (EOMSS), 319–320
7-oxabicyclo[4.1.0]hept-3-yl)methyl p-styrenesulfonate (EOMSS), 319
concept of thermally degradable photocrosslinking polymer, 318*f*
dissolution properties of crosslinked oligo(OHMSS), oligo(MOPSS), and oligo(EOMSS), 325, 326*f*
experimental, 319–321
FTIR spectral changes of photocrosslinked oligo(OHMSS) film, 324*f*
materials, 319–320
measurements, 320–321
photocrosslinking, 321–323
photocrosslinking and thermal degradation mechanisms, 325, 326*f*

photo-induced insolubilization of oligo(OHMSS), oligo(MOPSS), and oligo(EOMSS), 324*f*
preparation of polymers, 320
structures and properties of polymers, 322*t*
sulfonate esters, 318
synthesis of OHMSS, MOPSS, and EOMSS monomers, 321*f*
thermal degradation, 323, 325
uses, 318
Piezoelectric polymers
low Earth orbit (LEO), 154
See also Polyvinylidene fluoride (PVDF) polymers
Plantic Technologies Ltd., thermoplastic starch polymers, 296*t*
Plasmid deoxyribonucleic acid (DNA). *See* Deoxyribonucleic acid (DNA)
Plasticized starch
processing, 288–289
See also Thermoplastic starch polymers
Pollution, biodegradable materials reducing, 167
Polyamide 6. *See* Polymer clay nanocomposites
Polybutadiene, hydroxyl-terminated (HTPB). *See* Oxidative aging; Polymer degradation
Polycaprolactone (PCL), corn starch acetate/PCL blends, 292
Polyethylene (PE). *See* High density polyethylene (HDPE)
Polyhedral oligomeric silsesquioxane (POSS) polyimides
AO (atomic oxygen) exposure, 143, 145
AO reaction efficiency, 145
chemical structure of Si_8O_{11} main chain (MC)-POSS-polyimide, 143*f*
coefficients of thermal expansion, 149*t*
effect of temperature on erosion of, by hyperthermal O-atom beam, 144–145
erosion and temperature, 146–147
etch depths after exposure of hyperthermal O-atom beam, 148*t*
experimental, 142–145
exposure of, to low earth orbit (LEO), 143
physical properties, 147, 149
physical property characterization methods, 144
scanning electron microscopy (SEM) images, 146, 147*f*
self-passivation test, 145–146, 148*t*
space applications of MC-POSS-polyimide films, 149–150
sudden temperature changes, 149
surface characterization of scratched, 144
synthesis of, copolymers, 142
Poly(2-hydroxyethyl methacrylate) (PHEMA) hydrogels
applications, 302
changes in calcium content of calcium phosphates on surface of PHEMA and PHEMA + citrate, 310*f*
characterization of calcium deposits, 306
citrate ions forming strong ion pairs, 307–308
citric acid release from PHEMA + citric acid hydrogel, 305*f*
EDS (energy dispersive X-ray spectroscopic) analysis, 306
EDS spectra of PHEMA and PHEMA + citrate after implantation in rats, 313*f*
experimental, 304–306
inhibitory effect of citrate anions, 303
introduction of carboxylate anions, 302

in vitro calcification, 304–305
in vitro analysis, 307–310
in vivo calcification, 305–306
in vivo analysis, 310–311
modification through carboxymethylation, 302–303
preparation, 304
role of citric acid, 303
scanning electron microscopy (SEM) analysis, 306
SEM and light microscope (LM) images of PHEMA without citrate and with citrate after implantation in rats, 312*f*
semi-quantitative XPS analyses on calcium phosphate deposits, 308, 310
SEM micrographs after calcification in simulated body fluid (SBF), 309*f*
SEM micrographs of calcium citrate crystals, 308*f*
SEM micrographs of calcium phosphate deposits on citrate crystals, 308*f*
susceptibility to calcification, 302
ultraviolet (UV) analysis for citric acid, 304
XPS spectra of PHEMA and PHEMA + citrate hydrogels after implantation in rats, 314*f*
X-ray photoelectron spectroscopic (XPS) analysis, 306

Polyimides, nonaromatic
crystallinity of films by wide-angle X-ray diffraction (XRD), 282, 284*f*
derivation, 278
elongation vs. load curve, 284*f*
experimental, 278–279
film refractive index, 280, 282*t*
general procedure for polymerization and film preparation, 278–279
mechanical properties, 282, 284*f*
methods for measurements, 279
monomer and polymer synthesis, 279–280
solubility of films, 282, 285*t*
structures and abbreviations of alicyclic monomers, 280*f*
synthesis and properties, 282*t*
thermal properties of film, 281–282, 283*t*
thermogravimetric analysis (TGA) profiles of films, 281, 283*f*
transmission and reflective UV-vis-near infrared (NIR) spectra, 280, 281*f*
See also Polyhedral oligomeric silsesquioxane (POSS) polyimides; Transparent polyimides

Polymer clay nanocomposites
clay as nucleating agent, 271
composite designations and alkyl chain lengths, 264*t*
crystallization behavior of PA-6/MMT, 262
crystal structure, 269–271
differential scanning calorimetry (DSC) method, 264
DSC scans and crystal structure formation, 271, 272*f*
experimental, 263–265
flexural modulus, 268–269
Fourier transform infrared (FTIR) band assignments, 273*t*
hexadecylpyridinium as modifying cation, 262
intercalation of clay into matrix, 272, 274
materials, 263–264
matrix/clay interaction, 271–272, 274
mechanical properties, 267–269
mechanical testing method, 265
modifying hydrophilic surface of clay, 262

morphology using transmission electron microscopy (TEM), 266–267
nanocomposite morphology, 265–267
photoacoustic infrared spectroscopy (PAIR), 265, 274
tensile modulus, 268*f*
transmission electron microscopy (TEM) method, 264
X-ray diffraction (XRD) method, 264
XRD spectra from skin and core of injection molded test bars, 270*f*
XRD spectra of F132 nanocomposites, 266*f*
Polymer degradation
antioxidants and remote inhibition, 46
azoisobutyronitrile (AIBN) and benzoyl peroxide (BPO) experiments, 39
background, 38–39
choosing polypropylene (PP) as reactive polymer, 38–39
combined experiment and single sample pan experiment of HTPB and PP, 43–44, 45*f*
cured hydroxyl-terminated polybutadiene (HTPB), 39
dual-stage chemiluminescence (CL), 38, 44
experimental approach, 38–39
HTPB responses in Arrhenius diagram, 40, 41*f*
individual and combined degradation of PP and HTPB by CL, 41*f*
infectious cross-talk between polymers, 39–40, 41*f*
infectious intermediate volatiles, 44
monitoring, of PP and PP inhibited by volatile antioxidant, 42, 45*f*
PP degradation and initiation by BPO, 42, 43*f*
remote action of antioxidants, 42–44
remote action of peroxides, 40, 42
schematic of instrumental setup, 39*f*
simulated degradation of HTPB and PP, 43–44, 45*f*
See also Free radical reactions; Silicon oxide coatings
Polymeric materials. *See* Oxidative aging
Polymerization reaction
aromatic urethane hexaacrylate cure exotherm, 193*f*
aromatic urethane hexaacrylate photocures, 191*f*
calculated differential scanning calorimetry (DSC) curves using simple living polymer model, 185*f*
cationic curing mechanisms and modeling, 183–185
DSC exotherms from photo-initiated aliphatic urethane triacrylate resin, 188*f*
flash and continuous illuminations DSC curves for aliphatic urethane triacrylate, 189*f*
free radical curing mechanisms, 185, 187, 190, 192
light intensity effects on reaction exotherm, 186*f*
See also Light curing resin systems
Polymer lifetime prediction
accelerated aging tests, 7–10
accuracy for components and composites, 3–4
distributions of residual dipolar couplings for thermally aged silicone foam, 7*f*, 8
experiments with DC745U and M97 silica-filled silicone polymers, 4
field returned samples, 5–7

global orientational order parameter, 11–12
histogram of crosslink density in polymer network, 7*f*, 8
M97 elastomeric foams exposed to gamma radiation under compression, 8, 9*f*
MD (molecular dynamics) studies of aging mechanisms, 10–12
MD studies, 5
mechanical performance during production and disassembly, 3*f*
mechanical strain with radiation exposure or thermal degradation, 8, 9*f*
melt configurations for poly(dimethylsiloxane) (PDMS), 10*f*, 11
Multiple Quantum (MQ) NMR, 4
NMR (nuclear magnetic resonance) Mobile Universal Surface Explorer (MOUSE), 4
NMR relaxometry experiments, 4
photographs of undamaged and damaged DC745U ribbed pads, 3*f*
possible origins of damage, 6–7
simulations, 5
T_2 relaxation time MRI images of damaged and undamaged ribbed DC745U pads, 6*f*
thermal degradation and compression, 8, 9*f*
time dependence of orientational parameter for monomers at various stresses, 11*f*, 12
uncertainty, 3–4
understanding failure criteria, 13
uniaxial relaxometry using NMR MOUSE of damaged and undamaged DC745 parts, 6*f*
unilateral relaxometry via NMR MOUSE on pristine DC745 pad, 7*f*
See also Elastomer lifetime prediction
Polymer nanostructures
AFM (atomic force microscopy) for radii of nanowires, 222–223
AFM of poly(methylphenylsilane) (PMPS)-based nanowires, 226, 227*f*
chemical cores of polystyrene (PS) nanowires, 222–223
correlation between experimental and theoretical chemical core radius, 228*f*
correlation between gyration radius and degree of polymerization, 228
crosslinking of polysilane derivatives, 226–227
crosslinking reactions in chemical core, 224
energy distribution in ion track, 222–225
formula for coaxial energy in ion track, 224
global configuration of polymer molecules, 226, 228–229
ion track radius, 221
linear energy transfer (LET), 221
precise size control of nanowires, 226–229
radiation sensitivity of polymers, 221
radius of theoretical chemical core, 225
sizes of PS nanowires, 225*t*
Polymers
environmental issues, 93
radiation sensitivity, 221
See also Biodegradable polymers
Poly(methylphenylsilane) (PMPS). *See* Polymer nanostructures
Polyolefins. *See* Free radical reactions
Polypropylene (PP)

chemiluminescence monitored degradation and inhibited by volatile antioxidants, 42, 45*f*
degradation and initiation by benzoyl peroxide, 42, 43*f*
degradation by chemiluminescence, 41*f*
degradation studies, 38–39
fluorescence analysis of nitroxide retardation of oxidation, 65–69
fluorescence before and after oxidation, 66*f*
imaging luminescence of preoxidized stabilized PP, 51, 52*f*
infectious cross-talk between polymers, 39–40, 41*f*
influence of amines on oxidation of PP, 57, 58*f*
mechanism of degradation, 57
oxidation of unstabilized PP, 55, 57
oxygen uptake after oxidation and decomposition, 56*f*
remote action of antioxidants, 42–44
remote action of peroxides, 40, 42
simulated degradation, 45*f*
thermo-oxidation of stabilized PP films, 49, 51
See also Hindered amine stabilizers (HAS); Polymer degradation

Polysaccharides
biocompatibility and biodegradability, 167
carbonate radical, 176, 177*f*, 178
carboxymethyl chitin/chitosan and carboxymethyl cellulose structures, 168*f*
experimental, 168–170
hydrated electron, 171, 172*f*
ionizing irradiation of aqueous solution, 167–168
materials, 168
OH radical, 173–174, 175*f*
pulse radiolysis, 169–170
pulse radiolysis system, 170*f*
rate constants of reaction of inorganic radical with polymer chains, 174, 176
rate constants of reaction of radicals of water decomposition with polymer chains, 171, 173–174
sulphate radical, 174, 176, 177*f*

Polysiloxane elastomers. *See* Foamed polysiloxane elastomers

Polystyrene (PS)
nanowire radii by atomic force microscopy (AFM), 222–223
sizes of PS nanowires, 225*t*
See also Polymer nanostructures

Polytetrafluoroethylene (PTFE)
chemical crosslinking using fluorinated-pitch, 207–212
contact angle between droplet and surfaces of, radiation-crosslinked, (RX–PTFE), thermo-chemical-crosslinked, (CX–PTFE) and synergetic-crosslinked, (SX–PTFE), 215*t*
experimental, 206–207
experimental set-up for measuring outgassed species, 255*f*
flexural strength and flexural modulus of carbon fiber-reinforced RX–PTFE, and carbon fiber-reinforced SX–PTFE, 214*t*
^{19}F NMR spectroscopy of synergetic-crosslinked, 212–213
^{19}F NMR spectrum of heat-treated, with fluorinated-pitch, 209, 210*f*
ionizing radiation, 205
mass spectra of outgassed species from, 259*f*
materials and crosslinking treatments, 206
measurement methods, 206–207
mechanical properties of carbon fiber-reinforced, and carbon

In Polymer Durability and Radiation Effects; Celina, M., et al.;
ACS Symposium Series; American Chemical Society: Washington, DC, 2007.

fiber-reinforced PTFE with fluorinated-pitch, 211*t*
outgassed species from, 257
outgassing, 254
radiation-crosslinking, 205
reaction kinetics of thermo-chemical crosslinking of, with fluorinated-pitch, 211
scanning electron microscopy (SEM) photographs of, and fluorinated-pitch, 208*f*
synergistic crosslinking, 212–215
tensile strength and Young's modulus of carbon fiber-reinforced RX–PTFE and carbon fiber-reinforced SX–PTFE, 213, 214*f*
thermal properties of, radiation-crosslinked, thermo-crosslinked, and synergistic, 212*t*
thermal properties of heat-treated, with fluorinated-pitch, 208*f*
thermogravimetric analysis (TGA) curves of fluorinated-pitch, PTFE, and heat-treated PTFE with fluorinated-pitch, 209, 210*f*
See also Fluoropolymers
Polyurethane foam
accelerator factors for oxidation rate and compressive force, 35*f*
oxygen deficit trace for aged, 32–33
Poly(vinyl alcohol) (PVOH)
biochemical oxygen demand (BOD) curves, 97, 98*f*, 99*f*
blends with thermoplastic starch polymers, 291
degrees of degradation, 100, 101*f*
experimental, 95–96
oxygen uptake, 96, 97*f*, 98*f*
testing biodegradability, 94–95
ultimate BOD and polymer concentration, 99–100
See also Biodegradable polymers
Poly(vinylidene fluoride) (PVDF) polymers
atomic oxygen (AO), 158
bimorph performance, 155, 158, 159*f*
combined AO plasma and VUV radiation effects, 160, 162, 163*f*
copolymers of VDF and trifluoroethylene (TrFE), 154
d_{31} coefficients and storage moduli for bimorphs vs. temperature, 159*f*
experimental, 154
gel content of, exposed to gamma and VUV radiation, 161*f*
high performance polymers, 154
ionizing radiation, 160
loss of d_{33} piezoelectric coefficient vs. annealing temperature, 156*f*, 157*f*
remanent polarization of PVDF and $P(VDF_{80}$-$TrFE_{20})$ vs. temperature, 158*f*
surface SEM images before and after AO/VUV exposure, 163*f*
temperature effects, 154–155, 158
thin film piezoelectric polymers, 154
vacuum ultraviolet (VUV) radiation, 160
Prediction
nonlinear properties vs. aging time, 27
See also Elastomer lifetime prediction; Oxidative aging; Polymer lifetime prediction
Processing
modified techniques for thermoplastic starch, 291
review of, for thermoplastic starch, 289–290
understanding thermoplastic starch, 293–294

Profluorescent nitroxide
approach using 1,1,3,3-tetramethyldibenzo[e,g]isoindolin-2-yloxyl (TMDBIO), 60
chemiluminescence (CL) analysis of polymer oxidation, 62–65
early stage of CL curves during oxidation of polypropylene (PP) with TMDBIO, 63*f*
fluorescence analysis of nitroxide retardation of oxidation, 65–69
fluorescence increase from PP with TMDBIO, 66*f*
growth in fluorescence vs. time of PP oxidation with TMDBIO, 67*f*
increase in fluorescence intensity from TMDBIO doped PP vs. nitroxide concentration, 68*f*
primary free radical scavenger, 60
slope of retardation region of CL curve vs. TMDBIO concentration, 65*f*
See also Free radical reactions
Propagation
free radical reactions, 61*f*
reactions and rates, 61*f*
Proton radiation
cyclotron setup, 238*f*
description of effects, 235*f*
experimental conditions for carbon nanotubes, 237*t*
See also Carbon nanotubes (CNTs)
Pulse radiolysis. *See* Polysaccharides

Q

Quadrupole splitting (QS), Mössbauer active ^{119}Sn, 17

R

Radiation
combining, exposure with mechanical strain, 8, 9*f*
damage to space facility, 233
direct modification of carbon nanotube (CNT) surface, 234
sensitivity of polymers, 221
sources for CNT study, 235–236
See also Deoxyribonucleic acid (DNA)
Radiation chemistry. *See* Transparent polyimides
Radiation crosslinking. *See* Polytetrafluoroethylene (PTFE)
Radiation induced degradation. *See* Elastomer lifetime prediction
Radical production, oxidation of high density polyethylene, 138
Radicals
pulse radiolysis of polysaccharides, 170
See also Polysaccharides
Raman spectroscopy
radial breathing mode (RBM), 245–246
structural changes of carbon nanotubes, 245–246, 248*f*, 249*f*
Reactive blending, thermoplastic starch/polymer blends, 292–293
Reactive modification, thermoplastic starch polymers, 292–293
Refractive index, nonaromatic polyimide films, 280, 282*t*
Relationships, thermoplastic starch polymers, 293–294
Relative humidity, thermoplastic starch polymers, 294, 295*f*
Relaxation time T_2, effect of tin on polymer segment mobility, 23, 24*f*
Respirometer. *See* Differential respirometer
Respirometer, oxygen
determining ready biodegradability, 94–95
See also Biodegradable polymers

Rheology
dynamic shear, of alumina-filled composites, 332, 333*f*
thermoplastic starch, 289–290
See also Alumina-filled epoxy composites
Ridigization on Command™ (ROC). *See* Light curing resin systems
Rodenberg Biopolymers, thermoplastic starch polymers, 296*t*
Rubber, natural, oxygen deficit trace for aged carbon–filled, 32
Rubber aging study
abrasion, 86, 88
aged properties, 86, 88
baseline conditions, 85–86
complex property changes with time, 83–84
cure matrix, 84*t*
experimental, 84
hardness, 88, 89*f*
mean and standard deviation of moduli vs. time, 88*f*
mean and standard deviation of tensile strength vs. time, 87*f*
physical properties, 85*t*
sulfur bonds, 89–90
tensile strength change vs. time, 87*f*

S

Scanning electron microscopy (SEM)
calcification in simulated body fluid, 309*f*
calcium citrate crystals, 308*f*
calcium phosphate on citrate crystals, 308*f*
characterization of calcium deposits, 306
poly(2-hydroxyethyl methacrylate) (PHEMA) and PHEMA + citrate after implantation in rats, 311, 312*f*
Sensitivity, radiation, of polymers, 221
Silicon oxide coatings
experimental, 132–133
irradiation method, 132, 133*t*
oxidation during long-term storage, 138
sample and SiO_2 deposition, 132
See also High density polyethylene (HDPE)
Siloxane polymers
poly(dimethylsiloxane) (PDMS) melts, 10*f*, 11
silica-filled, in predicting lifetime, 4–5
See also Foamed polysiloxane elastomers; Polymer lifetime prediction
Simulations, molecular dynamics (MD) of poly(dimethylsiloxane) (PDMS), 5
Single-walled nanotubes (SWNTs). *See* Carbon nanotubes (CNTs)
Size control, nanowires, 226–229
Size distribution
fracture toughness of alumina-filled composites, 334, 335*f*
See also Alumina-filled epoxy composites
Solubility, polyimide films, 282, 285*t*
Space materials
main chain-polyhedral oligomeric silsesquioxane (MC-POSS) polyimides, 149–150
radiation effects, 233
See also Carbon nanotubes (CNTs) Polyhedral oligomeric silsesquioxane (POSS) polyimides; Polyvinylidene fluoride (PVDF) polymers
Space radiation, types, 235*f*
Squalane, oxidation, 53, 54*f*
Starch
gelatinization, 289

salt additives and, structure, 290
thermoplastic, 288–289
See also Thermoplastic starch polymers
Storage. *See* Rubber aging study
Storage modulus, adhesion of alumina-filled composites, 334
Stress at break, nylon and glass fiber reinforced nylon by treatment, 111*f*, 112*f*
Structure-property relationships
understanding thermoplastic starch, 293–294
See also Alumina-filled epoxy composites; Thermoplastic starch polymers
Sulfonate esters
precursor to alkenes, 318
See also Photocrosslinkable epoxy polymers; Polymer nanostructures; Polytetrafluoroethylene (PTFE)
Sulfur content
network morphologies in rubber, 89–90
rubber study, 84
Synergetic crosslinking (chemical-radiation)
polytetrafluoroethylene, 212–215
See also Polytetrafluoroethylene (PTFE)
Synthetic biodegradable polymers, classification, 94

T

Tear strength, rubber aging study, 86, 88
Tensile energy (TE)
ethylene-propylene-diene elastomer (EPDM), 78–79, 81*f*
See also Elastomer lifetime prediction
Tensile modulus, polymer clay nanocomposites, 268
Tensile strength
ethylene-propylene-diene elastomers (EPDM), 75, 76*f*, 77*f*
rubber aging study, 86, 87*f*
See also Elastomer lifetime prediction
Termination, free radical reactions, 61*f*
Theoretical oxygen demand (ThOD). *See* Biodegradable polymers
Thermal aging, effects watching Mössbauer tin intensities as function of age, 19, 20*f*
Thermal decrosslinking. *See* Photocrosslinkable epoxy polymers
Thermal degradation
combining with mechanical strain, 8, 9*f*
compression and, 8, 9*f*
concept of, photocrosslinking polymer, 318
mechanism, 325, 326*f*
sulfonate esters decomposing in polymers, 323, 325
See also Photocrosslinkable epoxy polymers
Thermal properties, nonaromatic polyimide films, 281–282, 283*t*
Thermo-chemical crosslinking. *See* Polytetrafluoroethylene (PTFE)
Thermogravimetric analysis (TGA), nonaromatic polyimide films, 281, 283*f*
Thermo-oxidation, stabilized polypropylene films, 49, 51
Thermoplastic polymers. *See* Nylon 6,6 (NY66)
Thermoplastic starch polymers
blends with poly(vinyl alcohol) (PVOH), 291
commercial applications and products, 294, 296

corn starch
acetate/polycaprolactone (PCL) blends, 292
crosslinked starch by organic esters, 292
diffusivity of water at different temperatures, 294, 295*t*
future developments, 296–297
models of gelatinization, 289
nanocomposite reinforcement, 293
processing plasticized starch, 288–289
reactive blending, 292–293
reactively modified, 292–293
relative humidity and mechanical properties, 294, 295*f*
research on processing, rheology and properties, 289–290
starch gelatinization, 289
structure breakdown by addition of salts, 290
structure-property-processing-performance-biodegradation relationships, 293–294
water sensitivity, 290–291
See also Biodegradable polymers

Time accelerated method
ethylene-propylene-diene (EPDM), 71
See also Elastomer lifetime prediction

Tin (^{119}Sn) catalysts
chain confinement effects in polymers, 20–21
distribution by X-ray fluorescence in fresh and thermally aged, 20, 21*f*
effect on polymer segment mobility, 23, 24*f*
Mössbauer active, 17
thermal aging effects watching Mössbauer tin intensities as function of age, 19, 20*f*

Tin 2-ethylhexanoate. *See* Foamed polysiloxane elastomers

Toughness, fracture
adhesion in particle filled composites, 335–336
diamine spacer length in epoxy composites, 335
equation for plane-strain, 331
particle size and size distribution of alumina-filled composites, 334, 335*f*
See also Alumina-filled epoxy composites

Transmission electron microscopy (TEM)
method, 264
nanocomposite morphology, 266–267

Transparent polyimides
applications of aromatic, 116
carbonyl groups of imides for Kapton and Ultem, 116–117
chemical structures for Kapton and Ultem, 117*f*
chemical structures of some, 119*f*
dependence of X-ray photoelectron spectroscopy (XPS) C1s/O1s surface atom ration on exposure time, 125, 126*f*
electron beam radiolysis method, 121
experimental, 120–121
γ- and e-beam radiolysis of, 125–126, 128
γ-radiolysis method, 121
geosynchronous earth orbits (GEO), 118, 120
G-values for radical formation, 126, 128
low earth orbits (LEO), 118, 120
photo-oxidation of surfaces of film by XPS studies, 123*f*, 124
preparation of, with low absorption, 117–118
radical concentration vs. ultraviolet (UV) exposure time in oxygen, 122*f*

radical formation, 126, 128
Raman spectroscopy studies of Ultem on radiolysis, 128, 129*f*
samples, 120
typical XPS C1s spectra of surface of film, 127*f*
UV photolysis method, 120
UV radiolysis of, 122–124
visible spectrum of Kapton and Ultem, 118*f*
visible transmission spectra of some, 121*f*
vacuum ultraviolet (VUV) photolysis method, 120
VUV radiolysis, 125
XPS O1s/C1s ratio for, in surface layers of films, 124
Trifluoroacetic anhydride (TFAA)
functionalizing alcohol groups, 27
See also Oxidative aging

U

Ultem polyimides
chemical structure, 117*f*
General Electric, 116
visible spectrum, 118*f*
See also Transparent polyimides
Ultimate biochemical oxygen demand (UBOD). *See* Biodegradable polymers
Ultimate elongation
ethylene-propylene-diene elastomers (EPDM), 74–75, 76*f*
relationship to modulus, 75, 77*f*, 78, 79*f*
See also Elastomer lifetime prediction
Ultrasensitive oxygen consumption (UOC) method
comparison of oxidation rates by respirometer and, 33, 34*f*
nuclear activation of ^{18}O in hydroxyl-terminated polybutadiene (HTPB), 27–28
Ultraviolet (UV) radiation
polyimides, 122–124
treatment modifying carbon nanotubes, 242, 244*f*
UV photolysis studies, 120
See also Carbon nanotubes (CNTs)
Ultraviolet (UV) spectrometry, citric acid analysis, 304, 305*f*
Ultraviolet (UV) stabilizers. *See* Hindered amine stabilizers (HAS)
Ultraviolet-visible-near infrared (NIR) spectroscopy, transmission and reflection, of nonaromatic polyimides, 280, 281*f*
Unmanned aerial vehicles (UAVs)
light curing materials for, 180–181
See also Light curing resin systems
Urethane based polyacrylates
application of inflatable wing, 187
aromatic, photocures, 190, 191*f*
cure exotherm, 192, 193*f*
free radical curing, 185, 187
See also Light curing resin systems

V

Vacuum ultraviolet (VUV) Radiolysis
combined atomic oxygen and, on poly(vinylidene fluoride) (PVDF) polymers, 160, 162
polyimides, 125, 126*f*
PVDF polymers, 160
VUV photolysis method, 120
See also Polyvinylidene fluoride (PVDF) polymers
Vinylidene fluoride-based polymers. *See* Polyvinylidene fluoride (PVDF) polymers

W

Water
diffusivity in thermoplastic starch polymers, 294, 295*t*
sensitivity of starch, 290
Wide angle X-ray diffractions (WAXD), crystallinity of polyimide films, 282, 284*f*

X

X-ray diffraction (XRD)
method, 264
nanocomposite crystal structure, 269–271
nanocomposite morphology, 265–266
X-ray photoelectron spectroscopy (XPS)
characterization of calcium deposits, 306
electron beam irradiation of single-walled nanotubes (SWNT), 241–242, 243*f*
poly(2-hydroxyethyl methacrylate) (PHEMA) and PHEMA + citrate hydrogels after implantation in rats, 311, 314*f*

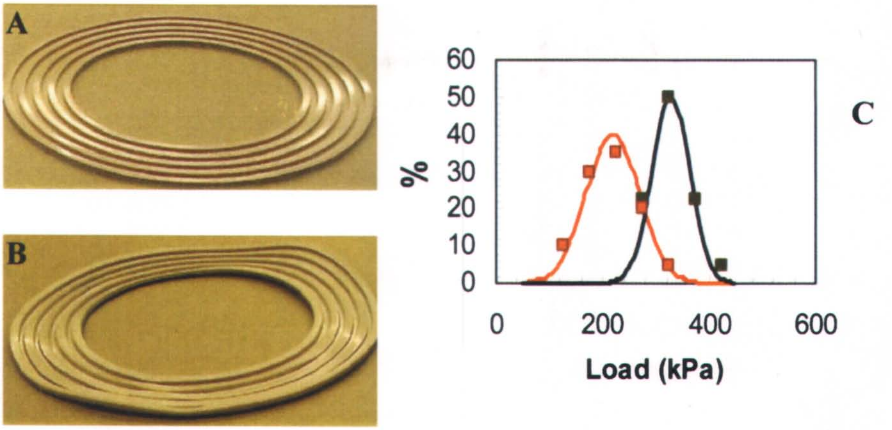

Figure 1.1. Photographs of (A) undamaged and (B) damaged DC745U ribbed pads; (C) histogram of percent load retention at a given compressive gap for open celled foam of M97 components at production (black) and disassembly 2-20 years after service (red).

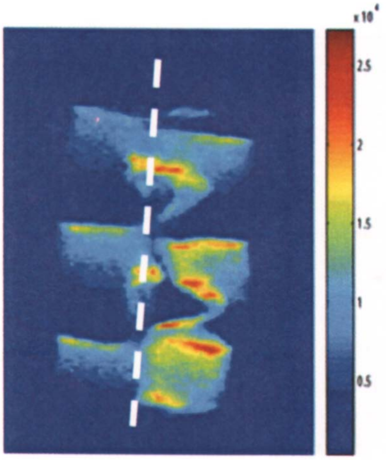

Figure 1.2. T_2 weighted MRI image back-to-back ribbed DC745U pads (undamaged on left, damaged on right). Intensity scale on right from low (blue) to high (red) T_2. (Reproduced with permission from reference 4. Copyright 2006 Elsevier.)

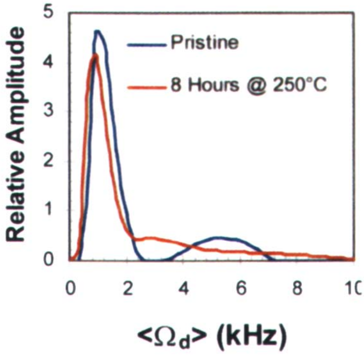

Figure 1.5. Distributions of residual dipolar couplings obtained from a Thikonov regularization of the MQ-NMR growth curve for thermally aged silicone foam. The residual dipolar coupling has been shown to be an indirect measure of crosslink density and represents essentially a histogram of the crosslink density in the polymer network. Aged samples have been shown to undergo chain scissioning reactions.

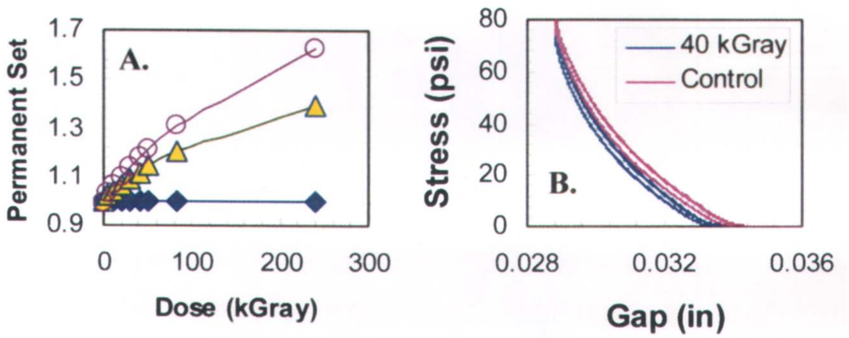

Figure 1.6. (A) Permanent tensile set in M97 solid elastomers exposed to gamma radiation while under no elongation (solid diamonds), 150% of unperturbed length (triangles), and 200% of unperturbed length (circles). (B) Stress as a function of compressed gap for M97 foam aged under compressed to 25% (deposited gamma radiation dose of 0 and 40 kGray). Note the delayed onset to stress at low compression due to permanent compression set.

In Polymer Durability and Radiation Effects; Celina, M., et al.;
ACS Symposium Series; American Chemical Society: Washington, DC, 2007.

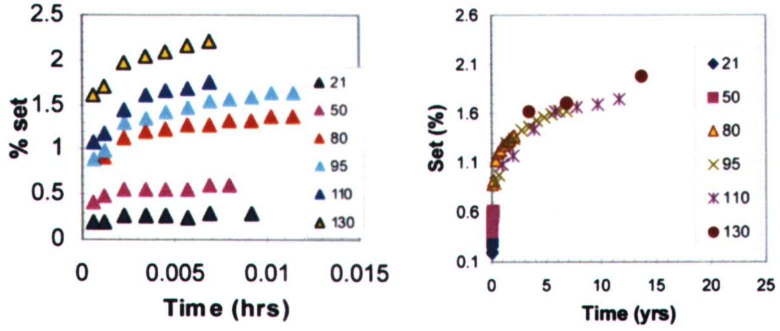

Figure 1.7. Results of time and temperature dependent studies of compression set in open-celled, porous M97 silicone foams. (A) % compression set as a function of time for the temperatures (°C) listed; (B) Master curve at 21 °C derived from a time-temperature-superposition analysis of the data in (A). The activation energy derived from this analysis was 78 kJ/mol.

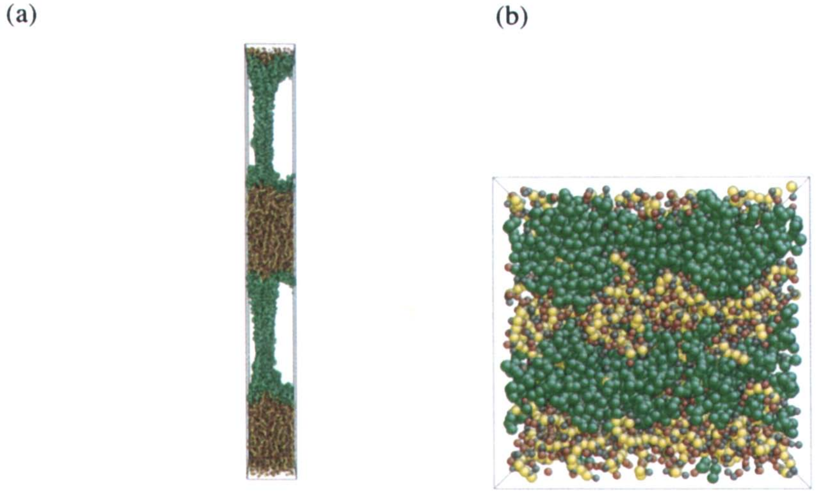

Figure 1.8. (a) Snapshot of the PMDS melt at σ = 60 MPa and t = 1.5 ns. Particles that are on the surface of the cavity are colored green. (b) Initial configuration of the PDMS melt and cavity particles are traced back to the initial configuration and colored green. (Reproduced with permission from reference 26. Copyright 2006 Elsevier.)

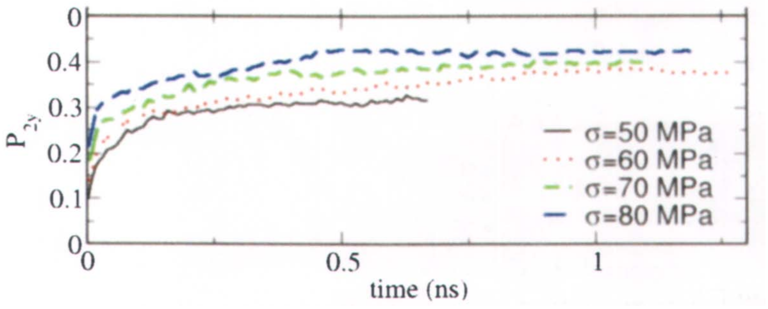

Figure 1.9. Time dependence of the orientational parameter P_{2y} at various stresses. Stress values increase from the bottom up.

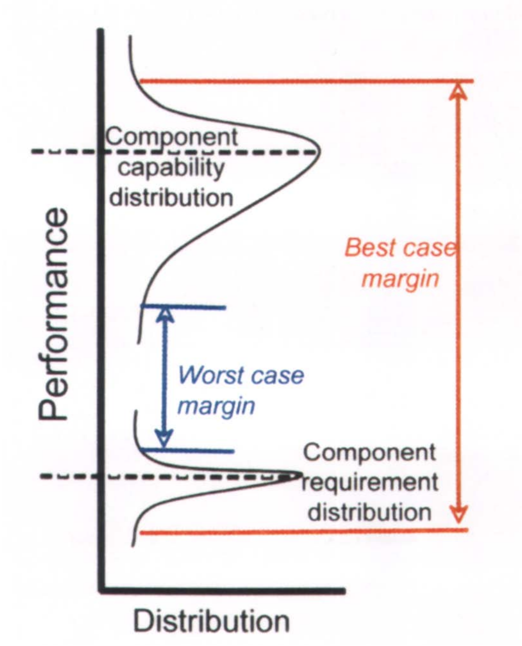

Figure 1.10. Comparison of hypothetical set of distibutions for a component's capability versus its requirement, with potential variations in performance margins illustrated.

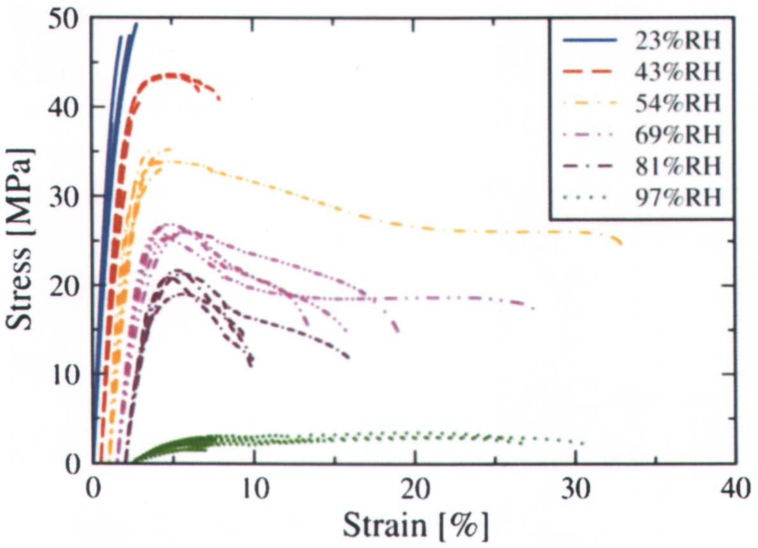

***Figure 24.1.** The effect of relative humidity (RH) on mechanical properties [stress-strain curves] of at thermoplastic starch polymer.*

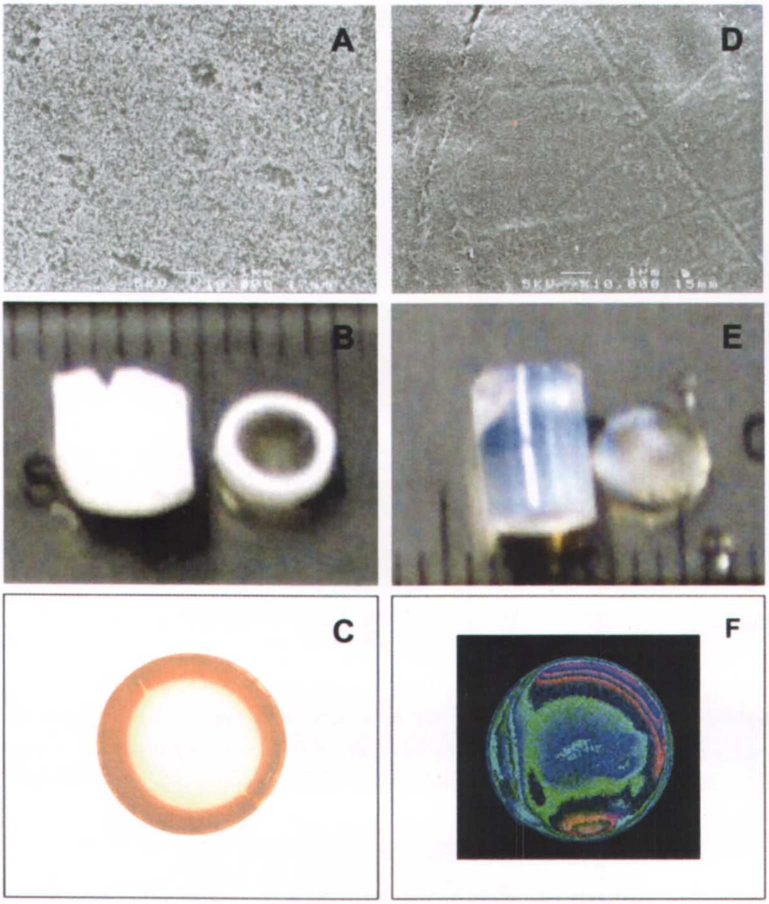

Figure 25.5. SEM, photographs, and LM images of PHEMA without citrate (A-C) and PHEMA plus citrate (D-F) after subcutaneous implantation in rats for 2 months